

NONLINEAR STOCHASTIC MODELING AND
ANALYSIS OF CARDIOVASCULAR SYSTEM
DYNAMICS – DIAGNOSTIC AND PROGNOSTIC
APPLICATIONS

By

HUI YANG

Bachelor of Science
China University of Mining and Technology
Beijing, China, 2002

Master of Science
China University of Mining and Technology
Beijing, China, 2005

Submitted to the Faculty of the
Graduate College of the
Oklahoma State University
in partial fulfillment of
the requirements for
the Degree of
DOCTOR OF PHILOSOPHY
May, 2009

UMI Number: 3387630

All rights reserved

INFORMATION TO ALL USERS

The quality of this reproduction is dependent upon the quality of the copy submitted.

In the unlikely event that the author did not send a complete manuscript and there are missing pages, these will be noted. Also, if material had to be removed, a note will indicate the deletion.



UMI 3387630

Copyright 2010 by ProQuest LLC.

All rights reserved. This edition of the work is protected against unauthorized copying under Title 17, United States Code.



ProQuest LLC
789 East Eisenhower Parkway
P.O. Box 1346
Ann Arbor, MI 48106-1346

NONLINEAR STOCHASTIC MODELING AND
ANALYSIS OF CARDIOVASCULAR SYSTEM
DYNAMICS – DIAGNOSTIC AND PROGNOSTIC
APPLICATIONS

Dissertation Approved:

Dr. Satish T. S. Bukkapatnam

Dissertation Adviser

Dr. Ranga Komanduri

Co-Adviser

Dr. William J. Kolarik

Dr. Zhenyu (James) Kong

Dr. A. Gordon Emslie

Dean of the Graduate College

COPYRIGHT

BY

HUI YANG

December, 2008

ACKNOWLEDGMENTS

I would like to express my deepest appreciation to my academic advisor, Dr. Satish T. S. Bukkapatnam, for his academic advice, inspirations, continuous motivations and generous financial support for my Ph. D study. I also owe my infinite gratitude to my co-advisor, Dr. Ranga Komanduri for his guidance, high standard, professionalism and immense impact on my research. Dr. Satish and Dr. Komanduri are wonderful teachers, excellent researchers, and inspiring advisors – the perfect mentors every graduate student can dream of. I feel fortune to come across them in my life. Sincere thanks are also due to my dissertation committee member, Dr. William J. Kolarik for introducing me heart reliability, risk analysis concepts. Special thanks to my dissertation committee member, Dr. James Kong for teaching me Bayesian statistics and providing technical advice. My heartfelt thanks are also owed to Dr. Bruce Benjamin, Dr. Martin Hagan, Dr. Lionel Raff and Dr. Randy S. Wymore, from Center of Signal Analysis and Integrated Diagnostics (SAID), for introducing neural network design, cardiovascular physiological knowledge and ECG feature extraction techniques.

Many thanks to all the friends and colleagues for their great friendship and encouragement throughout my PhD study in Stillwater.

My extreme appreciation goes to my wife, Yingfei Jia for her love, understanding and support at the time of difficulties.

Finally, thank my beloved parents for their encouragements, sacrifices, patiences and affections! I dedicate my dissertation to my dear father and mother!

TABLE OF CONTENTS

CHAPTER I	1
INTRODUCTION	1
1.1 Research motivations	1
1.2 Research objectives	3
1.3 Major contributions	4
1.4 Organization of the dissertation	5
1.5 References	7
CHAPTER II	8
BACKGROUND AND LITERATURE REVIEW	8
2.1 Cardiac conduction system.....	8
2.2 12-Lead electrocardiogram (ECG) and vectorcardiogram (VCG) signals.....	9
2.3 A primer on nonlinear dynamic analysis.....	12
2.4 Wavelet analysis of ECG signals	17
2.5 Databases.....	22
2.6 References	24
CHAPTER III	29
RESEARCH METHODOLOGY	29
3.1 Signal representation	30
3.1.1 Nonlinear adaptive wavelet representation of ECG signals	30
3.1.2 Dynamic VCG representation.....	31
3.2 Feature extraction and classification	32
3.2.1 Atrial fibrillation state classification.....	32
3.2.2 Myocardial infarction identification using recurrence quantification analysis of VCG signals.....	32
3.2.3 Vectorcardiographic octant features for the diagnostics of heterogeneous myocardial infarction	33
3.3 Simulation and prognostic modeling.....	35
3.3.1 Local recurrence prediction in nonstationary chaotic systems	35
3.3.2 Radial basis function simulation modeling of VCG signals.....	36

PART I SIGNAL REPRESENTATION

CHAPTER IV.....	37
CUSTOMIZED WAVELET REPRESENTATION OF ECG SIGNALS.....	37
4.1 Background	38
4.2 Phase space fiducial pattern extraction	40
4.3 Least square matching wavelet design.....	43
4.4 Implementation and results	46
4.5 Summary	53
4.6 References	54
CHAPTER V	57
DYNAMIC VCG REPRESENTATION.....	57
5.1 Background	58
5.2 Research methodology	60
5.2.1 Spatiotemporal VCG attractor representation.....	61
5.2.2 Lag reconstructed spatiotemporal ECG attractor.....	64
5.2.3 Color coding of spatiotemporal VCG representation	68
5.3 Results and discussion.....	70
5.4 Concluding remarks	79
5.5 References	80

PART II FEATURE EXTRACTION AND CLASSIFICATION

CHAPTER VI.....	83
ATRIAL FIBRILLATION STATE CLASSIFICATION.....	83
6.1 Introduction	83
6.2 Background	84
6.3 Feature extraction.....	87
6.3.1 Statistical Descriptors and Principal Component Analysis (PCA).....	87
6.3.2 QRST subtraction.....	90
6.4 AF state classification using CART model.....	92
6.5 Summary	98
6.6 References	99

CHAPTER VII	105
MYOCARDIAL INFARCTION IDENTIFICATION USING RECURRENCE QUANTIFICATION ANALYSIS (RQA) OF VCG SIGNALS	105
7.1 Introduction	105
7.2 Research methodology	107
7.3 Implementation and results	112
7.3.1 Recurrence quantification and feature extraction	113
7.3.2 Feature analysis.....	115
7.3.3 Classification.....	120
7.4 Summary	124
7.5 References	126
CHAPTER VIII	130
VECTORCARDIOGRAPHIC OCTANT FEATURES FOR THE DIAGNOSTICS OF HETEROGENEOUS MYOCARDIAL INFARCTION	130
8.1 Introduction	130
8.2 Feature extraction.....	132
8.3 Feature analysis	137
8.4 Classification.....	139
8.5 Discussions.....	144
8.6 Summary	146
8.7 References	147
PART III SIMULATION AND PROGNOSTIC MODELING	
CHAPTER IX	150
LOCAL RECURRENCE PREDICTION IN NONSTATIONARY CHAOTIC SYSTEMS	150
9.1 Introduction	150
9.2 Background	153
9.3 Local attractor topology analysis	156
9.4 Simulation experiment results.....	163
9.5 Summary	169
9.6 References	170

CHAPTER X	172
RADIAL BASIS FUNCTION SIMULATION MODELING OF VCG SIGNALS	172
10.1 Poincare sectioning of vectorcardiogram.....	173
10.2 Heart rate variability.....	174
10.3 Research methodology	176
10.4 Transformation from VCG to standard 12 lead ECG signals	178
10.5 Implementation results	178
10.6 Summary	185
10.7 Reference.....	186
CHAPTER XI	189
CONCLUSIONS AND FUTURE WORK	189
11.1 Conclusions	189
11.2 Future work	191

LIST OF TABLES

Table 6.1 Distribution of 80 recordings among learning sets and test sets.....	85
Table 6.2 Summary of final results of the 2004 PhysioNet Challenge.....	86
Table 6.3 S vs T learning data set RR interval and skewness of RR feature table	96
Table 6.4 S vs T testing data set RR interval and skewness of RR feature table	96
Table 7.1 Linear model misclassification results using F1 and other principal features (F2 F6).....	116
Table 7.2 Relative importance of principal features F1 to F6 using linear regression ...	121
Table 7.3 Results of linear regression classification for MI and HC.....	121
Table 7.4 Results of neural network (NN) classification for MI and HC.....	123
Table 8.1 VCG octant definition and color mapping.....	135
Table 8.2 Statistical analysis (Kolmogorov-Smirnov test) of three groups of features..	138
Table 8.3 Experiment results of CART classification model using stochastic training datasets	140

LIST OF FIGURES

Figure 1.1 Pie chart of death causes in the world	1
Figure 2.1 Electrophysiology of the heart and different waveforms for each of the specialized cells in the heart	8
Figure 2.2 Electrical and mechanical events diagram during one heart beat.....	9
Figure 2.3 The electrodes placement in VCG measurement system	10
Figure 2.4 Rossler attractor and local evolution	13
Figure 2.5 Rossler attractor recurrence plot.....	15
Figure 2.6 Time-frequency resolution of wavelet transforms	18
Figure 3.1 Schematic of research methodology.....	29
Figure 4.1 Procedure for customized wavelet design from system nonlinear dynamics..	38
Figure 4.2 An illustration of trajectories of an attractor intersecting a (planar) Poincare section	41
Figure 4.3 Time domain plot of a representative ECG signal trace (a01)	47
Figure 4.4 State space portrait reconstructed from time delay coordinates.....	48
Figure 4.5 ECG pattern ensembles extracted from Poincare section.....	49
Figure 4.6 Matching wavelet extracted from fiducial signal pattern	49
Figure 4.7 Matching wavelet representation entropy variation with various polynomial degrees	50

Figure 4.8 Entropy comparison between standard wavelets and matching wavelets	51
Figure 4.9 Entropy distribution for different wavelet representations, taken over all ECG signals in the database considered	52
Figure 4.10 Histogram of matching wavelet transform coefficients: (a) customized wavelet, (b) Morlet wavelet	53
Figure 5.1 Frames from dynamic VCG representation of a patient with myocardial infarction, anterior.....	63
Figure 5.2 Frames from lag reconstructed dynamic EKG attractor representation for a normal subject.....	67
Figure 5.3 Color coded dynamic VCG representation plot of a healthy control subject...69	
Figure 5.4 Color coded dynamic VCG representation plot of a patient with dysrhythmia and atrial fibrillation	72
Figure 5.5 Color coded dynamic VCG representation plot of a patient with myocardial infarction, infero-latera	74
Figure 5.6 Color coded dynamic VCG representation plot of a patient with myocardial infarction, antero-lateral.....	76
Figure 5.7 Color coded dynamic VCG representation plot of a patient with bundle branch block.....	78
Figure 6.1 Automated identification of peaks and endpoints of various waveforms in an ECG signal using an automated feature extraction routine	88
Figure 6.2 Time-scale representation (scalogram) of a representative ECG signal	89
Figure 6.3 Summary of QRST subtraction results for a representative ECG signal (from a T-case) showing the original signal (top), filtrate from thresholding containing	

predominantly ventricular components (middle) and residue from thresholding containing predominantly atrial and AF waves (bottom)	91
Figure 6.4 Frequency spectra of a representative ECG signal before and after QRST subtraction.....	92
Figure 6.5 (a) Peak frequencies of various N and T cases, (b) Peak frequencies of the first two (First 2) and last two (Last 2) beats of N and T ECG signals.....	93
Figure 6.6 (a) and (b) Learning and testing dataset RR interval and average features scatter plot, respectively. (Average feature is the average value of mean of QRS, mean of peak, mean of height of T wave, mean of QT interval, mean of ST segment, and mean of T duration)	95
Figure 7.1 Coordinate system used for obtaining VCG signals.....	107
Figure 7.2 A representative VCG plot showing the vector loops for P, QRS, and T wave activities	108
Figure 7.3 A graphical illustration of relationship among a VCG, the X,Y,Z time series and the unthresholded recurrence plot	110
Figure 7.4 A representative thresholded recurrence plot of VCG	111
Figure 7.5 Flow diagram showing research methodology used	112
Figure 7.6 Histogram comparisons between HC (filled green) and MI(not shaded) for the six RQA quantifiers, namely, recurrence rate (Γ), determinism (DET), linemax (LMAX), entropy (ENT), laminarity (LAM), and trapping time (TT) (Histogram x-axis is feature value, and y-axis is the normalized frequency)	114
Figure 7.7 Histogram distributions of PCA feature values F1 to F6 for MI (not shaded) and HC (shaded green) (Histogram x-axis is feature value and y-axis is the normalized frequency)	117

Figure 7.8 (a) to (e) Distribution of values of features F2 through F6 vs. F1 for MI (red \diamond) and HC (blue +) subjects with linear separator obtained using a genetic algorithm	118
Figure 7.9 Relative importance of RQA quantifiers in the first principal feature (F1) ..	119
Figure 7.10 Radial basis function (RBF) neural network (NN).....	122
Figure 7.11 Variation of % accuracy of the neural network (NN) (both training and testing) with the number of data points for MI and HC.....	124
Figure 8.1 Frank XYZ VCG ensembles, (a) X-direction; (b) Y-direction, (c) Z-direction	132
Figure 8.2 VCG attractor and its 2D projection plots with Q, R, T vectors	133
Figure 8.3 (a) VCG electrodes placement in human body; (b) the corresponding octant definitions	134
Figure 8.4 VCG trajectories with different octant colors in the 3D coordinate system, (a) HC; (b) MI	136
Figure 8.5 Kolmogorov-Smirnov statistic variations of 46 features.....	137
Figure 8.6 CART model cross validation curves and Tree size selection	141
Figure 8.7 Optimal CART tree structure for the classification of MI in PTB database .	142
Figure 8.8 Detailed classification of PTB database MI and HC in (a) step 1 and (b) step 2	143
Figure 8.9 Healthy control (368) and myocardial infarction (80) distribution in 3D feature space (Oct0MaxN, T octant position and Oct2AvgN).....	144
Figure 8.10 Oct0MaxN (a), T octant position (b) and Oct2AvgN (c) histogram plots ..	145

Figure 9.1 Graphical illustration of the relationship among Lorenz time series, attractor and recurrence plot.....	153
Figure 9.2 Overall framework of local recurrence prediction model	157
Figure 9.3 Edge detection in a Lorenz recurrence plot.....	160
Figure 9.4 Local eigen prediction model from ensembles within a stationary segment.	161
Figure 9.5 (a) top - original Lorenz time series, middle – random Gaussian noise, bottom – random permuted Lorenz time series contaminated by noise; (b) reconstructed noise-free Lorenz attractor vs. random permuted Lorenz attractor contaminated by noise ..	164
Figure 9.6 Five step prediction RMS error comparisons for Lorenz time series under different noise levels with various prediction models (ARMA(1,0), ARMA(3,3), RBF model and local recurrence model).....	166
Figure 9.7 Five step prediction RMS error comparisons for randomly permuted Lorenz time series under different noise levels with various prediction models (ARMA(1,0), ARMA(3,3), RBF model and local recurrence model).....	168
Figure 10.1 Overall framework of RBF simulation model of VCG signals.....	172
Figure 10.2 (a) An illustration of trajectories of an attractor intersecting a (planar) Poincare section; (b) Poincare sectioning of VCG trajectory	173
Figure 10.3 X, Y and Z ensemble components extracted from the Poincare sectioning of VCG trajectory.....	174
Figure 10.4 Weibull distribution fitting of RR interval time series.....	175
Figure 10.5 Uniform distributed radial basis function centers along VCG trajectory....	176
Figure 10.6 Patient001/s0010_re (a) Simulated VCG trajectory vs. actual VCG trajectory; (b) Frequency domain comparison between actual VCG and simulated VCG; (c) Time domain comparison between actual VCG and simulated VCG.....	180

Figure 10.7 Patient255/s0491_re (a) Simulated VCG trajectory vs. actual VCG trajectory;
(b) Frequency domain comparison between actual VCG and simulated VCG; (c) Time
domain comparison between actual VCG and simulated VCG..... 181

Figure 10.8 Patient005/s01011re (a) Simulated VCG trajectory vs. actual VCG trajectory;
(b) Frequency domain comparison between actual VCG and simulated VCG; (c) Time
domain comparison between actual VCG and simulated VCG..... 182

Figure 10.9 Patient106/s0030_re (a) Simulated VCG trajectory vs. actual VCG trajectory;
(b) Frequency domain comparison between actual VCG and simulated VCG; (c) Time
domain comparison between actual VCG and simulated VCG..... 183

Figure 10.10 Patient175/s0009_re (a) Simulated VCG trajectory vs. actual VCG
trajectory; (b) Frequency domain comparison between actual VCG and simulated VCG;
(c) Time domain comparison between actual VCG and simulated VCG..... 184

CHAPTER I

INTRODUCTION

In this chapter, motivations for selecting this research topic are presented. It is followed by the major thrust and scope of research. In the end, the organization of this dissertation is shown.

1.1 Research motivations

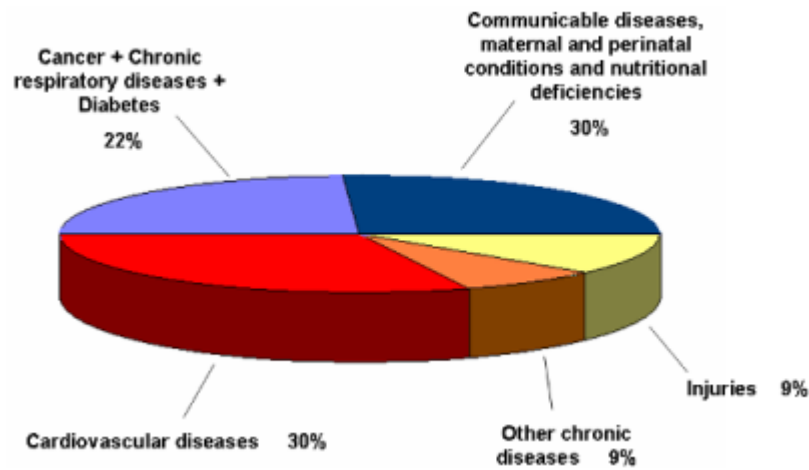


Figure 1.1 Pie chart of death causes in the world [1]

According to the World Health Organization (WHO) reports in 2008 (see Figure 1.1), *cardiovascular disease is the number one cause of death globally and is projected to remain the leading cause of death. An estimated 17.5 million people died from cardiovascular disease in 2005, representing 30% of all global deaths. Of these deaths, 7.6 million were due to heart attacks and 5.7 million were due to stroke [1].*

There are significant socioeconomic values for the diagnosis and prognosis of cardiovascular diseases. It is estimated that if appropriate action is taken by 2015, twenty million people will be saved from cardiovascular diseases every year [1]. The cardiovascular diseases will affect the quality of life of many people, increase the healthcare costs, take away people's earning and savings, and pose a heavy burden for the country's economies. Therefore, it is imperative to prevent and control the cardiovascular diseases.

The major tool used in clinical diagnostics of cardiovascular disorders is electrocardiogram (ECG), which is developed by Dr. William Einthoven in 1901. The ECG is a time-varying signal that captures the ionic current flow responsible for the contraction and subsequent relaxation of the cardiac fibers. The surface ECG is obtained by recording the potential difference between two electrodes placed on the surface of the skin.

Currently, with the advancement of information technology and sensor technology, the acquisition of ECG signals is not constrained by computation resources any more. The conventional 12-lead ECG and Frank XYZ VCG system enable the inspection of the heart from different perspectives and the ECG data can be digitalized at a high sampling rate and stored for many years. The availability of vast amounts of heart monitoring data offers an unprecedented opportunity to develop accurate real-time diagnostics and prognostics of cardiovascular system state and performance from a nonlinear dynamic perspective.

1.2 Research objectives

The study is to develop real-time monitoring and prognostic schemes for various cardiovascular diseases by analyzing the nonlinear stochastic dynamics underlying the complex heart system.

Multianalysis strategies are used to diagnose the patient's cardiovascular online status and make a further prognosis to assess the risk of heart disease. The employment of a nonlinear stochastic analysis combined with wavelet representations can extract effective cardiovascular features for this purpose. Those features will be more sensitive to the pathological dynamics instead of the extraneous noises. The conventional approaches (statistical and linear system) tend to have limitations for capturing signal variations resulting from changes in the cardiovascular system state.

The study includes signal representation, feature extraction, state classification and state prognosis from nonlinear dynamic principles. In cope with the main research objectives, the research tasks are divided into the following:

- Develop an effective compact representation method for the cardiovascular signals which will yield sensitive features to relevant ECG states and insensitive to variations in extraneous noise.
- Characterize the nonlinear spatiotemporal dynamics of cardiac vector loops and quantifying the recurring patterns in the vectorcardiogram (VCG) for the Myocardial Infarction (MI) classification.

- Develop the classification and regression tree (CART) model to integrate the medical doctor's knowledge towards the classification of three Atrial Fibrillation (AF) states
- Develop the real time prediction model for the heart risk assessment under dynamic conditions.
- Design the data-driven simulation model of cardiac electrical activities in various cardiovascular conditions.

1.3 Major contributions

This proposed research will provide versatile cardiovascular monitoring and prognosis schemes which combine the nonlinear dynamics, predictive modeling, artificial intelligence, and signal processing. Specific research contributions are as follows:

- New representation scheme for the ECG signals by an optimal wavelet function design which yields one order of magnitude compactness reduction compared to the conventional wavelets in terms of entropy.
- New spatiotemporal representation scheme for the VCG signals, which significantly assists the interpretation of vectorcardiogram and facilitates the exploration of related important spatiotemporal cardiovascular dynamics.
- Developed a classification and regression tree (CART) model to integrate the cardiologists' knowledge towards accurate classification of Atrial Fibrillation (AF) states from sparse datasets.

- Developed a Myocardial Infarction (MI) classification model using recurrence quantification analysis and spatial octant features of VCG attractor dynamics, which detects MI up to about 96% accuracy in both sensitivity and specificity.
- Designed a local recurrence prediction model for real time medical prognosis and risk assessment of cardiovascular problems, which is particularly suitable for the implementation in the nonlinear and nonstationary environment.

1.4 Organization of the dissertation

This chapter presents the motivation of research in this area, as well as research objectives and research contributions. Rest of the dissertation is organized as follows:

Chapter II: Background and literature review: This chapter describes the general fundamentals of cardiovascular electrical activities and relevant monitoring systems. Next, the databases used in the subsequent chapters for experimental and simulation studies are introduced. In addition, a review of pertinent literature with the wavelet, nonlinear dynamic study of ECG signals is presented.

Chapter III: Research methodology: This chapter presents the research methodology used in the dissertation study. The overall research methodology is grouped into three parts: signal representation, feature extraction and classification, and simulation and prognostic modeling.

PART I: Signal representation

Chapter IV: Customized wavelet representation of ECG signals: An optimal wavelet function design approach is established for the specific ECG signal representation. Implementation details, validations, results and conclusions are described.

Chapter V: Dynamic VCG representation: The time resolution drawbacks of conventional static VCG representation are resolved by real-time displaying the rotated VCG attractor on a computer monitor. It explores the VCG spatiotemporal information on the heart dynamics. The color coding methods of VCG attractor using cardiac vector curvature, velocity, and phase angle information are also introduced.

PART II: Feature extraction and classification

Chapter VI: Atrial fibrillation state classification: The approach, development, training, validation of atrial fibrillation classification and wavelet feature extraction are presented. The classification and regression tree (CART) model is detailed.

Chapter VII: Myocardial infarction identification using recurrence quantification analysis (RQA) of VCG signals: The recurrence behaviors and properties of VCG attractor are characterized and quantified. Recurrence quantifiers are used for the identification of myocardial infarction cases from the healthy control objects.

Chapter VIII: Vectorcardiographic octant features for the diagnostics of heterogeneous myocardial infarction: The spatial distributions of VCG trajectories are designed and studied in this chapter. The critical VCG octant features are extracted for the diagnostics of heterogeneous MIs. The training, validating, testing of CART classification models are detailed.

PART III: Simulation and prognostic modeling

Chapter IX: Local recurrence prediction in nonstationary chaotic systems: A local recurrence modeling approach is presented for the state and performance predictions in complex nonlinear and nonstationary systems. Extensive studies using

simulated and some real world datasets are shown to achieve significant prediction accuracy improvements over other alternative methods.

Chapter X: Radial basis function simulation modeling of VCG signals: The parameterized RBF network model is studied for the generation of simulated VCG signals and they are also transformed to get the standard 12-lead EKG signals by the generalized Dower transformation matrix or the estimated matrix from experiment data for the specific patient.

Chapter XI: Conclusions and future work: This chapter presents research contributions, general conclusions and future work.

1.5 References

- [1] "http://www.who.int/cardiovascular_diseases/en/," World Health Organization, 2008.

CHAPTER II

BACKGROUND AND LITERATURE REVIEW

This chapter will begin with the literature review about cardiac conduction system, 12-lead ECG and frank XYZ VCG system. It will be followed by the relevant research on the nonlinear dynamic and wavelet analysis of ECG signals.

2.1 Cardiac conduction system

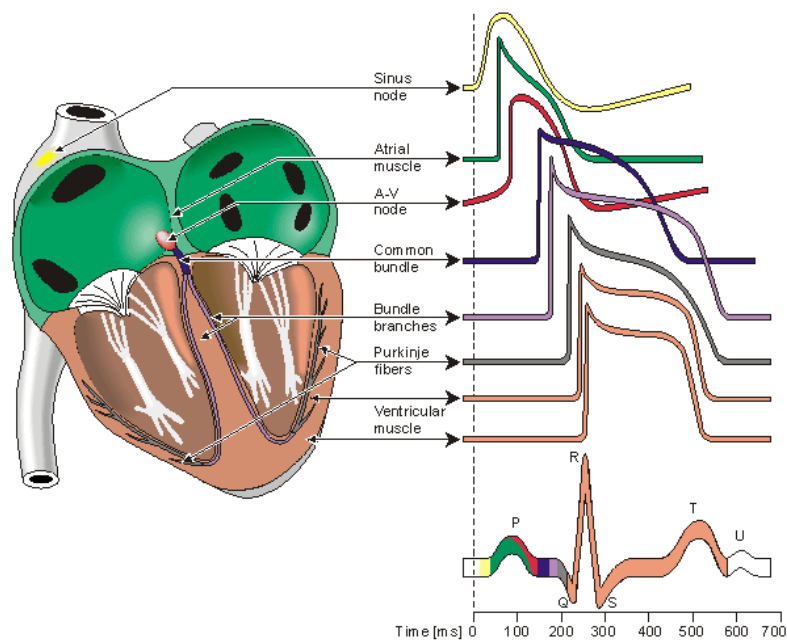


Figure 2.1 Electrophysiology of the heart and different waveforms for each of the specialized cells in the heart [1]

The heart consists of four compartments: the right and left atria and ventricles. It works as an autonomous control pump for circulating the blood in our bodies and constantly produces a sequence of electrical activities within every heart beat. The heart

electrical activities are generated by the biopotential variations because of the movement of three types of ions, namely, Calcium (Ca^{++}), Potassium (K^{+}) and Sodium (Na^{+}). As shown in Figure 2.1, the heart's electrical activity begins in the sinoatrial (SA) node to excite the atrial muscle contraction. Then AV node will propagate the stimulus through bundle of His and Purkinje fibers toward the ventricles. The SA node is the heart's pacemaker. The ordered stimulation starting from SA node leads to the efficient contraction of the heart, thereby pumping the blood throughout the body [2].

2.2 12-Lead electrocardiogram (ECG) and vectorcardiogram (VCG) signals

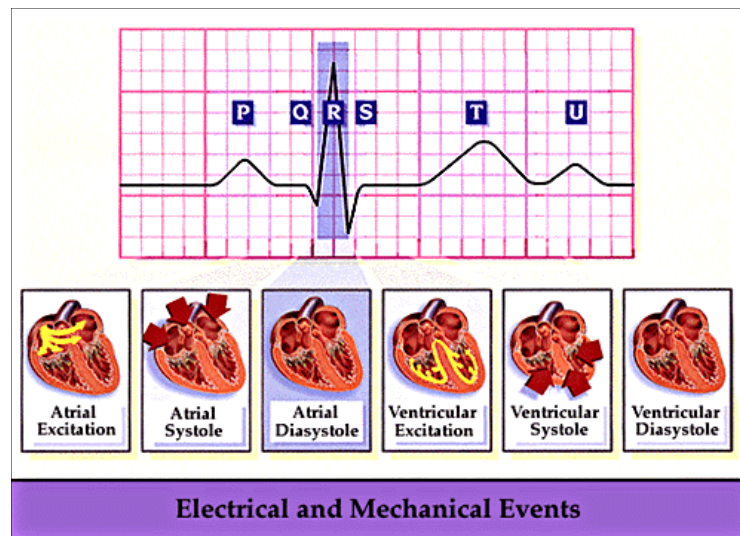


Figure 2.2 Electrical and mechanical events diagram during one heart beat [3]

Cardiac monitoring system is designed to measure the electrical biopotential changes in the heart. The electrocardiogram (ECG) system, designed by Augustus Waller in 1889 and further improved by Williem Einthoven in 1901, has been used for more than 100 years for the clinical diagnosis of cardiovascular disorders. Around 1904 Einthoven derived the famous “Einthoven triangle” to measure three ECG signals and calculate the approximate direction of cardiac vector. In 1956, Ernest Frank designed the Frank lead

system to measure the vectorcardiogram (VCG) in three corrected orthogonal coordinates, which provides a clear picture of the cardiac vector.

The surface ECG is obtained by recording the potential difference between two electrodes placed on the surface of the skin. A single normal cycle of the ECG represents the successive atrial and ventricular depolarization-repolarization events which occur with every heart beat and includes P, Q, R, S, T, and U waves (see Figure 2.2)

- P wave: the sequential activation of the right and left atria
- QRS complexes: right and left ventricular depolarization
- T wave: ventricular repolarization
- U wave: origin though not clear, is probably “post-depolarization” in the ventricles

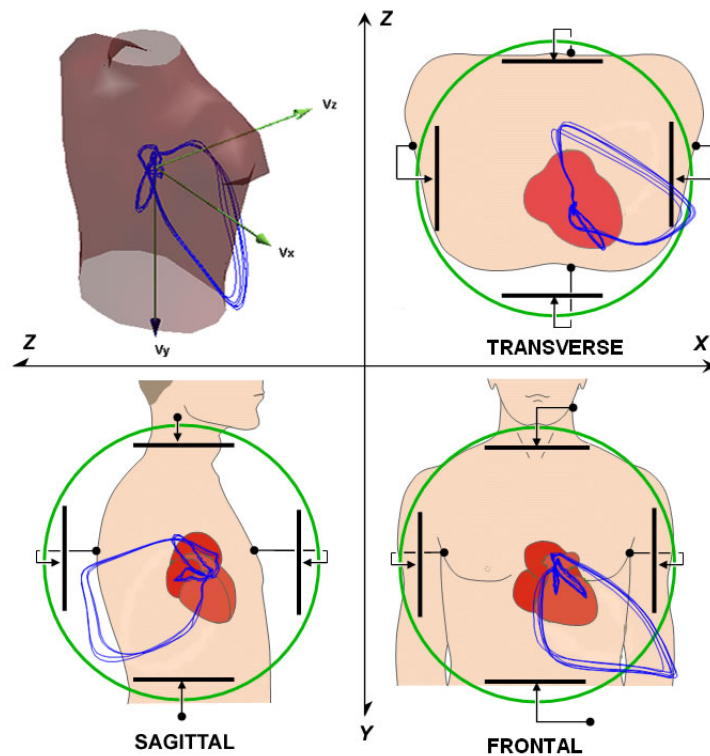


Figure 2.3 The electrodes placement in VCG measurement system [1]

The vectorcardiogram (VCG) observes the heart potentials as a cardiac vector in three orthogonal components instead of the scalar amplitude (ECG curve). In the rectangular coordinate system of the torso, VCGs are the mutually orthogonal bipolar measurements by placing parallel electrodes on the opposite sides of the torso (see Figure 2.3).

With the rapid development of information technology, the representation and analysis of 3D VCG loops are not constrained by computational resources and this resulted in renewed interests of VCG since 1990's. As demonstrated by Dower and his group [4-6], VCG signals and 12-lead ECG can be linearly transformed to each other without loss of useful information content pertaining to the heart dynamics. Dower matrix (Eq 2-1) is one of those generalized transformation matrices, and can be used to derive the 12-lead ECG signals from the 3-lead VCG.

$$\text{Dower transformation matrix } \mathbf{D} = \begin{bmatrix} -0.515 & 0.157 & -0.917 \\ 0.044 & 0.164 & -1.387 \\ 0.882 & 0.098 & -1.277 \\ 1.213 & 0.127 & -0.601 \\ 1.125 & 0.127 & -0.086 \\ 0.831 & 0.076 & 0.230 \\ 0.632 & -0.235 & 0.059 \\ 0.235 & 1.066 & -0.132 \end{bmatrix} \quad (\text{Eq 2-1})$$

If we have the VCG data in matrix form \mathbf{V} ($3 \times N$), the eight leads (I, II, v1-v6) \mathbf{S} ($8 \times N$) can be derived by $\mathbf{S} = \mathbf{D}\mathbf{V}$ except the derived augment leads.

The transformation study statistically shows the equivalence between 12-lead ECG and 3-lead VCG. However, it is difficult for the human beings to visually project a spatial VCG vector into any specified cardiac measurement angle determined by 12-lead

measurement systems, which is the conventional way to interpret heart electrical activities. In addition, the loss of temporal information in the static VCG representation posed extra barriers for medical doctors to closely relate the 12-lead ECG characteristics to VCG. But when it comes to the computer automated analysis of heart monitoring signals, the 12-lead ECG signals will introduce the “curse of dimensionality” problem, which is the fact that the convergence of any estimator to the true value of a smooth function defined on a space of high dimension is very slow because the exponential increase in volume associated with extra dimensions. Thus, VCG is a better option for the computer processing and analysis because it overcomes not only the loss of information by only analyzing one or two ECG signals, but also the dimensionality problems induced by 12-lead ECG. The usage of VCG for the diagnostics of cardiovascular diseases has been studied by many researchers [7-18], although very few investigations explored both spatial and temporal relationships.

2.3 A primer on nonlinear dynamic analysis

Much of the complexity in complex systems emerges from the underlying nonlinear stochastic dynamics. Effective models of the following form (Eq 2-2) can capture this complexity:

$$d\mathbf{x} = \underline{F}(\mathbf{x})dt + \underline{g}(\mathbf{x})d\beta \quad (\text{Eq 2-2})$$

where $\mathbf{x}(t)$ is a m -dimensional state vector, $\underline{F}(\bullet)$ is usually a nonlinear vector field, t is the time and the dynamic noise term $\underline{g}(\mathbf{x})d\beta$ accounts for the influence of extraneous phenomena [19-23]. Nonlinear dynamic cardiovascular signal analysis is based on the premise that the ECG signals emanate from a finite dimensional nonlinear dynamic

system. This is reasonable and more generic than conventional linear and stationary assumptions on the nature of cardiovascular system and it can lead to effective models that can compactly capture the salient behaviors of many complex systems. Dynamics underlying the ECG signals gathered under these conditions manifest in the vicinity of an invariant set called an attractor **A**, defined in the state space [24]. An example of such an attractor of a nonlinear system (Rossler system) is shown in Figure 2.4. The state space of Rossler and such nonlinear systems shows deterministic chaos where the state evolution switches between a horn (emerging through the neighborhood *U*) and cycle area (emerging through *V*).

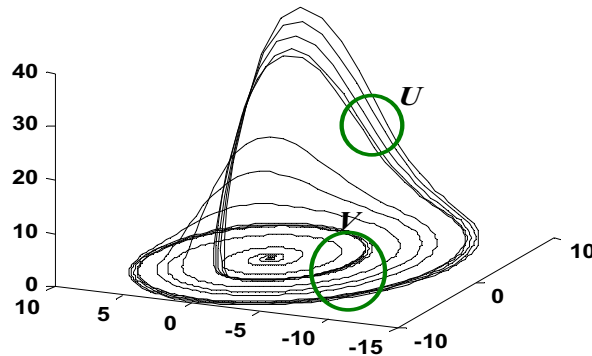


Figure 2.4 Rossler attractor and local evolution

However, in many real life cases, only a few signals (e.g., one lead ECG signal) are available in lieu of the complete measurements of the state vector $\underline{x}(t)$. However, many individual signal $y(t)$ contain adequate information to reconstruct most of the system dynamics. This is because of the high dynamic coupling existing among cardiovascular system. An equivalent state space (attractor) can be reconstructed from the delayed coordinates of the measurements $y(t)$ as

$$\underline{x}(t_i)=[y(t_i), y(t_i+\tau), y(t_i+2\tau), y(t_i+(m-1)\tau)] \quad (\text{Eq 2-3})$$

where m is the embedded dimension and τ is the time delay [25, 26]. The minimal

sufficient embedding dimension m to unfold the attractor is determined by false nearest neighbor method [27]. The optimal time delay τ is selected to minimize mutual information function $M(\tau)$, defined as

$$M(\tau) = \int_i p(t, t+\tau) \log \frac{p(t, t+\tau)}{p(t)p(t+\tau)} dt \quad (\text{Eq 2-4})$$

where $p(t, \tau)$ is the joint density function, and $p(t)$ and $p(t+\tau)$ are marginal density functions of $y(t)$ and $y(t+\tau)$, respectively.

Recurrence plots provide a convenient means to capture the topological relationships existing in the m -dimensional state space by calculating the distance from each state to all the others $D(i, j) := \|v(i) - v(j)\|$, where $\|\cdot\|$ is a norm (e.g., the Euclidean norm) and mapping the distance to a color scale. It shows the times at which a state of the dynamical system recurs, i.e., the time-pairs at which the trajectories of a system evolution come within a specified neighborhood. Recurrence plot is formed by calculating the Euclidean distance from each state vector to others and mapping the distance to a color scale. A representative recurrence plot constructed for the Rossler attractor is shown in Figure 2.5. The structures of a recurrence plot have distinct topology and texture patterns. The ridges locate the transition states at which the system evolves from one behavior (cycle area V) to the other (horn area U) (see Figure 2.4). The separations between dark diagonal lines (along 45° degree) indicate the near-periodicity of system behaviors over a given time segments. Recurrence-based methods have of late shown potential for representation and de-noising of measurements from complex systems [28-34].

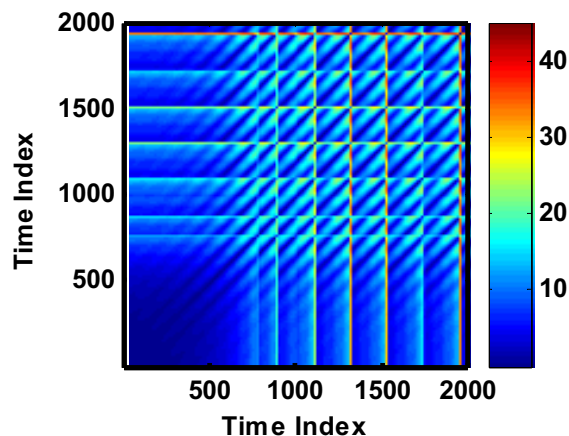


Figure 2.5 Rossler attractor recurrence plot

Recurrence plots are intriguing graphical displays of signal patterns, but representative nonlinear dynamical quantitative features need to be extracted to analyze the underlying processes and detect hidden rhythms. Statistical features, such as recurrence rate (%RR), determinism (%DET), laminarity (%LAM), linemax (LMAX), entropy (ENT), and trapping time (TT), are used as such typical recurrence quantifiers for the complexity characterization of VCG attractor .

The definitions of various recurrence quantifiers and their relationships with heart dynamics are summarized in the following [28-34]:

- 1) Recurrence rate (Γ) is the percentage of dark points on the TRP (the pairs of points whose distance is less than the corridor) [28-34]. It is calculated as:

$$\Gamma = \frac{1}{N^2} \sum_{i,j=1}^N T(i, j) \quad (\text{Eq 2-5})$$

where N is window size and $T(i, j)$ is the TRP with a value 1 or 0. Recurrence rate characterizes the global near-periodicity of cardiovascular activities and it is closely related to the heart rate dynamics. The higher the Γ , the larger the proportion of points located close to each other, and fewer the points are farther apart.

- 2) Determinism (DET) represents the proportion of recurrent points forming diagonal line structures. It measures the repeating or deterministic patterns in the heart dynamics, and tells how well the circulatory heart system functions [28-34].

$$DET = \frac{\sum_{l=l_{min}}^N lp(l)}{\sum_{i,j=1}^N T(i,j)} \quad (\text{Eq 2-6})$$

where l represents the length of lines parallel to the central diagonal line, l_{min} represents the minimal length of counted diagonal lines and $p(l)$ is the frequency distribution of diagonal line segments of length l . Periodic signal has long diagonal lines (big $DET \approx 100\%$), while chaotic signal has short diagonal lines (medium $DET < 50\%$) and a random white noise signal shows no diagonal lines ($DET \approx 0$).

- 3) Linemax (LMAX) is the length of the longest diagonal line segment in the TRP, which is related to the inverse of the largest positive lyapunov exponent [28-34]. The shorter the LMAX is, the more chaotic (less stable) is the signal. Thus, LMAX indicates stability of heart dynamics, and small LMAX implies that two close cardiac vectors in a VCG are diverging quickly from each other.
- 4) Entropy (ENT) is the Shannon information entropy of frequency distribution of diagonal line segments [28-34]. The predictability of heart activity decreases with increasing entropy given by

$$ENT = - \sum_{l=l_{min}}^N p(l) \ln p(l) \quad (\text{Eq 2-7})$$

where $p(l)$ is the frequency distribution of diagonal line segments of length l .

- 5) Laminarity (LAM) is analogous to DET except that it measures the vertical line structures and is given by

$$LAM = \frac{\sum_{v=v_{min}}^N vp(v)}{\sum_{v=1}^N vp(v)} \quad (\text{Eq 2-8})$$

where v represents the length of vertical lines, v_{min} represents the minimal length of counted vertical lines and $p(v)$ is the frequency distribution of vertical line segments of length v . Large LAM indicates heart takes a significant time to move from one activity to another, and it provides important non-stationary information for the heart system [28-34].

- 6) Trapping time (TT) provides a measure of how long the system remains in a specific state.

$$TT = \frac{\sum_{v=v_{min}}^N vp(v)}{\sum_{v=v_{min}}^N p(v)} \quad (\text{Eq 2-9})$$

These recurring pattern features are used to quantify the nonlinear dynamic complexity of VCG vector loops under MI and HC conditions [28-34].

2.4 Wavelet analysis of ECG signals

ECG signals are gathered and stored in analytical instruments (e.g., ECG machines) in the form of time-series. They can be transformed from the time domain into frequency, time-frequency, or other domains depending on the nature of the information required. These signals exhibit recurrent patterns spread over multiple scales, and significant

nonstationarity. Wavelet methods are most effective in capturing spatio-temporal content of such signals over multiple scales of resolution.

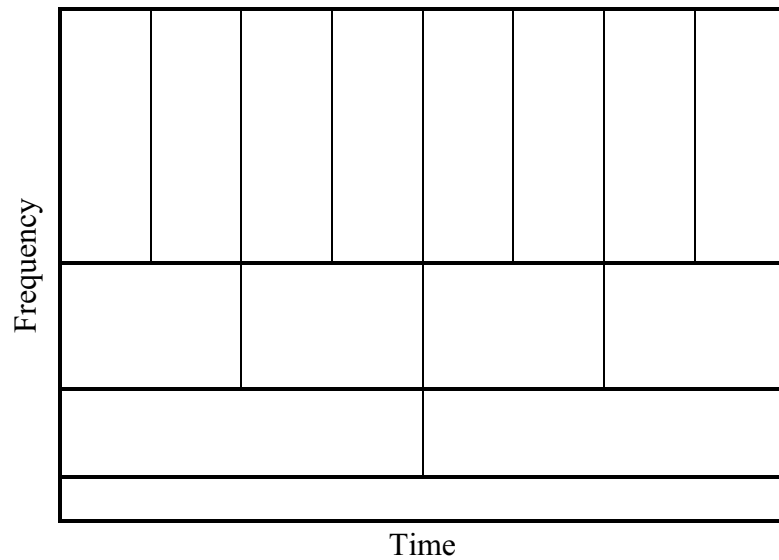


Figure 2.6 Time-frequency resolution of wavelet transforms

The wavelet representation can be useful for interrogating the spectral component prevailing at a given time instant. The high frequency bursts, which usually occur over short time intervals, can be analyzed with a sharper time resolution, while the low-frequency components, which usually occur over long-duration of a signal, can be analyzed with a better frequency resolution. Figure 2.6 shows various time and frequency bands captured by different wavelets, i.e., each wavelet capture the time and frequency range that from the boundaries of a particular box. Also, as illustrated in Figure 2.6, despite the change of widths and heights of the boxes, the area of the boxes is constant. At low frequencies, the height of the boxes are shorter which corresponds to better frequency resolutions, but their widths are longer which correspond to poor time resolution. At higher frequencies, the width of the boxes decreases, i.e., the time resolution gets better and the heights of the boxes increase, i.e., the frequency resolution gets poorer.

The admissible conditions for a real or complex-value continuous-time function $\psi(t)$ to be a “Wavelet” are as following:

(1) Reconstruction condition

$$C = \int_{-\infty}^{\infty} \frac{|\Psi(\omega)|^2}{|\omega|} d\omega \quad 0 < C < \infty \quad (\text{Eq 2-10})$$

$\Psi(\omega)$ stands for the Fourier transform of $\psi(t)$. This condition is sufficient, but not a necessary condition to obtain the inverse. It can guarantee to reconstruct a signal without loss of information. The admissibility condition implies that the Fourier transform of $\psi(t)$ vanishes at the zero frequency [35-37].

$$|\Psi(\omega)|^2 \Big|_{\omega=0} = 0 \quad (\text{Eq 2-11})$$

It indicates that wavelets must have a band-pass like spectrum.

(2) Wave condition

A zero at the zero frequency in condition (1) also means that the average value of the wavelet in the time domain must be zero, which means $\psi(t)$ must be an oscillatory wave [35-37].

$$\int_{-\infty}^{\infty} \psi(t) dt = 0 \quad (\text{Eq 2-12})$$

(3) Finite energy

The signal to analyze must have finite energy. When the signal has infinite energy it will be impossible to cover its frequency spectrum and its time duration with wavelets. Usually this constraint is formally stated as

$$\int_{-\infty}^{\infty} |\psi(t)|^2 dt < \infty \quad L^2(R) = \{f : R \mapsto C \mid \int_{-\infty}^{\infty} |f(t)|^2 dt < \infty\} \quad (\text{Eq 2-13})$$

and it is equivalent to saying that the L^2 -norm of our signal $f(t)$ should be finite [35-37].

(4) Regularity condition

This condition is to make the wavelet transform decrease quickly with decreasing scale s , and it states that the wavelet function should have some smoothness and concentration in both time and frequency domains. Regularity is closely related to the number of vanishing moments and it will determine how smooth a wavelet is. The order of regularity of a wavelet is the number of its continuous derivatives. The j 's moment of the function $\psi(t)$ is defined as $\int_{-\infty}^{+\infty} t^j \psi(t) dt$. When the wavelet's first k moments are zero $\int_{-\infty}^{+\infty} t^j \psi(t) dt = 0$ for $j = 0, \dots, k$, the number of Vanishing Moment of the wavelet is $k+1$. If a wavelet has k vanishing moments, suppression of signals that are polynomials of a degree lower or equal to k is ensured [35-37].

Summarizing, the admissibility conditions (1) (2) (3) gave us the wave, condition (4) regularity and vanishing moments gave us the fast decay or the *let*, and a function meeting the requirement of the above four conditions reaches the wavelet [38].

The Continuous Wavelet Transform (CWT) accomplishes the multi-resolution analysis by time-scaling and time-shifting the wavelet function $\psi(t)$ [35-37].

$$\psi_{j,k} = \frac{1}{\sqrt{j}} \psi\left(\frac{t-k}{j}\right) \quad (\text{Eq 2-14})$$

Where scaling factor j is for expanding or compressing and translation factor k is for the

time domain shifting. Continuous wavelet transform of the signal $x(t)$ using the analysis wavelet $\psi(t)$ is defined as:

$$b_{j,k} = \frac{1}{\sqrt{|j|}} \int_t x(t) \psi\left(\frac{t-k}{j}\right) dt \quad (\text{Eq 2-15})$$

Inverse continuous wavelet transform to reconstruct signal $x(t)$ is:

$$x(t) = \frac{1}{C} \int_{j=-\infty}^{\infty} \int_{k=-\infty}^{\infty} \frac{1}{j^2} b_{j,k} \cdot \psi_{j,k}(t) dj dk \quad (\text{Eq 2-15})$$

Actually, the continuous wavelet transform can be taken as $CWT(j, k) = \langle x(t), \psi_{j,k}(t) \rangle$ which is the cross correlation of the signal $x(t)$ with the mother wavelet at scale j and lag k . If $x(t)$ is similar to the mother wavelet at this scale j and lag k , then the coefficients will be large which indicates that customized wavelet function adapted to the ECG pattern may achieve the best performance [35-37].

Wavelet functions $\psi(t)$ are building blocks that can be used to simultaneously decompose signal characteristics in both time and frequency domains. Wavelet representations are particularly useful for the analysis of transients, aperiodicity, and other nonstationary signal features. Subtle changes in signal morphology can be highlighted over the scales of interest through the interrogation of the transform [35]. Consequently, the QRS complex can be distinguished from high P and T waves, noise, baseline drift, and other artifacts in different scales. The relation between the characteristic points of ECG signals and those of modulus maximum pairs of its wavelet transforms are almost straightforward to establish [39].

Over the past few years, wavelets have been used in the analysis of physiological signals, such as ECG, Electroencephalography (EEG), Electromyography (EMG), blood pressure, and respiration signals [35]. Researchers have been exploring the applicability of wavelets for capturing complex nonlinear dynamics of ECG [40-42]. However, not much attention was given for the detection of certain complex patterns inside the ECG signals. Conceivably, much of the information necessary for early diagnosis of various ailments are buried in these complex patterns. In this dissertation research, an optimal matched wavelet will be designed for ECG signals to find occurrences of certain complex recurring patterns.

2.5 Databases

The research undertaken will use cardiovascular datasets from the PhysioNet for the implementation and experiment studies. PhysioNet is a public service research resource for complex physiologic signals [43].

The VCG data analyzed in myocardial infarction (MI) study (368 myocardial infarction and 80 healthy control recordings) is from PTB database available from the PhysioNet. The recordings were collected at the Department of Cardiology of University Clinic Benjamin Franklin in Berlin, Germany. Each of these recordings contains 15 simultaneously recorded signals: the conventional 12-lead ECGs and the 3 Frank (XYZ) VCG signals. Each of these is digitized at 1000HZ, with 16 bit resolution over a range of ± 16.384 mV. The 80 healthy control recordings are from 54 healthy volunteers, and 368 MI recordings are from 148 patients. The recordings are typically about two minutes in length, with a small number of shorter records (none less than 30 seconds).

The ECG data used in the atrial fibrillation (AF) study is from the 2004 PhysioNet challenge “Spontaneous Termination of Atrial Fibrillation.” In this challenge, classification needs to be made among the following three categories of AF patients test signals:

- 1) **Group N:** Non-terminating AF (defined as AF that was not observed to have terminated for the duration of the long-term recording, at least an hour following the segment).
- 2) **Group S:** Soon to be terminating (AF that terminates one minute after the end of the record).
- 3) **Group T:** Terminating immediately (AF terminating within one second after the end of the record).

In all, 80 recordings of AF from 60 different subjects were made available in the database [43]. Each record is a one-minute segment of AF, containing two ECG signals, each at 128 samples/sec. The data is divided into a learning set and two test sets. The learning set contains 30 records in all, with 10 records in each of the three groups. The learning set records were obtained from 20 different subjects (10 from group N and 10 from group S/T). Test set A contains 30 records from 30 subjects. About half of these records belong to group N and the rest to group T. The goal is which records in test set A belong to group T. Test set B contained 20 records, 2 from each of 10 subjects (none represented in the learning set or in test set A). One record of each pair belongs to group S and the other to group T. The goal of the second challenge event is to identify which records belong to group T.

2.6 References

- [1] J. Malmivuo and R. Plonsey, *Bioelectromagnetism: Principles and Applications of Bioelectric and Biomagnetic Fields*. USA: Oxford University Press, July 18, 1995.
- [2] D. Dubin, *Rapid Interpretation of EKG's: An Interactive Course*: Cover Publishing Company, 2000.
- [3] Marquette-KH, "ECG Electrical and Mechanical Events Diagram," *Marquette Electronics*, 1996.
- [4] G. E. Dower and H. B. Machado, "XYZ data interpreted by a 12-lead computer program using the derived electrocardiogram," *Journal of electrocardiology*, vol. 12, pp. 249-261, 1979.
- [5] G. E. Dower, H. B. Machado, and J. A. Osborne, "On deriving the electrocardiogram from vectorcardiographic leads," vol. 3, p. 87, 1980.
- [6] G. E. Dower, A. Yakush, S. B. Nazzal, R. V. Jutzy, and C. E. Ruiz, "Deriving the 12-lead electrocardiogram from four (EASI) electrodes," *Journal of electrocardiology*, vol. 21, pp. S182-S187, 1988.
- [7] A. Benchimol, F. Reich, and K. B. Desser, "Comparison of the electrocardiogram and vectorcardiogram for the diagnosis of left atrial enlargement," *Journal of electrocardiology*, vol. 9, pp. 215-218, 1976.
- [8] I. Black, "The electrocardiogram and vectorcardiogram in congenital heart disease," *The Journal of Pediatrics*, vol. 69, pp. 846-716, 1966.
- [9] B. W. McCall, A. G. Wallace, and E. H. Estes, "Characteristics of the normal vectorcardiogram recorded with the Frank lead system," *The American Journal of Cardiology*, vol. 10, pp. 514-524, 1962.

- [10] J. NG, A. Sahakian, and S. Swiryn, "Vector Analysis of Atrial Activity from Surface ECGs Recorded During Atrial Fibrillation," *Computers in Cardiology*, vol. 29, pp. 21-24, 2002.
- [11] C. Olson and R. A. Wamer, "The quantitative 3-dimensional vectorcardiogram," *Journal of electrocardiology*, vol. 33, pp. 176-S74, 2000.
- [12] D. M. Schreck, J. D. Frank, E. R. Malinowski, L. E. Thielen, A. F. Bhatti, A. R. Rivera, and V. J. Tricarico, "Mathematical modeling of the electrocardiogram and vectorcardiogram using factor analysis," *Annals of Emergency Medicine*, vol. 23, pp. 617-76, 1994.
- [13] E. Simonson, N. Tuna, N. Okamoto, and H. Toshima, "Diagnostic accuracy of the vectorcardiogram and electrocardiogram : A cooperative study," *The American Journal of Cardiology*, vol. 17, pp. 829-878, 1966.
- [14] K. K. Talwar, S. Radhakrishnan, V. Hariharan, and M. L. Bhatia, "Spatial vectorcardiogram in acute inferior wall myocardial infarction: its utility in identification of patients prone to complete heart block," *International Journal of Cardiology*, vol. 24, pp. 289-292, 1989.
- [15] A. van Oosterom, Z. Ihara, V. Jacquemet, and R. Hoekema, "Vectorcardiographic lead systems for the characterization of atrial fibrillation," *Journal of electrocardiology*, 2006.
- [16] J. L. Willems, E. Lesaffre, and J. Pardaens, "Comparison of the classification ability of the electrocardiogram and vectorcardiogram," *The American Journal of Cardiology*, vol. 59, pp. 119-124, 1987.
- [17] F. N. Wilson and F. D. Johnston, "The vectorcardiogram," *American Heart Journal*, vol. 16, pp. 14-28, 1938.
- [18] A. C. Witham, "Quantitation of the vectorcardiogram," *American Heart Journal*, vol. 72, pp. 284-286, 1966.

- [19] S. T. S. Bukkapatnam, S. Kumara, and A. Lakhtakia, "Real-time chatter control in machining using chaos theory," *CIRP Journal of Manufacturing Systems*, vol. 29, pp. 321-326, 1999.
- [20] S. T. S. Bukkapatnam, S. R. T. Kumara, and A. Lakhtakia, "Dependence of computed trajectories on the step size in a nonlinear dynamic system: An investigation into cutting tool dynamics," *IIE Transactions*, vol. 27, pp. 519-529, 1995.
- [21] S. T. S. Bukkapatnam, S. R. T. Kumara, and A. Lakhtakia, "Local Eigenfunctions-Based Suboptimal Wavelet Packet Representation of Contaminated Chaotic Signals," *IMA Journal of Applied Mathematics*, vol. 63, pp. 149-160, 1999.
- [22] S. T. S. Bukkapatnam, S. R. T. Kumara, A. Lakhtakia, and P. Srinivasan, "Neighborhood Method and its Coupling with the Wavelet Method for Nonlinear Signal Separation of Contaminated Chaotic Time-Series Data," *Signal Processing*, vol. 82, pp. 1351-1374, 2002.
- [23] S. T. S. Bukkapatnam, A. Lakhtakia, and S. R. T. Kumara, "Analysis of sensor signals shows turning on a lathe exhibits low-dimensional chaos," *Physical Review E*, vol. 52, pp. 2375-2387, 1995.
- [24] H. Kantz and T. Schreiber, *Nonlinear Time Series Analysis*. Cambridge: Cambridge University Press, 1997.
- [25] F. Takens, *Detecting strange attractors in turbulence, lecture notes in mathematics* vol. 898: Springer, Berlin, 1981.
- [26] H. Yang, S. T. Bukkapatnam, and R. Komanduri, "Nonlinear adaptive wavelet analysis of electrocardiogram signals," *Physical Review E (Statistical, Nonlinear, and Soft Matter Physics)*, vol. 76, p. 026214, 2007.

- [27] M. B. Kennel, R. Brown, and H. D. I. Abarbanel, "Determining embedding dimension for phase-space reconstruction using a geometrical construction," *Physical Review A*, vol. 45, p. 3403, 1992.
- [28] S. T. S. Bukkapatnam, "Recurrence-based piecewise eigen representation of contaminated chaotic signals," *Phys Rev E (under review)*, 2007.
- [29] N. Marwan, N. Wessel, U. Meyerfeldt, A. Schirdewan, and J. Kurths, "Recurrence plot based measures of complexity and their application to heart-rate-variability data," *Physical Review E*, vol. 66, Aug 2002.
- [30] N. Thomasson, T. J. Hoepfner, C. L. W. Jr., and J. P. Zbilut, "Recurrence quantification in epileptic EEGs," *Physics Letters A*, vol. 279, pp. 94-101, 2001.
- [31] J. P. Zbilut, A. Giuliani, and C. L. Webber, "Recurrence quantification analysis as an empirical test to distinguish relatively short deterministic versus random number series," *Physics Letters A*, vol. 267, pp. 174-178, 2000.
- [32] Y. Zhu and N. V. Thakor, "Adaptive recurrent filter for ectopic beat and arrhythmia detection," *IEEE Engineering in Medicine and Biology Society 10th Annual International Conference*, 1988.
- [33] L. Matassini, H. Kantz, J. Holyst, and R. Hegger, "Optimizing of recurrence plots for noise reduction," *Physical Review E*, vol. 65, p. 021102, 2002.
- [34] N. Marwan, M. Carmen Romano, M. Thiel, and J. Kurths, "Recurrence plots for the analysis of complex systems," *Physics Reports*, vol. 438, pp. 237-329, 2007.
- [35] P. S. Addison, "Wavelet Transforms and the ECG: A Review," *Physiology Measurement*, vol. 26, pp. 155-199, 2005.
- [36] D. B. Percival and A. T. Walden, *Wavelet Methods for Time Series Analysis*: Cambridge University Press, 2000.

- [37] G. Strang and T. Nguyen, *Wavelets and Filter Banks*: Wellesley-Cambridge Press, 1996.
- [38] C. Valens, "A Really Friendly Guide To Wavelets," 1999-2004.
- [39] C. Li, C. Zheng, and C. Tai, "Detection of ECG Characteristic Points Using Wavelet Transforms," *IEEE Transactions on Biomedical Engineering*, vol. 42, p. 21, 1995.
- [40] A. Stefanovska and M. Bracic, "Physics of the human cardiovascular system," *Contemporary Physics*, vol. 40, pp. 31 - 55, 1999.
- [41] F. Ravelli and R. Antolini, "Complex dynamics underlying the human electrocardiogram," *Biological Cybernetics*, vol. 67, pp. 57-65, 1992-05-07.
- [42] H. E. Stanley, "Statistical physics and physiology: monofractal and multifractal approaches," *Physica A: Statistical Mechanics and its Applications*, vol. 270, p. 309, 1999.
- [43] A. Goldberger, L. Amaral, L. Glass, J. Hausdorff, P. Ivanov, R. Mark, J. Mietus, G. Moody, C. Peng, and H. Stanley, "PhysioBank, PhysioToolkit, and PhysioNet: Components of a New Research Resource for Complex Physiologic Signals," *Circulation* 101, vol. 23, pp. e215-e220, 2000 (June 13).

CHAPTER III

RESEARCH METHODOLOGY

This chapter outlines the research methodology used in subsequent chapters. A schematic of the methodology for developing cardiovascular monitoring and prognostic schemes from the study of nonlinear stochastic dynamics underlying the ECG signals is shown in Figure 3.1. Its five modules can be divided as follows:

- Signal representation
- Feature extraction and state classification
- Simulation and prognostic modeling

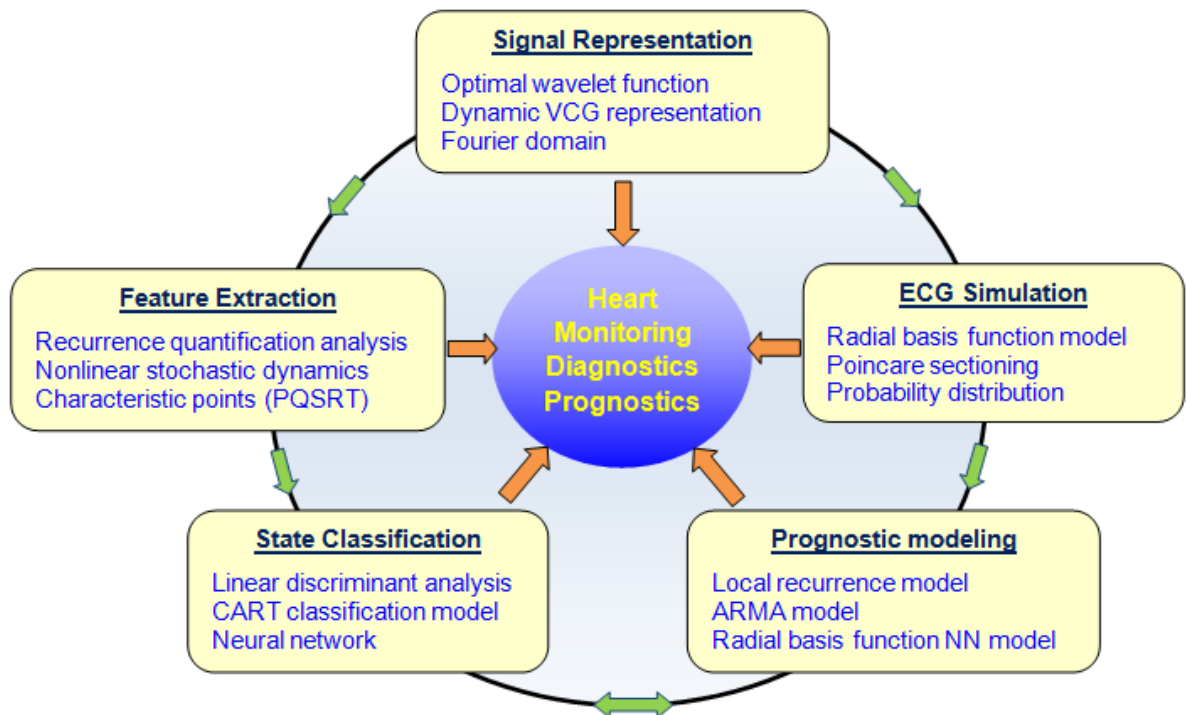


Figure 3.1 Schematic of research methodology

3.1 Signal representation

In the first part of research methodology, cardiovascular signals are presented in alternative domains, such as time, frequency, time-frequency domains, or state space, so that mathematical description of the salient patterns contained in the signal as well as the procedures for feature extraction will be much simpler and efficient in the transformed space.

3.1.1 Nonlinear adaptive wavelet representation of ECG signals

Wavelet representation can provide an effective time-frequency analysis for nonstationary signals, such as the electrocardiogram (ECG) signals, which contain both steady and transient parts. In recent years, wavelet representation has been emerging as a powerful time-frequency tool for the analysis and measurement of ECG signals. The ECG signals contain recurring, near-periodic patterns of P, QRS, T, and U waveforms, each of which can have multiple manifestations. Identification and extraction of a compact set of features from these patterns is critical for effective detection and diagnosis of various ailments. This section will present an approach to extract a fiducial pattern of ECG based on the consideration of the underlying nonlinear dynamics. The pattern, in a nutshell, is a combination of eigenfunctions of the ensembles created from a Poincare section of ECG dynamics. The adaptation of wavelet functions to the fiducial pattern thus extracted yields two orders of magnitude (some 95%) more compact representation (measured in terms of Shannon signal entropy). Such a compact representation can facilitate in the extraction of features that are less sensitive to extraneous noise and other variations. The adaptive wavelet can also lead to more efficient algorithms for beat

detection and QRS cancellation as well as for the extraction of multiple classical ECG signal events, such as widths of QRS complexes and QT intervals.

3.1.2 Dynamic VCG representation

Vectorcardiogram (VCG) signals monitor the spatiotemporal cardiac electrical activity along three pseudo-orthogonal planes, namely, frontal, transverse, and sagittal planes of the body. However, the absence of temporal resolution in the conventional static representation of VCG signals is a major impediment to a medical doctor in the interpretation and clinical usage of VCG. This is especially so since cardiologists depend heavily on the intervals and segment durations in the ECG signals, i.e. temporal resolution. On a paper, only three orthogonal X,Y,Z lead vectors can be shown, and the fourth dimension, namely, the temporal scale can not be shown as it constitutes the fourth dimension. Alternately, a combination of any three vectors can be shown on a paper. In this investigation, we present an approach that captures the critical spatiotemporal heart dynamics by displaying VCG signals on a computer screen, instead of on a paper, the real time motion of a cardiac vector in a 3-D space. Such a dynamic display of 3-D heart activity can be realized even with one lead ECG signal (e.g., ambulatory ECG) through an alternative lag reconstructed spatiotemporal EKG attractor representation from nonlinear dynamics principles. The VCG representation can also be color coded for spatiotemporal representation with additional heart dynamical properties of cardiac vector movements, such as the curvature, velocity, and phase angle. The dynamic VCG representation is shown to significantly enhance the interpretability of vectorcardiogram and facilitate the identification of related spatiotemporal cardiovascular dynamics.

3.2 Feature extraction and classification

The second part of research methodology involves the extraction of invariant dynamical quantifiers that describe the specific patterns in the signal and are sensitive to the state variables to be estimated. Moreover, in the classification stage, the extracted features are associated with an appropriate representation of unknown state variables. In this part, atrial fibrillation and myocardial infarction will be studied.

3.2.1 Atrial fibrillation state classification

Atrial fibrillation (AF), in general, can sustain indefinitely since the ventricles continue to perform the essential function of blood circulation, albeit inefficiently. Nevertheless, the risks of sustained AF can be serious, and may include strokes and myocardial infarction (MI) caused by the formation of blood clots within stagnant volumes in the atria. AF may be subdivided into three different forms, namely, paroxysmal AF (self terminating), persistent AF, and permanent AF. This section presents the results of signal analysis and a classification technique, namely, Classification and Regression Tree (CART), for detecting spontaneous termination or sustenance of AF.

3.2.2 Myocardial infarction identification using recurrence quantification analysis of VCG signals

Myocardial infarction (MI), also known as heart attack, is one of the leading causes of death in the world. It is resulted from the occlusion of the coronary artery and insufficient blood supply to myocardium. Locations of myocardial infarction can be in inferior, septal, anteroseptal, anterior, apical, and other portions of the heart. The necrosis

or death of myocardial cells in a certain location of the heart will lead to changes in the underlying cardiovascular dynamics.

Heart monitoring signals, such as the conventional 12-lead electrocardiogram (ECG) and 3-lead (Frank XYZ) vectorcardiogram (VCG) provide valuable information on the underlying dynamic activities from different perspectives of the heart. Dower demonstrated that a 12-lead ECG signals can be linearly transformed to 3-lead vectorcardiogram, which is commonly known as Dower transformation. It is, therefore, imperative to analyze the VCG signals and explore its relationships with cardiovascular disorders just in the same way as 12-lead ECG is used in the clinical practice. Techniques from nonlinear dynamical system analysis, such as recurrence quantification analysis (RQA) provide effective means to establish these relationships. This section presents the application of RQA for detecting myocardial infarction (MI) from VCG signals. Significant differences were observed in the laminarity, determinism, and local divergence of VCG trajectories between Healthy Control (HC) subjects and MI patients. MI classification accuracies based on the extracted nonlinear dynamical invariants from the VCG recurrence plots were found to be as high as 97% for neural network and linear regression classification model.

3.2.3 Vectorcardiographic octant features for the diagnostics of heterogeneous myocardial infarction

Vectorcardiogram (VCG), three orthogonal cardiac components, was reported to be a promising candidate for the diagnostics of MI. But few, if any, of previous VCG diagnostic approaches could achieve $> 90\%$ accuracy in both specificity and sensitivity.

This investigation assesses new vectorcardiographic octant features towards the effective detection of heterogeneous myocardial infarction.

VCG octant features and conventional electrocardiogram (ECG) interval features were extracted from 448 VCG recordings in Physionet PTB database, which includes 368 MIs and 80 HCs. Statistical feature analysis shows that cardiac vector length distributions in octant 0 (x-negative, y-negative, z-negative) and octant 2 (x-negative, y-positive, z-negative), T vector length and octant position are the most prominent features to distinguish MIs from HCs. It is significant at 69% level ($p\text{-value}=9.63\text{E-}29$) for the Oct0MaxN (the maximum vector length in octant 0) distribution differences between MI (0.38 ± 0.16) and HC (0.54 ± 0.04). The majority (74/80) of HCs' T vector positions (T_pos) is also found to cluster in octant 6 (x-positive, y-positive, z-negative), while MIs spread over all the eight octants. Additionally, Oct2AvgN (the average vector length in octant 2) and Oct0VarN (the variations of all vector lengths in octant 0) show >60% statistical distribution differences. With only four octant features (Oct0MaxN, T_pos, Oct2AvgN and Oct0VarN), a simple Classification and Regression Tree (CART) model can yield classification accuracy with 96.74% sensitivity and 96.25% specificity. The stochastic experiments with different percentage of training data size also reveal high sensitivity (mean: 96%) and specificity (mean: 82%) for heterogeneous MI and HC classification.

Octant 0, octant 2, and T vector information in vectorcardiogram are found to be very important for the diagnostics of heterogeneous MIs. Random classification experiments demonstrate the generality and effectiveness of CART model and vectorcardiographic

octant features. This study is definitely indicative of potential clinical applications of MI diagnostic model from the VCG octant features.

3.3 Simulation and prognostic modeling

The third section will focus on the cardiovascular disorder simulation and prognostic modeling. The mathematical prediction model can be used for prognosis of the patient's health status with the online monitoring ECG signals, and it updates the prediction results in real time and provides the instantaneous alarm for the dangers. Such prognostic results help determine whether it makes more sense to attempt certain treatments or to withhold them, and thus play an important role in medical decision support. In this section, a local recurrence prediction model will be developed to accommodate the nonlinear and nonstationary environments in the complex physiological process. Next, Radial Basis Function (RBF) simulation model for the VCG signals is shown to simulate the patient's cardiovascular electrical activities from a data-driven's perspective.

3.3.1 Local recurrence prediction in nonstationary chaotic systems

A local recurrence modeling approach that considers the underlying nonlinear stochastic dynamics and nonstationarities is designed for predicting the state of complex physical systems. This approach uses heretofore unexplored premise of treating nonstationarity as to cause finite time detours of system dynamics from an attractor's vicinity. The local recurrence property, exhibited over a certain sets of time and state space segments, is used to partition system trajectory into multiple near-stationary segments. Consequently, local eigen representations of each segment can capture both dynamics and nonstationarities. Extensive studies using simulated and real world datasets

reveal significant prediction accuracy improvements over other conventional alternative methods.

3.3.2 Radial basis function simulation modeling of VCG signals

The vectorcardiogram (VCG) represents human's heart potential variations and regulations in the vector form, and it has been shown to be very important for some disease assessments. This section presents a general data-driven method for the modeling and simulation of human VCG and standard 12-lead electrocardiogram (EKG) signals. The heartbeat variations and VCG X, Y, Z ensemble components are extracted by the Poincare sectioning of the VCG trajectory. The Heart Rate Variability (HRV) is modeled as a Weibull distribution, and Radial Basis Function (RBF) network model is trained with experiment data to simulate the VCG trajectory and thus duplicate the heart electric activity. The parameterized RBF network model is used for the generation of simulated VCG signals and they are transformed to get the standard 12-lead EKG signals by the generalized Dower transformation matrix or the estimated matrix from experiment data for a specific patient. This investigated RBF network model is shown to closely capture the same heart activities as the actual data in time domain, frequency domain. Such a well-trained data-driven model can facilitate the study of VCG, feature extraction from VCG and 12-lead EKG signals, and further prognosis of diseases.

PART I

SIGNAL REPRESENTATION

CHAPTER IV

CUSTOMIZED WAVELET REPRESENTATION OF ECG SIGNALS

Patterns from the surface electrocardiogram (ECG) signals are widely used in the diagnosis of various cardiac disorders [1-3]. Similar to the pattern recognition techniques used successfully in speech, fingerprinting etc. [4, 5], ECG signal pattern matching may also provide the opportunity to recognize the same person (biometric identification) and diagnose heart diseases by means of the similarity comparison with the evaluated patterns of a typical patients' ECG in the collected databases. This chapter presents a new technique for customizing the wavelet functions adapted to the ECG signal pattern through the use of nonlinear dynamic principles. In specific, we show that using tools such as Poincare section, one can achieve extremely compact signal representation (two orders of magnitude reduction in signal entropy) that can be more sensitive to different ECG signal patterns. The remainder of chapter 4 is organized as follows: Section 4.2 gives a brief background of the applications of wavelet transform in surface ECG analysis; Section 4.3 is the phase space fiducial pattern extraction; Section 4.4 is the least squares matching wavelet design; Section 4.5 presents the implementation of designing a customized ECG wavelet function and its comparison with standard wavelet library, and Section 4.6 presents the conclusions from the reported research and perspectives on future investigations.

4.1 Background

There are several existing families of standard wavelets, such as Haar, Daubechies, Coiflet and so on [6]. The choice of wavelet basis functions plays a significant role in determining the compactness of the resulting wavelet representation. There is no consistent answer to the question: Which is the best wavelet? Some wavelets are better suited for detecting some particular problems, such as discontinuities and breakdown (e.g., Haar wavelet to detect discontinuities), while others are superior for long term evolution or compression (for e.g., a sufficiently regular wavelet with at least k ($k>3$) vanishing moments will be better to compactly represent a smooth signal).

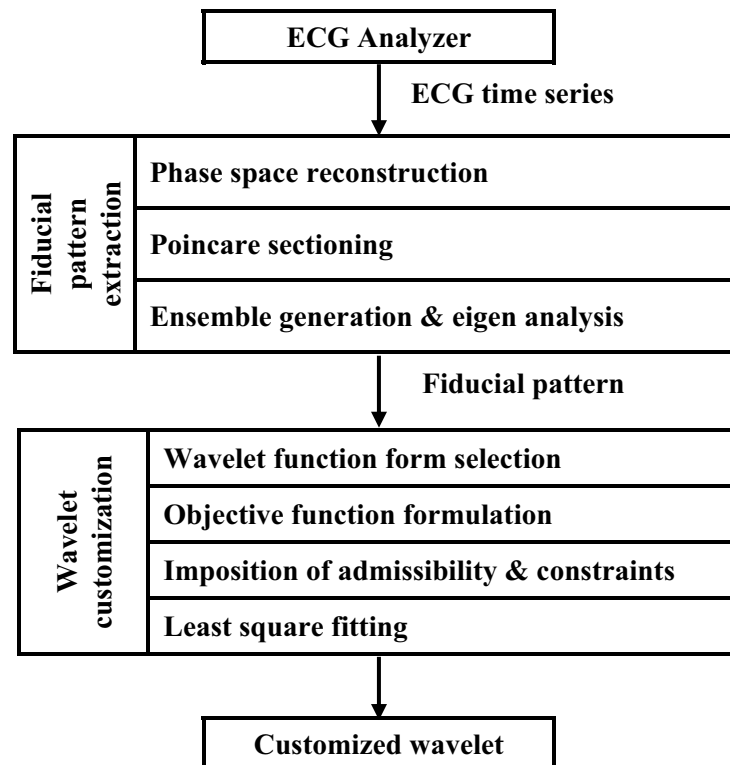


Figure 4.1 Procedure for customized wavelet design from system nonlinear dynamics

Nonetheless, it is generally understood that closer the basis functions match the signal patterns, the more compact the representation will be. As shown in Figure 4.1, this

chapter presents a customized wavelet function design using least square fitting for the fiducial signal pattern extracted from the nonlinear system dynamic characterization of signal state space. In the first step, system phase space trajectory will be reconstructed from the observed time series. False nearest neighbor test and mutual information test provide the necessary parameters, namely, embedding dimension d_E and time delay d_τ [7]. After the reconstruction of phase space, those ensembles can be extracted from Poincare sectioning of the trajectory [8]. The Karhunen-Loeve (KL) transformation of those extracted signal ensembles provides the fiducial signal pattern for the least square customized wavelet design stage. We use polynomial wavelet structures and a constrained least square fit procedure to fit the structure to match as closely as possible, subject to admissibility and regularity constraints. The details of the two major steps of fiducial pattern extraction and wavelet fitting are presented in the following two subsections. Finally, representation entropy is calculated to compare the performance of various wavelets. Signal entropy, h is a measure of parsimony of representation [9, 10]. Here, the normalized entropy with ECG signal energy is used as follows:

$$h = -\iint_{\tau,s} p(\tau,s) \log p(\tau,s) d\tau ds \quad (\text{Eq 4-1})$$

where

$$p(\tau,s) = \frac{|\Psi_x^\psi(\tau,s)|^2}{\|x(t)\|^2}, \quad (\text{Eq 4-2})$$

$\Psi_x^\psi(\tau,s)$ is a continuous wavelet transform coefficient at scale s , and translation τ , and $\|x(t)\|^2$ is signal energy. The smaller the value of signal entropy, the greater is the parsimony of the representation [11, 12]. Intuitively, “high entropy” means the

representation coefficients $\Psi_x^y(\tau, s)$ is from a uniform (boring) distribution, i.e., the histogram of distribution of values of coefficients would be flat, and “low entropy” means that coefficients $\Psi_x^y(\tau, s)$ is from varied distribution (consisting of multiple distinct peaks and large valleys) The varied distribution of representation provides the accurate detection of signal pattern.

4.2 Phase space fiducial pattern extraction

Natural systems generally show nonstationary and complex behaviors. The Karhunen-Loeve (KL) transform provides an optimal representation for second order stochastic processes. The KL representation of a stochastic process $x(t)$ is given by

$$x(t) = \sum_j b_j \alpha_j(t). \quad (\text{Eq 4-3})$$

Here, b_j 's are KL representation coefficients, and the basis function $\alpha_j(t)$ are the linearly independent solutions of

$$\int_{\mathbf{R}} K(t, \tau) \alpha_j(\tau) d\tau = \vartheta_j \alpha_j(t), \quad (\text{Eq 4-4})$$

where $K(t, \tau)$ is the autocovariance function calculated from a set of signal ensembles. It is evident that ϑ_j are eigenvalues, and $\alpha_j(t)$ are eigenfunctions of $K(t, \tau)$, and are therefore orthogonal. The order of eigenvalues, highest to lowest, indicates the components in order of significance. The KL basis can be approximated using a set of ensembles of the process $x(t)$ such that the mean square error (MSE) between a given set of ensembles and their projection to the subspaces spanned by each basis function of the KL representation is minimized.

However, in the absence of multiple realizations of $x(t)$, underlying nonlinear dynamics should be taken into account in order to extract ensembles needed to develop optimal representations (i.e., basis set) of signals from these systems. The nonlinear and stochastic dynamic characterization of a system is usually helpful in providing information on the dimensionality and the functional form of models that can capture the observed behaviors [7].

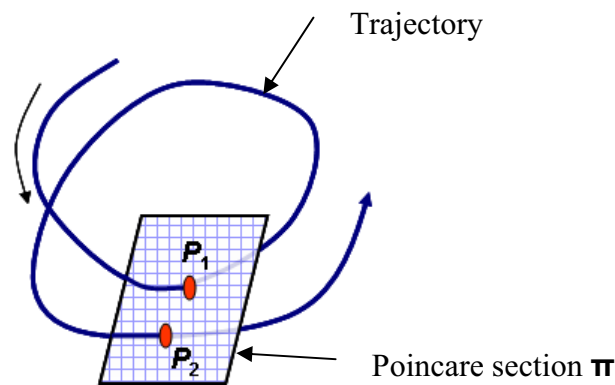


Figure 4.2 An illustration of trajectories of an attractor intersecting a (planar) Poincare section

The time evolution of the phase space trajectories emanated from the system explains the underlying nonlinear dynamics. Usually, the measured observations of a process can not include all possible state variables. Couplings among the system's components imply that each single component contains necessary information about the dynamics of the larger system. The embedding theorem of Takens [13] guarantees that the reconstructed trajectory portrays the dynamics in the higher dimensional state space. It states that a diffeomorphism exists between the reconstructed phase space with the state vector given by

$$\underline{x}(t_n) = [x(t_n), x(t_{n+d_\tau}), x(t_{n+2d_\tau}), \dots, x(t_{n+(d_E-1)d_\tau})] \quad (\text{Eq 4-5})$$

and original phase space, if $d_E \geq 2D + 1$, where d_E is the embedding dimension, d_τ is the time delay, and D is the dimension of the compact manifold containing the attractor. This implies that the dimension and entropy spectra of the reconstructed attractor are the same as those of the original one.

Poincare section is a d_E-1 dimensional hyperplane intersecting with the phase space trajectories (see Figure 4.2). The recurrence property of a chaotic attractor \mathbf{A} shows that for every $\varepsilon < 0$ and almost every $\underline{x}(0) \in \mathbf{A}$, $\exists t > 0$ such that $\|\underline{x}(0) - \underline{x}(t)\| < \varepsilon$, in effect, the trajectories with an attractor remain bounded. Those points P_i , $i = 1, 2, \dots$ at which the trajectory intersects the Poincare section follow a return map. For strictly periodic trajectory, the points P_i , $i = 1, 2, \dots$ will overlap (i.e., $\varepsilon \equiv 0$) such that the duration between P_i to P_{i+1} along the trajectory constitutes the period. For chaotic systems no two P_i 's overlap. For near-periodic signals, such as ECG, each strand emanating from a Poincare section intersection point P_i and lasting approximately till the next intersection P_{i+1} along the trajectory may be treated as a realization of a stochastic process from an invariant probability space [12]. Due to heart rate variability, some ensembles move faster, i.e., the two successive intersections occur over shorter intervals, compared to the others [14, 15]. In this investigation the length (time duration) of the ensembles is taken as the time interval between the intersections of the fastest ensemble. Moreover, those collected near-periodic ensembles provide an effective way for the Karhunen-Loeve (KL) representation of this signal. In this ECG investigation, the largest eigenvalue \mathcal{G}_{\max} is 4.3026 which implies that 98.34% of the total variation occurs along the leading (the first one out of 41) eigenfunctions. Intuitively, each eigenfunction $\alpha(\bullet)$ captures the shape of

a specific mode of variation (roughly, a degree of freedom) of $\underline{x}(\bullet)$. The fiducial pattern $\zeta(t)$ of a signal emerging from a process with d -degrees of freedom (or topological dimension D , where $d = \lceil D \rceil$) is obtained as the optimal projection of the ensembles onto the space spanned by $\alpha_1(\bullet), \alpha_2(\bullet), \dots, \alpha_d(\bullet)$. For computational convenience (during matching wavelet design), the support of $\zeta(t)$ is rescaled so that $t \in [0, 1]$.

4.3 Least square matching wavelet design

The continuous wavelet transform Ψ_x^ψ of the signal $x(t)$ using the analysis wavelet $\psi(t)$ is:

$$\Psi_x^\psi(\tau, s) = \frac{1}{\sqrt{|s|}} \int_t x(t) \tilde{\psi}\left(\frac{t-\tau}{s}\right) dt \quad (\text{Eq 4-6})$$

where $\tilde{\psi}$ is the dual of $\psi(t)$ [16]. If $x(t)$ is similar to the wavelet basis functions, then the coefficients Ψ_x^ψ will likely be large only for a few basis functions. Thus, the customized wavelet function adapted to the ECG pattern may achieve the best performance. We design the wavelet function using a least squares approach [6, 17, 18]. A wavelet basis function $\psi(t)$ is approximated as a polynomial regression of degree M :

$$\begin{aligned} \psi(t) &= a_0 + a_1 t + a_2 t^2 + \dots + a_M t^M = \sum_{m=0}^M a_m t^m = U(t) \theta^T \\ U(t) &= [1 \quad t \quad t^2 \quad \dots \quad t^M] \\ \theta &= [a_0 \quad a_1 \quad a_2 \quad \dots \quad a_M] \end{aligned} \quad (\text{Eq 4-7})$$

Let us assume that N -sample time-series of fiducial ECG pattern $\zeta(t)$ be available such that:

$$Z_N = \{\zeta(t_n), \quad 0 \leq t_n \leq 1\} \quad (\text{Eq 4-8})$$

Similarly, we can reduce operator $U(t)$ to a Vandermonde matrix A , whose elements are powers of t , will be as following:

$$A = \begin{bmatrix} 1 & t_1 & t_1^2 & \cdots & t_1^M \\ 1 & t_2 & t_2^2 & \cdots & t_2^M \\ \vdots & \vdots & \vdots & \cdots & \vdots \\ 1 & t_N & t_N^2 & \cdots & t_N^M \end{bmatrix} \quad 0 \leq t_1, \dots, t_N \leq 1 \quad (\text{Eq 4-9})$$

It is important that the function $\psi(t)$ which can not only best fit the fiducial signal pattern $\zeta(t)$ but also satisfy the wavelet admissibility and regularity conditions (Percival and Walden¹¹). The admissibility requirements for any valid real or complex-value continuous-time function $\psi(t)$ to be a wavelet basis function can be summarized as: reconstruction, zero mean, finite energy and regularity constraints. The first three defines the *wave*, and the last condition determines the rate of decay or the *let*. A function satisfied with all the four conditions can be a valid *wavelet* for CWT [18].

Since the fiducial pattern $\zeta(t)$ is a finite length signal, the finite energy requirement

is automatically met. The zero mean condition $\int_{-\infty}^{\infty} \psi(t) dt = 0$ implies that the Fourier

transform of $\psi(t)$ vanishes at the zero frequency $\left| F_{\psi}(\omega) \right|_{\omega=0}^2 = 0$, where $F_{\psi}(\omega)$ stands for

the Fourier transform of $\psi(t)$. So, it will also make sure that $C_{\psi} = \int_{-\infty}^{\infty} \frac{|F_{\psi}(\omega)|^2}{|\omega|} d\omega$ is finite

for the success of inverse continuous wavelet transform:

$$x(t) = \frac{1}{C_{\psi}} \int_s \int_{\tau} \Psi_x^{\psi}(\tau, s) \frac{1}{s^2} \psi\left(\frac{t-\tau}{s}\right) d\tau ds \quad C_{\psi} = \int_{-\infty}^{\infty} \frac{|F_{\psi}(\omega)|^2}{|\omega|} d\omega \quad (\text{Eq 4-10})$$

Summarizing, the least square M th degree polynomial fitting with regularity K for the wavelet design will add zero mean and regularity conditions, and the deduction of revised matrix \tilde{A} and Z_N is as following.

(1) Zero mean

$$\int_0^1 \psi(t) dt = \left(a_0 t + \frac{a_1 t^2}{2} + \dots + \frac{a_M t^{M+1}}{M+1} \right) \Big|_0^1 = 0 \quad (\text{Eq 4-11})$$

(2) Regularity

The i^{th} moment of the function $\psi(t)$ is defined as $\int_{-\infty}^{+\infty} t^i \psi(t) dt$. If the function's first i moments are zero $\int_{-\infty}^{+\infty} t^i \psi(t) dt = 0$ for $0 \leq j \leq k$, the number of vanishing moment of the function $\psi(t)$ is $k+1$.

$$\int_0^1 t^i \psi(t) dt = \left(\frac{a_0 t^{i+1}}{i+1} + \frac{a_1 t^{i+2}}{i+2} + \dots + \frac{a_M t^{i+M+1}}{i+M+1} \right) \Big|_0^1 = 0 \quad 1 \leq i \leq k \quad (\text{Eq 4-12})$$

New Vandermonde matrix \tilde{A} will contain powers elements of t and the wavelet constraints.

$$\tilde{A} = \begin{bmatrix} 1 & t_1 & t_1^2 & \dots & t_1^M \\ \vdots & \vdots & \vdots & \dots & \vdots \\ 1 & t_N & t_N^2 & \dots & t_N^M \\ 1 & 1/2 & 1/3 & \dots & 1/(M+1) \\ 1/2 & 1/3 & 1/4 & \dots & 1/(M+2) \\ \vdots & \vdots & \vdots & \dots & \vdots \\ 1/(k+1) & 1/(k+2) & 1/(k+3) & \dots & 1/(k+M+1) \end{bmatrix} \quad 0 \leq t_1, \dots, t_N \leq 1 \quad (\text{Eq 4-13})$$

$$\theta = [a_0 \ a_1 \ a_2 \ \dots \ a_M] \text{ and } Z_N = [\zeta(t_1), \dots, \zeta(t_N), 0, 0, \dots, 0]^T \quad (\text{Eq 4-14})$$

The N -sample estimate of the coefficients vector $\hat{\theta}_N$ of the matching polynomial wavelet function can be determined to minimize the objective function $V_N(\theta, Z_N)$

$$V_N(\theta, Z_N) = \frac{1}{N} \sum_{t=1}^N (Z_N - \tilde{A}^T \theta)^2 \quad (\text{Eq 4-15})$$

$$\hat{\theta}_N = \arg \min_{\theta} \{V_N(\theta, Z_N)\} \quad (\text{Eq 4-16})$$

and the estimate can be obtained using the pseudoinverse:

$$\theta^T = Z_N (\tilde{A}^T \tilde{A})^{-1} \tilde{A}^T \quad (\text{Eq 4-17})$$

4.4 Implementation and results

As discussed in the research methodology section, the coefficients of a compact wavelet representation need to be more sensitive to variation in the underlying processes (physiological) and less sensitive to noise variation. Thus, feature sets extracted from a compact representation tend to be lighter (i.e. fewer and more sensitive) and more effective in estimating various anomalies (here, different AF states). For implementation and validation of the present approach, we utilized the ECG data from the 2004 PhysioNet challenge named Spontaneous Termination of Atrial Fibrillation (AF), posted on the PhysioNet website [19, 20]. Atrial Fibrillation (AF) is one of the serious cardiac disorders that affect millions of human beings, and its early detection can have a significant bearing on the quality of healthcare. In this contest, classification needs to be made among the following three categories of AF patients test signals:

- 1) **Group N:** Non-terminating AF (defined as AF that was not observed to have terminated for the duration of the long-term recording, at least an hour following the segment).

- 2) **Group S:** Soon to be terminating (AF that terminates one minute after the end of the record).
- 3) **Group T:** Terminating immediately (AF terminating within one second after the end of the record).

In all, 80 recordings of AF from 60 different subjects were made available in the database. Each record is a one-minute segment of AF, containing two channel ECG signals (Lead I and II), each at 128 samples/sec. Figure 4.3 contains ECG signal trace taken from a subject with AF for the duration of approximately 10 heartbeats. The trace shows a QRS complex with a significant R-peak followed by a T-wave. The signal is superposed with higher frequency (>6Hz) atrial fibrillation F-waves in lieu of P-waves.

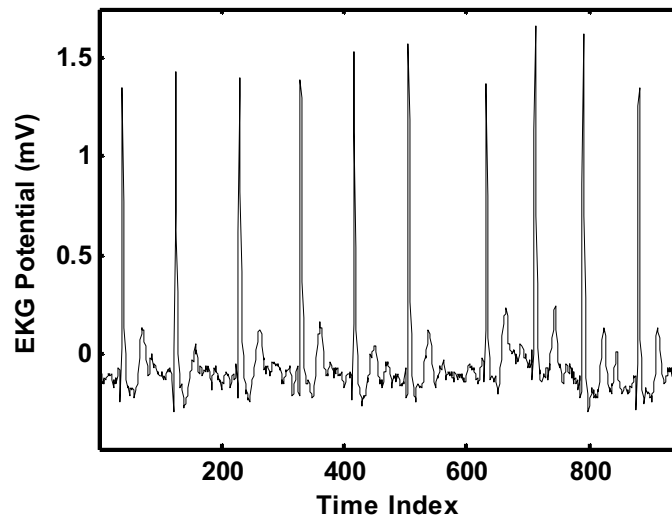


Figure 4.3 Time domain plot of a representative ECG signal trace (a01)

After the false nearest neighbor and mutual information test [7, 21], the optimal embedding dimension and time delay were determined for reconstruction of the state space from the ECG traces using time delay coordinates in d_E embedding dimensions as

$$\underline{x}(t_n) = [x(t_n), x(t_{n+d_\tau}), x(t_{n+2d_\tau}), \dots, x(t_{n+(d_E-1)d_\tau})]$$

space shows a large loop of QRS complex extending top-down and left to right, with the R-peaks occurring at the top and right extrema. A T-loop as well as an irregular ball formed by the F-waves are observed near the origin (bottom left corner). The Poincare sections Π_1 and Π_2 of the state portrait, as shown in Figure 4.4 can be used to gather alternative sets of pattern ensembles.

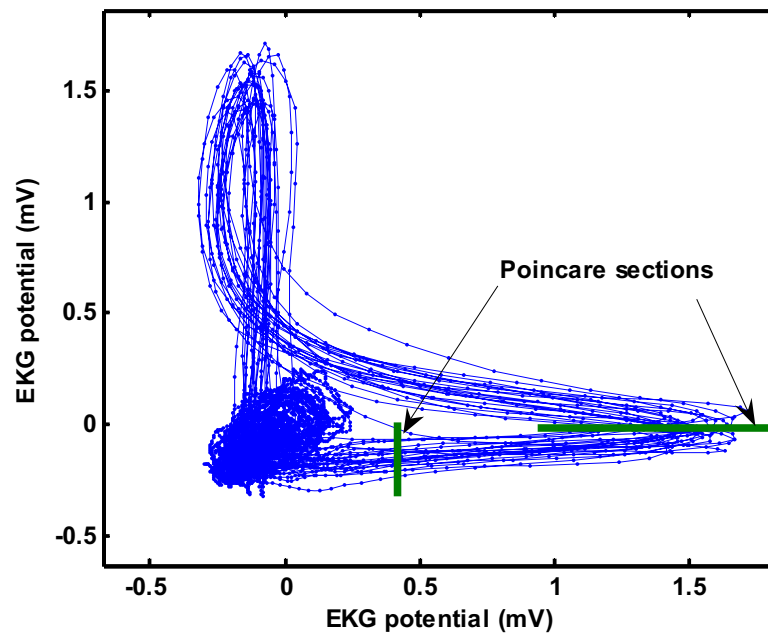


Figure 4.4 State space portrait reconstructed from time delay coordinates

The choice of the Poincare section Π affects the shape of the pattern as well as the performances (entropy) of the representation. For e.g., one needs to choose the Poincare section such that the flow lines are directed about one or two flat planes, in which case Π takes the form of a simple planar object. Also, it is desirable that the local Lyapunov exponent λ_{\max} of the state is close to or below zero about Π . This will help in making sure the resulting wavelet easily satisfies the constraints imposed by Eqs. (4-11) and (4-12). In this context, wavelet customized through Poincare section Π_1 can yield better

performances than that through Poincare section π_2 as shown in Figure 4.4. Figure 4.5 shows the ensembles gathered from Poincare section π_1 . The fiducial ECG signal pattern used for the wavelet design stage can be extracted from dominant eigenfunctions estimated using the KL representation. Figure 4.6 shows the least square matching wavelet design result. The resulting wavelet $\psi(t)$ holds significant similarities to the fiducial pattern $\zeta(t)$ and capture a majority of the variations among the ensembles.

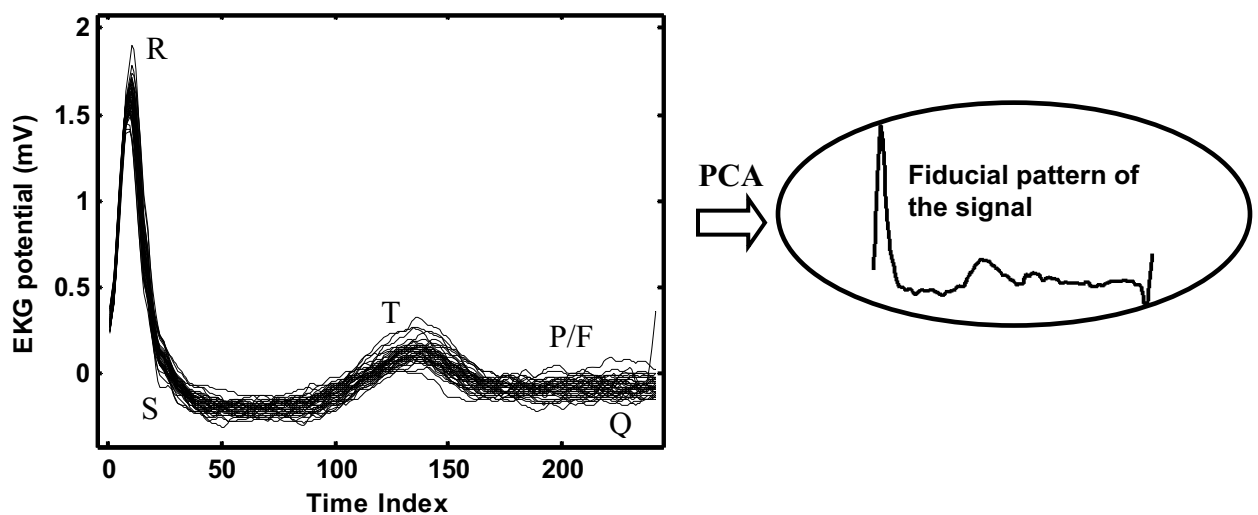


Figure 4.5 ECG pattern ensembles extracted from Poincare section

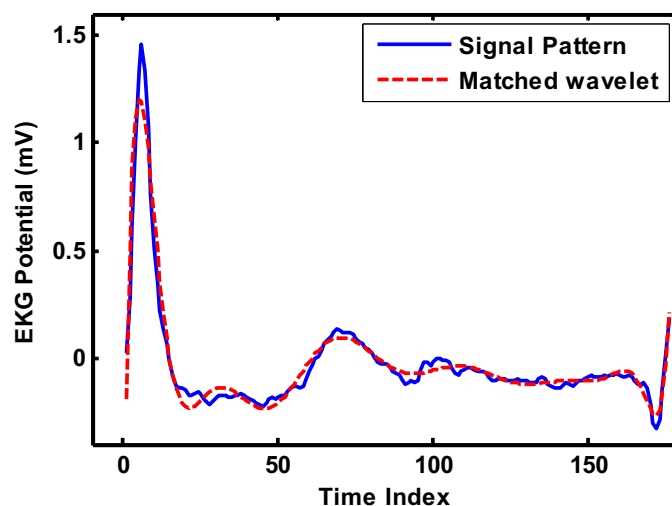


Figure 4.6 Matching wavelet extracted from fiducial signal pattern

Figure 4.7 shows the variation of entropy (Eq. (4-1)) with the polynomial degree of the wavelet function $\psi(t)$ that matches the fiducial pattern. The minimal entropy for matching wavelet (shown in Figure 4.7) is found to have a polynomial degree of 13.

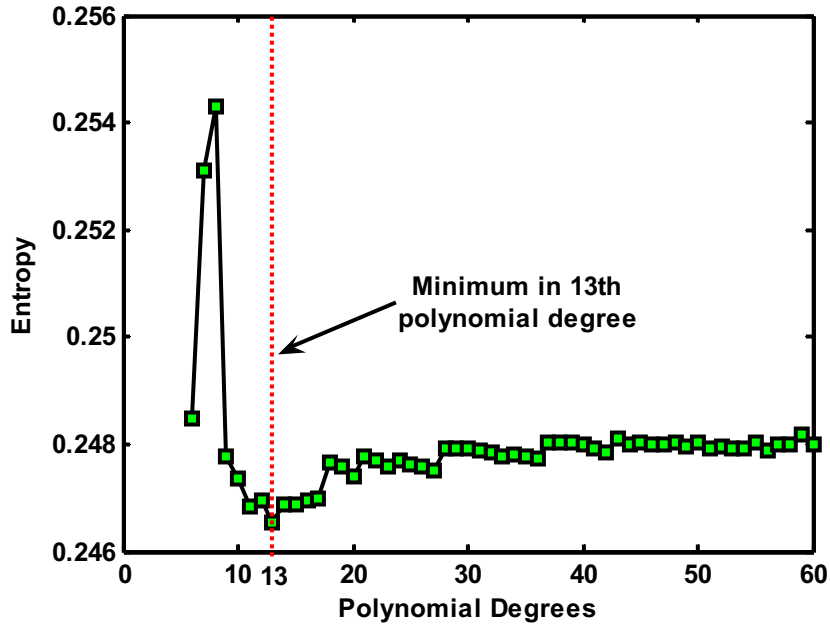


Figure 4.7 Matching wavelet representation entropy variation with various polynomial degrees

As summarized in Figure 4.8, the customized wavelets an ECG from a non-terminating AF case, obtained through Poincare sections π_1 and π_2 of the reconstructed state space, denoted $a01pat_pi1$ and $a01pat_pi2$, respectively, and customized wavelets from normal ECG pattern ($nmpat_pi1$ and $nmpat_pi2$), shown in the last four bars on the right side, are about 95% (approximately two orders of magnitude) more compact than all standard available wavelet bases investigated (shown on the left side), namely, db2 (Daubechies-2), sym2 (Symlet-2), haar (Haar), mexh (Mexican hat), meyr (Meyer), dmeyr (Discrete Meyer), morl (Morlet), db10 (Daubechies-10), sym10 (Symlet-10). Also, the wavelets customized for a normal ECG signal seems to yield more compact

representations for a signal from a non-terminating AF case (i.e., a01 signal in the PhysioNet [20]).

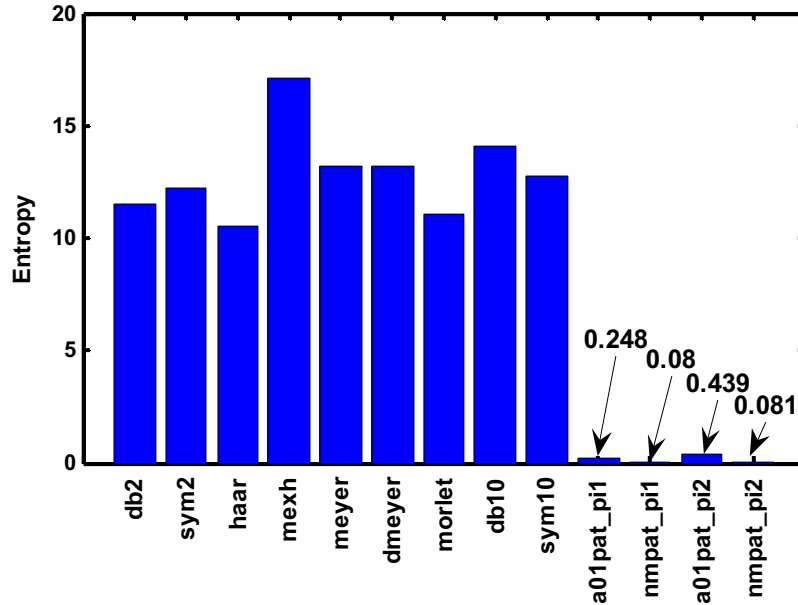


Figure 4.8 Entropy comparison between standard wavelets and matching wavelets

The two orders of magnitude increase in the compactness of ECG signal representation with customized wavelet (measured in terms of entropy reduction) is further evidenced from the examination of the distribution of entropies for eleven signals (a01, a02, a03, b01, b02, n01, n02, s01, s02, t01, t02) in the PhysioNet database for the AF challenge with the eleven alternative wavelet bases including the standard and the customized wavelets (see Figure 4.9). Interestingly, the wavelets customized for an ECG signal from a normal case yield about five times lower entropy compared to that from a non-terminating AF case. Also, it may be noted that, although both customization yield ignorantly low entropy compared to standard wavelet basis, the entropy of wavelet adapted from Poincare section π_2 is twice as large as that from Poincare section π_1 . It is

evidently due to the fact that the customized wavelet from π_1 naturally closes to satisfying the wavelet constraint Eqs. (4-11) and (4-12).

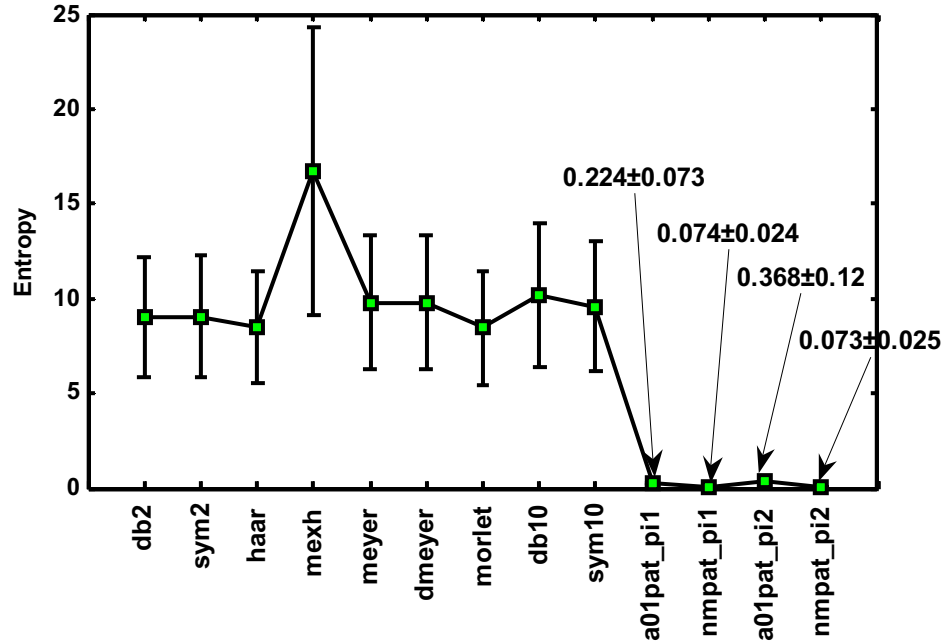


Figure 4.9 Entropy distribution for different wavelet representations, taken over all ECG signals in the database considered

Reasons for the compactness of the representations are further evident from an examination of the histograms of wavelet coefficients of the representations (see Figure 4.10). The figure shows the distribution of wavelet coefficients within various bins of the histogram. The coefficients from the customized wavelet representation (see Figure 4.10 (a)) are concentrated around zero with few large coefficients. Such a low entropy distribution, with few large coefficients and several near-zero coefficients can lead to clearer demonstration and identification of various salient events in ECG signals. In contrast, coefficients of a representation from a standard library wavelet (see Figure 4.10 (b)) are spread uniformly, providing no clear distinction between significant and non-

significant coefficients. Therefore, we have used the customized wavelets for QRST cancellation and feature extraction.

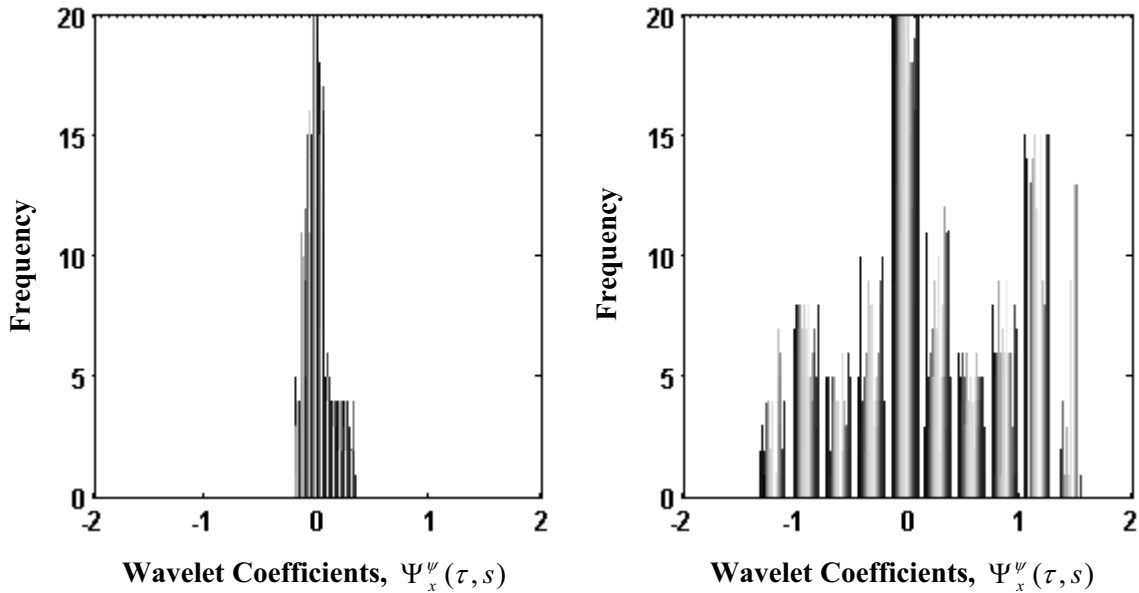


Figure 4.10 Histogram of matching wavelet transform coefficients: (a) customized wavelet, (b) Morlet wavelet

4.5 Summary

The choice of various basis functions is known to determine the compactness of a wavelet representation. In general, the closer the basis function captures the signal characteristics, the more compact is the representation, and more likely are the features sensitive to relevant ECG states and insensitive to variations in extraneous noise. In this chapter, we have customized the basis functions of a continuous wavelet representation by choosing polynomial wavelet basis functions that match the characteristics of a fiducial 1-beat long ECG signal pattern extracted from the Poincare sectioning of ECG state space. The customized representations were found to be roughly two orders of magnitude more compact (measured in term of signal entropy) than the wavelet basis functions available in the standard wavelet library. The unraveling of scale-time distribution of signal content in wavelet representation can facilitate the identification of

various ECG events including the onsets, peaks, and offsets of various ECG waveforms for different beats. Further, it provides a means for QRST subtraction to suppress ECG signal components that emerge from ventricular sources.

4.6 References

- [1] Z.D.Yum, J.Q.Xu, and G.P.Li, "Recognition of cardiac patterns based on wavelet analysis," in *Proceedings of the 2003 IEEE International Symposium on Intelligent Control*, Houston, Texas, October 5-8. 2003, pp. 642-645.
- [2] Z. Huang, "Genetic Algorithm Optimized Feature Extraction and Selection for ECG Pattern Classification," in *Department of Electrical and Computer Engineering*. vol. M.S. Thesis: Michigan State University, 2002.
- [3] R. Boussejot and D. Kreisler, "ECG Signal Analysis by Pattern Comparison," *Computers in Cardiology*, vol. 25, pp. 349-352, 1998.
- [4] A. K. Jain, R. P. W. Duin, and J. Mao, "Statistical Pattern Recognition: A Review," *IEEE Transactions on Pattern Analysis and Machine Intelligence*, vol. 22, pp. 4-37, January 2000.
- [5] T. Irino and H. Kawahara, "Signal Reconstruction from Modified Wavelet Transform - An application to Auditory Signal Processing," *IEEE Transactions on Signal Processing*, vol. 41, pp. 3549-3554, 1993.
- [6] D. B. Percival and A. T. Walden, *Wavelet Methods for Time Series Analysis*: Cambridge University Press, 2000.
- [7] H. Kantz and T. Schreiber, *Nonlinear Time Series Analysis*. Cambridge: Cambridge University Press, 1997.
- [8] S. T. S. Bukkapatnam, "Recurrence-based piecewise eigen representation of contaminated chaotic signals," *Physical Review E (under review)*, 2007.
- [9] M. V. Wickerhauser, "Lectures on Wavelet Packet Algorithms," Nov. 18, 1991.

- [10] R. R. Coifman and M. V. Wickerhauser, "Entropy-Based Algorithms for Best Basis Selection," *IEEE Transactions on Information Theory*, vol. 38, pp. 713--718, 1992.
- [11] S. T. S. Bukkapatnam, "Compact nonlinear signal representation in machine tool operations," in *ASME Design Engineering and Technology Conference, DETC-VIB 8068*, Las Vegas, NV, September 12-15, 1999.
- [12] S. Bukkapatnam, S. Kumara, and A. Lakhtakia, "Local eigenfunctions-based suboptimal wavelet packet representation of contaminated chaotic signals," *IMA Journal of Applied Mathematics*, vol. 63, pp. 149-160, 1999.
- [13] F. Takens, *Detecting strange attractors in turbulence, lecture notes in mathematics* vol. 898: Springer, Berlin, 1981.
- [14] F. Marciano, M. L. Migaux, D. Acanfora, G. Furgi, and F. Rengo, "Quantification of Poincare maps for the evaluation of heart rate variability," 1994, pp. 577-580.
- [15] G. D'Addio, G. D. Pinna, R. Maestri, G. Corbi, N. Ferrara, and F. Rengo, "Quantitative Poincare plots analysis contains relevant information related to heart rate variability dynamics of normal and pathological subjects," 2004, pp. 457-460.
- [16] I. Daubechie and B. Han, *Pairs of Dual Wavelet Frames from Any Two Refinable Functions*. New York: Springer, May 12, 2004.
- [17] C. Valens, "A Really Friendly Guide to Wavelets," 1999-2004.
- [18] G. Strang and T. Nguyen, *Wavelets and Filter Banks*: Wellesley-Cambridge Press, 1996.
- [19] G. Moody, "Spontaneous Termination of Atrial Fibrillation: A Challenge from PhysioNet and Computers in Cardiology 2004," *Computers in Cardiology*, vol. 31, pp. 101-104, 2004.

- [20] A. Goldberger, L. Amaral, L. Glass, J. Hausdorff, P. Ivanov, R. Mark, J. Mietus, G. Moody, C. Peng, and H. Stanley, "PhysioBank, PhysioToolkit, and PhysioNet: Components of a New Research Resource for Complex Physiologic Signals," *Circulation* 101, vol. 23, pp. e215-e220, 2000 (June 13).
- [21] S. Bukkapatnam, A. Lakhtakia, and S. Kumara, "Analysis of sensor signals shows turning on a lathe exhibits low-dimensional chaos," *Physical Review -E.*, pp. 2375-2387, 1995.

CHAPTER V

DYNAMIC VCG REPRESENTATION

The conventional 12-lead electrocardiogram (ECG) and the 3-lead Frank X,Y,Z vectorcardiogram (VCG) signals are recorded at the body surface to monitor the underlying heart's electrical activities and used to provide valuable information for the medical diagnosis of the cardiovascular condition of a patient. The heart activities are monitored from various perspectives by these signals. The 12-lead ECG is more commonly used than the 3-lead VCG because medical doctors have been accustomed to using them in clinical diagnosis for more than one hundred years. It has thus proven its value, time tested, and considered as the Gold Standard. However, much of that information is redundant and even in that, only a small fraction of the data is used in the analysis by the physicians based on experience and expertise and oftentimes on the memorization of ECG signals for different cardiological disorders. This is a difficult task and the cardiologists are constantly looking for alternatives.

VCG monitors the cardiac electrical activity in three pseudo-orthogonal X,Y, Z planes of the body, namely, frontal, transverse, and sagittal (see Figure 2.3) [1]. It is traditionally projected to different planes (X-Y plane, X-Z plane and Y-Z plane) which captures the time correlations, or plot as a static attractor in a 3D space that provides the topological relationships. The absence of combined spatiotemporal information in the

VCG representations reported earlier, expects the interpreters to have not only the spatial but also the temporal imaginations.

This chapter presents a dynamic VCG representation approach to capture the spatiotemporal dynamics underlying the cardiac electrical activities. Instead of reading signals from a paper which at most gives three dimensions, the monitor of the computer is used to view all four dimensions, namely, the three X, Y, and Z components and one time scale. The example VCGs used in this investigation are gathered from the PTB database, which is available from the PhysioNet – a public service of the research source for the complex physiological signals [2]. Each of the recordings in the database contains 15 simultaneously recorded signals, namely, the conventional 12-lead ECGs and the three orthogonal Frank XYZ leads VCG signals digitized at 1 kHz, with a 16 bit resolution over a range of ± 16.384 mV.

The remainder of this chapter is organized as follows: Section 5.1 presents a brief background on the linear transformation between 3-lead VCG and the 12-lead ECG; Section 5.2 provides the research methodology used; Section 5.3 presents a discussion of the pathological patterns in VCG signals, and Section 5.4 covers the conclusions based on the research reported here.

5.1 Background

The electrocardiogram, designed by Augustus Waller in 1889 and further improved by Williem Einthoven in 1901, has been used for more than 100 years for the clinical diagnosis of cardiovascular disorders. Einthoven denoted the P, QRS, and T waves in the EKG signal to the sequences of atrial and ventricular depolarization and repolarization activities. Around 1904 Einthoven *et al.* [3] derived the famous “Einthoven triangle” to

measure three EKG signals and calculate the approximate direction of the cardiac vector. In 1956, Ernest Frank designed the Frank lead system to measure the VCG in three corrected orthogonal coordinates, which provides a clear picture of the cardiac vector.

With the rapid development of information technology (IT) and the availability of computing hardware at reasonable cost, the representation and analysis of 3D VCG loops are not constrained by computational resources and this has resulted in renewed interest in VCG since 1990's. Dower and his colleagues [4-6] conducted pioneering research based on Frank's tank torso model studies and introduced a linear transformation matrix to convert 3-lead VCG signals into 12-lead ECG signals without a significant loss of clinically useful information regarding heart dynamics. The inverse Dower transformation matrix is used to derive the 3-lead VCG from the 12-lead ECG. Some even consider Dower transformation matrix as generalized or universal transformation matrix [4-7] although this has not been established to date and one finds different transformation matrices for healthy subjects and patients with cardiological disorders [8].

The transformation studies show the statistical equivalence between the 12-lead ECG and the 3-lead VCG. However, it is difficult for the human beings to visually project a spatial VCG vector into any specified cardiac measurement angle determined by the 12-lead measurement systems, which is the conventional way for the ECG interpretation. In addition, the absence of temporal information in the static VCG representation poses extra barriers for medical doctors to closely relate the 12-lead ECG characteristics to the 3-lead Frank X, Y, Z VCG signals. But when it comes to the computer automated analysis of heart monitoring system, the 12-lead ECG signals will introduce the "curse of dimensionality" problem, which is the convergence of any

estimator to the true value of a smooth function defined on a space of high dimension is very slow because of the exponential increase in volume associated with extra dimensions. Thus, VCG is a better option for computer processing and analysis because it overcomes not only the loss of information from the analysis of only one or two ECG signals but also the dimensionality problems induced by the 12-lead ECG. The usage of VCG for the medical diagnosis has been studied by many researchers [9-20] although investigations exploring both spatial and temporal relationships of the VCG signals are rarely, if any, found. It is hoped that present approach of spatiotemporal VCG representation would greatly improve the exploration of spatiotemporal cardiovascular dynamics and lead to automated computer analysis. This approach will be introduced in the following sections.

5.2 Research methodology

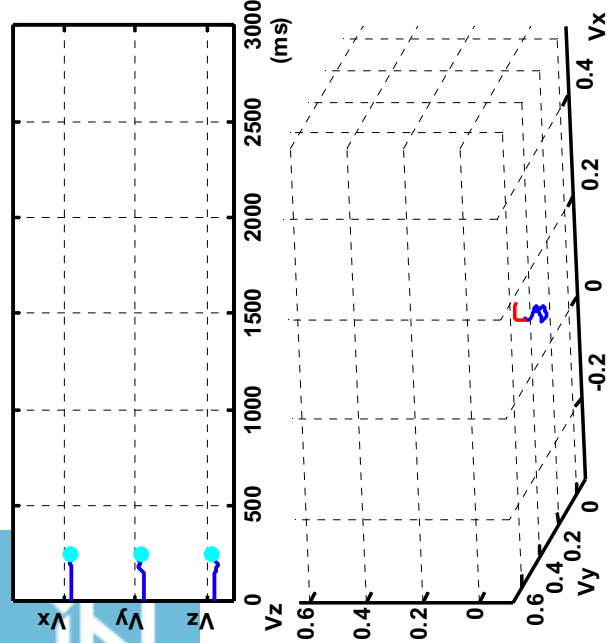
The three VCG vector loops, namely, P, QRS, and T waves contain three dimensional recurring, near-periodic patterns of heart dynamics. The dynamic VCG representation can provide doctors with an easier way to understand, interpret, and use vectorcardiograms. This approach includes presenting VCG signals as a real time motion of cardiac vector in 3D space, and color coding of the magnitude of the cardiac vector movement with the curvature, velocity, and phase angle etc. In addition, an alternative lag reconstructed heart attractor representation from nonlinear dynamics principles is provided, if there is only one dimensional heart monitoring signal available. The proposed dynamic representation of the vector loops can be rotated freely on the monitor to analyze the loop's form in real time.

5.2.1 Spatiotemporal VCG attractor representation

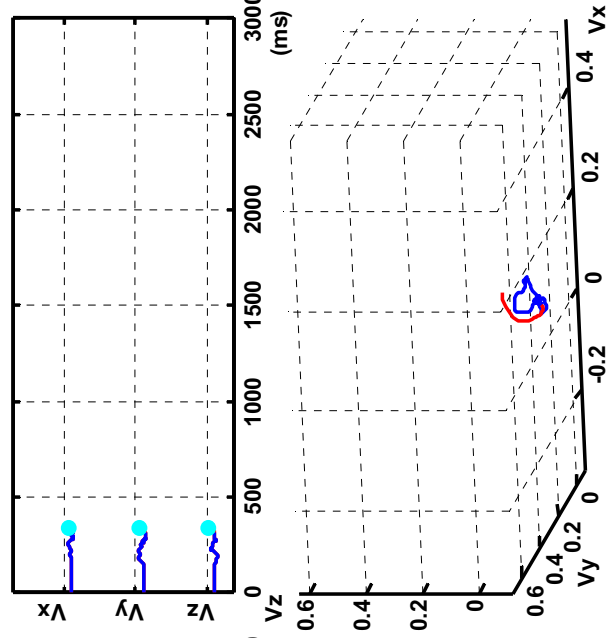
In the Frank XYZ lead system, a vectorcardiogram is represented as three orthogonal scalar measurements with respect to time as shown in Eq 5-1. The dynamic VCG representation embeds the cardiac vector, composed of three scalar measurements as x, y, z components, in real time. As shown in Figure 5.1, the representation is divided into two parts. The top half plots the three scalar x, y, z components in real time and the bottom half presents the movement of cardiac vector in 3D space simultaneously.

$$\begin{cases} \mathbf{v}_x = \mathbf{f}(t) \\ \mathbf{v}_y = \mathbf{g}(t) \\ \mathbf{v}_z = \mathbf{h}(t) \end{cases} \quad (\text{Eq 5-1})$$

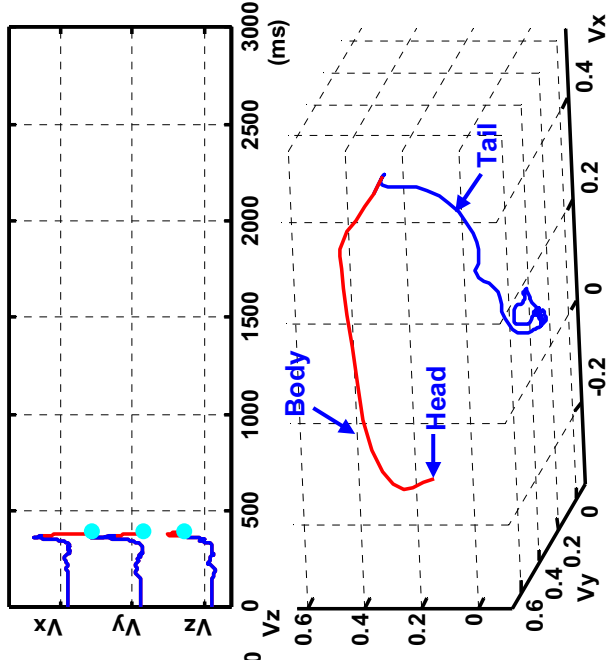
Patient005\s0101Ire: Myocardial infarction, anterior



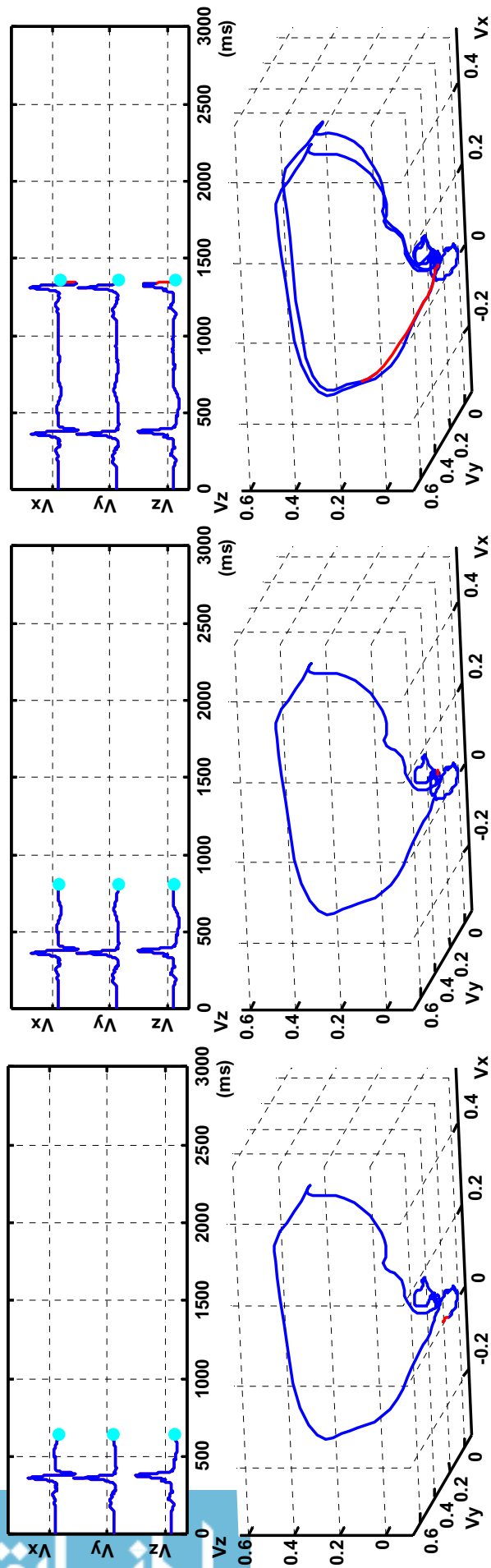
(a) Beginning of P Wave



(b) End of P wave



(c) QRS complex



(d) Middle of T wave

(e) End of T wave

(f) Second QRS complex

Figure 5.1 Frames from dynamic VCG representation of a patient with myocardial infarction, anterior

Therefore, this explicitly real time dynamic VCG representation makes it easier for doctors to utilize it with prior interpretation expertise and experiences of time-based ECG. As shown in Figure 5.1 (c), this representation consists of three components: head (green), body (red), and tail (blue). Head gives the current position of the cardiac vector. Body records a short history of the cardiac movement which clearly indicates where the current vector is from. It avoids the confusion regarding which heart activity loop the current cardiac vector belongs to because those loops usually have some intersections in the isoelectric point. Tail provides the full history from the start of the recording time that captures the full topological shapes of the VCG attractor. Figure 5.1 (a) bottom VCG trajectory shows the beginning of P wave which is the start of atrial depolarization after the SA node excitation. This cardiac activity is also indicated from the projections of cardiac vector on the X, Y, Z Cartesian axes as shown in the Figure 5.1 (a) top plot. In Figure 5.1 (b), we can see the complete P wave loop and Q wave onset (interventricular septum depolarization). When it comes to Figure 5.1 (c), the QRS loop is presented to manifest the ventricular depolarization activities. It is followed by ventricular repolarization shown as T wave loop in Figure 5.1 (d) (e). Figure 5.1 exhibits the next heart activity cycle. Figure 5.1 clearly shows that the P, QRS, and T waves can be easily located in the VCG attractor with respect to time.

5.2.2 Lag reconstructed spatiotemporal ECG attractor

In many real life cases, only a few measurements (e.g., lead I ECG signal) are available in lieu of the complete measurements of three cardiac vector components recorded for a given time period. Takens embedding theorem [18] states that many individual measurements contain adequate information to reconstruct most of the system

attractor dynamics because of the high dynamic coupling existing among the real world system. Therefore, an equivalent cardiac vector space (attractor) can be reconstructed from the delayed coordinates of the only measurement $y(t)$ as

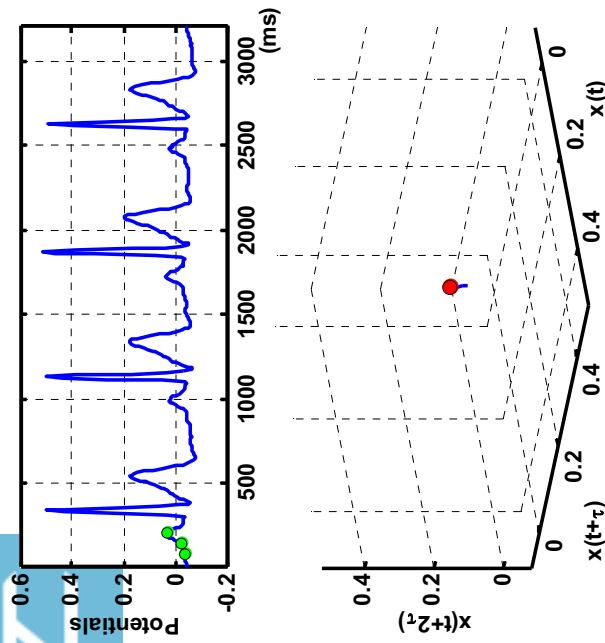
$$\underline{y}(t_i) = [y(t_i), y(t_i + \tau), y(t_i + 2\tau)] \quad (\text{Eq 5-2})$$

where τ is the time delay. The optimal time delay τ is selected to minimize mutual information function $M(\tau)$, defined as

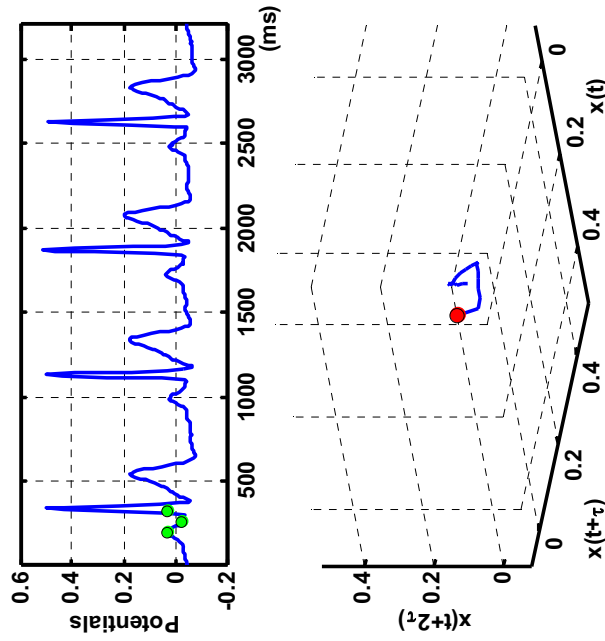
$$M(\tau) = \int_i p(t, t + \tau) \log \frac{p(t, t + \tau)}{p(t)p(t + \tau)} dt \quad (\text{Eq 5-3})$$

where $p(t, \tau)$ is the joint density function, and $p(t)$ and $p(t + \tau)$ are marginal density functions of $y(t)$ and $y(t + \tau)$, respectively [21].

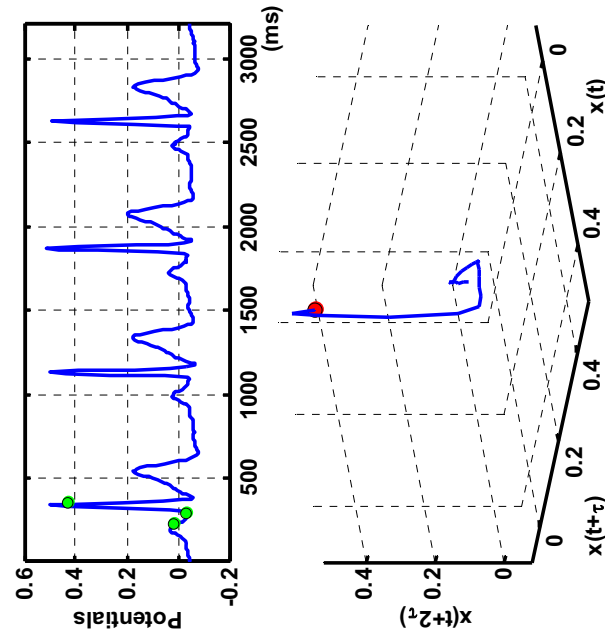
As shown in Figure 5.2, animation of the lag reconstructed EKG attractor can also provide the similar spatiotemporal information as the VCG attractor described in Section 5.2.1.



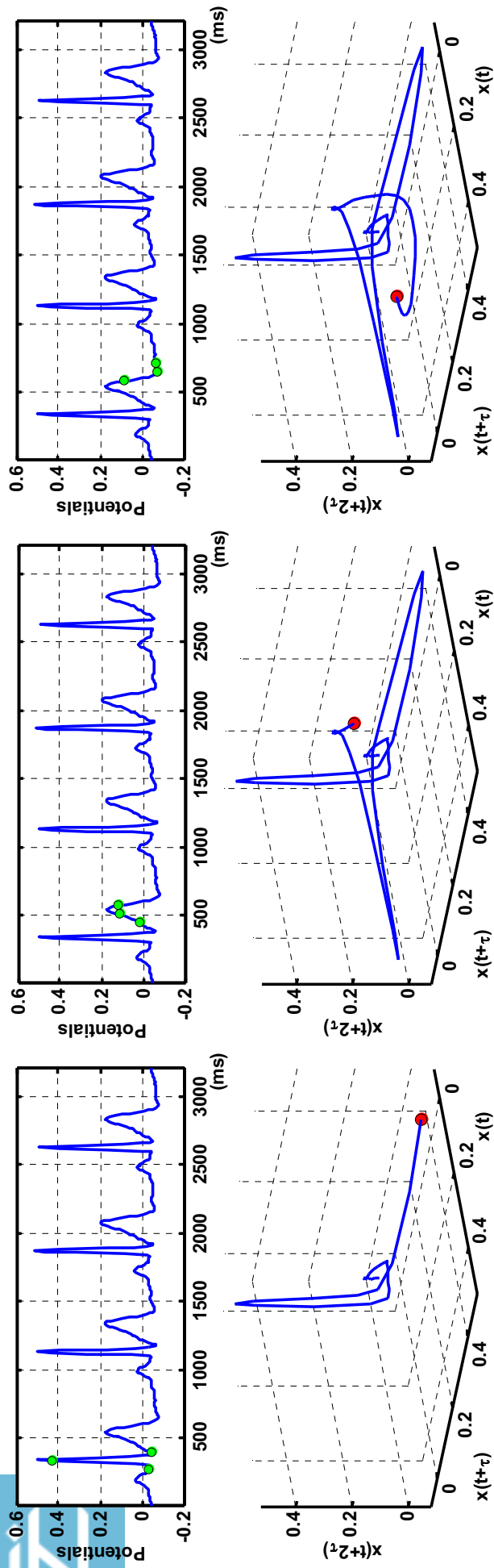
(a) Beginning of P Wave



(b) End of P wave



(c) Start of QRS complex



(d) During QRS complex (e) During T wave (f) End of T Wave

Figure 5.2 Frames from lag reconstructed dynamic EKG attractor representation for a normal subject

5.2.3 Color coding of spatiotemporal VCG representation

Color coding scheme can be used to incorporate additional dynamical attributes of the VCG attractor, such as curvature, "speed" ($dv = \Delta v/\Delta t$, and $\Delta v = ||v(t) - v(t+1)||$) and phase angle. The estimate of the curvature can be made by taking the cross product between the two vectors from the current point to the points a certain distance on either side. The phase angles of the cardiac vector are calculated using Eq 5-4.

$$\cos \theta = \frac{v_x}{\sqrt{v_x^2 + v_y^2 + v_z^2}}, \cos \alpha = \frac{v_y}{\sqrt{v_x^2 + v_y^2 + v_z^2}}, \text{ and } \cos \beta = \frac{v_z}{\sqrt{v_x^2 + v_y^2 + v_z^2}} \quad (\text{Eq 5-4})$$

The magnitude of the color indicators, such as curvature, speed, phase angles are mapped into a color scale. Thus, the color coding scheme can be plotted in real time and provide the fifth dimension of VCG besides X, Y, Z, and time scale. As shown in Figure 5.3, the color coded animated VCG representation incorporates the extra cardiac vector movement information and facilitates doctor's interpretation of valuable spatiotemporal patterns associated with certain cardiological diseases. Figure 5.3 bottom plot shows the cardiac vector potential variation speed plot, and the middle VCG plot displays every vector's speed in one specific color corresponding to the color bar listed in the right of the middle VCG plot. The same color bar range is applied to all the color coded dynamic VCG representation so as to see the differences among those colorful plots. As illustrated by the color VCG attractor in Figure 5.3, the cardiac vector in QRS loop moves fastest, T wave is the second, P wave is the third, and the isoelectric points are the slowest.

Patient266/s0502_re: Healthy control
RR: 696.03±4.67ms, QT: 435.62±5.17ms

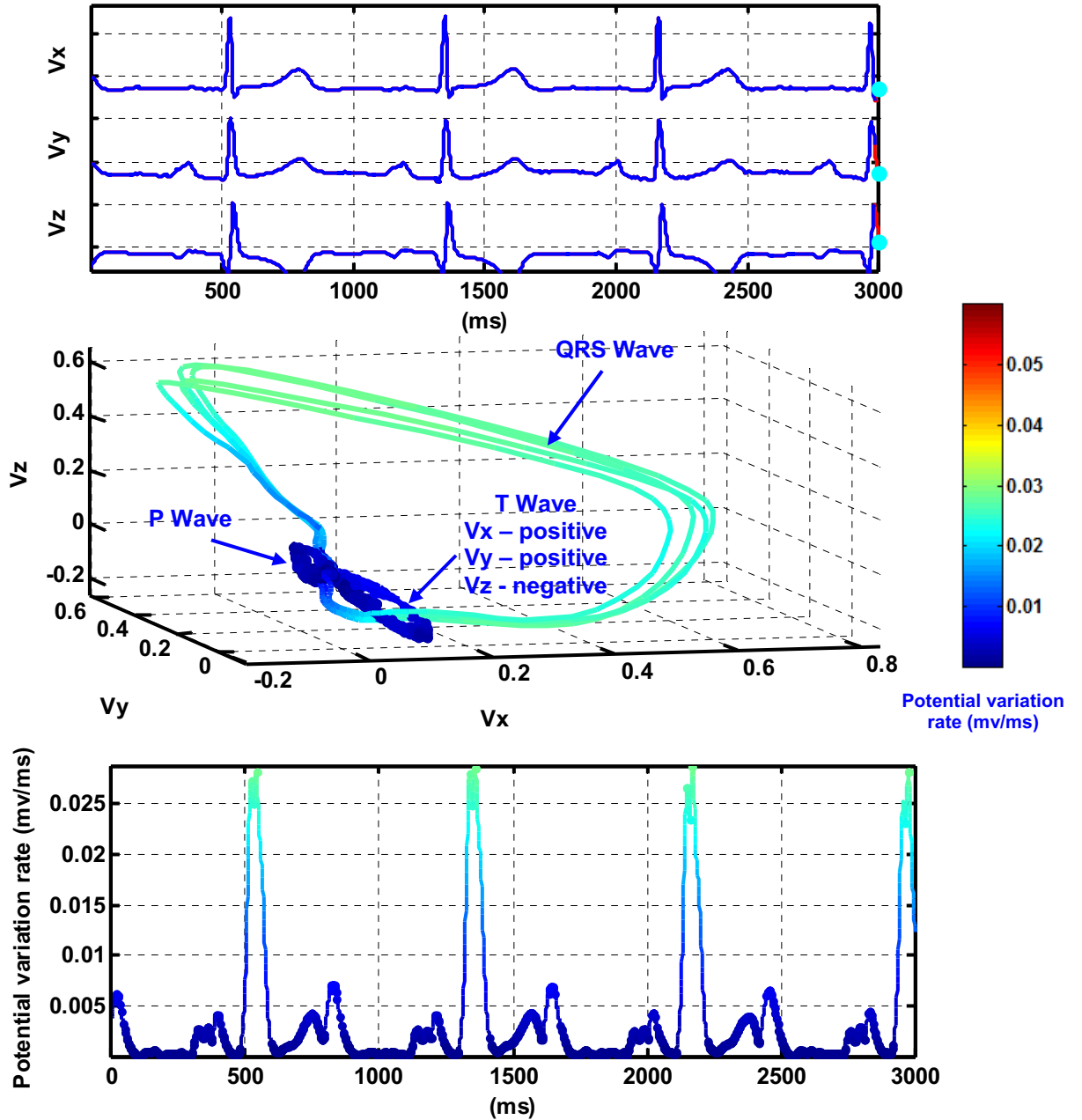


Figure 5.3 Color coded dynamic VCG representation plot of a healthy control subject

5.3 Results and discussion

Many researchers have studied the pathological patterns in the VCG signals and demonstrated the advantages of VCG in diagnosing certain diseases [9-20]. Statistical transformation studies showed the equivalence of 12-lead EKG and 3-lead VCG. Therefore, an effective VCG representation can provide same heart characteristics as acquired from the conventional ECG signals. The useful heart characteristics to be determined include heart rate, rhythm, electrical axis, and other pathology patterns. As shown in Figure 5.3, the healthy control VCG plot presents the normal heart rhythm as P, QRS, and T loops. The peak of T wave loop is found to be in the octant (XYZ: ++-) for most of the healthy control cases. Statistical analysis shows that only 6 out of 80 healthy recordings in PTB database flee from the octant (XYZ: ++-). But for the peak of T wave loop in PTB myocardial infarction cases, only 31.79% (117/368) are found to stay in the octant (XYZ: ++-) and the rest 68.21% of myocardial infarction cases get into the other octants. The speed color coding scheme manifest the real time movement velocity of the cardiac vector, which is rarely able to be observed on a paper. The color of QRS loop is continuous in the healthy control case. For instance, Figure 5.3 shows a consistent light green color, which is usually not the case for some disease subjects. It may also be noted that the more red color shown in QRS loop, the higher R peak is. In addition, Q wave and S wave are inside the QRS loop in the vectorcardiogram and close to the P loop and T loop. Since this dynamic VCG representation is printed on a paper statically, it is not straightforward to identify which side of QRS loop is Q wave. It is well known that Q wave is ahead of R wave and S wave. Therefore Q wave can be easily located on the monitor from real time motion of dynamic VCG representation. Here, the Q wave is

marked in Figure 5.3 and the normal subject is found to not have a significant Q wave because the amplitude of Q wave does not noticeably incline to the negative direction of X, Y, or Z directions.

But P wave loop is found missing and abnormal in the case of atrial fibrillation VCG plot and fibrillation waves take the place of P wave (see Figure 5.4). It is also found that the attractor of atrial fibrillation patient is approximately parallel to the X-Y plane, which indicates a shift in the heart electrical axis. Figure 5.4 shows the color coded dynamic VCG representation for a dysrhythmia and atrial fibrillation patient. P wave is ahead of QRS loop. Before the VCG trajectory goes to the QRS wave, it is found to be trapped in the anarchy P area. The speed of cardiac vector movement is displayed as the darkest blue color (minimal potential variation rate), which demonstrated clearly abnormal excitations from SA node to Atrial. The presence of chaotic fibrillation wave before QRS loop discloses that the atrial fibrillation case has limited capability to harness Atrial and SA node. The time elapsed for the completion of one VCG cycle (PQRST) provides the RR intervals, and it can be calculated for the study of heart rate variability using Poincare sectioning of VCG trajectory. In Figure 5.4, the RR interval is found to be longer than the normal case. It may also be noted that the color change in QRS loop is not as consistent as the normal case in Figure 5.3, which indicates abnormalities in ventricular depolarization.

Patient157\s0338re: Dysrhythmia and atrial fibrillation
RR: 1571.20±108.34ms, QT: 476.50±3.64ms

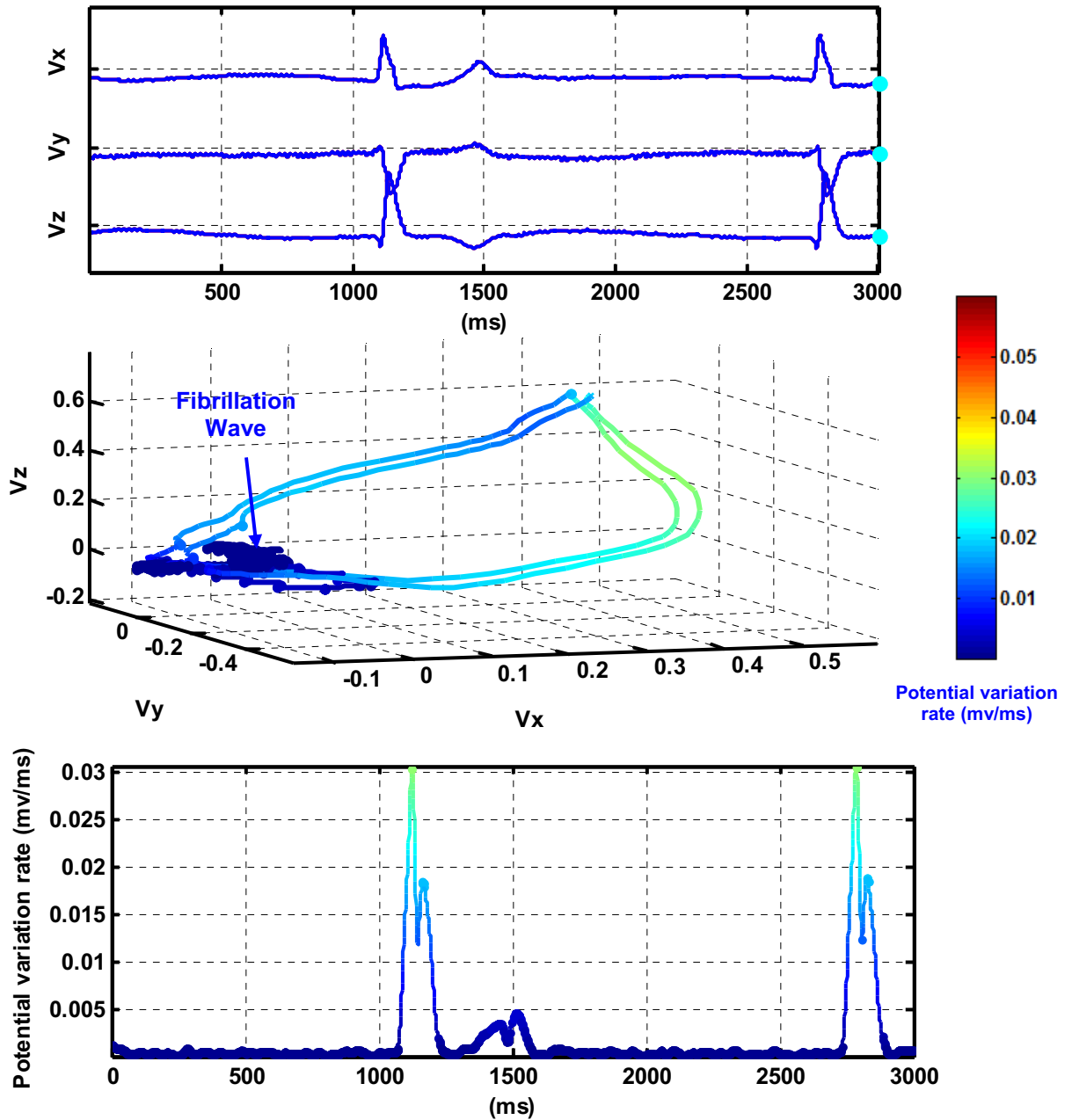


Figure 5.4 Color coded dynamic VCG representation plot of a patient with dysrhythmia and atrial fibrillation

Further, the pathology patterns, such as significant Q wave, inverted T wave for myocardial infarction patients can also be indentified from the VCG plot. A large Q wave towards the negative direction along the Y-axis can be seen in Figure 5.5 because the Y-axis magnitude of starting moment of the QRS loop is significantly larger than the Y-axis magnitude of R peak. The T wave octant is also found to be shifted to X-positive, Y-negative and Z-positive, which indicates the inverted T wave. A significant Q wave can also be located from Figure 5.5 Vy direction. It may be noted that the minimal negative direction of Vy is less than -0.2 , but the maximal positive direction is only 0.2 . Q wave is the starting of QRS loop, which can be easily reserved from dynamic VCG representation. Therefore Q wave is found to be beyond -0.2 and Q/R ratio is greater than 1 in the Vy direction. Such a significant Q wave is definitely a typical sign of myocardial infarction. The discontinuous color variations in QRS loop also indicate the 'W' patterns in ventricular depolarization, which are pathological patterns for some diseases.

Patient001/s0010_re: Myocardial infarction, infero-latera
RR: 732.16±8.75ms, QT: 430.16±3.12ms

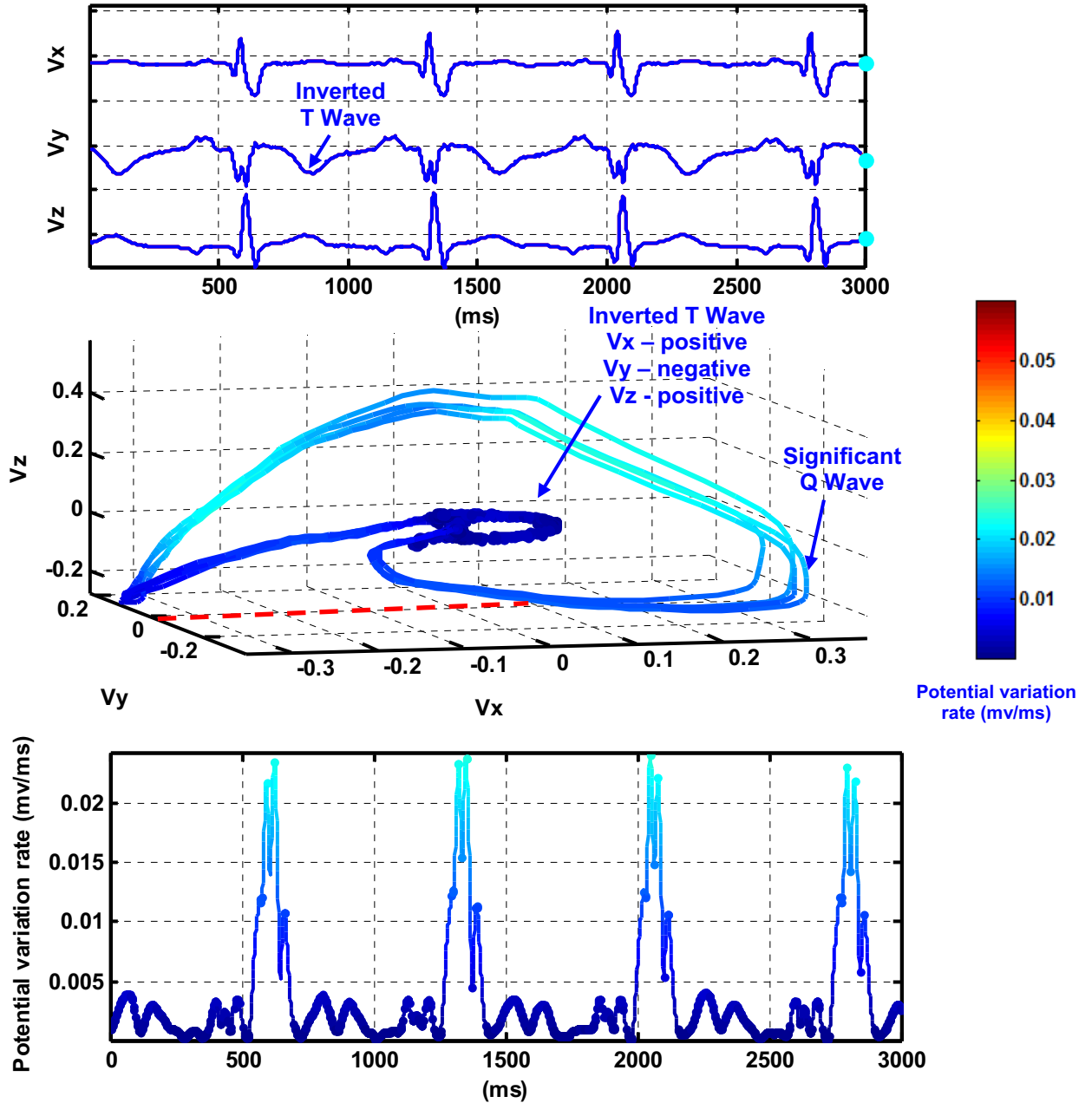


Figure 5.5 Color coded dynamic VCG representation plot of a patient with myocardial infarction, infero-latera

Figure 5.6 clearly shows a significant Q wave along X and Y axes. It may also be noted that Q and S wave are significantly larger than R wave. Thus, this tiny R wave results in a deep valley in the Figure 5.6 bottom cardiac vector potential variation speed plot. It is also revealed more obviously in the Figure 5.6 middle VCG plot. This myocardial infarction case exhibits an even worse significant Q wave situation than Figure 5.5. A significant Q wave can be located from both V_x and V_y directions. We can find that the minimal negative direction of V_y is less than -0.6 , but the maximal positive direction is less than 0.2 . The minimal negative direction of V_x is less than -0.2 , but the maximal positive direction is only 0.05 . Q wave is located in the dynamic VCG representation (see Figure 5.6) and Q/R ratio is found to be greater than 1 in both V_x and V_y directions. The discontinuous color variations in QRS loop are shown as light blue – dark blue – light blue. It indicates the ‘W’ patterns in the QRS wave of this patient, which is resulted from the tiny R wave compared to Q and S waves. It may also be noted that cardiac vector speed is showing to be dark blue in both P and T wave areas. Slow movement in these two locations also represents the SA excitation and ventricular repolarization abnormalities.

Patient063/s0214lre: Myocardial infarction, antero-lateral
RR: 822.96±101.62ms, QT: 401.30±31.38ms

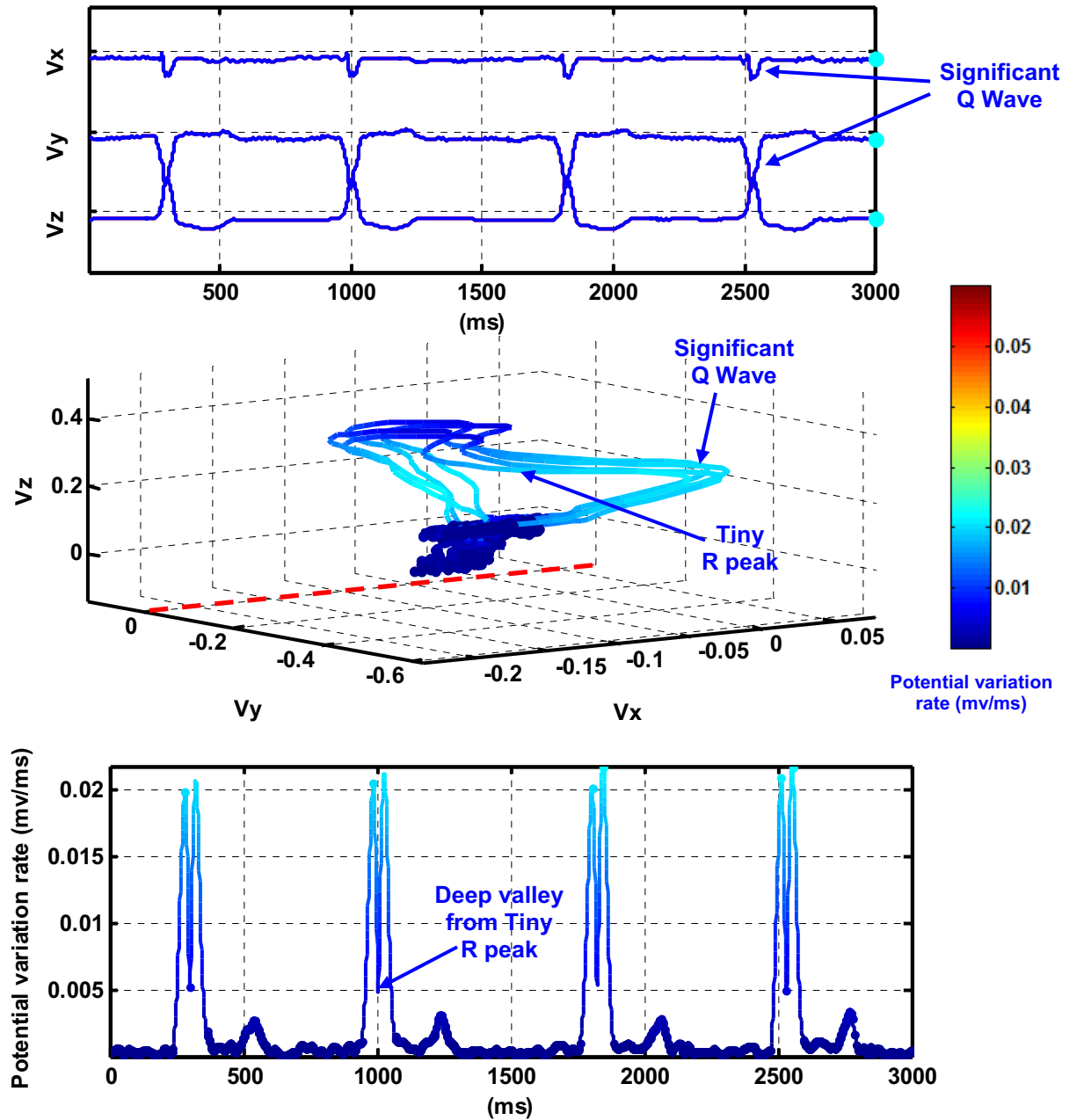


Figure 5.6 Color coded dynamic VCG representation plot of a patient with myocardial infarction, antero-lateral

As shown in Figure 5.7, two R peaks can be found in the plot which are designated as “*M* waves” and are one of the typical pathological patterns for the bundle branch block patient. The discontinuous color variations in QRS loop are shown as yellow - light blue – dark red. It indicates the ‘*M*’ patterns in the R wave of this patient, which is resulted from the disease of bundle branch block. The ‘*M*’ wave pattern shows that both ventricles are not depolarized simultaneously. The delay in the blocked bundle branch allows the unblocked ventricle to begin depolarizing before the blocked ventricle. This kind of slightly later effect in one ventricle produces pathological ‘*M*’ wave and widen QRS loop. It may also be noted that the dark red color appears in this VCG trajectory. Since the same color scale is employed, and Figure 5.3, Figure 5.4, Figure 5.5, Figure 5.6 do not have red color in the VCG attractor, it is also concluded that R peak amplitude is the largest in the bundle branch block subject.

Patient208/s0429_re: Bundle branch block
RR: 745.48 ± 7.77 ms, QT: 465.15 ± 14.74 ms

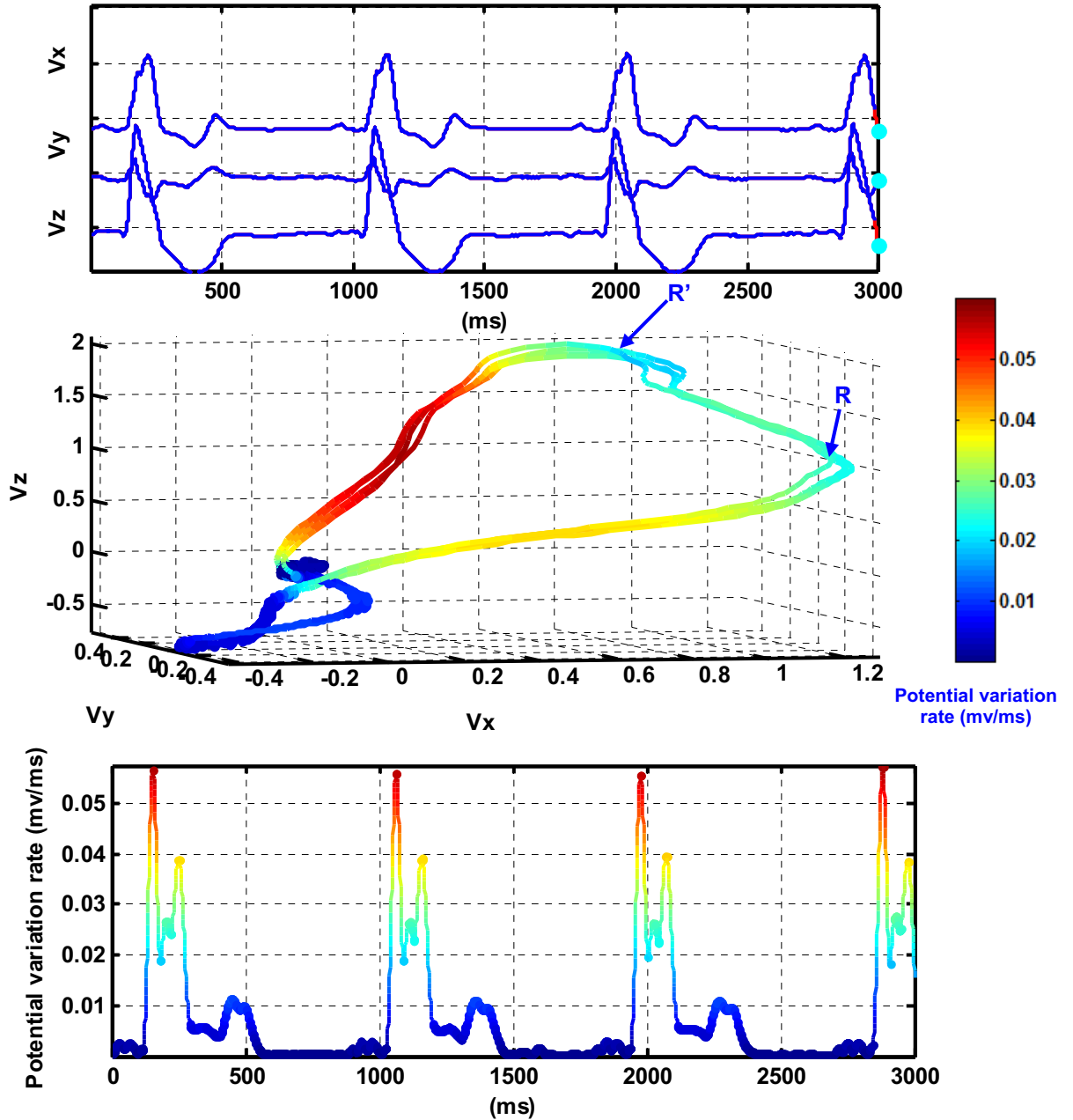


Figure 5.7 Color coded dynamic VCG representation plot of a patient with bundle branch block

From the VCG attractor comparisons among healthy control (HC), myocardial infarction (MI), atrial fibrillation (AF), and bundle branch block, it can be shown that a rotatable real time dynamic VCG representation can capture these important heart characteristics as reported from the 12-lead ECG plot. It is convenient to find the pathological patterns of various cardiovascular disorders from the dynamic VCG representation. One perspective of view or static representation on a paper will pose additional difficulties to the interpretations of VCG trajectory. The incorporation of time and color in dynamic VCG representation will greatly facilitate and assist the inspection of VCG attractor.

Moreover, 3-lead VCG signals are better options for computer automated analysis and process than the 12-lead ECG because of the dimension reduction. From the rotated dynamic VCG representation, it is also found that the spatial distributions of VCG trajectory are remarkably different between myocardial infarction and healthy control. In our chapter VIII, VCG features, namely, max Q vector magnitude, max Q vector octant, max R vector magnitude, max R vector octant, max T axis magnitude, max T vector octant, heart rate, and ST segment integration area etc., are extracted to identify the myocardial infarction from healthy control. T wave morphology related information was statistically found to be the most important features, and the classification accuracy was as high as 97.28% for myocardial infarction and 93.75% for healthy control cases in the PTB database.

5.4 Concluding remarks

In this present investigation, we have made an attempt to represent the VCG signals in 3D space in real time by viewing the signals on a computer monitor instead of as a static picture which can at best record 3 dimensions. This approach overcomes the drawbacks of conventional static VCG representation and provides the spatiotemporal information on the heart dynamics.

The alternative lag reconstructed heart attractor animation from nonlinear dynamics principles can address the sometime difficult situations for the study of cardiac vector when there is only one heart monitoring signal available. The VCG representation can also be color coded for spatiotemporal representation with the curvature, velocity, and phase angle etc. of the vector loops for valuable information about the heart's dynamic activities. It is believed that the proposed five dimension dynamic VCG representation, namely, X, Y, Z, time, and color, can significantly enhance the interpretability of the vectorcardiogram and assist in the identification of the underlying spatiotemporal heart dynamics.

5.5 References

- [1] J. Malmivuo and R. Plonsey, *Bioelectromagnetism: Principles and Applications of Bioelectric and Biomagnetic Fields*. USA: Oxford University Press, July 18, 1995.
- [2] A. Goldberger, L. Amaral, L. Glass, J. Hausdorff, P. Ivanov, R. Mark, J. Mietus, G. Moody, C. Peng, and H. Stanley, "PhysioBank, PhysioToolkit, and PhysioNet: Components of a New Research Resource for Complex Physiologic Signals," *Circulation* 101, vol. 23, pp. e215-e220, 2000 (June 13).
- [3] S. S. Barold, "Willem Einthoven and the Birth of Clinical Electrocardiography a Hundred Years Ago," *Cardiac Electrophysiology Review*, vol. 7, pp. 99-104, 2003.
- [4] G. E. Dower and H. B. Machado, "XYZ data interpreted by a 12-lead computer program using the derived electrocardiogram," *Journal of electrocardiology*, vol. 12, pp. 249-261, 1979.
- [5] G. E. Dower, H. B. Machado, and J. A. Osborne, "On deriving the electrocardiogram from vectorcardiographic leads," vol. 3, p. 87, 1980.
- [6] G. E. Dower, A. Yakush, S. B. Nazzal, R. V. Jutzy, and C. E. Ruiz, "Deriving the 12-lead electrocardiogram from four (EASI) electrodes," *Journal of electrocardiology*, vol. 21, pp. S182-S187, 1988.

- [7] V. P. Hubert, "Advantages of Three Lead Cardiographic Recordings," *Annals of the New York Academy of Sciences*, vol. 126, pp. 873-881, 1965.
- [8] P. W. Macfarlane and T. D. V. Lawrie, *Comprehensive Electrocardiology: Theory and Practice in Health and Disease, Chapter 11 Lead Systems*. New York, NY: Pergamon Press, 1989.
- [9] A. Benchimol, F. Reich, and K. B. Desser, "Comparison of the electrocardiogram and vectorcardiogram for the diagnosis of left atrial enlargement," *Journal of electrocardiology*, vol. 9, pp. 215-218, 1976.
- [10] I. Black, "The electrocardiogram and vectorcardiogram in congenital heart disease," *The Journal of Pediatrics*, vol. 69, pp. 846-716, 1966.
- [11] B. W. McCall, A. G. Wallace, and E. H. Estes, "Characteristics of the normal vectorcardiogram recorded with the Frank lead system," *The American Journal of Cardiology*, vol. 10, pp. 514-524, 1962.
- [12] J. Ng, A. V. Sahakian, W. G. Fisher, and S. Swiryn, "Surface ECG Vector Characteristics of Organized and Disorganized Atrial Activity During Atrial Fibrillation," *Journal of Electrocardiology*, vol. 37, pp. 91-98, 2004.
- [13] C. Olson and R. A. Wamer, "The quantitative 3-dimensional vectorcardiogram," *Journal of electrocardiology*, vol. 33, pp. 176-S74, 2000.
- [14] D. M. Schreck, J. D. Frank, E. R. Malinowski, L. E. Thielen, A. F. Bhatti, A. R. Rivera, and V. J. Tricarico, "Mathematical modeling of the electrocardiogram and vectorcardiogram using factor analysis," *Annals of Emergency Medicine*, vol. 23, pp. 617-76, 1994.
- [15] E. Simonson, N. Tuna, N. Okamoto, and H. Toshima, "Diagnostic accuracy of the vectorcardiogram and electrocardiogram : A cooperative study," *The American Journal of Cardiology*, vol. 17, pp. 829-878, 1966.

- [16] K. K. Talwar, S. Radhakrishnan, V. Hariharan, and M. L. Bhatia, "Spatial vectorcardiogram in acute inferior wall myocardial infarction: its utility in identification of patients prone to complete heart block," *International Journal of Cardiology*, vol. 24, pp. 289-292, 1989.
- [17] A. van Oosterom, Z. Ihara, V. Jacquemet, and R. Hoekema, "Vectorcardiographic lead systems for the characterization of atrial fibrillation," *Journal of electrocardiology*, 2006.
- [18] J. L. Willems, E. Lesaffre, and J. Pardaens, "Comparison of the classification ability of the electrocardiogram and vectorcardiogram," *The American Journal of Cardiology*, vol. 59, pp. 119-124, 1987.
- [19] F. N. Wilson and F. D. Johnston, "The vectorcardiogram," *American Heart Journal*, vol. 16, pp. 14-28, 1938.
- [20] A. C. Witham, "Quantitation of the vectorcardiogram," *American Heart Journal*, vol. 72, pp. 284-286, 1966.
- [21] H. Yang, S. T. Bukkapatnam, and R. Komanduri, "Nonlinear adaptive wavelet analysis of electrocardiogram signals," *Physical Review E (Statistical, Nonlinear, and Soft Matter Physics)*, vol. 76, p. 026214, 2007.

PART II

FEATURE EXTRACTION AND CLASSIFICATION

CHAPTER VI

ATRIAL FIBRILLATION STATE CLASSIFICATION

6.1 Introduction

Atrial fibrillation (AF) is the most common form of arrhythmia, affecting some 2.2 million Americans annually. AF can sustain indefinitely, since the ventricles continues to perform the essential function of blood circulation. During AF, the heart's two small upper chambers (the atria) (see Figure 2.2) quiver instead of beating effectively. The risks of sustained atrial fibrillation are nevertheless serious, and include strokes and myocardial infarctions caused by the formation of blood clots with stagnant volumes in the atria [1]. About 15% of strokes occur in patients are traced to AF. The likelihood of developing AF increases with age with about 3-5% of patients over 65 have atrial fibrillation and is more for men than for women.

In surface electrocardiogram (ECG) from patients with AF, regular electrical impulses of the sinoatrial node (P wave) as shown in Figure 2.2 are replaced by disorganized, rapid electrical impulses (Fibrillation or F wave) which result in irregular heart beats [2-5]. The atrial electrical activity is very rapid (approximately 400 to 700 beats/min), but each electrical impulse results in the depolarization of only a small islet of atrial myocardium rather than the entire atrium. A typical ECG in AF shows a rapid irregular tachycardia in which recognizable P waves are absent. QRS complexes are generally normal, and the ventricular rate in patients with untreated AF generally ranges

between 150 and 220 beats/min. However, in elderly patients, ventricular rates in untreated AF are typically slower [1].

Evidence shows that spontaneously terminating (paroxysmal) AF is a precursor to the development of sustained AF [6]. Subtle changes in rhythm during the final minutes or seconds of such episodes may lead to (or predict) termination of AF. Improved understanding of the mechanisms of spontaneous termination of AF may lead to improvements in the treatment of sustained AF. The remainder of chapter 6 is organized as follows: Section 6.2 gives a brief background of the 2004 PhysioNet challenge for classification of AF states; Section 6.3 contains the study of feature extraction through statistical analysis and QRST subtraction; AF state classification using classification and regression tree (CART) model is discussed in Section 6.4; and Sections 6.5 discuss the results and future improvements.

6.2 Background

In this chapter, the ECG data posted on the world-wide web (www) from the 2004 PhysioNet challenge “Spontaneous Termination of Atrial Fibrillation” is utilized. In this contest, classification needs to be made among the following three categories of AF patients test signals:

- 1) **Group N:** Non-terminating AF (defined as AF that was not observed to have terminated for the duration of the long-term recording, at least an hour following the segment).
- 2) **Group S:** Soon to be terminating (AF that terminates one minute after the end of the record).

- 3) **Group T:** Terminating immediately (AF terminating within one second after the end of the record).

In all, 80 recordings of AF from 60 different subjects were made available in the database [7]. Each record is a one-minute long segment of ECG signals sampled from two channels at 128 Hz sampling rate. The data is divided into a learning set and two test sets. The learning set contains 30 records in all, with 10 records in each of the three groups. The learning set records were obtained from 20 different subjects (10 from group N and 10 from group S/T). Test set A contains 30 records from 30 subjects. About half of these records belong to group N and the rest to group T. The first goal of the challenge, referred to as Event A, is to determine which records in test set A belong to group T and which records to group N. Test set B contained 20 records, 2 from each of 10 subjects (none represented in the learning set or in test set A). One record of each pair belongs to group S and the other to group T. The second goal, referred to as Event B, is to identify which records belong to group T and which records belong to S. It may be noted that the data provided was sparse (as shown in Table 6.1) making it all the more difficult and challenging. Some 20 groups participated in the challenge and submitted their results to an autoscorer. Each team was allowed up to five attempts in each event, and only the best score received in each event was used to determine the final rankings. Final results for the 2004 PhysioNet Challenge are summarized in Table 6.2.

Table 6.1 Distribution of 80 recordings among learning sets and test sets

	Group N	Group S	Group T
Learning set	n01, n02, ... n10	s01, s02, ... s10	t01, t02, ... t10
Test set A	15 records	-	15 records
Test set B	-	10 records	10 records

Table 6.2 Summary of final results of the 2004 PhysioNet Challenge

Reference	Method	Results		Reported Performance	Remarks
		Event I (N&T)	Event II (S&T)		
Petrutiu [8]	Bandpass filtering, QRST subtraction, FFT to residual signal, overall peak frequency, 10 s peak frequency, 1 s peak frequency and the trend of peak frequency change	Training: 20/20 Testing: 29/30	Training: 20/20 Testing: 20/20	Event I: 97.5% Event II: 100%	Performance averaged over the test cases only
Hayn [9]	QRST subtraction & short time Fourier transform to the AA signal, classification with features: peak AF frequency and mean RR interval	Training: 20/20 Testing: 28/30	Training: 20/20 Testing: 16/20	Event I: 96% Event II: 90%	Averaged over training and testing cases
Cantini [10]	Separate AA from VA using: (1) adaptive filtering QRST subtraction (2) mean beat subtraction, features: RR interval and peak atrial frequency (event I), peak frequency of last two seconds change (event II)	Training: 19/20 Testing: 27/30	Training: 16/20 Testing: 18/20	Event I: 92% Event II: 85%	Averaged over training and testing cases
Lemay [11]	Highpass filtering, features: skewness of AA segments, mean of RR interval difference in ten seconds, F wave peak intervals, atrial activity amplitude, total power below 0.6Hz on both leads, cross-covariance values for two leads, estimated spectral density above 20Hz across AA segments on both leads, linear modeling	Training: 20/20 Testing: 20/30	Training: 20/20 Testing: 12/20	Event I: 80% Event II: 80%	Averaged over training and testing cases
Castells [12]	Principal Component Analysis (PCA), PQRST cycle	Training: 20/20 Testing: 27/30	N/A	Event I: 94% Event II: N/A	Averaged over training and testing cases
Nilsson [13]	Spatio-temporal QRST subtraction and Time-Frequency Analysis	Training: 19/20 Testing: 27/30	Training: 16/20 Testing: 14/20	Event I: 92% Event II: 75%	Averaged over training and testing cases

Most successful approaches followed the procedure of filtering the noise and artifacts [8, 10, 11, 14], QRST subtraction [15-20], frequency spectrum analysis of the resulting filtrate (which predominantly captures atrial activity) [8, 21-26], classification [11, 24, 27] and so on. Six groups developed methods that yielded 90% or more accurate results for event A (N vs. T classification). Studies show that atrial activity slows down and regularizes prior to self-termination of AF, mechanisms of atrial activity are reflected through surface ECG [1-3, 5, 26, 28, 29]. However, event B (S vs. T classification) seemed to be more difficult, since the accuracies ranged from 60-90% for most cases. It is commendable that the team from Northwestern University [8] was able to arrive at the highest classification accuracy of 97% for the N vs.T and 100% for S vs. T. One major finding of this challenge contest is that spontaneously terminating AF can be discriminated accurately from sustained AF by analysis of surface ECG signal segments sampled over a period of one minute or less [6].

6.3 Feature extraction

6.3.1 Statistical Descriptors and Principal Component Analysis (PCA)

Various signal processing algorithms have been developed to detect the QRS complex and the characteristic points of ECG spectra [14, 30-41]. This stage is crucial in basic ECG monitoring systems and important for cardiac events classification. Figure 6.1 shows an intermediate result of an automated feature extraction algorithm developed here depicting the successful identification of peaks and endpoints of various waves of a representative ECG signal. All signals were first passed through a bandpass filter to capture a clean signal whose frequency range is between 0.5 and 60 Hz before subjecting them to wavelet transform as discussed in the foregoing. Pre-filtering minimizes the

influence of artifacts, respiration, baseline shift and other spurious signal components, so that the features extracted are more likely to accurately track variations in the AF states.

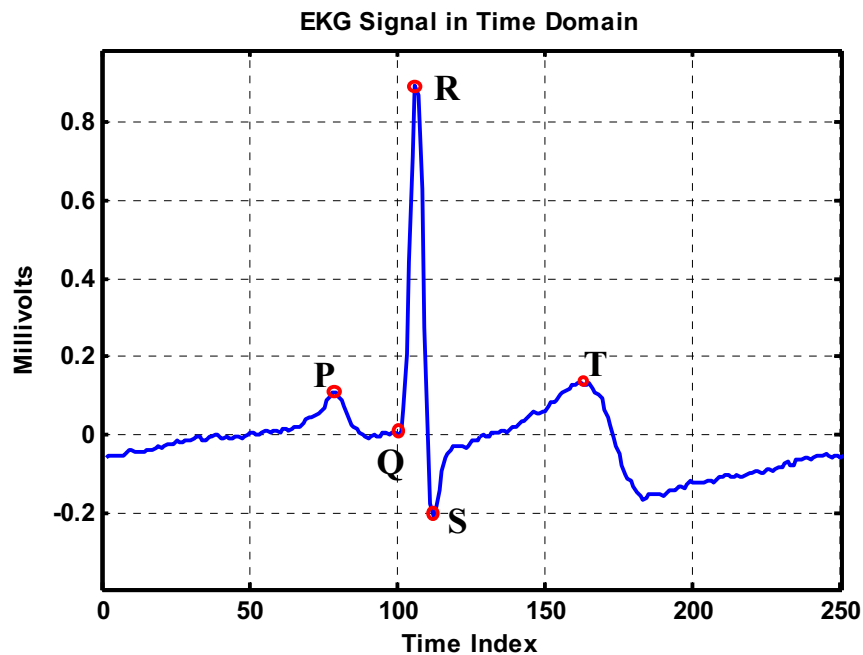


Figure 6.1 Automated identification of peaks and endpoints of various waveforms in an ECG signal using an automated feature extraction routine

Wavelets are attractive for ECG feature extraction because the spatio-temporal features of an ECG signal are presented over multiple scales through the use of a wavelet transform. Consequently, the QRS complex can be distinguished from high P and T waves, noise, baseline drift, and other artifacts. The relation between the characteristic points of ECG signals and those of modulus maximum pairs of its wavelet transforms are almost straightforward to establish. For example, Figure 6.2 shows a representative scalogram (time-scale representation) obtained from a continuous wavelet transform (CWT) of an ECG signal segment shown in Figure 6.2. The brighter (white) portions refer to the time-scale segments in the scalogram that contain large magnitudes of wavelet coefficients and the dark portions identify the segments having small wavelet coefficients. Scale 2 of the scalogram clearly demarcates the time locations of R peaks.

The information on R-peak locations gets diffused as one moves up on the scales, as evidenced by progressive smearing of the white bands. However, around scale 7, delineations between R, T, and P waves become somewhat apparent. However, for scales >7 , these bands diffuse out in time to a point where the delineations are no longer clear. Scale 2 of a scalogram has been used to locate the peaks of the R waves, and thus determine, for each beat, the heart rate (HR) and heart rate variability (HRV). Scale 7 coefficients were used to determine the peaks of the P and T waves as well as the onset and offset points of each wave.

Continuous Wavelet Transform to ECG Signal in Different Scales

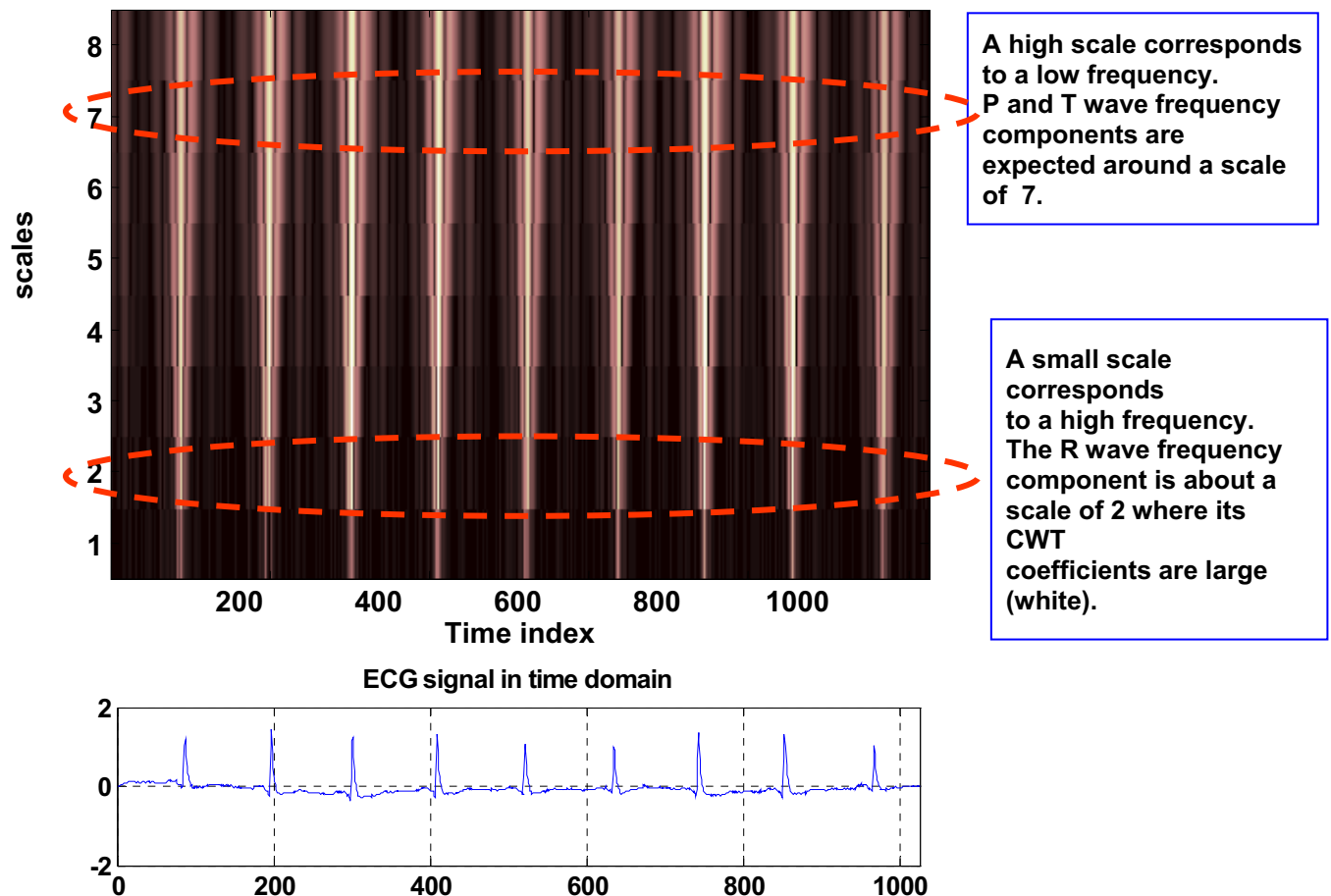


Figure 6.2 Time-scale representation (scalogram) of a representative ECG signal

The feature sets extracted from large arrays of signals has been further tightened, and made more sensitive to the relevant variations in underlying dynamics through the use of decomposition methods, such as principal component analysis (PCA) and independent component analysis (ICA). PCA techniques [42] are widely used to reduce the dimension of the input (feature) vectors in situations where the dimension of the input vector is large, but the components of the vectors are highly correlated (redundant). PCA orthogonalizes the components of the input vectors (so that they are uncorrelated with each other), and orders the resulting orthogonal components (principal components) so that those with the largest variation are considered first, and eliminates those components that contribute the least to the variation in the data set.

6.3.2 QRST subtraction

During atrial fibrillation, the P waves are absent and are replaced by rapid (usually of smaller amplitude) fibrillation waves (or F-waves) of varying durations and morphologies. The QRST complex (which represents ventricular activity) dominates the spectral content of ECG waves during AF, limiting the ability to detect various AF events. Therefore, the ECG signal components capturing the ventricular activity (i.e., QRST complex) should be subtracted from the surface ECG for more effective diagnosis of AF events [15-20, 43]. In this chapter, a wavelet representation is used to identify time segments and scales where much of the ECG signal content emerges from various ventricular activities, and apply and threshold such that the filtrate contains mostly ventricular components and the residue contains atrial components. The rationale for this approach lies in the fact that the wavelet transform coefficients for ventricular activity are much larger than those for atrial activity, particularly during active AF. Results from this

cancellation approach are summarized in Figure 6.3 and Figure 6.4. It is evident that much of the QRST information in the ECG has been culled out through the application of the thresholding filter. The frequency domain plot of the QRST cancelled ECG (Figure 6.4, bottom) clearly delineates the spectral content of the waves of atrial origin, which were not evident from the examination of the frequency spectrum of the original ECG (Figure 6.4, top). The frequency and amplitudes of these atrial ECG components serve as additional features for AF state classification.

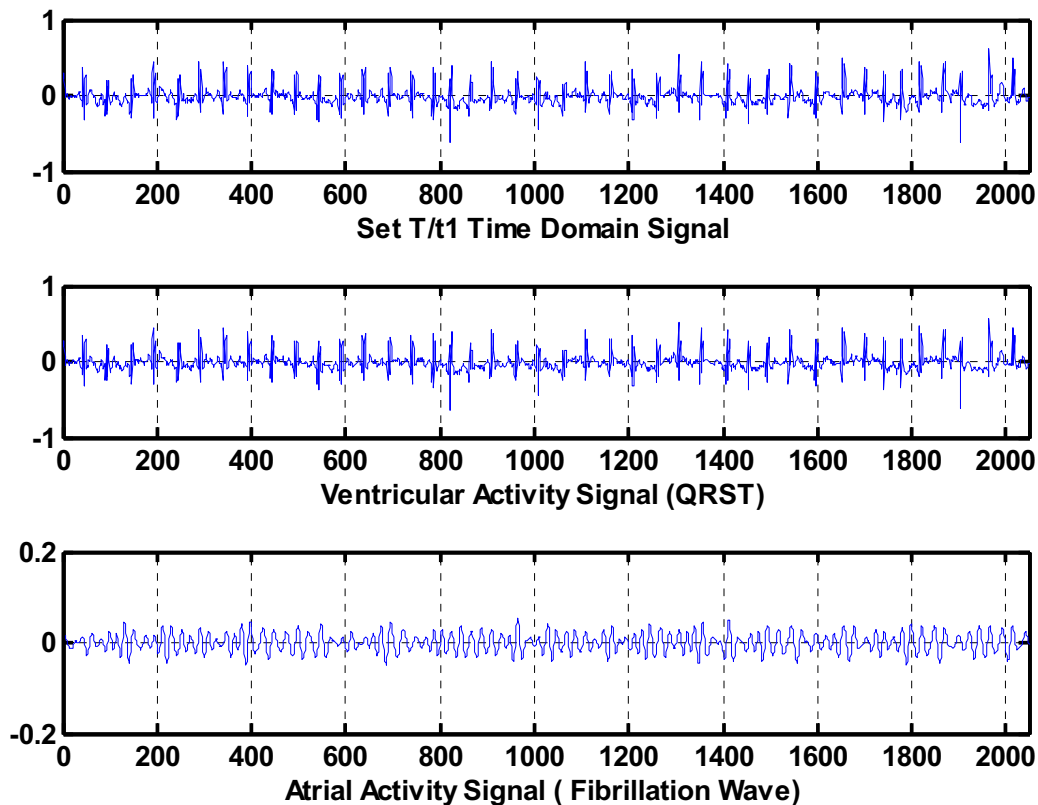


Figure 6.3 Summary of QRST subtraction results for a representative ECG signal (from a T-case) showing the original signal (top), filtrate from thresholding containing predominantly ventricular components (middle) and residue from thresholding containing predominantly atrial and AF waves (bottom)

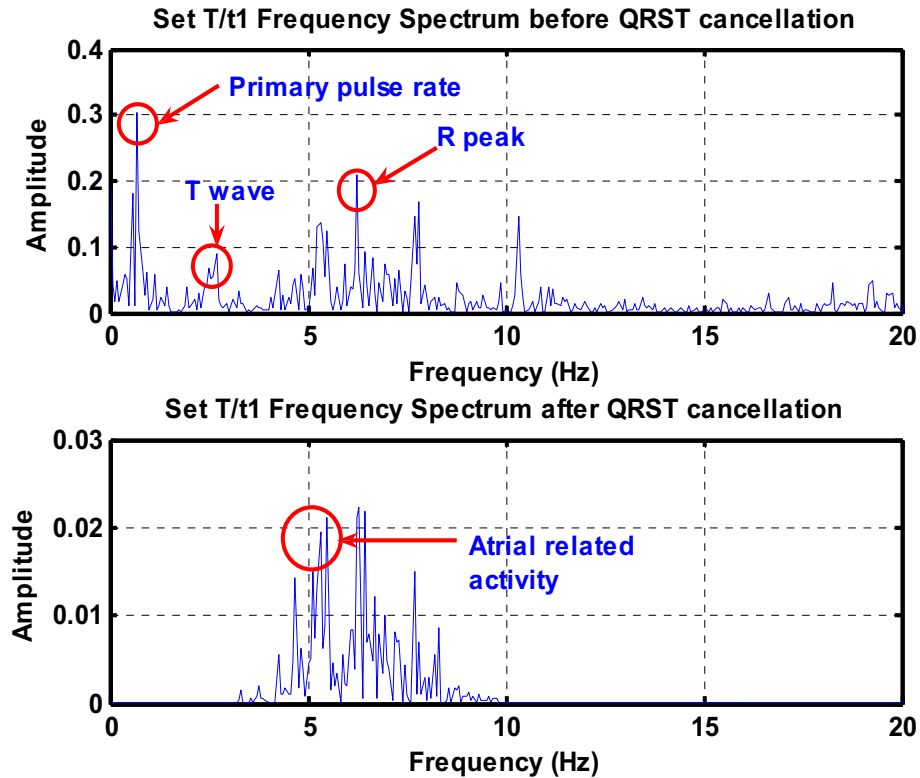
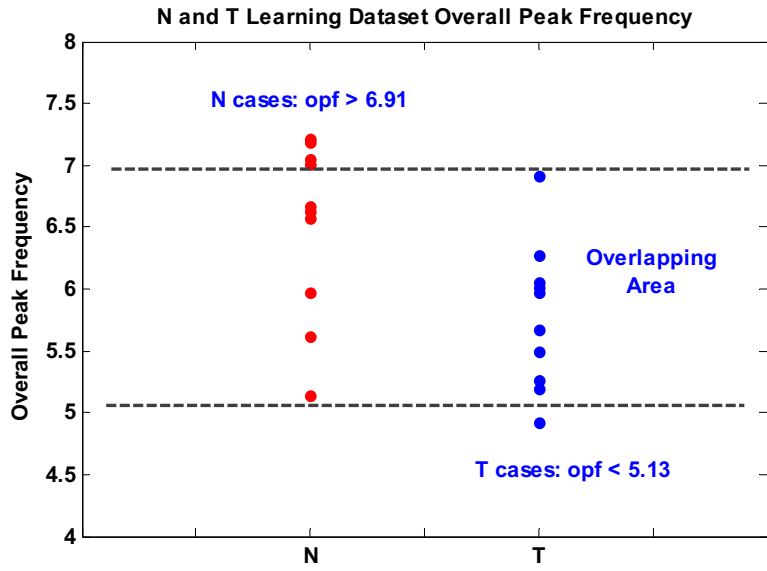


Figure 6.4 Frequency spectra of a representative ECG signal before and after QRST subtraction

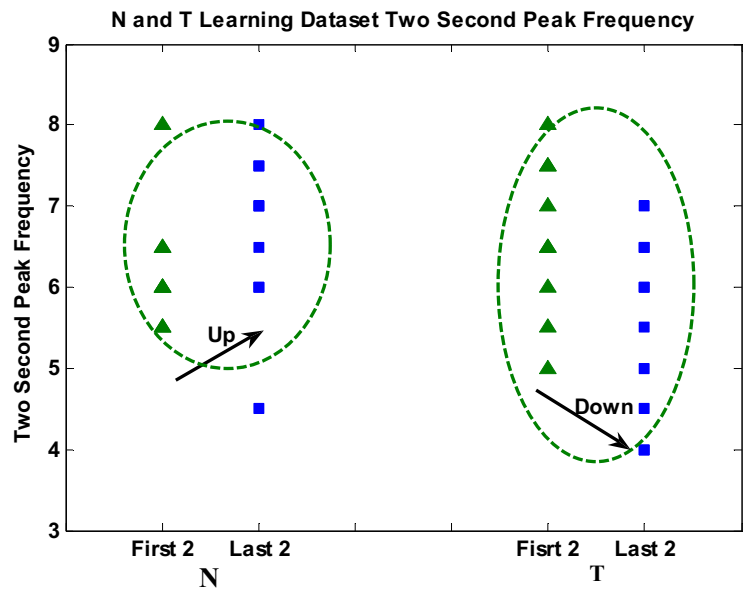
6.4 AF state classification using CART model

The CART analysis uses decision rules learned from the pattern (clustering) of features in a training data set to classify different groups of objects. This approach can be quite effective for creating clinical decision rules that combine physiological knowledgebase with signal analysis [27].

The application of CART analysis to detect AF events (N, S, and T) consists of selecting the features to serve as discriminatory variables and build a decision tree recursively. The CART tree is built using recursive splitting of the feature space defined by 3 extracted input features based on one target variable that takes one of the following 3 values: N, S, or T.



(a)



(b)

Figure 6.5 (a) Peak frequencies of various N and T cases, (b) Peak frequencies of the first two (First 2) and last two (Last 2) beats of N and T ECG signals

For N vs T classification, subtle changes in the rhythm during the final seconds of the ECG traces of such episodes may indicate termination of AF [25]. Therefore, ECG features that capture the initial (first 2 seconds) and final moments (last 2 seconds) of AF signal may serve as discriminatory variables for identifying AF termination. Specifically, the following 3 features were extracted from the ECG signals after QRST subtraction:

- 1) Overall peak frequency (OPF)
- 2) Peak frequency of the first 2-second interval of the ECG trace (PFF)
- 3) Peak frequency of the last 2-second interval of the ECG trace (PFL)

For N vs T classification, we found the maximum value of the OPF for all T signals in the learning data set to be 6.91 Hz (which is lower than some N cases), whereas the minimum value of OPF for all N signals in the learning data set was 5.13 Hz (which is higher than some T cases) (Figure 6.5 a). Therefore, we set 6.91 Hz as the upper limit of OPF for T cases and 5.13 Hz as the lower limit of OPF for N cases. Among the learning set, any signal with an OPF \geq 6.91 Hz was classified as an N signal; and any signal with OPF \leq 5.13 Hz was classified as a T signal. For those cases with an OPF between 5.13 and 6.91 Hz, we found that the PFF is greater than the PFL in most T cases. Therefore, any signal with an OPF between 5.13 and 6.91 Hz was classified as T signal if PFF \geq PFL, and N signal otherwise (Figure 6.5 b). Based on these observations, a CART model with the following decision rules was developed for classifying the N and T cases:

1. If the OPF $>$ 6.91 HZ, then the object is N.
2. If the OPF $<$ 5.13 HZ, then the object is T.
3. For OPF within the interval from 5.13 to 6.91 HZ, the object is classified as T if the PFF $>$ PFL, and N case otherwise.

This model correctly classified 28 of 30 N and T cases during testing, leading to an accuracy of 93%.

For the S vs T classification, it may be noted that for every S recording, a corresponding T recording was taken from the same patient. Therefore, the first step in S vs T classification involved applying an optimal pairing method to identify the pairs of S

and T recordings from the same patient based on the ECG signal morphology information (Figure 6.6). This information included ECG features such as the arithmetic mean of P-wave width, height of P wave, QRS width, height of QRS, QT length, T-wave width, and RR interval from the time domain signal plots.

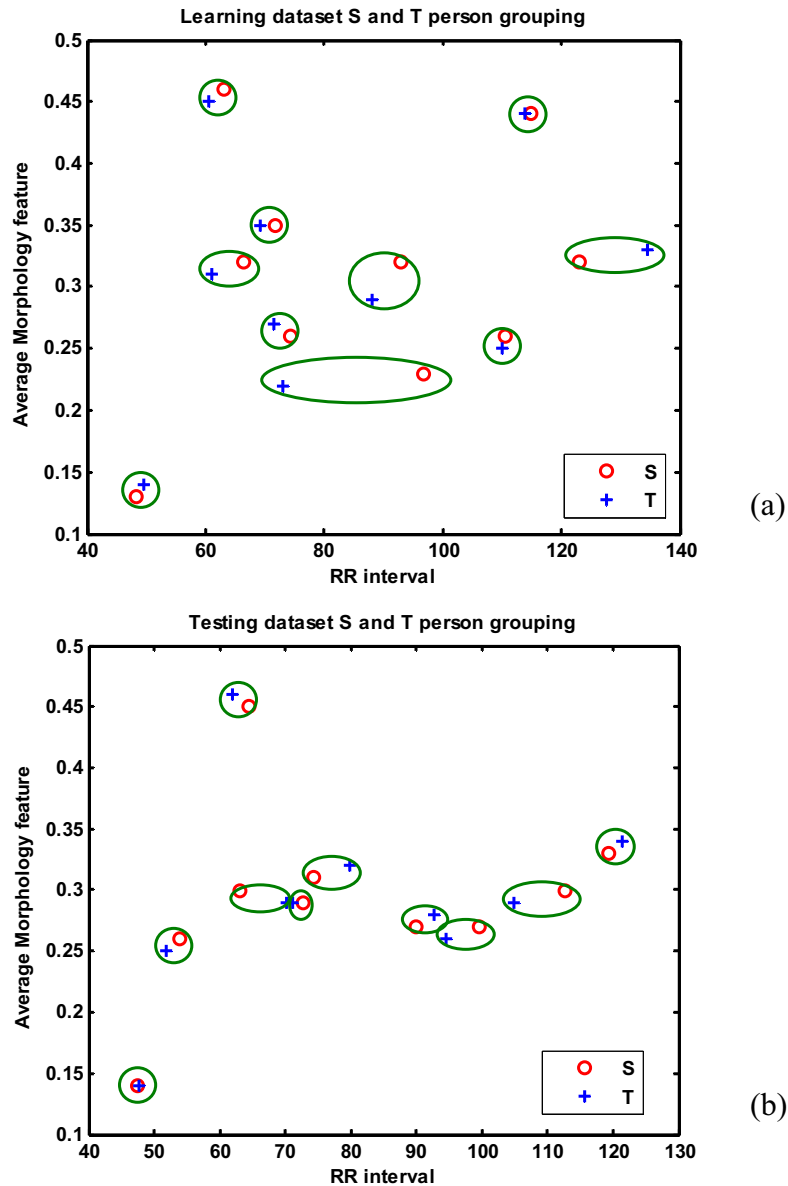


Figure 6.6 (a) and (b) Learning and testing dataset RR interval and average features scatter plot, respectively. (Average feature is the average value of mean of QRS, mean of peak, mean of height of T wave, mean of QT interval, mean of ST segment, and mean of T duration)

Table 6.3 S vs T learning data set RR interval and skewness of RR feature table

	Group S			Group T		
Person	Case	RR Interval	Skewness RR	Case	RR Interval	Skewness RR
a	s01	48.28 ^a	1.45	t01	49.62 ^a	1.37
g	s07	96.87	0.50 ^b	t07	73.15	1.37 ^b
h	s06	110.57	0.42 ^b	t06	110.13	0.85 ^b
i	s05	114.80	0.34 ^b	t05	113.77	1.05 ^b
j	s03	123.15	0.62 ^b	t03	134.39	1.74 ^b
b	s04	62.97 ^c	1.57	t04	60.65 ^c	1.02
c	s10	66.31 ^c	0.67	t10	61.08 ^c	0.84
d	s02	71.70 ^c	0.66	t02	69.33 ^c	0.72
e	s08	74.27 ^c	0.94	t08	71.58 ^c	0.89
f	s09	92.91	-0.40 ^d	t09	88.16	-0.25 ^d

^a Rule 2; ^b Rule 3; ^c Rule 4; ^d Rule 5

Table 6.4 S vs T testing data set RR interval and skewness of RR feature table

	Group S			Group T		
Person	Case	RR Interval	Skewness RR	Case	RR Interval	Skewness RR
1	b14	47.47 ^a	1.04	b16	47.58 ^a	1.64
3	b09	62.96	0.92 ^b	b08	71.03	2.51 ^b
2	b20	53.87 ^c	1.01	b12	51.89 ^c	1.69
4	b01	64.48 ^c	0.91	b03	61.93 ^c	1.26
5	b02	72.72 ^c	0.84	b07	70.21 ^c	0.43
6	b04	74.31	0.39 ^d	b13	79.92	0.42 ^d
7	b05	90.01	0.51 ^d	b19	92.74	0.60 ^d
8	b18	99.53	0.94 ^d	b11	94.50	1.00 ^d
9	b10	112.67	-0.39 ^d	b15	104.94	-0.38 ^d
10	b06	119.30	-0.50 ^d	b17	121.35	0.35 ^d

^a Rule 2; ^b Rule 3; ^c Rule 4; ^d Rule 5

After grouping ECG traces from the same person, the S and T classification was performed based on 2 features: average RR interval and skewness of RR interval, which capture the heart rate and heart rate variability, respectively. Heart rate activities are

closely related to the state transitions from soon-to-be-terminating AF to terminating AF. As shown in Table 6.3 and Table 6.4, the average RR interval was found to decrease from S to T, whereas the skewness of the RR interval increases from S to T for the same person, in most cases, from the learning data set. In addition, no S cases were found to have both higher skewness of RR and smaller average RR interval than T cases for the same person, except in one case. This finding implies that the RR interval trend in the S case has either a longer average RR interval or a smaller skewness of the RR interval than the T case for the same person.

Based on the learning data set, we found that the data can be divided into 2 groups based on the average RR interval: those whose average RR intervals are greater than or less than 75 milliseconds. The skewness of the RR interval increases from S to T for those patients whose RR intervals are greater than 75 milliseconds, and the average RR interval decreases from S to T for those RR intervals less than 75 milliseconds. However, if the patient has a very high heart rate, for example, the average RR interval is 50 milliseconds, then it may serve as a major feature instead of the skewness of RR interval because the higher heartbeat rate will not cause significant RR interval variations unless there is a sudden disruption in the heart activity. With these findings, both learning data set (sets S and T) and testing data set (set B) are correctly classified. The CART classification rules, created based on the learning data for events I and II, are given as following:

- 1) Find pairs of recordings (object A and object B) from the same patient.
- 2) If $(RR \text{ interval} < 50)$ in one pair, then the object with bigger RR interval is T.

(this condition refers to extremely high heart rate ($HR=1/RR$) case)

- 3) If $\frac{\text{Skewness RR (object A)}}{\text{Skewness RR (object B)}} > 2$ or $\frac{\text{Skewness RR (object A)}}{\text{Skewness RR (object B)}} < 0.5$, then object with greater Skewness for RR is T.
- 4) If the bigger RR interval for object A and object B ≤ 75 , object A is S if RR interval decreases from object A to object B.
- 5) If the bigger RR interval for object A and object B > 75 , object A is S, if Skewness of RR increases from object A to object B.

It may be noted that heart rate analysis based on average RR interval and its variation, and QRST subtraction techniques using wavelet threshold filter are different from those reported in the literature.⁹ In N vs T classification, we used 3 features as inputs for CART classification, which is one less than the number of features used in Petrutiu et al⁹, without significantly compromising on the accuracy (93% for the N vs T testing data set and 100% for the S vs T testing data set). Furthermore, the CART decision tree has the potential to integrate medical expertise to generate a number of clinical decision rules for improving the diagnostic accuracy for different AF states.

6.5 Summary

The CART model patterned after a previous such attempt yielded the best results for N vs T and S vs T classifications. Interestingly, the CART classifier for N vs. T uses one less feature than in the previous work [8], and it was found to yield over 95% accuracies for classifying between N vs. T. Also, application of three decision rules is sufficient to classify between N vs. T.

CART classification of S vs. T is found to depend on pairing the ECGs of every individual subject (one taken when the subject is at S condition and the other at T). The

optimal pairing algorithm was found to achieve a fairly accurate pairing using the aggregate ECG features. Based on the pairing information, five decision rules were generated to derive the CART classifier for S vs. T. From a practical standpoint the decision rules obtained through CART can be easily coded in the form of a rule-based diagnostic system, and can be useful for automatic classification between S and T events.

The CART models constructed using temporal relationships among features yielded high accuracy for both N vs T and S vs T classifications. These results matched the best results reported in the 2004 Challenge Competition [6] for N vs T classification.

To improve the accuracy of identification of various AF episodes further, it is necessary (a) to get access to a significantly larger database of both normal and AF cases and (b) to seek expertise of the cardiologists in providing relevant features and diagnostics for various cardiologic disorders.

6.6 References

- [1] J. Ng, A. V. Sahakian, W. G. Fisher, and S. Swiryn, "Surface ECG Vector Characteristics of Organized and Disorganized Atrial Activity During Atrial Fibrillation," *Journal of Electrocardiology*, vol. 37, pp. 91-98, 2004.
- [2] M. Stridh, L. Sörnmo, C. J. Meurling, and S. B. Olsson, "Characterization of Atrial Fibrillation Using the Surface ECG: Time-Dependent Spectral Properties," *IEEE Transactions on Biomedical Engineering*, vol. 48, pp. 19-27, 2001.
- [3] Q. Xi, A. V. Sahakian, J. NG, and S. Swiryn, "Atrial Fibrillatory Wave Characteristics on Surface Electrogram: ECG to ECG Repeatability Over Twenty-Four Hours in Clinically Stable Patients," *Journal of Cardiovascular Electrophysiology*, vol. 15, p. 911, 2004.

- [4] S. B. Olsson, "Atrial brillation - where do we stand today?," *Journal of Internal Medicine*, pp. 19-28, 2001.
- [5] L. E. Sadek and K. M. Ropella, "Detection of Atrial Fibrillation From the Surface Electrocardiogram Using Magnitude Squared Coherence," *IEEE-EMBC and CMBEC Theme 1: Cardiovascular System*, pp. 179-180, 1995.
- [6] G. Moody, "Spontaneous Termination of Atrial Fibrillation: A Challenge from PhysioNet and Computers in Cardiology 2004," *Computers in Cardiology*, vol. 31, pp. 101-104, 2004.
- [7] A. Goldberger, L. Amaral, L. Glass, J. Hausdorff, P. Ivanov, R. Mark, J. Mietus, G. Moody, C. Peng, and H. Stanley, "PhysioBank, PhysioToolkit, and PhysioNet: Components of a New Research Resource for Complex Physiologic Signals," *Circulation* 101, vol. 23, pp. e215-e220, 2000 (June 13).
- [8] S. Petrutiu, A. Sahakian, J. Ng, and S. Swiryn, "Analysis of Surface Electrocardiogram to Predict Termination of Atrial Fibrillation: The 2004 Computers in Cardiology/PhysioNet Challenge," *Computers in Cardiology*, vol. 31, pp. 105-108, 2004.
- [9] D. Hayn, K. Edegger, D. Scherr, P. Lercher, B. Rotman, W. Klein, and G. Scheier, "Automated Prediction of Spontaneous Termination of Atrial Fibrillation from Electrocardiograms," *Computers in Cardiology*, vol. 31, pp. 117-120, 2004.
- [10] F. Cantini, F. Conforti, M. Varanini, F. Chiarugi, and G. Vrouchos, "Predicting the End of an Atrial Fibrillation Episode: The PhysioNet Challenge," *Computers in Cardiology*, 2004.
- [11] M. Lemay, Z. Ihara, J. Vesin, and L. Kappenberger, "Computers in Cardiology/PhysioNet Challenge 2004: AF Classification Based on Clinical Features," *Computers in Cardiology*, vol. 31, pp. 669-672, 2004.

- [12] F. Castells, J. Igual, J. Millet, and J. J. Rieta, "Atrial activity extraction from atrial fibrillation episodes based on maximum likelihood source separation," *Signal Processing*, pp. 523-535, 2005.
- [13] F. Nilsson, M. Stridh, A. Bollmann, and L. Sornmo, "Predicting Spontaneous Termination of Atrial Fibrillation with Time-Frequency Information," *Computers in Cardiology*, vol. 31, pp. 657-660, 2004.
- [14] X. Qiuzheng and Y. HenHu, "Neural Network based Adaptive matched Filtering for QRS detection," *IEEE Transactions on Biomedical Engineering*, vol. 39, p. 317, 1992.
- [15] J. Rieta and V. Zarzoso, "Atrial activity extraction based on blind source separation as an alternative to QRST cancellation for atrial fibrillation analysis," *Computers in Cardiology*, pp. 69-72, 2000.
- [16] M. Mlynash, A. SippensGroenewegen, F. Roithinger, Y. Goseki, P. Steiner, and M. Lesh, "Automated QRST Substraction Algorithm for Analysis of T Wave Obscured Ectopic Atrial Beats," *Proceedings of The First Joint BMES/EMBS Conference Serving Humanity, Advancing Technology*, 1999.
- [17] J. Waktare, K. Hnatkova, C. Meurling, H. Nagayoshi, T. Janota, A. Camm, and M. Malik, "Optimal Lead Configuration in the Detection and Subtraction of QRS and T Wave Templates in Atrial Fibrillation," *Computers in Cardiology*, vol. 25, pp. 629-632, 1999.
- [18] M. Stridh and L. Sörnmo, "Spatiotemporal QRST Cancellation Techniques for Analysis of Atrial Fibrillation," *IEEE Transactions on Biomedical Engineering*, vol. 48, pp. 105-112, 2001.
- [19] M. Stridh and L. Sornmo, "Spatiotemporal QRST cancellation techniques for improved characterization of atrial fibrillation in the surface ECG," in *Proceedings - 19th International Conference - IEEE/EMBS*, Chicago, 1997.

- [20] Q. Xi, A. Sahakian, and S. Swiryn, "The Influence of QRS Cancellation on Signal Characteristics of Atrial Fibrillation in the Surface Electrocardiogram," *Computers in Cardiology*, vol. 29, pp. 13-16, 2002.
- [21] J. E. Slocum and K. M. Ropella, "Correspondence Between The Frequency Domain Characteristics Of Simultaneous Surface And Intra-Atrial Recordings Of Atrial Fibrillation," *Computers in Cardiology*, pp. 781-784, 1994.
- [22] P. Langley, J. Bourke, and A. Murray, "Frequency Analysis of Atrial Fibrillation," *Computers in Cardiology*, vol. 27, pp. 65-68, 2000.
- [23] M. Stridh, L. Sornmol, C. Meurling, and B. Olsson, "Frequency Trends of Atrial Fibrillation Using the Surface ECG," in *Proceedings of The First Joint BMES/EMBS Conference: Serving Humanity, Advancing Technology*, 1999, p. 272.
- [24] F. Roberts, R. Povinelli, and K. Ropella, "Rhythm Classification Using Reconstructed Phase Space of Signal Frequency Sub-bands," *Computers in Cardiology*, vol. 30, pp. 61-64, 2003.
- [25] Q. Xi, A. Sahakian, J. Ng, and S. Swiryn, "Stationarity of Surface ECG Atrial Fibrillatory Wave Characteristics in the Time and Frequency Domains in Clinically Stable Patients," *Computers in Cardiology*, vol. 30, pp. 133-136, 2003.
- [26] D. Raine, P. Langley, A. Murray, and A. Dunuwille, "Surface Atrial Frequency Analysis in Patients with Atrial Fibrillation: A Tool For Evaluating the Effects of Intervention," *Journal of Cardiovascular Electrophysiology*, vol. 15, pp. 1021-1027, 2004.
- [27] R. J. Lewis, "An Introduction to Classification and Regression Tree (CART) Analysis," in *Annual Meeting of the Society for Academic Emergency Medicine*, San Francisco, California, 2000.
- [28] J. Ng, A. V. Sahakian, W. G. Fisher, and S. Swiryn, "Atrial Flutter Vector Loops Derived From the Surface ECG: Does the Plane of the Loop Correspond

- Anatomically to the Macroreentrant Circuit?," *Journal of Electrocardiology*, vol. 36, pp. 181-186, 2003.
- [29] J. NG, A. Sahakian, and S. Swiryn, "Vector Analysis of Atrial Activity from Surface ECGs Recorded During Atrial Fibrillation," *Computers in Cardiology*, vol. 29, pp. 21-24, 2002.
- [30] G. M. Friesen and T. C. Jannett, "A comparison of the noise sensitivity of nine QRS detection algorithms," *IEEE Transactions on Biomedical Engineering*, vol. 37, pp. 85-98, 1990.
- [31] J. Moraes and M. Freitas, "A QRS complex detection algorithm using electrocardiogram leads," *Computers in Cardiology*, pp. 205-208, 2002.
- [32] M. Risk and J. Bruno, "Measurement of QT interval and duration of the QRS complex at different ECG sampling rates," *Computers in Cardiology*, pp. 495-498, 2005.
- [33] S. C. Saxena and V. Kumar, "QRS detection using new wavelets," *Journal of Medical Engineering and Technology*, pp. 7-15, 2002.
- [34] P. S. Hamilton and W. J. Tompkins, "Quantitative investigation of QRS detection rules using the MIT-BIH arrhythmia database," *IEEE Transactions on Biomedical Engineering*, p. 1157, 1986.
- [35] I. I. Christov, "Real time electrocardiogram QRS detection using combined adaptive threshold," *Biomedical Engineering Online*, 2004.
- [36] B. U. Kohler and C. Henning, "The principles of software QRS detection," *IEEE Engineering in Medicine and Biology*, pp. 42-57, 2002.
- [37] S. Kadambe and R. Murray, "Wavelet transform-based QRS complex detector," *IEEE Transactions on Biomedical Engineering*, vol. 46, pp. 838-848, 1999.

- [38] J. Pan and W. J. Tompkins, "A real-time QRS detection algorithm," *IEEE Transactions on Biomedical Engineering*, pp. 230-236, 1985.
- [39] R. C. Graeber, "Wavelet packet-based detection of QRS complexes and study of QRS complex area to duration ratio," Albert Nerken School of Engineering, 1998.
- [40] C. Li, C. Zheng, and C. Tai, "Detection of ECG characteristic points using wavelet transforms," *IEEE Transactions on Biomedical Engineering*, vol. 42, p. 21, 1995.
- [41] Y. Zhu and N. V. Thakor, "Adaptive recurrent filter for ectopic beat and arrhythmia detection," *IEEE Engineering in Medicine and Biology Society 10th Annual International Conference*, 1988.
- [42] F. Castells, J. Rieta, C. Mora, J. Millet, and C. Sanchez, "Estimation of Atrial Fibrillatory Waves from One-Lead ECGs Using Principal Component Analysis Concepts," *Computers in Cardiology*, vol. 31, pp. 413-416, 2004.
- [43] C. Sanchez, J. Millet, J. Rieta, and F. Castells, "Packet Wavelet Decomposition: An Approach for Atrial Activity Extraction," *Computers in Cardiology*, vol. 29, pp. 33-36, 2002.

CHAPTER VII

MYOCARDIAL INFARCTION IDENTIFICATION USING RECURRENCE

QUANTIFICATION ANALYSIS (RQA) OF VCG SIGNALS

7.1 Introduction

According to the U.N. World Health Organization (WHO), myocardial infarction (MI), also known as coronary heart attack, is a leading cause of fatality in the world. It results from the occlusion of the coronary artery and insufficient blood supply to myocardium [1]. It can take place in the inferior, septal, anteroseptal, anterior, apical, or lateral parts of a heart, and it often leads to necrosis or death of myocardial cells in the nearby heart locations. Onset of MI can also alter the underlying electrical potential fields and cardiovascular dynamics. Signals from conventional 12-lead electrocardiograms (ECG) and/or 3-lead vectorcardiogram (VCG) signals, recorded at the surface of the body, are widely used in the current methods to detect MI. These signals are generated due to the sequence of electrical activities taking place in the human heart.

Several methods have been used previously for detecting MI using 12-lead ECG [2, 3]. Also, most of the previous approaches used conventional ECG features, such as variations in ST wave segments, depth of Q-wave, ST elevation, inversion of T-wave, and other event intervals [4-6]. Consideration of nonlinear stochastic dynamics underlying the measured signals, especially with the use of more intuitive VCG has not been reported in the literature. In this chapter we study the variations in heart dynamics

underlying the measured VCG loops obtained from healthy control (HC) vs. Myocardial Infarction (MI) subjects through the application of recurrence quantification analysis (RQA) [7], a technique borrowed from nonlinear dynamics systems theory, and MI detection using neural network (NN) classification of recurrence quantifiers. Recurrence quantifiers were found to be useful means to detect cardiological disorders, such as atrial fibrillation (AF) [8]. The present work follows our previous investigations based on using wavelets to compactly capture information from ECG signals [9] and to use advanced classification techniques to identify Atrial Fibrillation (AF) episodes [10].

The VCG data [368 MI and 80 HC recordings] available in the PhysioNet Database [11] was analyzed in this investigation. Each of these recordings contains 15 simultaneously recorded signals, namely, the conventional 12-lead ECG and the 3-lead Frank (XYZ) VCG. The signals were digitized at 1 kHz sampling rate with a 16-bit resolution over a range of ± 16.384 mV. The 80 HC recordings are acquired from 54 healthy volunteers, and 368 MI recordings are acquired from 148 patients. The recordings are typically ~ 2 min in duration, and all the signals were recorded for at least 30 sec long.

The results of recurrence quantification analysis of VCG signals show that laminarity, determinism, and other properties of VCG trajectories (defined in Appendix A [12, 13]) from HC segments are significantly different from those of MI patients. A radial basis neural network (NN) that uses these recurrence quantities as input features was able to provide an effective classification ($>90\%$ accuracy) between HC and MI. The remainder of this chapter is organized as follows: Section 7.2 presents the methods used in the analysis, Section 7.3 contains the overall implementation approach as well as

results from feature extraction and MI classification for the PhysioNet PTB database, and Section 7.4 presents discussion and conclusions arising out of this investigation.

7.2 Research methodology

A human heart is essentially an autonomous electro-mechanical pump. The vectorcardiogram (VCG) signals capture the heart potentials as a dynamic cardiac vector in three orthogonal components [14]. VCGs are mutually orthogonal bipolar measurements obtained from electrodes placed at appropriate locations of the torso as shown in Figure 2.3.

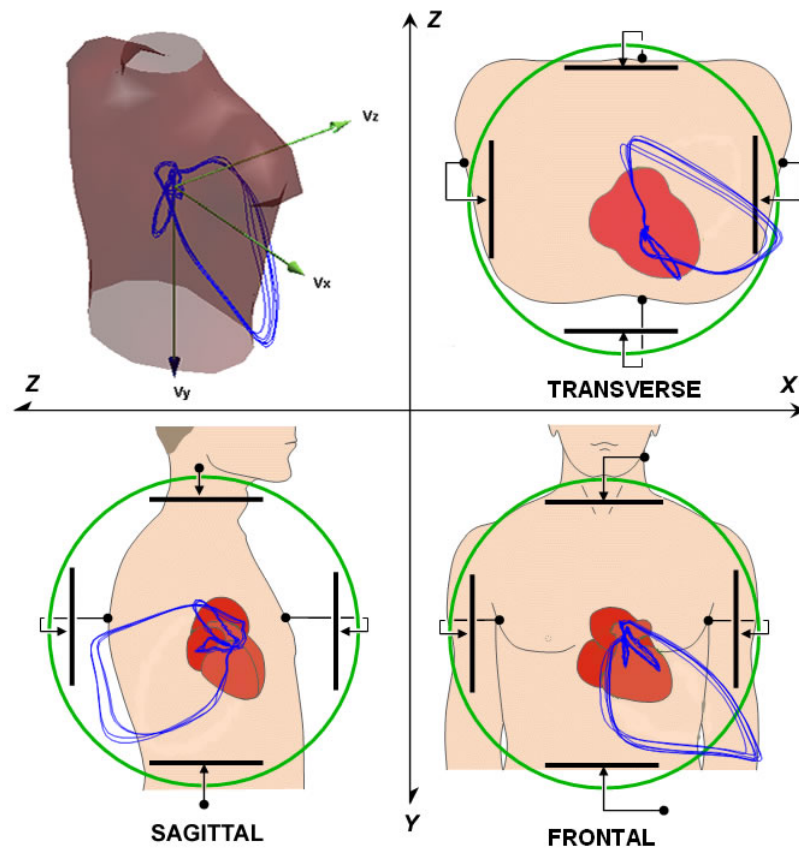


Figure 7.1 Coordinate system used for obtaining VCG signals

VCG are not as commonly used in the medical practice as the 12-lead ECG because, among other reasons, the interpretations of 3D VCG loops are not commonly

taught and require specialized knowledge of spatial decomposition of the heart vector. Since X, Y, and Z constitute the three axes, and the time, the fourth axis, they cannot be displayed on a paper. For this, dynamic vectorcardiography is needed, which can be displayed only on a computer screen. Some ECG monitoring equipment uses the VCG for calculation and storage purposes, but present the derived 12-lead ECG for the interpretation by medical doctors. However, for automated computer analysis and diagnosis both 12-lead ECG and 3-lead VCG are equally applicable.

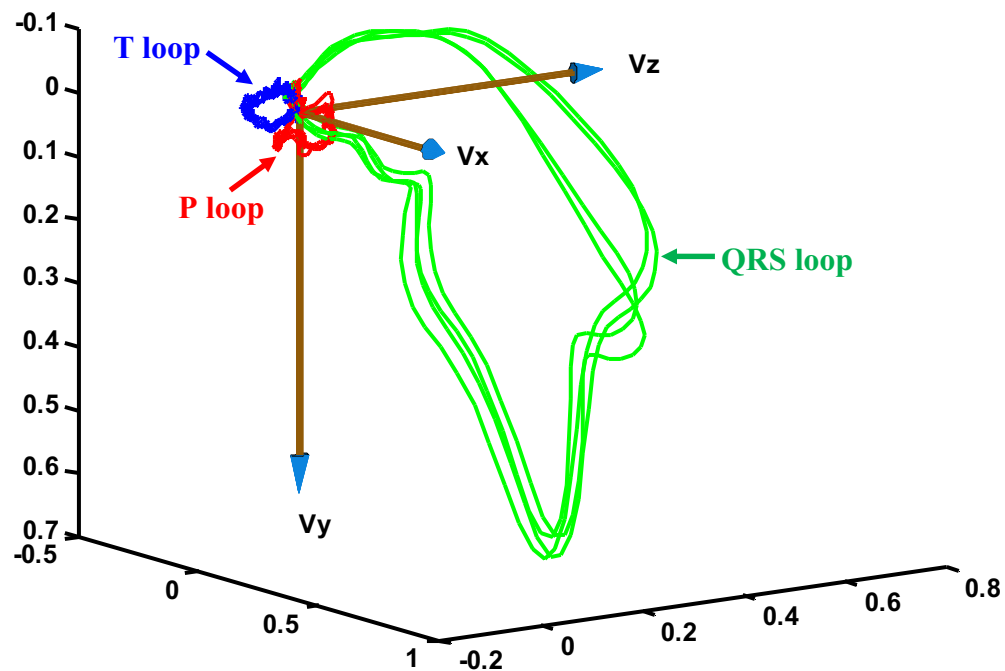


Figure 7.2 A representative VCG plot showing the vector loops for P, QRS, and T wave activities

Dower and his group [15-17] have conducted pioneering studies on VCG signal analysis and demonstrated that the 3-lead VCG and 12-lead ECG can be linearly transformed from one to the other without significant loss of clinical information regarding heart dynamics. Also, since VCG requires fewer leads to be placed on the

subject, it offers additional advantages for remote and continuous patient monitoring. Therefore, it is imperative to analyze the VCG signals and explore the relationships with cardiovascular conditions.

The VCG vector loops contain 3D recurring, near-periodic patterns of heart dynamics. Each heart beat consists of three loops corresponding to P, QRS, and T wave activities. The 3D loops can be visualized in the X-, Y- and Z- space domain with time entering implicitly (see Figure 7.2). Identification and extraction of a compact set of features from these patterns is critical for effective detection and diagnosis of various ailments. Complex nonlinear stochastic dynamics (of human cardiovascular system) underlying these VCG vector loops pose significant challenges to the extraction of features that can track cardiovascular anomalies. Some previous studies have characterized this nonlinear stochastic dynamics of human heart to exhibit low dimensional chaos [18-20].

Features extracted based on conventional statistical approaches and linear system perspectives alone tend to have limitations for capturing signal variations resulting from changes in the cardiovascular system dynamics resulting from different myocardial damage levels. The use of a rigorous nonlinear analysis based on combining multifractal embedding principles [21] with recurrence analysis [22, 23] can lead to extraction of effective features. The strength of these methods emerges from their effective use of the recurring patterns of loops exhibited by VCG and many other physiological signals. Through effective use of recurrence properties, it is possible to specify an appropriate tight set of features that track the relevant cardiovascular state variations and are insensitive to other extraneous variations.

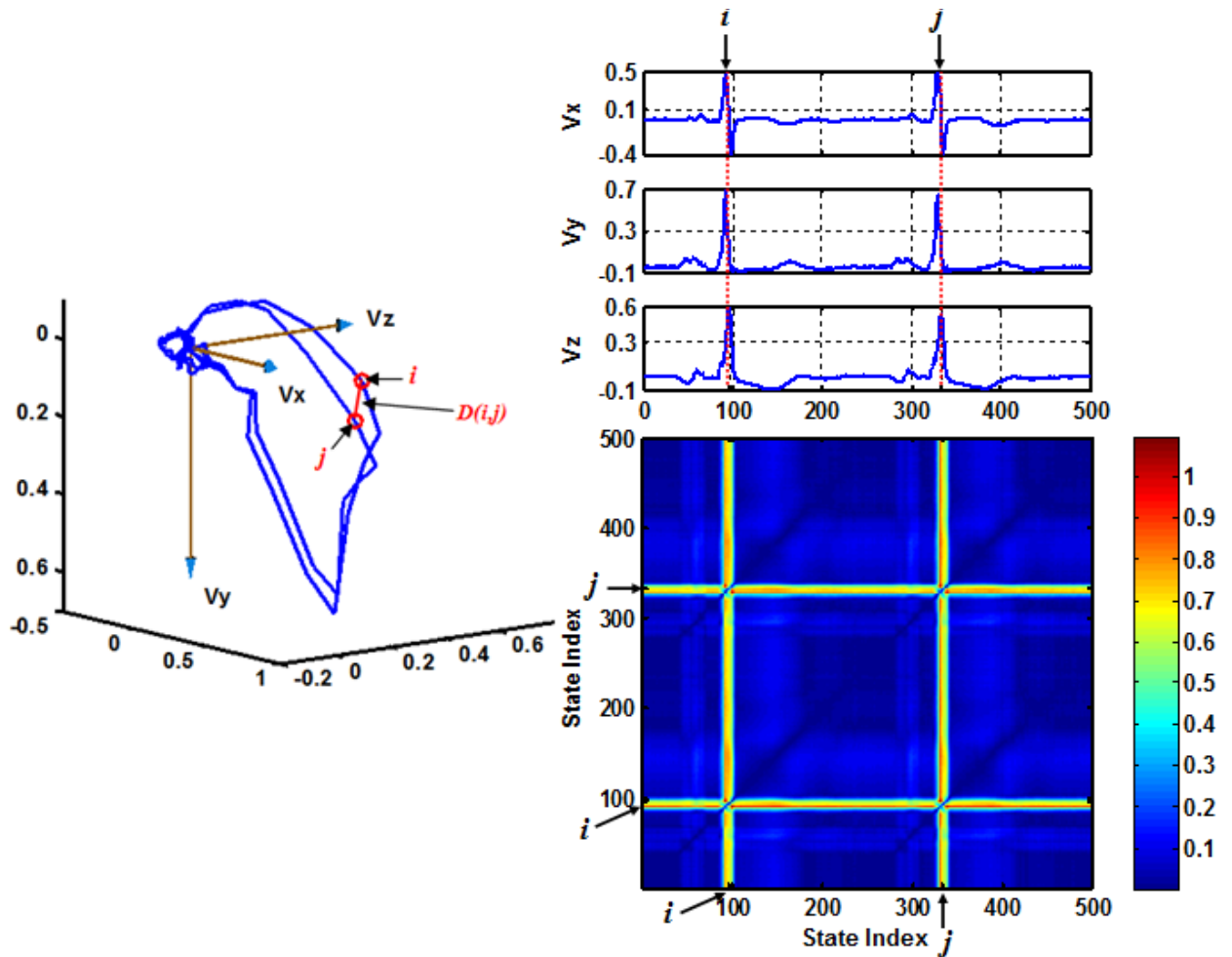


Figure 7.3 A graphical illustration of relationship among a VCG, the X,Y,Z time series and the unthresholded recurrence plot

The recurring patterns in the nonlinear system state space can be captured using recurrence plots. It provides a convenient means to capture the topological relationships existing in the 3D VCG vector space in the form of 2D images. As shown in Figure 7.3, the unthreshold recurrence plot (UTRP) delineates the distances of every point $x(i)$, realized at time index i in a VCG, to all the others, i.e., $D(i, j) := \varphi(\|x(i) - x(j)\|)$, where $\|\cdot\|$ is a distance measurement (e.g., the Euclidean norm) and $\varphi(\cdot)$ is the color code that maps the distance to a color scale. As shown in Figure 7.3, the color code of the distance between the i^{th} and j^{th} embedded vectors is located in coordinate (i, j) of the recurrence plot. If the color code at the point is blue, then the points are located close to each other

in the VCG, and if the color code is red, the points are located farther apart in a VCG. While the thresholded recurrence plot (TRP) methods (see Figure 7.4) only draw points when the distance $\|x(i) - x(j)\|$ between two vectors is below a cutoff distance r : $T(i, j) := \Theta(r - \|x(i) - x(j)\|)$, where Θ is the Heaviside function [22, 23].

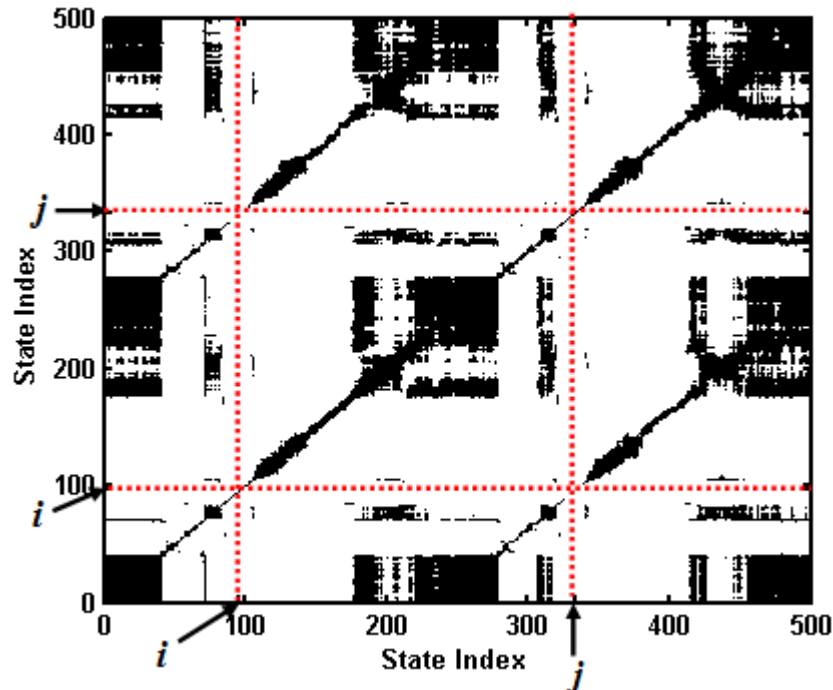


Figure 7.4 A representative thresholded recurrence plot of VCG

Thus, a recurrence plot shows the times at which a state of the dynamical system exhibits recurrence, i.e., the time-pairs at which the trajectories of a system evolution come within a specified neighborhood. The structures of a recurrence plot have distinct topology and texture patterns (see Figure 7.3 and Figure 7.4). The recurring dark (blue) diagonal (45°) lines indicate the near-periodicity of the system behaviors over given time segments with a period, heart rate, equal to the separations between successive diagonal lines. Recurrence-based methods have recently shown potential for representation, denoising and prediction of measurements from complex systems. This present work

involves extracting representative nonlinear dynamical features from the recurrence plots of VCG vector loops for classifying between MI and HC. The classification techniques used are based on neural networks (NN) and linear discriminant analysis methods which can lead to effective mapping of the features that capture the symptoms of MI conditions.

7.3 Implementation and results

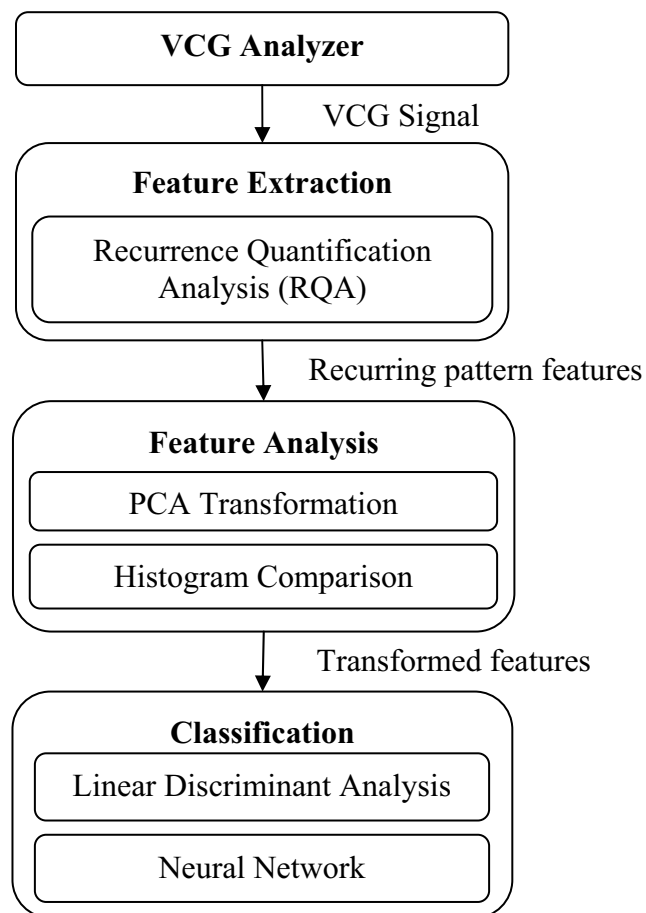


Figure 7.5 Flow diagram showing research methodology used

The overall approach implemented for analyzing the nonlinear dynamics underlying VCG signals and classifying between HC and MI are summarized in Figure 7.5 and detailed in the following subsections, consists of the following three steps:

- (1) Recurrence quantification analysis (RQA): Presentation of the 3D VCG signals in the form of a 2D unthresholded recurrence plot so that mathematical description of the salient patterns contained in the signal as well as the procedures for feature extraction can be much compactly captured, and nonlinear dynamic quantifiers that describe the specific recurring patterns in the VCG are efficiently extracted.
- (2) Feature analysis and conditioning: Orthogonalizing the recurrence quantifiers so that the significant correlations that exist between some of the recurrence quantifiers are eliminated, leading to the removal (projecting out) of the redundant information in the feature set. The extracted features should be sensitive to the state variables to be estimated.
- (3) MI classification: Associating, through both linear and nonlinear maps, the extracted features with an appropriate representation of unknown state variables.

7.3.1 Recurrence quantification and feature extraction

Recurrence plots are graphical displays of signal patterns, but quantitative features need to be extracted to analyze the underlying processes and detect hidden rhythms in the graphics. Statistical quantifiers of complexity, such as recurrence rate (Γ), determinism (DET), linemax (LMAX), entropy (ENT), laminarity (LAM), and trapping time (TT) serve as such typical recurrence quantifiers that can be estimated from an appropriately constructed Threshold Recurrence Plots (TRP) [12]. The definitions of the above six recurrence quantifiers and their relationships with heart dynamics are summarized in Appendix A [12, 13]. These quantitative features are extracted based upon the patterns across the diagonal or vertical lines in the thresholded recurrence plot.

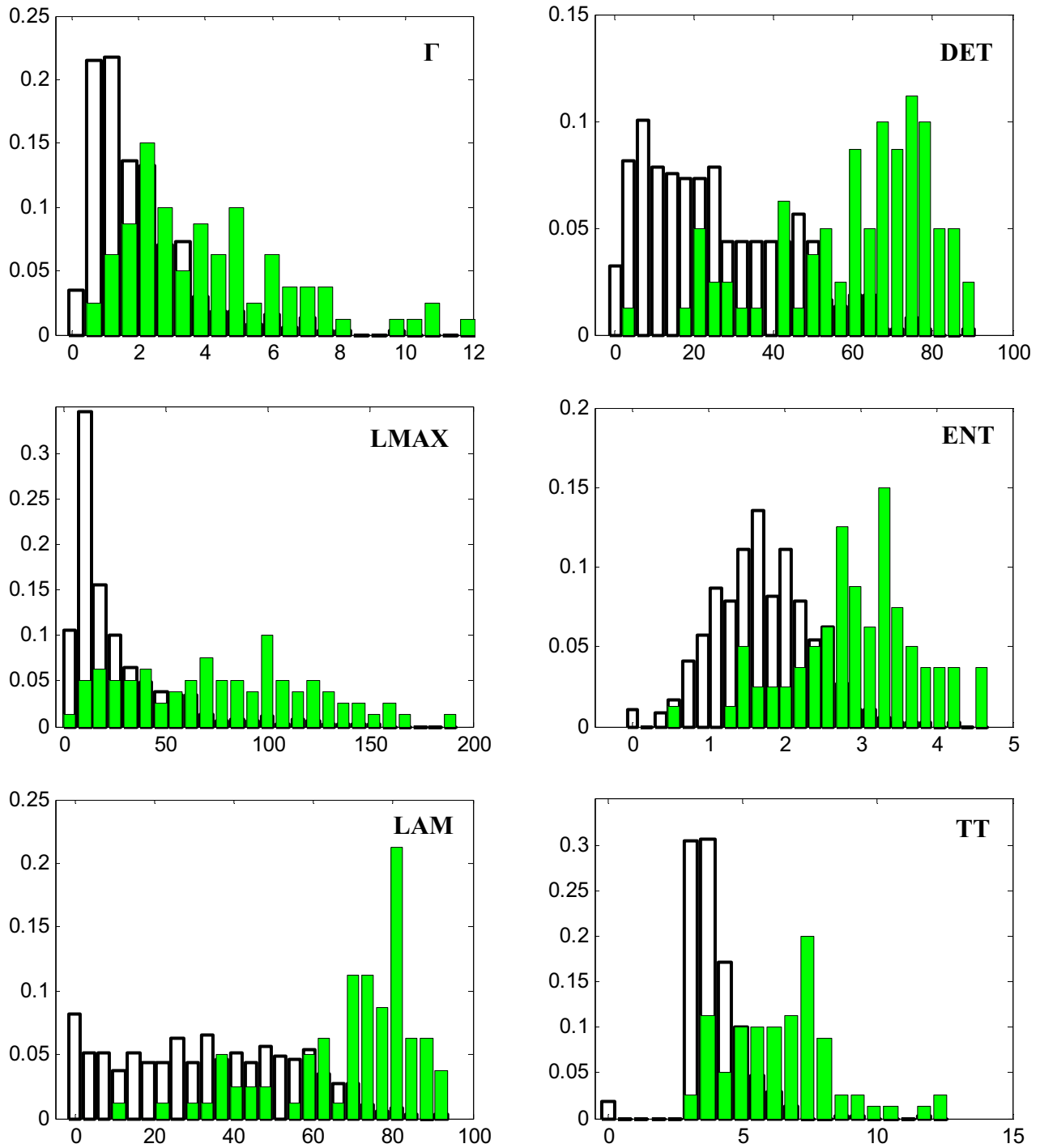


Figure 7.6 Histogram comparisons between HC (filled green) and MI(not shaded) for the six RQA quantifiers, namely, recurrence rate (Γ), determinism (DET), linemax (LMAX), entropy (ENT), laminarity (LAM), and trapping time (TT) (Histogram x-axis is feature value, and y-axis is the normalized frequency)

Figure 7.6 shows the histogram comparisons between HC and MI for the six RQA quantifiers Γ , DET, LMAX, ENT, LAM, and TT extracted from VCG signals. It may be noted that quantifier ranges of the six recurrences for HC are higher than those for MI, implying that dynamic properties of HC are more volatile than MI. The more complex variability of heart dynamics shown in the HC cases are also pointed out in Goldberger's study on fractal dynamics in physiology [20]. The distinct distributions across the MI and HC groups provide effective raw features for the following principal component analysis (PCA) and neural network (NN) classification.

7.3.2 Feature Analysis

The six recurrence features were further tightened by projecting out redundant information, and made more sensitive to the relevant variations in underlying dynamics. Principal component analysis (PCA) techniques are commonly used to reduce the dimension of the input (feature) vectors in situations where the dimension of the input vector is large but the components of the vectors are highly correlated (redundant). PCA orthogonalizes the components of the input vectors (so that they are uncorrelated with each other), and orders the resulting orthogonal components (principal components) so that those with the largest variation are considered first, and projects those components that contribute the least to the variation in the data set [9].

PCA transforms the original six nonlinear dynamical features into six orthogonal principal components, named F1, F2, ..., F6. The first principal component captures the largest variations in the nonlinear dynamical feature datasets, and the principal components are uncorrelated thus facilitating linear classification. We have found from

our earlier investigations that linear classifier is more accurate for uncorrelated principal components than the correlated original nonlinear dynamical features [10].

Figure 7.7 shows the histogram distribution of PCA transformed feature values for MI (bars not shaded) and HC (shaded green). Histograms of F1 show a statistically significant difference between the distributions for MI vs. HC, as gathered from a two-sample Kolmogorov-Smirnov test. Thus, the first principal feature F1 captures most of the differences between MI and HC. Histogram distributions for the other features, especially F3, F4, and F5 also show some differences, but not as statistically significant as F1, between MI and HC. These features can provide additional degrees of freedom, especially for classification with nonlinear discriminant boundaries.

Table 7.1 Linear model misclassification results using F1 and other principal features (F2-F6)

Features	Misclassification results	
	MI (368)	HC(80)
F1 and F2	12	34
F1 and F3	17	30
F1 and F4	19	32
F1 and F5	14	33
F1 and F6	20	31

This is further evident from feature distribution plots shown in Figure 7.8 (a) to (e). They show the plots of the principal feature F1 against the other 5 principal features (F2 through F6). A genetic algorithm is used to determine the optimal linear boundary in the feature space separate the feature values of MI (red +) from the HC (blue \diamond) feature values. This boundary line maximizes the discrimination, and hence the classification accuracies using every pair of features formed by F1 and other five principal features (F2-F6). The clear separation of HC and MI across F1 axis, marked by $< 45^\circ$ deviation from the vertical of the linear boundary indicates that F1 is the most significant discriminating feature.

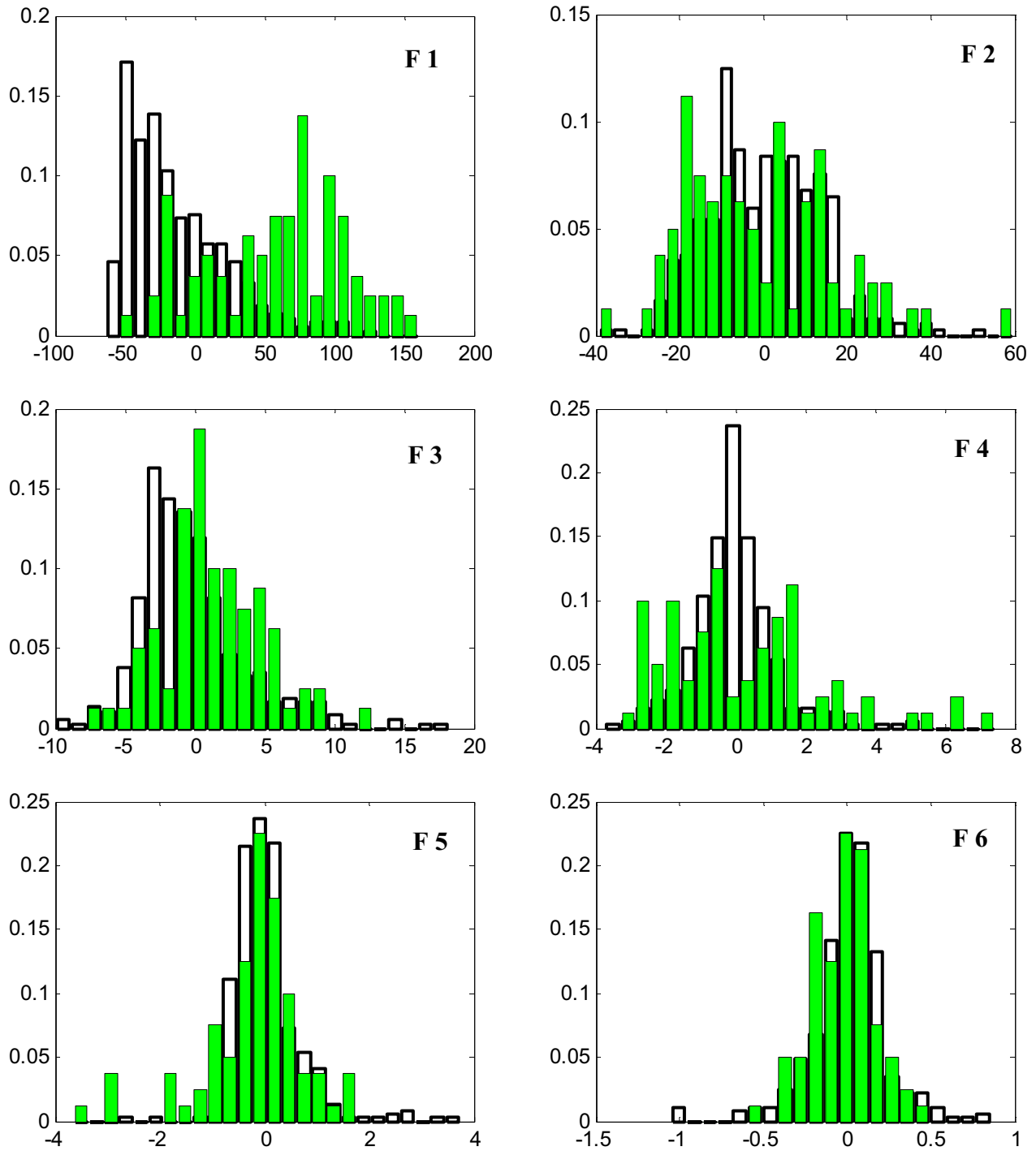


Figure 7.7 Histogram distributions of PCA feature values F1 to F6 for MI (not shaded) and HC (shaded green) (Histogram x-axis is feature value and y-axis is the normalized frequency)

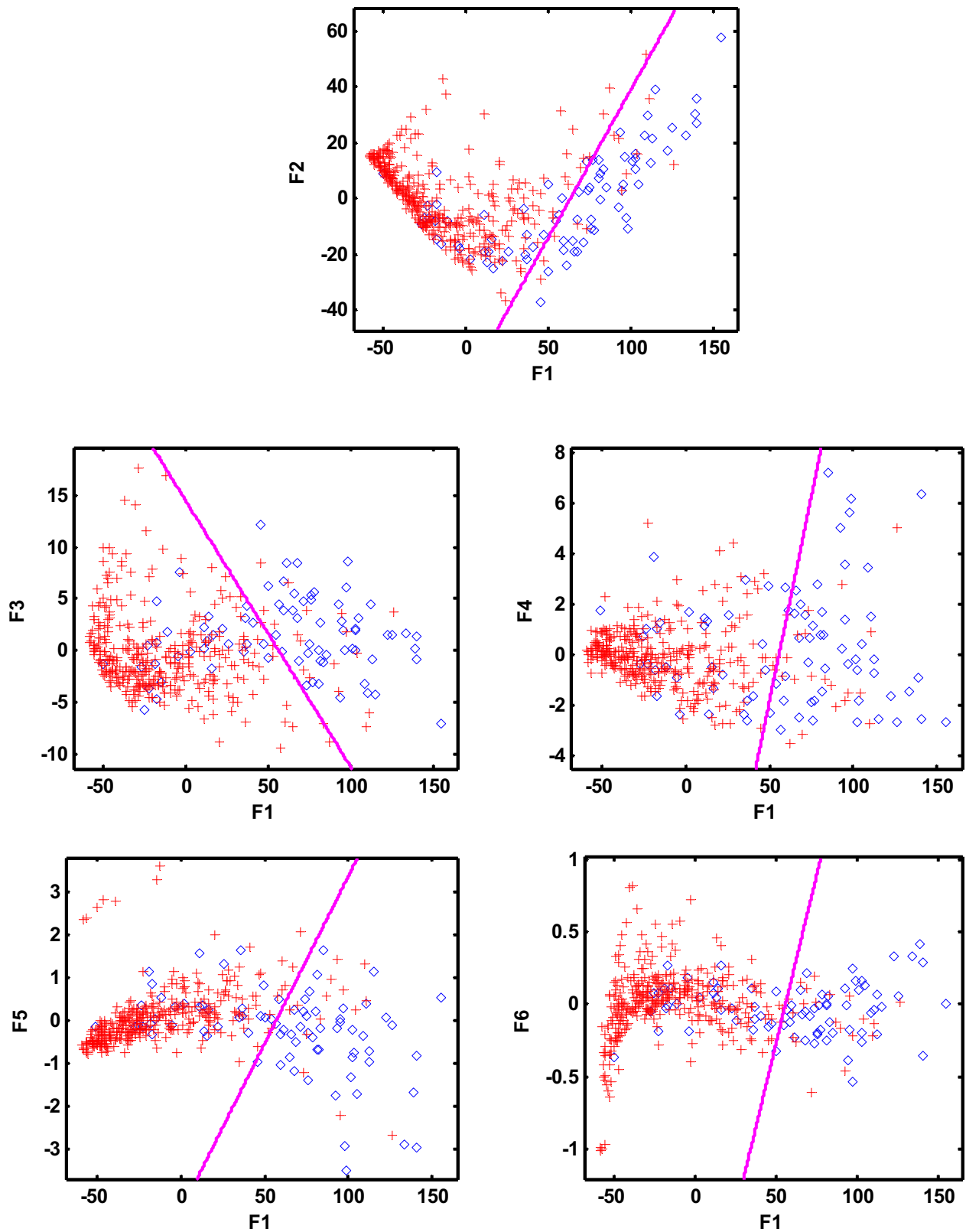


Figure 7.8 (a) to (e) Distribution of values of features F2 through F6 vs. F1 for MI (red \diamond) and HC (blue +) subjects with linear separator obtained using a genetic algorithm

Table 7.1 shows the linear model misclassification results using F1 and other principal features (F2 through F6). As will be demonstrated in Section III.C, the linear classification with all six features can distinguish ~ 97% of MI patients. The features extracted from recurrence analysis are, therefore, adequately discriminatory to capture the dynamic variations between HC and MI, and ensure a high classification accuracy for the MI patients. It may be noted that a non-linear model can further increase the classification accuracies.

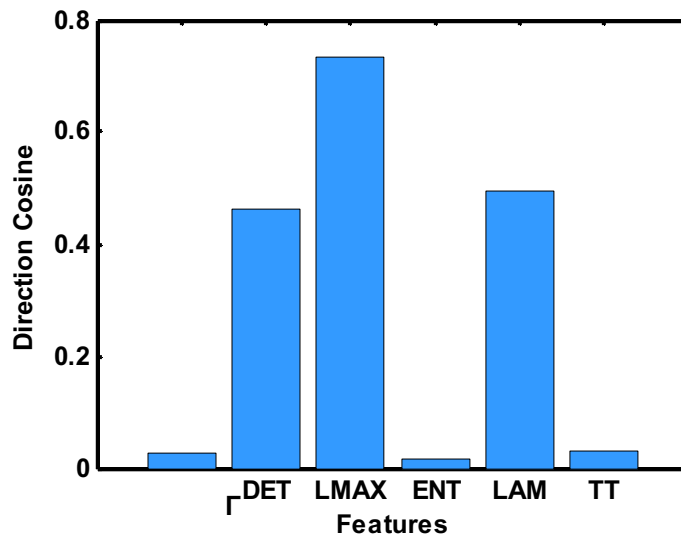


Figure 7.9 Relative importance of RQA quantifiers in the first principal feature (F1)

Since F1 is clearly the most discriminating feature, we next examine the relative contributions of the six RQA features for F1. As shown in the Figure 7.9, LAM, DET and LMAX are the most important features capturing the corresponding pathological variations of myocardial infarction in the first principal feature F1. PCA results show that MI conditions are related to stability, mixing rates of VCG trajectories, and periodicity in the cardiovascular system.

7.3.3 Classification

Linear discriminant analysis was used first to facilitate training of a simple classifier to capture the complex relationships connecting the PCA transformed features and MI. A classifier essentially is a model that maps the features to the patient's health conditions, namely, healthy control (HC, coded -1) or myocardial infarction (MI, coded +1). The states are coded such that a mathematical mapping between the feature values and the patient's conditions is possible. During the model building or the training phase of the classifier, the model parameters are adjusted so that, when features extracted from VCG signals of HC cases are presented, model outputs a value closer to -1, and so on. Linear discriminant analysis assumes that a linear hyperplane serves as a boundary separating HC and MI points in the feature space, and it uses a least square fit to determine the coefficients which give the best fit. The hyperplane that captures the relationships between the input features and the output response is of the form

$$y = a_0 + a_1x_1 + a_2x_2 + \dots + a_nx_n + \varepsilon$$

where a_i are the coefficients and x_i represents the input features. The residual error ε of the difference between the actual value and the model output determines whether the presented VCG is taken from HC or MI subject. As shown in Table 7.2, the magnitude of $\sqrt{\lambda} \times a_i$ coefficients as well as the corresponding p-values¹ are calculated to test the statistically significant levels of the features used. Larger the $\sqrt{\lambda} \times a_i$ value, the more important is the corresponding feature. Contrarily, smaller the p-value, the more significant is the feature. Table 7.2 shows that the contributions of the principal features

¹ The p-value is that probability that any variation in the input feature will result in a statistically significant change in the output response, and p-value should be < 0.05 for the input feature to be significantly discriminating.

F1 followed by F3, F4, and F5 which are the most discriminating features for MI vs. HC. These results are consistent with the initial observation on the discriminatory power of the principal features.

Table 7.2 Relative importance of principal features F1 to F6 using linear regression

Feature	F1	F2	F3	F4	F5	F6
PCA eigenvalue λ	2237.1857	205.1453	15.0914	2.0983	0.5264	0.0503
$\sqrt{\lambda}$	47.2989	14.3229	3.8848	1.4486	0.7255	0.2243
Linear regression coeff. a_i	-0.0098	0.0017	-0.0314	-0.0469	0.1382	0.2908
$ \sqrt{\lambda} \times a_i $	0.4561	0.0582	0.1505	0.0841	0.1341	0.0241
p-value	0	0.076	0	0.0129	0	0.448

Table 7.3 Results of linear regression classification for MI and HC

S. No.	Training data points		% Testing accuracy*			
	MI (368)	HC (80)	MI		HC	
			Mean	Std	Mean	Std
1	332(90%)	72(90%)	97.75	2.46	53.50	14.27
2	295(80%)	64(80%)	97.42	1.87	54.44	10.82
3	276(75%)	60(75%)	96.77	1.99	56.15	10.10
4	246(67%)	54(67%)	96.98	1.61	54.85	7.63
5	184(50%)	40(50%)	97.22	1.37	53.40	6.85
6	123(33%)	27(33%)	96.43	1.53	53.21	7.15
7	74(20%)	16(20%)	96.19	1.90	52.22	9.35
8	37(10%)	8(10%)	94.60	3.48	49.99	13.08

* accuracy is only calculated for testing dataset

As shown in Table 7.3, the linear classifier can identify MI very accurately (~ 97% accuracy) with high consistency (small standard deviations). Such high classification accuracies indicate that the features extracted from the recurrence analysis are significant discriminating features even for the linear classifiers. However, it can be seen that the accuracy of the linear classifier for HC is rather low. This is likely because, as will be shown later, the current HC samples are significantly sparse to capture the diverse variations in cardiac dynamics of HC subjects. The HC subjects show more variations in the heart dynamics and poses difficulties for the linear classifiers.

Next, a radial basis function (RBF) neural network (NN) was used to classify HC and MI cases [24]. An advantage of using NN is that it can provide a nonlinear boundary separating MI and HC cases. In particular, the RBF network uses radial basis function, which can take advantage of the clustering and separation of the feature values in the feature space to reduce the amount of training as well as the need for extensive input patterns. The functional form relating the features to the heart condition can be different at different locations of the feature space. This is particularly useful because the distribution of features in 2-D plots in Figure 7.7 show a considerable grouping of the feature values of HC and MI groups.

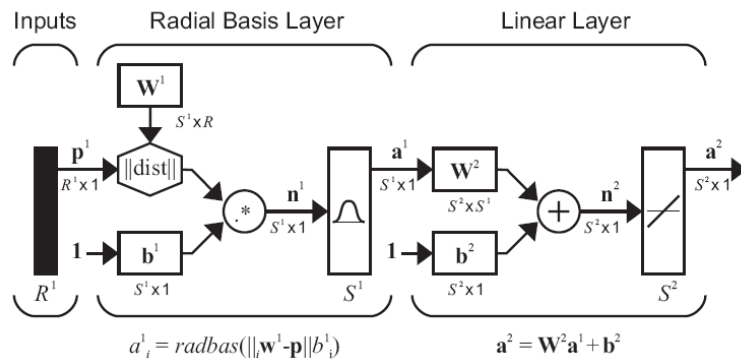


Figure 7.10 Radial basis function (RBF) neural network (NN)[24]

Figure 7.10 is a schematic of the radial basis function (RBF) neural network (NN) used in this investigation. The network consists of 2 layers – a radial basis layer and a linear layer. In the first layer, distances (difference) of the input feature vector \mathbf{p}^1 from rows of the weight matrix \mathbf{W}^1 are computed. It is then multiplied by the bias \mathbf{b}^1 to form net input \mathbf{n}^1 going into the neuron. Each row of the weight matrix \mathbf{W}^1 acts as a center for a transfer function. The transfer function should be local, i.e., the response of the transfer function should be maximum near the center and should vanish to zero as the inputs disperse away from the center. The activation \mathbf{a}^1 of layer 1 is obtained by transforming \mathbf{n}^1

using a symmetric transfer function. Most common choice for the transfer function is Gaussian function. The Gaussian function responds only to a small region of the input space where the Gaussian is centered. The second layer of the network is a linear layer. Training RBF network involves adjusting center and spread of the Gaussian function.

The results of RBF classification are summarized in Table 7.4. It shows that the RBF neural network improved the classification accuracy of both MI and HC (see Table 7.3 and Table 7.4) compared to linear classifier by using the nonlinear classification boundary and local analysis. It may also be noted that HC subject conditions are more diverse than the MI subject. Notably the RBF classifiers improved the accuracy of HC by 20% to 75%.

Table 7.4 Results of neural network (NN) classification for MI and HC

Training data points		Number of neurons	% Accuracy for MI classification				% Accuracy for HC classification			
			Training		Testing		Training		Testing	
MI (368)	HC (80)		Mean	Std	Mean	Std	Mean	Std	Mean	Std
332 (90%)	72 (90%)	350	99.60	1.24	98.70	1.98	78.60	5.63	75.00	6.14
295 (80%)	64 (80%)	250	99.10	1.63	98.40	2.12	71.60	6.18	71.50	7.13
220 (60%)	72 (90%)	200	98.82	2.59	96.62	2.86	73.20	5.81	75.00	6.23
220 (60%)	64 (80%)	200	96.84	2.61	96.40	2.94	69.10	6.28	68.20	6.89
148 (40%)	48 (60%)	150	95.74	5.96	94.81	6.89	65.80	10.86	65.62	12.21
148 (40%)	32 (40%)	150	95.48	6.14	92.27	6.58	58.93	12.28	56.25	14.45

Total Number ECG data sets: MI 368 and HC 80 data sets

We also investigated the influence of the number of training and testing patterns on the accuracy of the classifier. Figure 7.11 shows the variation of the percentage accuracy with the number of points used in RBF training. We chose the same number of data points for MI as HC subjects. It can be seen that the accuracy of MI cases has come down and show a similar trend for both HC and MI when the number of training data points is sparse (<100), implying that availability of more HC data can improve the accuracy

further. Also, since the accuracy of MI subjects improves very slowly at higher accuracies (>90%), significant data need to be available if we were to increase the accuracy to two 9's (99%), or three 9's (99.9%). Also, from examining the variation of classification accuracies for MI and HC with the sizes of training and testing patterns as shown in Figure 7.11, it is evident that the accuracies would improve for HC with increase in the number of training data points.

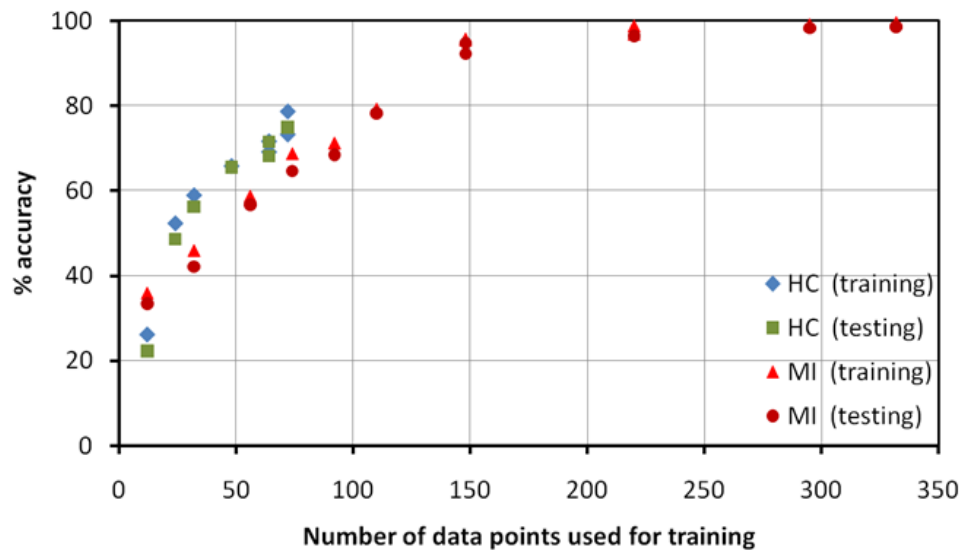


Figure 7.11 Variation of % accuracy of the neural network (NN) (both training and testing) with the number of data points for MI and HC

7.4 Summary

In this chapter, an attempt was made to analyze the VCG signals using nonlinear dynamics approaches by applying the recurrence quantification analysis (RQA) for feature extraction to distinguish MI patients from the HC subjects. A linear classifier was found to correctly identify MI about 94% of the times. However the linear classifier was able to correctly classify HC cases about 45% of the times. A neural network classifier was used to improve MI classification accuracies to about 97%, and HC to about 75%. It was also shown that the classification accuracies for HC cases are likely to improve with

the availability of additional VCG data. These results indicate that the VCG features extracted using RQA are good indicators of the cardiovascular conditions, and the NN classifiers capture the nonlinear relationships connecting the recurrence features with patients' conditions. Based on these findings, the following conclusions may be arrived.

1. The recurrence plot representation of VCG signals captures the complex patterns buried in the VCG vector loops and the underlying nonlinear dynamics. The study of the patterns quantified using the RQA were found to provide useful information for detecting MI.

2. It was found that many of the VCG features extracted using RQA contained highly redundant information. Principal component analysis (PCA) is used to reorient the features to align in such a way as to remove significant correlation between features. The principal feature F1 was found to be the most discriminatory feature and the VCG features LMAX, LAM, and DET extracted using RQA are the three leading contributors for F1.

3. Results of linear discriminant analysis showed strong relationships between the extracted recurring patterns related features and the patients' cardiovascular conditions. Over 90% of the MI signals were correctly classified using the principal features. However, the linear classifier was not adequate to identify HC subjects (~50%). This was somewhat surprising as one would expect this to be the case for MI patients (due to various types of MI) than HC subjects. This is likely a limitation of the linear classifier in capturing the diverse patterns of HC subjects.

4. Neural network model identifies the nonlinear mapping from the extracted features to the patients' conditions and provides high accuracies for MI classification (>95%),

which make the real-time and practical implementation plausible. It also improves the accuracy for identifying HC to above 75%. It was also shown that the training and testing accuracies can improve with the availability of more VCG recordings, especially of the HC subjects, for training and testing.

5. Investigation of the effects of the number of training and testing patterns on the percent accuracy of the classifier has found similar trends for both HC and MI, implying that availability of more data would improve the accuracy further in the case of HC. Also, from examining the variation of classification accuracies for MI and HC with the sizes of training and testing patterns, it is evident that the accuracies will be improved with an increase in the size of training data points.

6. It appears that improve the accuracy of identification of HC subjects as well as various myocardial infarction (MI) patients to double nines (99%) or triple nines (99.9%), the following are needed: (1) access to larger data collections of myocardial infarction and health control cases, and (2) expertise of the cardiologists in providing relevant input parameters and analysis of the data.

7.5 References

- [1] D. Dale, *Rapid Interpretation of ECG's: An Interactive Course*: Cover Publishing Company, 2000.
- [2] M. C. MacLachlan, B. F. Nielsen, M. Lysaker, and A. Tveito, "Computing the size and location of myocardial ischemia using measurements of ST-segment shift," *Biomedical Engineering, IEEE Transactions on*, vol. 53, pp. 1024-1031, 2006.

- [3] P. Porela, H. Helenius, and L. M. Voipio-Pulkki, "Automated ECG injury scores in the prediction of the myocardial infarction (AMI) size," in *Computers in Cardiology 1998*, 1998, pp. 305-308.
- [4] D. Lemire, C. Pharand, J. Rajaonah, B. A. Dube, and A. R. LeBlanc, "Wavelet time entropy, T wave morphology and myocardial ischemia," *Biomedical Engineering, IEEE Transactions on*, vol. 47, pp. 967-970, 2000.
- [5] E. Pueyo, L. Sornmo, and P. Laguna, "QRS Slopes for Detection and Characterization of Myocardial Ischemia," *Biomedical Engineering, IEEE Transactions on*, vol. 55, pp. 468-477, 2008.
- [6] K. K. Talwar, S. Radhakrishnan, V. Hariharan, and M. L. Bhatia, "Spatial vectorcardiogram in acute inferior wall myocardial infarction: its utility in identification of patients prone to complete heart block," *International Journal of Cardiology*, vol. 24, pp. 289-292, 1989.
- [7] N. Marwan, M. Carmen Romano, M. Thiel, and J. Kurths, "Recurrence plots for the analysis of complex systems," *Physics Reports*, vol. 438, pp. 237-329, 2007.
- [8] R. Sun and Y. Wang, "Predicting termination of atrial fibrillation based on the structure and quantification of the recurrence plot," *Medical Engineering & Physics*, vol. In Press, Corrected Proof.
- [9] H. Yang, S. T. Bukkapatnam, and R. Komanduri, "Nonlinear adaptive wavelet analysis of electrocardiogram signals," *Physical Review E (Statistical, Nonlinear, and Soft Matter Physics)*, vol. 76, p. 026214, 2007.
- [10] S. Bukkapatnam, R. Komanduri, H. Yang, P. Rao, W.-C. Lih, M. Malshe, L. M. Raff, B. Benjamin, and M. Rockley, "Classification of atrial fibrillation episodes from sparse electrocardiogram data," *Journal of Electrocardiology*, vol. 41, pp. 292-299, 2008.
- [11] A. Goldberger, L. Amaral, L. Glass, J. Hausdorff, P. Ivanov, R. Mark, J. Mietus, G. Moody, C. Peng, and H. Stanley, "PhysioBank, PhysioToolkit, and PhysioNet:

components of a new research resource for complex physiologic signals," *Circulation* 101, vol. 23, pp. e215-e220, 2000 (June 13).

- [12] N. Marwan, N. Wessel, U. Meyerfeldt, A. Schirdewan, and J. Kurths, "Recurrence plot based measures of complexity and their application to heart-rate-variability data," *Physical Review E*, vol. 66, Aug 2002.
- [13] A. Facchini, H. Kantz, and E. Tiezzi, "Recurrence plot analysis of nonstationary data: The understanding of curved patterns," *Physical Review E*, vol. 72, p. 021915, 2005.
- [14] J. Malmivuo and R. Plonsey, *Bioelectromagnetism: principles and applications of bioelectric and biomagnetic fields*. USA: Oxford University Press, July 18, 1995.
- [15] G. E. Dower and H. B. Machado, "XYZ data interpreted by a 12-lead computer program using the derived electrocardiogram," *Journal of electrocardiology*, vol. 12, pp. 249-261, 1979.
- [16] G. E. Dower, H. B. Machado, and J. A. Osborne, "On deriving the electrocardiogram from vectorcardiographic leads," vol. 3, p. 87, 1980.
- [17] G. E. Dower, A. Yakush, S. B. Nazzal, R. V. Jutzy, and C. E. Ruiz, "Deriving the 12-lead electrocardiogram from four (EASI) electrodes," *Journal of electrocardiology*, vol. 21, pp. S182-S187, 1988.
- [18] P. C. Ivanov, L. A. N. Amaral, A. L. Goldberger, S. Havlin, M. G. Rosenblum, Z. R. Struzik, and H. E. Stanley, "Multifractality in human heartbeat dynamics," *Nature*, vol. 399, pp. 461-465, 1999.
- [19] H. E. Stanley, "Statistical physics and physiology: monofractal and multifractal approaches," *Physica A: Statistical Mechanics and its Applications*, vol. 270, p. 309, 1999.
- [20] A. L. Goldberger, L. A. N. Amaral, J. M. Hausdorff, P. C. Ivanov, C. K. Peng, and H. E. Stanley, "Fractal dynamics in physiology: alterations with disease and

aging," *Proceedings of the National Academy of Sciences*, vol. 99, pp. 2466-2472, February 19, 2002 2002.

- [21] H. Kantz and T. Schreiber, *Nonlinear time series analysis*. Cambridge: Cambridge University Press, 1997.
- [22] M. C. Casdagli, "Recurrence plots revisited," *Physica D*, vol. 108, pp. 12-44, 1997.
- [23] J. P. Eckmann, S. O. Kamphorst, and D. Ruelle, "Recurrence plots of dynamical systems," *Europhys Lett*, vol. 4, pp. 973-977, 1987.
- [24] M. T. Hagan, H. B. Demuth, and M. H. Beale, *Neural network design*: PWS Pub. Co., December 29, 1995.

CHAPTER VIII

VECTORCARDIOGRAPHIC OCTANT FEATURES FOR THE DIAGNOSTICS OF HETEROGENEOUS MYOCARDIAL INFARCTION

8.1 Introduction

Coronary heart disease is the leading cause of death in the United States (America Heart Association - AHA). Myocardial infarction, also known as heart attack, is resulted from the occlusion of the coronary artery and insufficient blood supply to myocardium. It can take place in the anterior, inferior, posterior, infero-lateral, anterior-septal, posterior-lateral etc. parts of a heart. The myocardial infarction triad is ischemia, injury, and necrosis, and any of the three may occur alone. Ischemia is normally from the reduced blood supply, injury indicates acuteness of infarct, and infarction is the symptom of myocardium necrosis [1].

The 12-lead electrocardiograms (ECG), recorded at the surface of the body, are widely used in clinical diagnostic applications of myocardial infarction. The ECG diagnosable myocardial infarctions can be divided as following:

- Q wave infarction, which is diagnosed by the presence of pathological Q waves. A pathological Q wave is defined as at least 40 ms duration or 1/3 downward deflection of the entire QRS magnitude, and found in most 12-lead ECG except lead III and lead aVR.

- Non-Q wave infarction, which is diagnosed in the presence of ST elevation or depression, and T wave abnormalities.

It is conceptually known that 12-lead ECG examines the same heart activity from 12 different perspectives of view, and vectorcardiogram (VCG) is only 3-lead orthogonal heart electrical activity measurements. The VCG vector loops contain 3D recurring, near-periodic P, QRS, and T wave activity patterns in eight octants. Dower et al.[2-4] reveals that 12-lead ECGs can be linearly transformed to 3-lead VCGs without a significant loss of clinically useful information regarding heart dynamics. But VCG trajectory is not as commonly utilized as 12-lead ECG traces because of spatial imagination requirements (for e.g., rotation and projection of VCG trajectory), the loss of temporal information, and medical doctors' accustomed trainings of 12-lead ECG interpretation for one hundred years. However, VCG will be a better option for computer processing and analysis because it overcomes not only the information loss from only one or two ECG signals but also the dimensionality problems induced by the 12-lead ECG.

The VCG recordings (368 MIs and 80 HCs) available in the PhysioNet PTB Database[5, 6] were considered in this study. Each of these recordings contains 15 simultaneously recorded signals, namely, the conventional 12-lead ECG and the 3-lead Frank (XYZ) VCG. The signals were digitized at 1 kHz sampling rate with a 16-bit resolution over a range of ± 16.384 mV. The 80 HC recordings are acquired from 54 healthy volunteers, and 368 MI recordings are acquired from 148 patients. Within the MI recordings, there are 89 inferior, 56 infero-lateral, 19 infero-postero-lateral, 1 infero-posterior, 47 anterior, 43 antero-lateral, 77 antero-septal, 2 antero-septo-lateral, 3 lateral,

4 posterior, 5 postero-lateral and 22 unknown site cases. Those VCG recordings are typically ~ 2 min in duration, and all the signals were recorded for at least 30 sec long.

8.2 Feature extraction

To characterize and quantify heterogeneous myocardial infarction, three groups of features are collected as following:

- (1) Conventional ECG features: mean and standard deviation of RR interval, QT interval, ST elevation or depression;
- (2) VCG vector features: magnitude of Q wave, R wave, T wave vector, angle between R and T vector, azimuth R vector angle, and azimuth T vector angle;
- (3) VCG octant features: octant location of Q, R, T vectors, percentage of vector points in an octant, and maximum, average, variance of vector magnitude distributions in each octant.

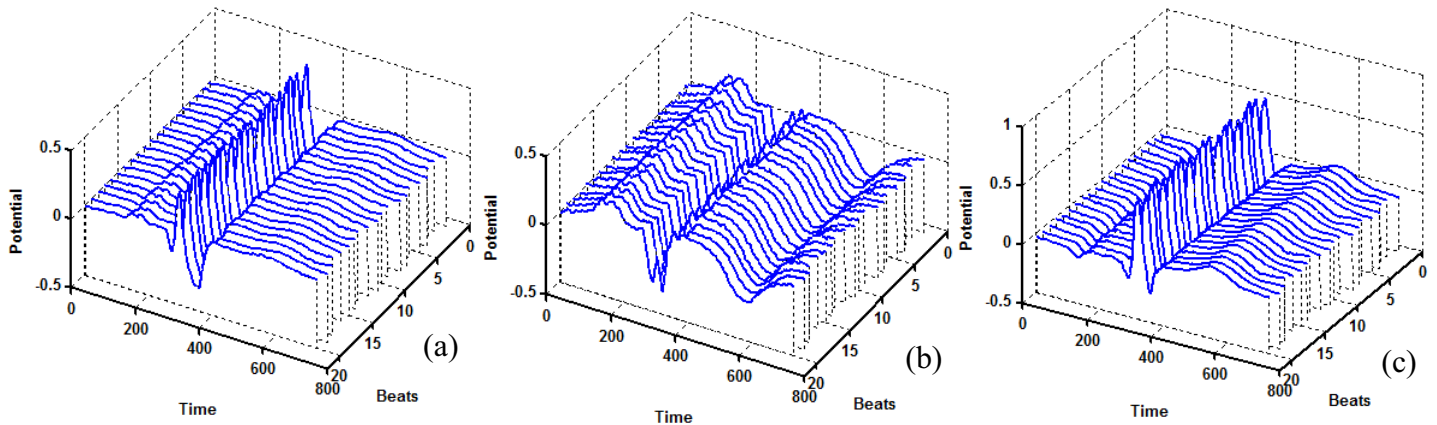


Figure 8.1 Frank XYZ VCG ensembles, (a) X-direction; (b) Y-direction, (c) Z-direction

Traditional ECG intervals, for e.g., RR and QT intervals, are highly variable measurements. The heart rate variability, respiration, artifacts, power-line interference are known to generate ECG near-periodicities and influence the interval calculation. As shown in Figure 8.1, we calculate the mean and standard deviation of those intervals

through the extracted heart beat ensembles over time. Figure 8.1 (a) (b) (c) illustrate the Frank X, Y, Z ensembles. It may be noted that same direction ensembles are sharing similar morphologies, but there are still beat-to-beat variations due to heart rate variability. The group of conventional interval features is extracted as RR average (RR avg), RR standard deviation (RR std), QT average (QT avg), QT standard deviation (QT std). The ST segment integration area (ST_itg) is determined by computing the areas from J point (location where QRS complex joins the ST segment) to J+80 ms if heart rate (HR) is less than 100 beat/min (or J+72 ms if $100 < HR < 110$, or J+64 ms if $110 < HR < 120$, or J+60 ms if $HR > 120$) [7]. Since myocardial infarction often causes the ST elevation or depression in 12-lead ECG signals, the drifts from isoelectric line, therefore, will also result in the increase of VCG ST segment area.

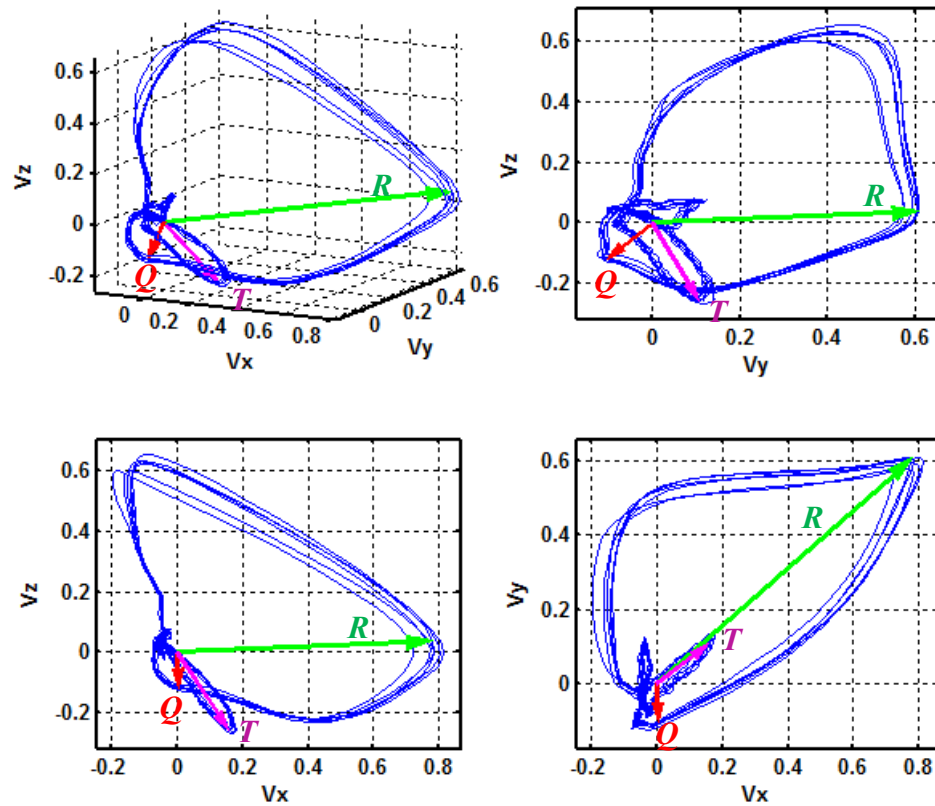


Figure 8.2 VCG attractor and its 2D projection plots with Q, R, T vectors

The group of VCG vector features are designed to capture the myocardial infarction pathological patterns, for e.g., Q vector length (Q_mag) will help identify the Q wave infarction. Increasing of T wave amplitude is related to the T vector magnitude (T_mag). R vector magnitude (R_mag) indicates the size of the ventricular chambers and proximity of chest electrodes to ventricular chamber etc. As shown in Figure 8.2, the aforementioned Q, R, T vectors are from the isoelectric point in VCG to the remotest points in the respective Q, R, T loops. In addition, the angle between R and T vector are computed to provide more information about the myocardial ischemia, injury, necrosis and their locations in myocardium. Previous study shows that QRS loop and T loop are close to each other in normal cases, while far from each other in some cardiovascular diseases [8].

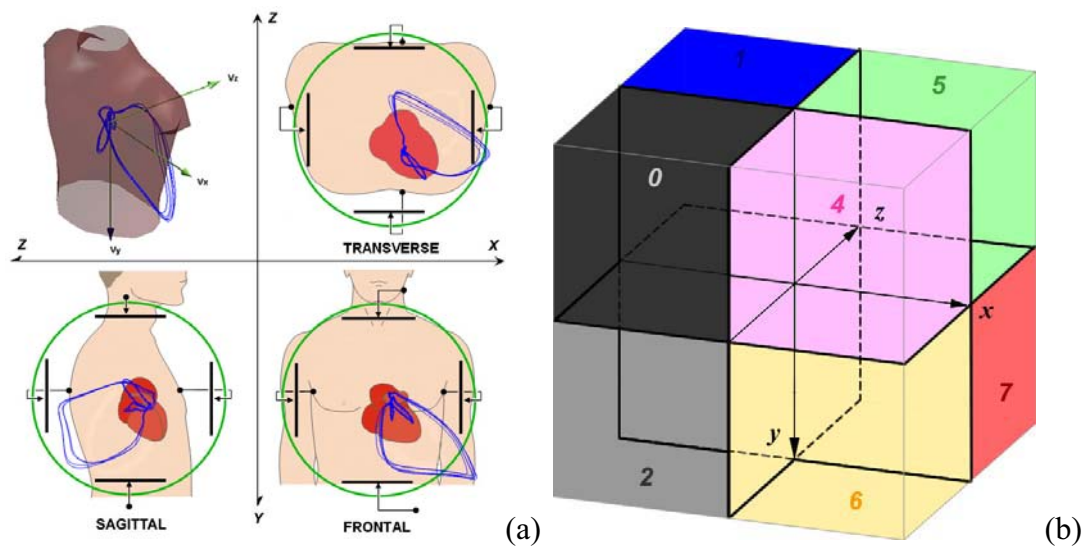










Figure 8.3 (a) VCG electrodes placement in human body; (b) the corresponding octant definitions

As shown in Figure 8.3, a new octant numbering system is designed to be used with the VCG measurement system. Binary code 0 is employed to represent the negative

direction in X, Y, or Z axis, and 1 is for the positive direction. For instance, if the octant lays in all negative XYZ directions, binary coding will be 000 and the resulted octant number is also 0. The details of eight octant binary coding are shown in Table 8.1. Based upon the VCG electrode placements in the human torso, the coordinate system in Figure 8.3 (b) is rotated to illustrate the exact position of every octant in the human body. All the octants with even numbering are found to be in the anterior locations, and odd in the posterior. Both octant 0 and octant 2 are found to be located in the right anterior side. This binary octant definition system does not need to be memorized but deduced, and is easier for users to find the octant spatial location.

Table 8.1 VCG octant definition and color mapping

Octant	X	Y	Z	Binary code	Location (X, Y, Z)	Color code
0	-	-	-	(000)	Right -superior-anterior	Black 
1	-	-	+	(001)	Right -superior-posterior	Blue 
2	-	+	-	(010)	Right -inferior-anterior	Gray 
3	-	+	+	(011)	Right -inferior-posterior	Cyan 
4	+	-	-	(100)	left-anterior-superior	Magenta 
5	+	-	+	(101)	left -superior-posterior	Green 
6	+	+	-	(110)	left -inferior-anterior	Yellow 
7	+	+	+	(111)	left -inferior-posterior	Red 

It may be noted that former VCG studies about the diagnostics of cardiovascular diseases (CVD) investigated T loop morphology[8-10], angles of QRS, T loops, QRS loop area[11-15], VCG attractor fractal dynamics[16], QRS and T vector length [17-19] etc., but few approaches investigated the relationships of CVDs to cardiac vector length distributions in each octant and T vector octant locations. Our dynamic VCG representation study in chapter V gave some clues about the intrinsic relationships between cardiovascular diseases and VCG octant information. As illustrated in Figure 8.4, the healthy control has significant differences in the VCG octant distributions from

myocardial infarction. Eight specific colors are used to paint the vector points in each octant (see Table 8.1). For instance, it may be noted in Figure 8.4 that red line segments (octant 7) have different magnitudes and percentages to the whole trajectory for HC and MI. Therefore, the group of VCG octant features is investigated for a high separation probability of myocardial infarction from healthy control. T vector position will locate those T wave inversion and abnormal cases. R vector octant provides information about the heart electrical axis. Vector point magnitude and proportion in all eight octants indicates the cardiac vector changing directions and strengths in different local areas etc.

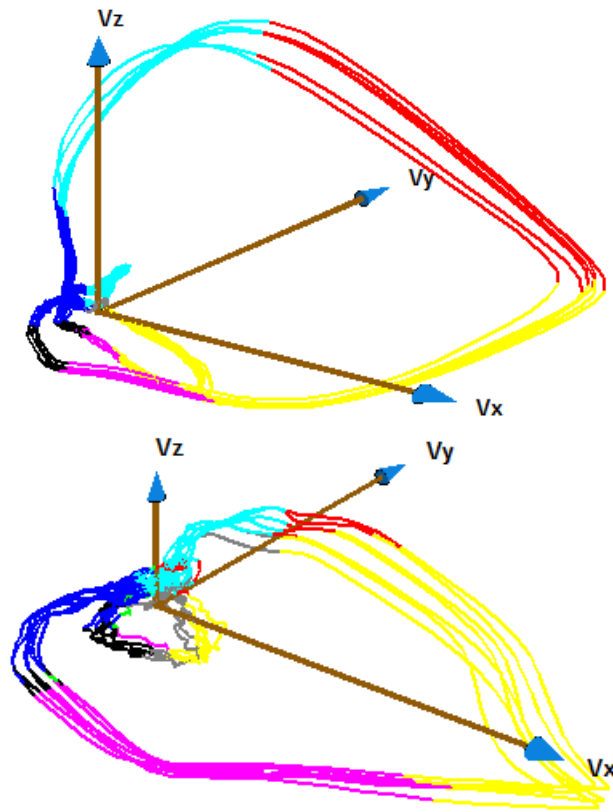


Figure 8.4 VCG trajectories with different octant colors in the 3D coordinate system, (a) HC; (b) MI

8.3 Feature analysis

The Kolmogorov–Smirnov goodness-of-fit hypothesis test (KS test) is performed to examine the differences in both location and shape of empirical cumulative distribution functions of the forty six features between HC and MI samples. The feature sample empirical distribution function E_n for n iid observations X_i is defined as

$$E_n(x) = \frac{1}{n} \sum_{i=1}^n I(X_i < x), \text{ where } I(X_i < x) \text{ is the indicator function. The Kolmogorov-}$$

Smirnov statistic is $D = \sup_x |E_{n_{MI}}(x) - E_{n_{HC}}(x)|$, which is the maximum difference

between HC and MI feature empirical distribution functions, and the asymptotic p -value

is calculated as $p = \exp(-2 \times (\sqrt{\tilde{n}} + 0.12 + \frac{0.11}{\sqrt{\tilde{n}}})^2 \times D^2)$, where $\tilde{n} = \frac{n_{MI} \times n_{HC}}{n_{MI} + n_{HC}}$. If the

probability value $p < 0.05$, the distribution differences are considered statistically significant and the hypothesis that the distributions are distinct will be TRUE. Table 8.2 shows the KS test statistics, and the mean and standard deviation of 46 features of the MI and HC recordings from PTB database.

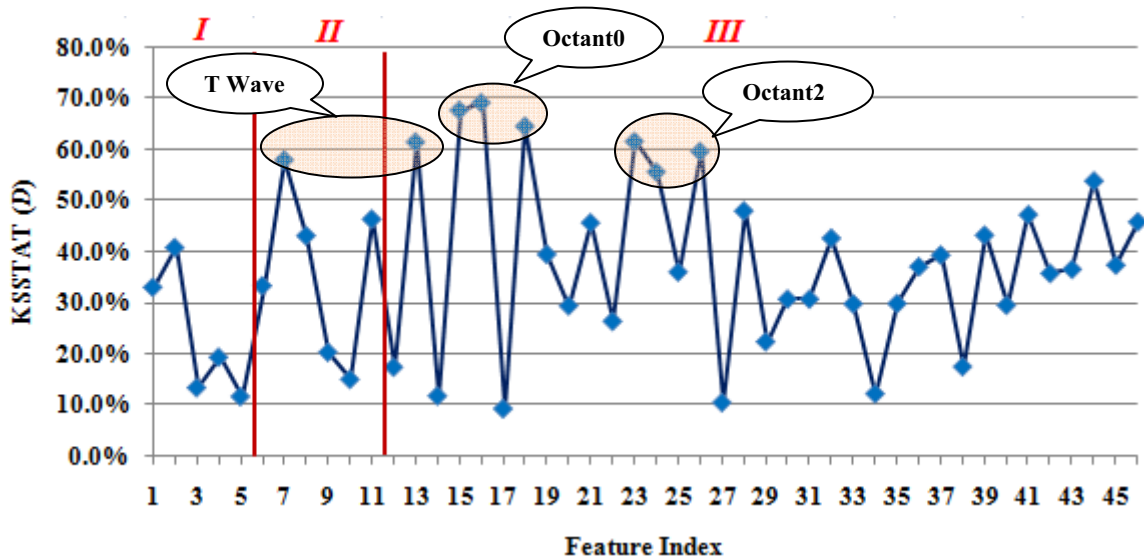


Figure 8.5 Kolmogorov-Smirnov statistic variations of 46 features

Table 8.2 Statistical analysis (Kolmogorov-Smirnov test) of three groups of features

Group	No.	Feature	Hypothesis	p-value	KSSTAT(D)	MI(mean)	MI(std)	HC(mean)	HC(std)
I	1	RR avg	TRUE	7.27E-07	33.0%	811.47	168.84	911.92	152.12
	2	RR std	TRUE	3.00E-10	40.8%	59.74	262.20	49.33	28.40
	3	QT avg	FALSE	1.80E-01	13.3%	387.69	46.91	385.32	32.06
	4	QT std	TRUE	1.28E-02	19.3%	14.37	34.93	12.23	20.50
	5	ST_ltg	FALSE	3.23E-01	11.6%	1.54	1.00	1.61	0.74
II	6	Q_mag	TRUE	5.69E-07	33.3%	0.33	0.19	0.45	0.16
	7	T_mag	TRUE	2.70E-20	58.0%	0.25	0.14	0.40	0.14
	8	R_mag	TRUE	2.09E-11	43.2%	1.17	0.39	1.57	0.50
	9	Tang	TRUE	7.54E-03	20.3%	116.90	31.50	119.35	15.44
	10	Rang	FALSE	9.63E-02	14.9%	65.66	25.86	68.90	23.60
	11	RTang	TRUE	3.95E-13	46.4%	101.52	44.88	56.64	28.39
III	12	R_pos	TRUE	3.38E-02	17.3%	6.01	1.41	6.46	1.02
	13	T_pos	TRUE	8.71E-23	61.6%	3.46	2.26	5.88	0.72
	14	Q_pos	FALSE	3.12E-01	11.7%	0.27	0.92	0.00	0.00
	15	Oct0AvgN	TRUE	1.48E-27	67.8%	0.09	0.04	0.12	0.01
	16	Oct0MaxN	TRUE	9.63E-29	69.3%	0.38	0.16	0.54	0.04
	17	Oct0Ratio	FALSE	6.16E-01	9.2%	0.22	0.16	0.21	0.15
	18	Oct0VarN	TRUE	4.30E-25	64.7%	0.01	0.01	0.01	0.00
	19	Oct1AvgN	TRUE	1.24E-09	39.5%	0.10	0.07	0.12	0.02
	20	Oct1MaxN	TRUE	1.59E-05	29.4%	0.61	0.22	0.74	0.25
	21	Oct1Ratio	TRUE	9.56E-13	45.7%	0.21	0.16	0.39	0.17
	22	Oct1VarN	TRUE	1.60E-04	26.4%	0.01	0.01	0.01	0.01
	23	Oct2AvgN	TRUE	7.26E-23	61.7%	0.11	0.05	0.15	0.02
	24	Oct2MaxN	TRUE	9.99E-19	55.7%	0.44	0.26	0.62	0.30
	25	Oct2Ratio	TRUE	4.41E-08	36.0%	0.14	0.11	0.06	0.05
	26	Oct2VarN	TRUE	1.83E-21	59.7%	0.01	0.01	0.02	0.01
	27	Oct3AvgN	FALSE	4.57E-01	10.4%	0.09	0.03	0.09	0.02
	28	Oct3MaxN	TRUE	4.88E-14	48.0%	0.61	0.30	0.82	0.36
	29	Oct3Ratio	TRUE	2.28E-03	22.3%	0.11	0.10	0.06	0.05
	30	Oct3VarN	TRUE	5.50E-06	30.7%	0.01	0.01	0.01	0.01
	31	Oct4AvgN	TRUE	5.50E-06	30.7%	0.10	0.03	0.09	0.01
	32	Oct4MaxN	TRUE	3.69E-11	42.7%	0.72	0.23	0.64	0.32
	33	Oct4Ratio	TRUE	1.17E-05	29.8%	0.09	0.08	0.04	0.04
	34	Oct4VarN	FALSE	2.71E-01	12.1%	0.01	0.01	0.01	0.01
	35	Oct5AvgN	TRUE	1.12E-05	29.8%	0.17	0.10	0.15	0.09
	36	Oct5MaxN	TRUE	1.58E-08	37.1%	0.98	0.38	1.22	0.53
	37	Oct5Ratio	TRUE	1.48E-09	39.3%	0.04	0.05	0.03	0.09
38	Oct5VarN	TRUE	3.21E-02	17.4%	0.05	0.07	0.05	0.06	
39	Oct6AvgN	TRUE	1.84E-11	43.3%	0.13	0.03	0.16	0.03	
40	Oct6MaxN	TRUE	1.46E-05	29.5%	1.02	0.42	1.30	0.45	
41	Oct6Ratio	TRUE	1.31E-13	47.3%	0.13	0.10	0.18	0.05	
42	Oct6VarN	TRUE	5.74E-08	35.8%	0.03	0.02	0.03	0.03	
43	Oct7AvgN	TRUE	2.58E-08	36.6%	0.25	0.10	0.32	0.09	
44	Oct7MaxN	TRUE	1.44E-17	53.9%	1.48	0.41	2.05	0.48	
45	Oct7Ratio	TRUE	1.14E-08	37.4%	0.06	0.04	0.04	0.03	
46	Oct7VarN	TRUE	7.81E-13	45.9%	0.13	0.09	0.26	0.12	

For each VCG signal recording, forty six features are calculated, but such a high-dimensional feature space is not suitable for the classification in term of the computational efficiency. Two sample KS tests between HC and MI help identify important features that track the relevant cardiovascular state variations and are insensitive to other extraneous variations, and determine an appropriate tight subset of features which are most essential for the classification.

Table 8.2 shows that the Kolmogorov-Smirnov statistic variations of 46 features in three groups. It may be noted that T_mag is the most significant feature in group I and II, and its maximum difference level is 58%. We can find out eight features whose KSSTAT (D) values are greater than 55%, and they are Oct0MaxN (69.3%), Oct0AvgN (67.8%), Oct0VarN (64.7%), Oct2AvgN (61.7%), T_pos (61.6%), Oct2VarN (59.7%), T_mag (58%) and Oct2MaxN (55.7%). VCG octant features in group III contribute seven out of eight such important features. The statistical feature analysis implies that the eight feature subsets incorporate most of the discriminating information of the total forty six features. It is also intriguing to discover that octant 0, octant 2, and T vector related information are the most prominent eight features to distinguish MIs from HCs, and they are used to build the classification and regression tree (CART) model towards the detection of MI and HC recordings in the Physionet PTB database.

8.4 Classification

The CART classification model uses decision rules learned from the pattern (clustering) of features in a training data set to classify different groups of objects. Tree-structured models are first proposed by Morgan and Songuist in 1963 for the analysis of

survey data [20]. This approach can be quite effective for creating clinical decision rules that combine medical knowledgebase with data analysis.

Table 8.3 Experiment results of CART classification model using stochastic training datasets

Run No.	Training data points			% Testing Accuracy					
				MI		HC		Total	
	percentage	MI (368)	HC (80)	Mean	Std	Mean	Std	Mean	Std
1	10.0%	37	8	92.34	4.50	77.47	15.96	89.70	4.49
2	20.0%	74	16	95.48	2.56	78.09	9.06	92.39	2.33
3	33.3%	123	27	95.97	2.25	80.68	9.73	93.26	1.76
4	50.0%	184	40	96.84	1.65	81.50	7.66	94.11	1.44
5	66.7%	246	54	96.40	1.98	83.54	7.67	94.16	1.82
6	75.0%	276	60	97.03	1.77	82.75	9.00	94.49	1.79
7	80.0%	295	64	96.89	2.29	82.38	8.63	94.30	2.21
8	90.0%	332	72	97.08	2.88	82.50	15.39	94.43	3.00

* Each run randomly selects the training data points in the specified percentage and does the classification for 100 times. The classification accuracy statistics are only calculated from testing dataset.

Table 8.3 presents the CART classification model experiment results for PTB database with randomly selected percentage of training datasets. The training dataset size is varied from 10% to 90% of the whole data. It may be noted that the average MI testing accuracy is higher than 92.34% for all eight training sizes, but the standard deviation of MI testing accuracy is a little bigger when the training data size is as small as 10% or as large as 90%. This is resulted from the random selection of training datasets, and the feature space may not be fully explored for a small portion of data. This small portion of data, either in the testing or training group, may not be captured by the training samples' patterns. The mean testing accuracy for HC is higher than 77.47%, and standard deviation of HC testing accuracy follows the same trend as MI. While most HC testing standard deviations are bigger than MI, this is because the HC population size (80) is less than MI

(368). This random training and testing experiment shows the generality and effectiveness of CART classification model with vectorcardiographic octant features.

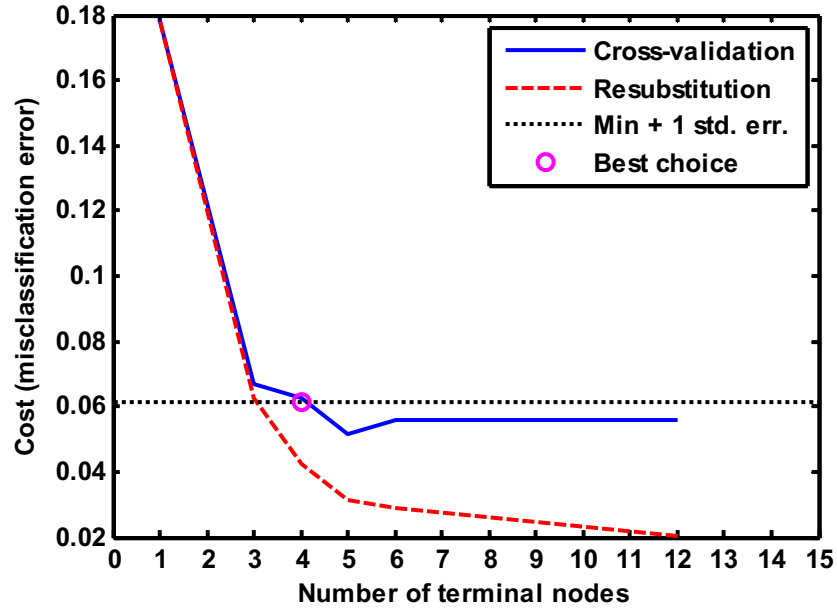


Figure 8.6 CART model cross validation curves and Tree size selection

To prevent the well-known “overfitting” problems in the machine learning model, cross-validation techniques are utilized to find a generalized, optimal and simpler tree structure for the MI and HC classification. In our case we remove a subset of 10% of the data, build a tree using the other 90%, and use the tree to classify the removed 10%. This process is repeated by removing each of ten subsets one at a time. As shown in Figure 8.6, the resubstitution error is kept decreasing as the tree size grows, but the cross-validation results show that the error rate increases with the tree size beyond a certain point. The best choice of pruned tree has the small cross-validation error and is roughly as good as a more complex tree.

The optimal tree structure for PTB database MI and HC classification is as shown in Figure 8.7. It may be noted that 96.74% MI and 96.25% HC in the PTB database can be correctly detected with two simple if-then rules and four VCG octant features as following:

- (1) If $\text{Oct0MaxN} < 0.52$ or $T_pos < 5.5$, then the recording is MI;
- (2) For the rest recordings after step 1, If $\text{Oct2AvgN} < 0.123$ or $\text{Oct0VarN} > 0.015$, then the recording is MI;

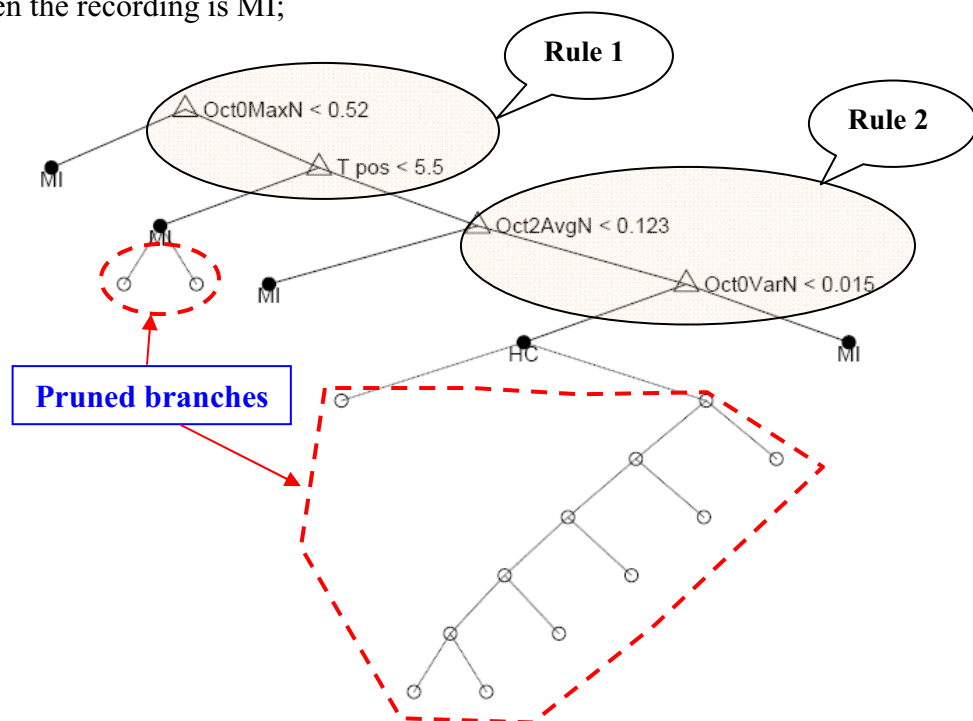


Figure 8.7 Optimal CART tree structure for the classification of MI in PTB database

The detailed classifications of each step are as shown in Figure 8.8. The MI recording is represented as red Δ in the feature space and HC as blue \square . In step 1, 24 MIs and 4 HCs are incorrectly classified. For the overlapping area with 24 MIs and 76 HCs in step 1, applying step 2 rules will correctly classify 14 MIs and 75 HCs. Therefore, the detail accuracies can be calculated as following:

Step 1: %MI = $100 \times (1 - 28/368) = 92.39\%$; %HC = $100 \times (1 - 2/80) = 97.50\%$

Step 2: %MI = $100 \times (1 - 12/368) = 96.74\%$; %HC = $100 \times (1 - 3/80) = 96.25\%$

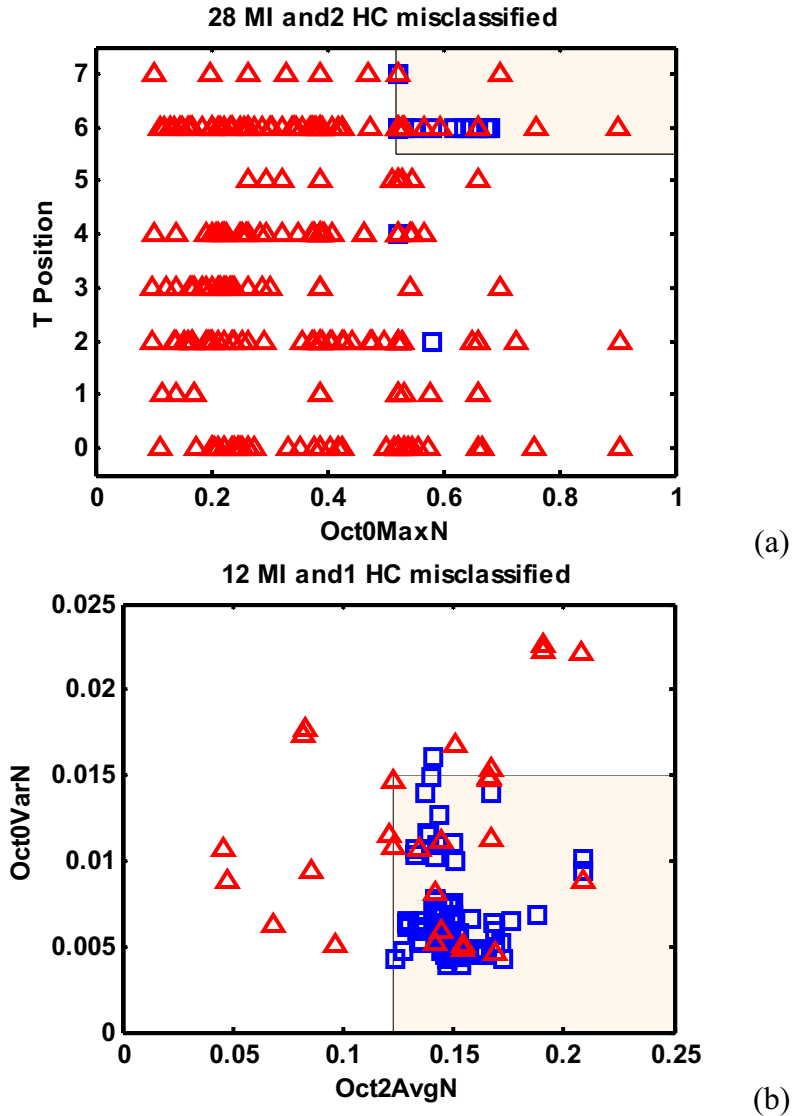


Figure 8.8 Detailed classification of PTB database MI and HC in (a) step 1 and (b) step 2

Figure 8.9 shows the healthy control (368) and myocardial infarction (80) recordings in the PTB database characterized by three features. The first feature is Oct0MaxN, which is the maximal vector magnitude in the first octant. The second feature T position is the T wave peak's octant location. The third feature Oct2AvgN is the average vector magnitude in the octant 2. These three octant features discriminate the

healthy from myocardial infarction subjects. The healthy controls are shown to be cluster in the green circle area, while myocardial infarction patients spread outside that green area.

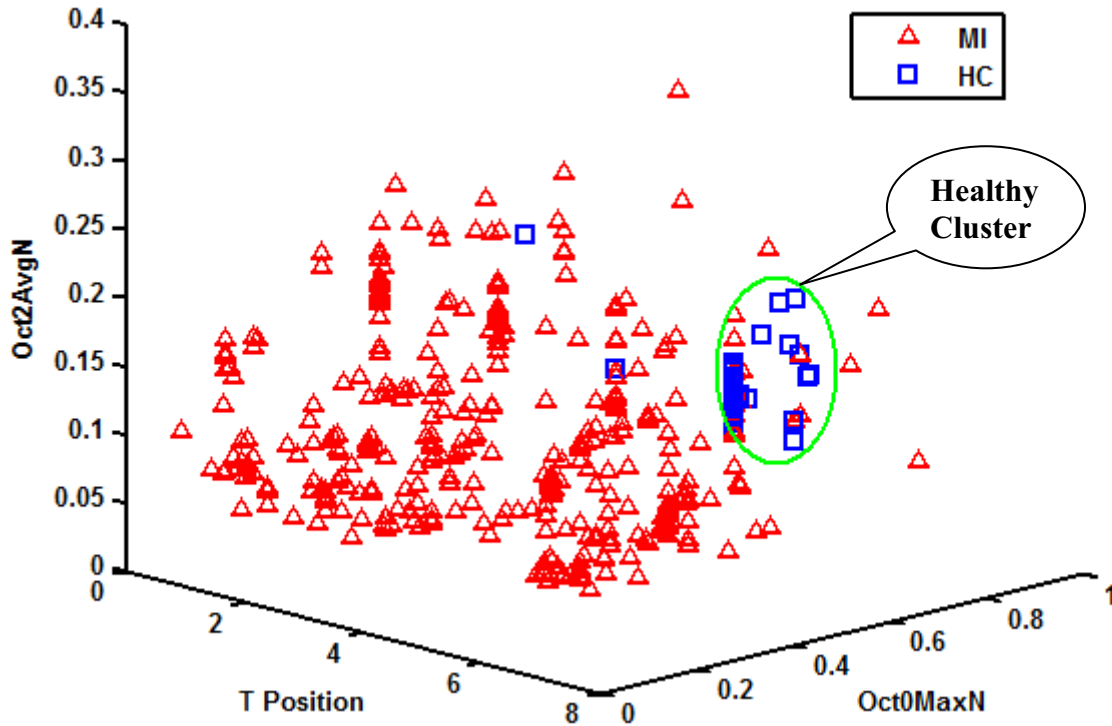


Figure 8.9 Healthy control (368) and myocardial infarction (80) distribution in 3D feature space (Oct0MaxN, T octant position and Oct2AvgN)

8.5 Discussions

It is generally agreed that Q wave, ST segment, and T wave are very substantial for the identification of myocardial infarction. But conventional ECG intervals and previously proposed VCG features are not adequate to capture the essential characteristics of MI. The newly proposed VCG octant features can amazingly achieve high MI and HC classification accuracies using two simple rules and four VCG octant features. It may also be noted that step 1 can detect 92.39% of MI and 97.5% of HC with just two features Oct0MaxN and T octant position.

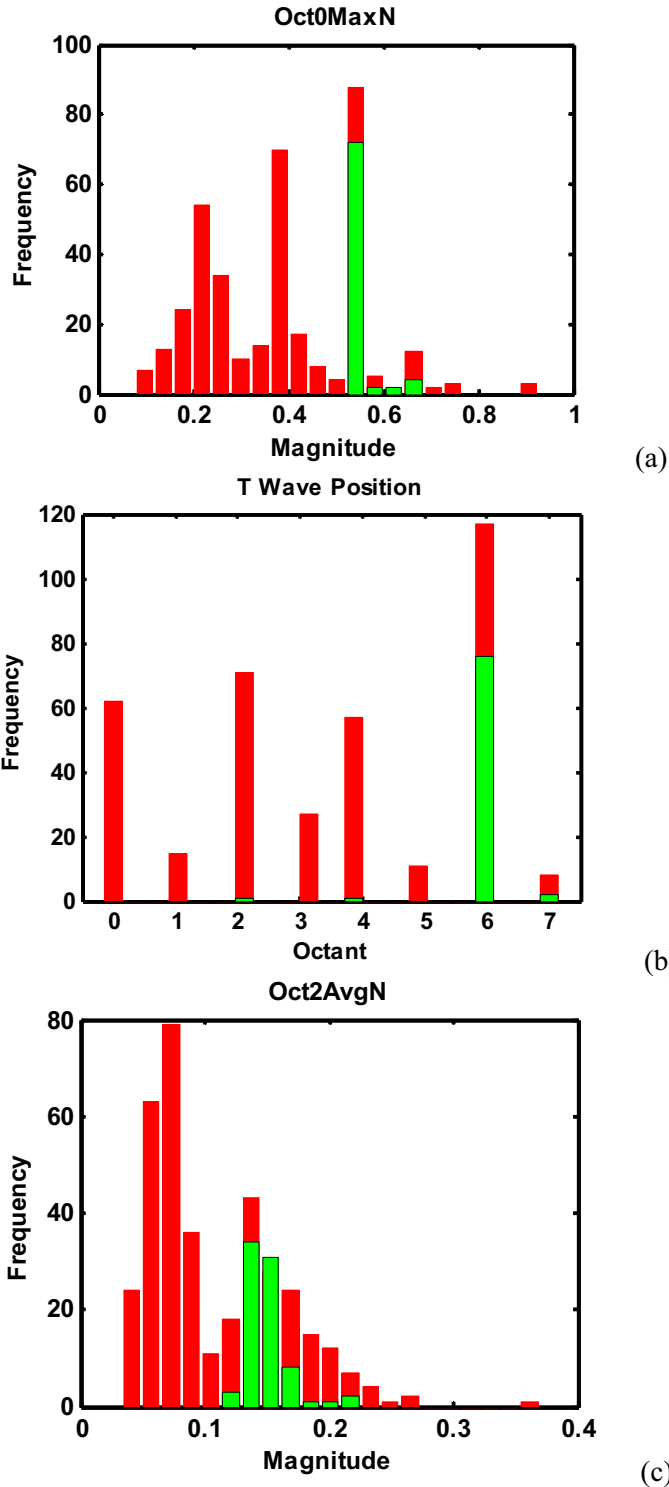


Figure 8.10 Oct0MaxN (a), T octant position (b) and Oct2AvgN (c) histogram plots

Figure 8.10 shows the distribution plots of feature Oct0MaxN, T octant position and Oct2AvgN. It may be noted that Oct0MaxN has significant distribution differences

between MI (0.38 ± 0.16) and HC (0.54 ± 0.04). In addition, the majority (76/80) of HCs' T vector positions is also found to cluster in octant 6 (x-positive, y-positive, z-negative), while MIs spread over all the eight octants. Q wave is frequently traveling around octant 0 in the VCG trajectory because Q wave is mostly negative in x, y, and z directions. Oct2AvgN also shows dissimilarity in the distribution between healthy and myocardial infarction patients. Both octant 0 and octant 2 are found to be located in the right anterior side. Therefore, myocardial infarction subjects are statistically shown to have abnormal electrical activities in the right anterior positions of the body. The VCG octant features are shown to yield more statistical differences than conventional interval features in Figure 8.5 and Table 8.2. The extra useful information can be found in 3D VCG spatial dynamics than 12-lead ECG signals. It will also be much convenient to extract VCG octant features with computer analysis than inspecting the 12-lead ECG traces and memorizing ECG interval rules.

8.6 Summary

In this investigation, octant 0, octant 2, and T vector information in vectorcardiogram are found to be very important for the diagnostics of heterogeneous MIs. Statistical feature analysis shows that cardiac vector length distributions in octant 0 and octant 2, T vector length and octant position are the most prominent features to distinguish MIs from HCs. It is significant at 69% level ($p\text{-value}=9.63E\text{-}29$) for the Oct0MaxN (the maximum vector length in octant 0) distribution differences between MI (0.38 ± 0.16) and HC (0.54 ± 0.04). The majority (76/80) of HCs' T vector positions is also found to cluster in octant 6 (x-positive, y-positive, z-negative), while MIs spread over all the eight octants. Additionally, Oct2AvgN and Oct0VarN show >60% statistical

distribution differences. With only four octant features (Oct0MaxN, T_pos, Oct2AvgN and Oct0VarN), a simple Classification and Regression Tree (CART) model can yield classification accuracy with 96.74% sensitivity and 96.25% specificity. The stochastic experiments with different percentage of training data size also reveal high sensitivity (mean: 96%) and specificity (mean: 82%) for heterogeneous MI and HC classification, which demonstrate the generality and effectiveness of CART model and vectorcardiographic octant features. This study is definitely indicative of potential clinical applications of MI diagnostic model from the proposed VCG octant features.

8.7 References

- [1] D. Dubin, *Rapid Interpretation of EKG's: An Interactive Course*: Cover Publishing Company, 2000.
- [2] G. E. Dower and H. B. Machado, "XYZ data interpreted by a 12-lead computer program using the derived electrocardiogram," *Journal of electrocardiology*, vol. 12, pp. 249-261, 1979.
- [3] G. E. Dower, H. B. Machado, and J. A. Osborne, "On deriving the electrocardiogram from vectorcardiographic leads," vol. 3, p. 87, 1980.
- [4] G. E. Dower, A. Yakush, S. B. Nazzal, R. V. Jutzy, and C. E. Ruiz, "Deriving the 12-lead electrocardiogram from four (EASI) electrodes," *Journal of electrocardiology*, vol. 21, pp. S182-S187, 1988.
- [5] A. Goldberger, L. Amaral, L. Glass, J. Hausdorff, P. Ivanov, R. Mark, J. Mietus, G. Moody, C. Peng, and H. Stanley, "PhysioBank, PhysioToolkit, and PhysioNet: Components of a New Research Resource for Complex Physiologic Signals," *Circulation* 101, vol. 23, pp. e215-e220, 2000 (June 13).

- [6] G. B. Moody, H. Koch, and U. Steinhoff, "The PhysioNet/Computers in Cardiology Challenge 2006: QT interval measurement," in *Computers in Cardiology, 2006*, 2006, pp. 313-316.
- [7] F. Jager, A. Taddei, G. B. Moody, M. Emdin, G. Antolic, R. Dorn, A. Smrdel, C. Marchesi, and R. G. Mark, "Long-term ST database: a reference for the development and evaluation of automated ischaemia detectors and for the study of the dynamics of myocardial ischaemia," *Medical & Biological Engineering & Computing*, vol. 41, pp. 172-183, 2003.
- [8] G. Bortolan and I. Christov, "Myocardial infarction and ischemia characterization from T-loop morphology in VCG," in *Computers in Cardiology 2001*, 2001, pp. 633-636.
- [9] D. Lemire, C. Pharand, J. Rajaonah, B. Dube, and A. R. LeBlanc, "Wavelet time entropy, T wave morphology and myocardial ischemia," *Biomedical Engineering, IEEE Transactions on*, vol. 47, pp. 967-970, 2000.
- [10] A. Rubulis, J. Jensen, G. Lundahl, J. Tapanainen, L. Wecke, and L. Bergfeldt, "T vector and loop characteristics in coronary artery disease and during acute ischemia," *Heart Rhythm*, vol. 1, pp. 317-325, Sep 2004.
- [11] T. Yamazaki, V. F. Froelicher, J. Myers, S. Chun, and P. Wang, "Spatial QRS-T angle predicts cardiac death in a clinical population," *Heart Rhythm*, vol. 2, pp. 73-78, Jan 2005.
- [12] C. D. Cowdery, G. S. Wagner, J. W. Starr, G. Rogers, and J. C. Greenfield, "New Vectorcardiographic Criteria for Diagnosing Right Ventricular Hypertrophy in Mitral-Stenosis - Comparison with Electrocardiographic Criteria," *Circulation*, vol. 62, pp. 1026-1032, 1980.
- [13] P. Hugenholtz, H. D. Levine, and G. H. Whipple, "A Clinical Appraisal of Vectorcardiogram in Myocardial Infarction .1. Cube System," *Circulation*, vol. 24, pp. 808-&, 1961.

- [14] T. C. Chou, Masangka.Mp, R. Young, G. F. Conway, and R. A. Helm, "Simple Quantitative Vectorcardiographic Criteria for Diagnosis of Right Ventricular Hypertrophy," *Circulation*, vol. 48, pp. 1262-1267, 1973.
- [15] A. de Torbal, J. A. Kors, G. van Herpen, S. Meij, S. Nelwan, M. L. Simoons, and E. Boersma, "The electrical T-axis and the spatial QRS-T angle are independent predictors of long-term mortality in patients admitted with acute ischemic chest pain," *Cardiology*, vol. 101, pp. 199-207, 2004.
- [16] H. Yang, M. Malshe, S. T. S. Bukkapatnam, and R. Komanduri, "Recurrence quantification analysis and principal components in the detection of myocardial infarction from vectorcardiogram signals," in *Proceedings of the 3rd INFORMS Workshop on Data Mining and Health Informatics (DM-HI)*, Washington, DC, 2008.
- [17] W. Carson and Y. Z. Tseng, "Maximal Spatial St-Vector Patterns in Patients with Acute Anteroseptal Myocardial-Infarction," *International Journal of Cardiology*, vol. 43, pp. 165-173, Feb 1994.
- [18] G. E. Burch, J. A. Abildskov, and J. A. Cronvich, "Studies of the Spatial Vectorcardiogram in Normal Man," *Circulation*, vol. 7, pp. 558-572, 1953.
- [19] A. Uehata, A. Kurita, B. Takase, K. Mizuno, K. Isozima, K. Satomura, K. Arakawa, T. Shibuya, N. Aosaki, F. Osuzu, K. Hosono, H. Hayakawa, K. Munakawa, and S. Seki, "Incidences of Coronary-Artery Stenosis and Mean Qrs Vector on the Frontal Plane Vectorcardiogram in Patients with Inferior Myocardial-Infarction," *Japanese Circulation Journal-English Edition*, vol. 47, pp. 860-860, 1983.
- [20] J. N. Morgan and J. A. Sonquist, "Problems in the Analysis of Survey Data, and a Proposal," *Journal of the American Statistical Association*, vol. 58, pp. 415-434, 1963.

PART III

SIMULATION AND PROGNOSTIC MODELING

CHAPTER IX

LOCAL RECURRENCE PREDICTION IN NONSTATIONARY CHAOTIC SYSTEMS

This chapter reports a local recurrence modeling approach for state and performance predictions in complex nonlinear and nonstationary systems. Nonstationarity is treated as the switching force between different stationary systems, which is shown as a series of finite time detours of system dynamics from the vicinity of an attractor of a nonlinear process. Recurrence characteristics of the attractor are used to partition the system trajectory into multiple near-stationary segments. Consequently, piece-wise eigen analysis of ensembles in each near-stationary segment can capture both nonlinear stochastic dynamics and nonstationarities. Extensive studies using simulated and real world datasets reveal significant prediction accuracy improvements over other alternative methods.

9.1 Introduction

Complex dynamics of many real-world systems can be effectively captured using nonlinear stochastic dynamic models of the form:

$$d\underline{x} = \underline{F}(\underline{x})dt + \underline{g}(\underline{x})d\underline{\beta} \quad (\text{Eq 9-1})$$

where \underline{x} is a m -dimensional state vector, $\underline{F}(\bullet)$ is usually a nonlinear vector field, and the stochastic term $\underline{g}(\underline{x})d\underline{\beta}$ accounts for the influence of extraneous phenomena. Nonetheless,

in many real life situations, only a few process output measurements y , or coupled high dimensional measurements are available in lieu of the complete state vector \underline{x} .

In such scenarios, traditional system identification and time series prediction approaches are widely used to model the process outputs y as a linear or nonlinear function of p past values of y and q previous realizations of independent noise (shock) events ε_t . ARMA (autoregressive moving average) models assume both stationarity and linearity, while ARIMA models incorporate a simple case of nonstationarity, namely low frequency components [1]. These classical time series models cannot capture the complexities presented in nonlinear chaotic processes. Prediction based on Kalman filters tend to heavily depend on the model structure [2]. Polynomial models with global or arbitrary local support tend to be unstable and not adequate for extrapolation [3]. Neural network and sequential Bayesian models are known to need prohibitively large datasets for prediction under highly nonstationary conditions and they consume significant model training times [4]. Delay differential equations $\dot{\underline{x}}(t_n) = f(\underline{x}(t_n), \underline{x}(t_n - \tau_1), \dots, \underline{x}(t_n - \tau_k))$ work well under deterministic conditions, but they pose acute stability issues due to possible trajectory crossing under noisy conditions. Remarkably, none of the previous approaches are generally suitable for prediction under nonlinear and highly nonstationary conditions. Most of these conventional linear and nonlinear prediction approaches assume stationarity and model system dynamics by deterministic parts plus random measurement noise. The predictable deterministic parts often get distorted to some extent by time domain differencing, smoothing or frequency domain filtering. In particular, complex systems generate high-dimensional, nonlinear, nonstationary, noisy datasets with dozens to hundreds (to even thousands) of state variables. The presence of data

complexity and high level nonstationarities significantly deteriorate the traditional methods' near-term prediction accuracies.

Meanwhile, modern industries are investing in a variety of sensors and plant floor information systems to carefully monitor and manage the engineering systems including automotive assembly lines, power plants, microelectronic manufacturing system, and financial markets, etc. Large amounts of datasets and cheaper computational resources offer an unprecedented opportunity to predict manufacturing system state and performance from a nonlinear dynamic systems theoretic standpoint. Nonlinear dynamic approaches can provide a better understanding of underlying physical mechanisms, and give an advantage for the prediction of system behaviors.

The present approach exploits the inherent nonlinear stochastic dynamics of complex manufacturing systems to improve predictive capability under noisy and nonstationary conditions. Here, nonstationarity includes not just simple drifts in various statistical moments over time, but also intermittent low and high dimensional chaotic behaviors resulting from the random fluctuations of the model parameters. Central to our approach is the segmentation of global performance signature (time-series) into multiple stationary segments using recurrence analysis [5]. Stationary segmentation will lead to reduced order models that can capture the local evolution patterns (including the complexity and nonstationarities) better than any global model.

The remainder of this chapter is organized as follows: Section 9.2 reviews the relevant work of state space prediction and recurrence analysis; Research methodology is presented in Section 9.3; Section 9.4 demonstrates the simulation and real world

experiments of local recurrence prediction model; Section 9.5 concludes the reported research.

9.2 Background

Nonlinear dynamic prediction approaches rely on reconstructing the state space of a nonlinear process from the measured signals $y(t)$. Takens' embedding theorem [6] stated as follows is the theoretic base for the complex system state space reconstruction.

Takens' delay embedding theorem (1981): *Let \mathbf{M} be a compact manifold of topological dimension d . For pairs (ϕ, h) , where $\phi: \mathbf{M} \rightarrow \mathbf{M}$ is a smooth (at least C^2) diffeomorphism and $h: \mathbf{M} \rightarrow \mathbf{R}$ a smooth function, it is a generic property that the $(2d+1)$ -fold observation map $H_k[\phi, h]: \mathbf{M} \rightarrow \mathbf{R}^{2d+1}$ defined by $\underline{x} \mapsto (h(\underline{x}), h(\phi(\underline{x})), \dots, h(\phi^{2d}(\underline{x})))$ is an immersion (i.e. H_k is one-to-one between M and its image with both H_k and H_k^{-1} differentiable).*

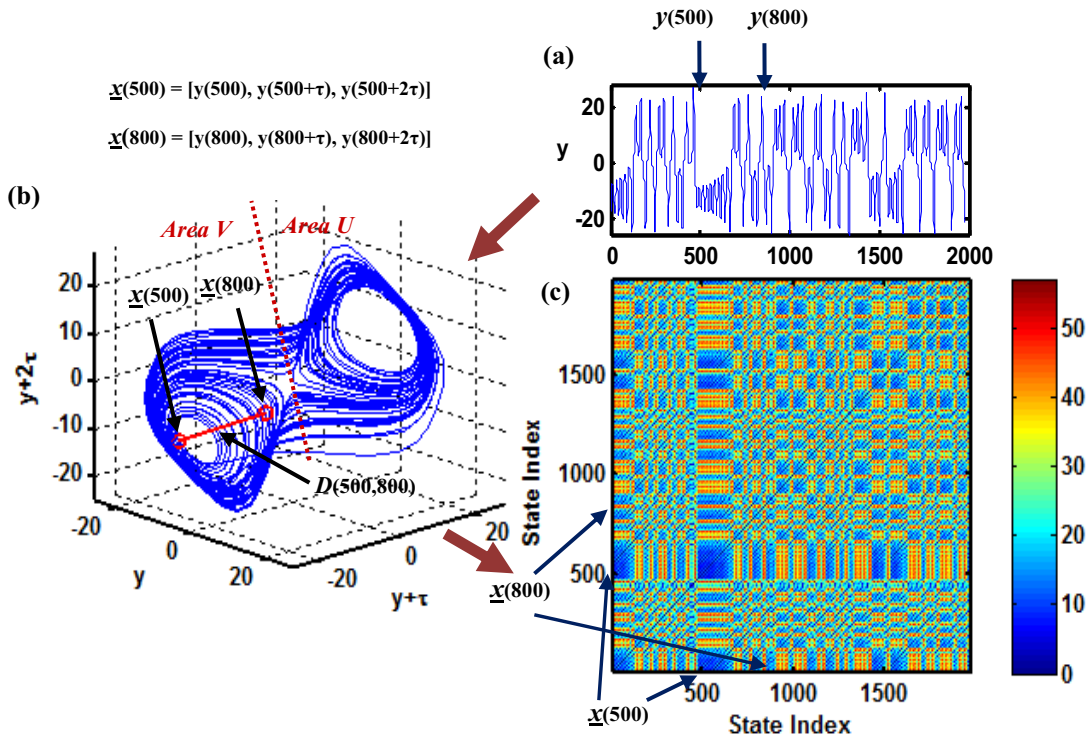


Figure 9.1 Graphical illustration of the relationship among Lorenz time series, attractor and recurrence plot

Takens' delay embedding theorem shows the system dynamics can be adequately reconstructed by using the time-delay coordinates of the individual measurements because of the high dynamic coupling existing in physical system. For discrete time series y (see Figure 9.1 (a)), state vector \underline{x} (Figure 9.1 (b)) is reconstructed using a delay sequence of points in $\{y(t_n)\}$ as,

$$\underline{x}(t_n) = [y(t_n), y(t_n+\tau), y(t_n+2\tau), \dots, y(t_n+(m-1)\tau)] \quad (\text{Eq 9-2})$$

where m is the embedding dimension ($m \geq 2d+1$) and τ is the time delay. The optimal sufficient embedding dimension m to unfold the attractor is determined by false nearest neighbor method [7]. The mutual information function [8] is used to minimize both nonlinear dynamic and linear correlations for the choice of optimal time delay τ .

System dynamics often manifest in the vicinity of an attractor \mathbf{A} (e.g., Lorenz attractor [9] shown in Figure 9.1 (b)), which is an invariant set defined in an m -dimensional state space. Lorenz attractors show unique topological patterns where trajectory evolution switches between two cycle areas (area U and area V). State space prediction approaches look for the relationships of the present system state \underline{x} (a sequence of points in the measured time series) to the nearby states in the embedding space and their evolutions. It has been shown that global nonlinear dynamics can be synthesized by multiple linear components, each of which shares the same local evolutions in an attractor's vicinity [10]. The digressions of local evolution patterns, specifically, finite time detours from an attractor's vicinity, are treated as nonstationarities. The aforementioned nonstationarity may result from chaos, linear model switching or

parameter fluctuations (dynamic noise) and/or many forms of transient and intermittent behaviors.

Despite high levels of nonlinearity, stochasticity and nonstationarity in the complex system behaviors, local evolution of system state space often exhibits recurrence characteristics as stated in the following theorem.

Poincare recurrence theorem (1890) [11]: *Let T be a measure-preserving transformation of a probability space (\mathbf{A}, μ) , and let $\Omega \subset \mathbf{A}$ be a measurable set. Then for any $J \in \mathbb{N}$, $\mu(\{\underline{x} \in \Omega \mid \{T^j(\underline{x})\}_{j \geq J} \subset \mathbf{A} \setminus \Omega\}) = 0$.*

Poincare recurrence theorem implies that if one has a measure preserving transformation, the trajectories eventually reappear at neighborhood Ω of former points with probability one. A recurrence plot (see Figure 9.1 (c)) is used to identify the aforementioned nonlinear and nonstationary structures in the state space. It delineates the distances of every point $\underline{x}(t_i)$, the state vector realized at time t_i , to all the others in the reconstructed state space, i.e., $D(t_i, t_j) := \Theta(\|\underline{x}(t_i) - \underline{x}(t_j)\|)$, where $\|\cdot\|$ is a distance measurement (e.g., the Euclidean norm) and $\Theta(\cdot)$ is the color code that maps the distance to a color scale [12]. As shown in Figure 9.1, the distances between the 500th and 800th points in the state space is shown as a color code at the coordinates (500,800) and (800, 500) of the recurrence plot. If the color code at the recurrence plot is blue, then the points are located close to each other in the state space, and if the color code is red, the points are located farther apart. Thus, a recurrence plot represents the topological relationships existing in the m -dimensional state space in the form of 2D images. The ridges locate the nonstationarities and the switchings between local behaviors [13], for e.g., the system

evolves from one behavior (area U) to the other (area V) (see Figure 9.1). The separations between dark diagonal lines (along 45° degree) indicate the time periods between the recurring system behaviors over certain time segments. Recurrence-based methods have of late shown potential for representation and de-noising of measurements from complex systems [14, 15]. This present work is one of the first investigations into the use of recurrence analysis for state space prediction in highly nonstationary conditions.

9.3 Local attractor topology analysis

The present local recurrence modeling approach is built on a premise, heretofore unexplored, that despite high levels of nonstationarity, system dynamics are structurally stable and nonstationarities are treated to cause finite time detours from the attractor's vicinity. Therefore, local recurrence characteristics, exhibited over certain time segments, are leveraged to delineate the various local evolution patterns and nonstationary regimes (finite-time detours) from attractor \mathbf{A} and develop compact local models.

As summarized in Figure 9.2, central to our approach is the partitioning of a measured time series into multiple near-stationary segments. Every strand of the system trajectory within each segment bears a similar evolution pattern. Therefore stationary assumptions hold therein within each segment. Pattern analysis and segmentation are performed on a recurrence plot $D(t_i, t_j)$ to identify these time segments. This segmentation leads to reduced order models that can effectively capture the local evolutions of dynamic system's state space (including complexity and nonstationarity) better than with any stationary model. For illustration purposes, let us consider a Lorenz attractor shown in Figure 9.1 (b). All trajectories emerging from a region (e.g., U) have a similar local

evolution pattern. However, these local evolution patterns can be vastly dissimilar for the trajectories emerging from two arbitrary regions, say, U and V . Local dynamics within each of these regions can be simplified as unstable periodic orbits (UPOs) defined about certain fixed points, and the global dynamics can be derived from concatenating the trajectories from each of these regions as stated in the following.

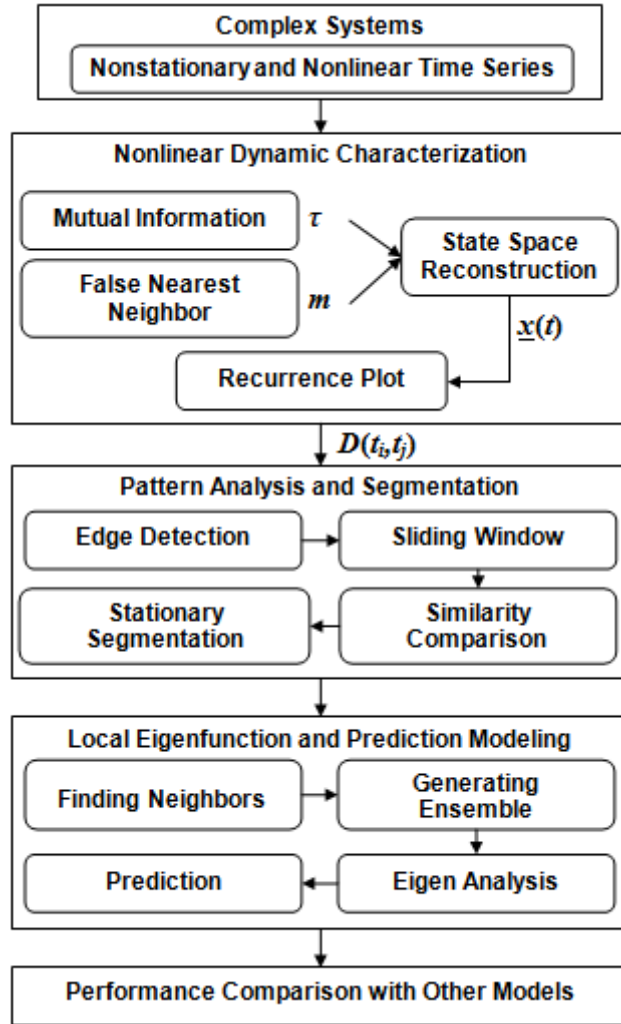


Figure 9.2 Overall framework of local recurrence prediction model

Proposition 1: *Dynamics about an attractor of complex nonlinear system can be approximated by linear affine systems linked by switching laws, i.e.,*

$$\dot{\underline{x}} = F(\underline{x}) \approx \sum_i f_i [s(\underline{x}) - \gamma_i] A_i (\underline{x} - \underline{x}_i) \quad (\text{Eq 9-3})$$

where A_i defines the local linear dynamics of affine subsystems, $s(\bullet)$ defines the switching surface, $f_i[\bullet]$ is a Boolean switching function that transits the dynamics among multiple linear or affine systems, each defined over fixed points \underline{x}_i , and γ_i determine the locations of the switching surface [10].

It has recently been shown that the system trajectories within a region i locally evolve as unstable periodic orbits defined about certain saddle or foci type fixed points \underline{x}_i [10]. Such local dynamics for region i can be captured at a specified parameter setting using a linear system of the form $\dot{\underline{x}}^{(i)} = A_i(\underline{x} - \underline{x}_i)$.

The system trajectories in an attractor can be derived from solving this piecewise affine model. The global trajectories switch between the multiple local patterns as they evolve about saddle type fixed points, i.e., $\underline{x} = \underline{x}^{(1)} \oplus \underline{x}^{(2)} \oplus \dots \oplus \underline{x}^{(z)}$. For instance, a Lorenz attractor may be approximated using piecewise affine model consisting of two linear components. The Jacobians of the respective linear/affine part are evaluated about the corresponding saddles or foci type fixed points [10]. The saddle type fixed points help determine the boundaries of the orbits defined about the foci.

Switching from one piecewise affine system to another takes place whenever the system trajectories shift from exhibiting an unstable periodic behavior about a fixed point to the other. The Boolean functions $f_i[\bullet]$ is defined as following:

$$f_i[s(\underline{x}) - \gamma_i] = \begin{cases} 1, & s(\underline{x}) - \gamma_i \geq 0 \\ 0, & s(\underline{x}) - \gamma_i < 0 \end{cases} \quad (\text{Eq 9-4})$$

This function is designed to make sure that only one of them equals unity at a given location γ_i . A very minor perturbation in the states can switch the evolution path from one region to the other. The points forming the transition states are rare or far from the local regions U and V , i.e., $\{\underline{x}(b_i)\}_{i=1}^B \subseteq \partial U \cap \partial V$. Within regions U and V , the trajectory flow

lines are laminar, and the divergence rate between closeby trajectories is close to zero. The transition points are marked by significant changes in the divergence rates.

Recurrence patterns can be used to systematically identify the transitions. A recurrence plot is symmetric about the diagonal, and patterns are equally distributed along horizontal and vertical directions. If the distribution of states $\underline{x}(t)$ in the embedding space is homogeneous, then the recurrence plot is also homogeneous. The presence of such homogenous recurrence patterns implies a typically stationary process which has short relaxation times in comparison with time spanned by recurrence plot. Interruptions in the homogenous patterns indicate that some states over these times $\{\underline{x}(b_i)\}_{i=1}^B$ are not interior points of local sets U or V . Those states correspond to transition points between various local homogeneous sets [13]. Hence, the disruptions in the recurrence plot can be used to detect finite time detours from local vicinity of attractors, namely nonstationarities.

The transition points between various local homogeneous sets, resulting from the underlying chaotic dynamics and/or nonstationarities, can be detected by applying the Sobel operator I_u and I_v on recurrence plot $D(t_i, t_j)$. Where I_u and I_v are defined in terms of a 3×3 matrix pair

$$I_u = \begin{bmatrix} +1 & 0 & -1 \\ +2 & 0 & -2 \\ +1 & 0 & -1 \end{bmatrix} \quad I_v = \begin{bmatrix} +1 & +2 & +1 \\ 0 & 0 & 0 \\ -1 & -2 & -1 \end{bmatrix} \quad (\text{Eq 9-5})$$

The intensity gradient magnitude $G_{u,v}$ at a point (t_i, t_j) in the recurrence plot is given by

$G_{u,v} = \sqrt{G_u^2 + G_v^2}$, and G_u and G_v are the horizontal and vertical gradient estimations defined as following:

$$G_u = I_u * D \text{ and } G_v = I_v * D \quad (\text{Eq 9-6})$$

where $*$ is the convolution or vector product operation.

Since $I_u = I_v^T$ and recurrence plot is symmetrical, any of the three gradient measurements $|G_u|$, $|G_v|$ or $G_{u,v}$ can be equally used to extract the transition boundaries. From equation (3), we can see that Sobel operators are equivalent to 2-D high pass filters. It can compactly capture the high frequency nonhomogeneous patterns better than the original recurrence plots.

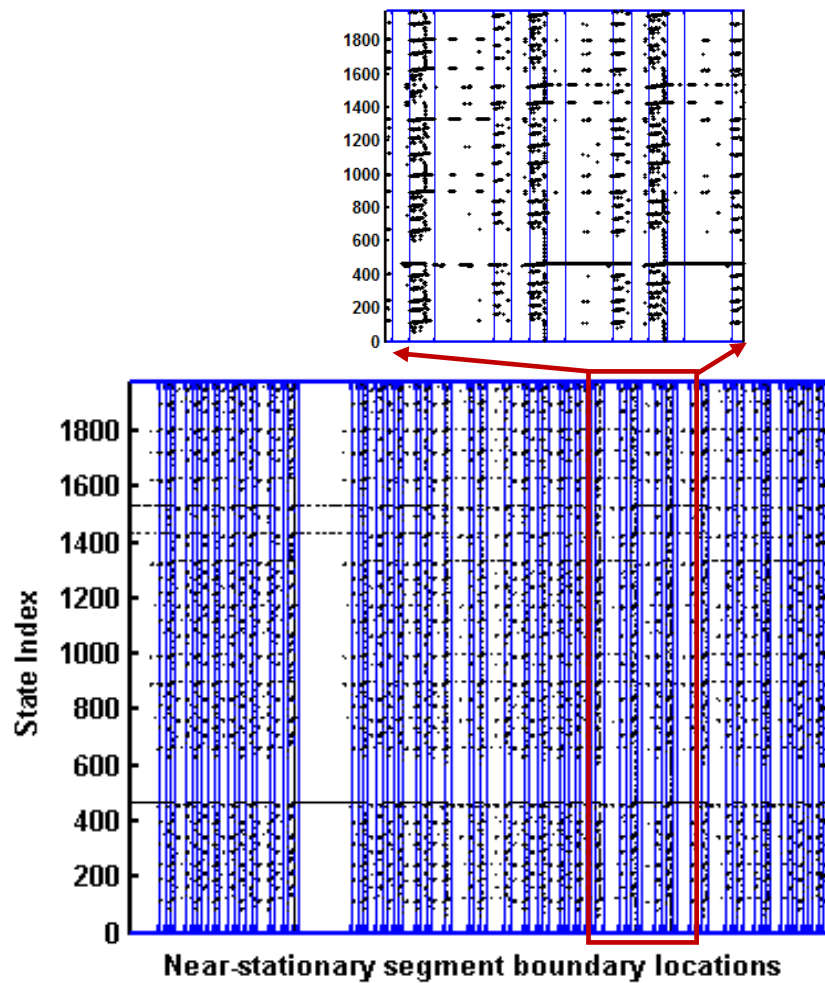


Figure 9.3 Edge detection in a Lorenz recurrence plot

Thus, by applying the Sobel operator to recurrence plots, we reduce the amount of data to be processed, filter out information that may be regarded as less relevant, and

preserve the important nonhomogeneous structural properties. Boundaries of linear and stationary segments are shown as horizontal and vertical edges in the $G_u(t_i, t_j)$ image. Histogram similarities of adjacent sliding windows are compared to locate these boundaries. Such edge detection methods give prominence to high frequency components in the image, for e.g., the boundaries of objects, the boundaries of surface markings or curves that correspond to discontinuities in surface orientation. The length of each segment depends on the local divergence rate of trajectories emanating from a given neighborhood. As shown in Figure 9.3, the transition states or saddle points $\{\underline{x}(b_i)\}_{i=1}^B$ are identified in the Lorenz recurrence plot (also refer to Figure 9.1). The enlarged portion in Figure 9.3 shows the homogeneity of point distributions in each segment.

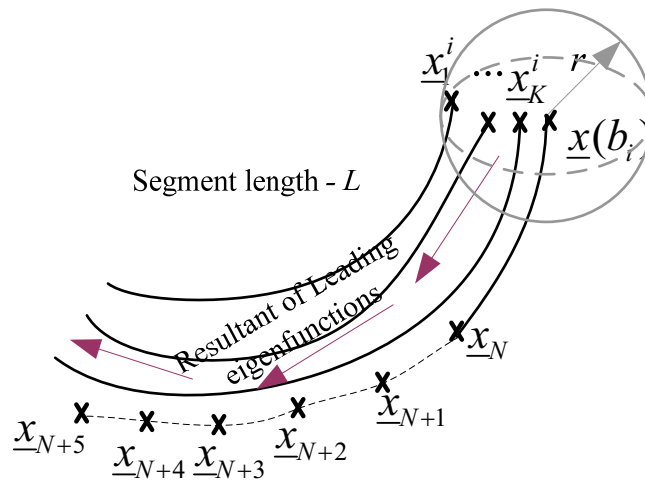


Figure 9.4 Local eigen prediction model from ensembles within a stationary segment

In our approach, ensembles are generated within a near-stationary segment to provide a more homogeneous set for eigen analysis. Therefore eigen representation can capture the essential dynamics without being influenced by nonstationarities in the state space. The local eigen representation of segment i uses the K ensembles extracted from the nearest neighbors $\{\underline{x}_k^i\}_{k=1}^K$ of a segment's starting point $\underline{x}(b_i)$ (see Figure 9.4). The ensembles of length L_i are collected from the historical data such that $K+L_i < N$, the

length of time series. All the ensembles are generated from the realized states, and consequently, the model is causal. Intuitively, each eigenfunction estimated from those ensembles $\alpha(\bullet)$ captures the shape of a specific mode of variation (roughly, a degree of freedom) within the segment [16]. The leading variation modes of a system with d active degrees of freedom can be obtained as the projection of the ensembles onto the space spanned by $\alpha_1(\bullet)$, $\alpha_2(\bullet)$, ..., $\alpha_d(\bullet)$. Thus, the local eigen representation captures major variations of the ensembles as well as nuances of the ensembles in each stationary segment, and it is extrapolated along the leading eigen directions to predict the future states (see Figure 9.4). Whenever the system evolves (due to chaos) or drifts (due to nonstationarity) into a different regime, a new local eigen representation is established to capture the new patterns. The advantage of local representation is evident from the following result.

Proposition 2: *Local eigen (L_2 -optimal) representations obtained from segmenting a chaotic attractor are more parsimonious than a global ensemble representation.*

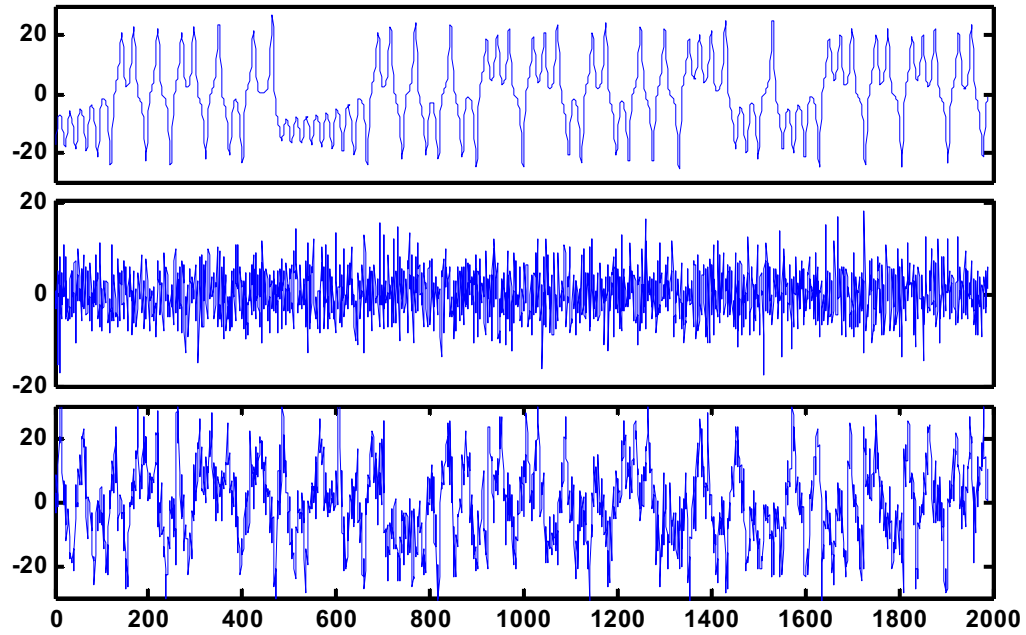
More often than not, the operators A_i defined in equation (1) either do not have a full rank, or have a highly ill-conditioned eigen system where one or more eigen values are significantly lower than the rest. For example, in affine approximation of Lorenz-like systems [10], the local eigenvectors of A_i 's tend to be significantly smaller along the directions normal to the planes of the "butterfly wings," and generally speaking, along the so-called nullclinic directions [10], of a Lorenz attractor compared to the other orthogonal directions. The eigen directions that lie along the nullclinic directions, and hence the signal components projected along these directions, can be ignored. Therefore much of the salient evolutions about a certain fixed point on the attractor can be captured

by considering very few eigen basis functions. Consequently, the local representations, defined between two successive “switching points,” will be more compact than a representation based on global ensembles. From a noise reduction standpoint, consideration of fewer basis functions implies that signal energy is concentrated along limited number of directions.

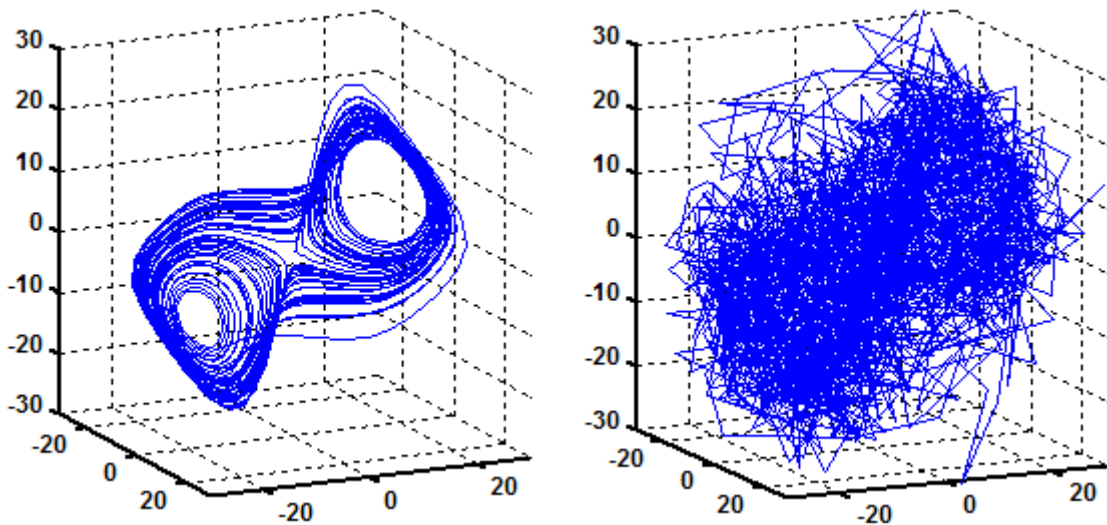
9.4 Simulation experiment results

In this section, we report our evaluation of the performance of local recurrence model using both simulated and real world datasets. The prediction results are compared to traditional time series models (e.g. ARMA) and some of the well known nonlinear models (e.g. polynomial, neural network, radial basis function (RBF)). It may be noted that few if any of the previous approaches is suitable for prediction under highly nonstationary and noisy conditions. Polynomial models and delay differential equation models are not included for comparison because the experimental results are observed to easily diverge from or fail to predict the actual system behaviors. Only radial basis function models provided some promising predictability. However the local recurrence model is able to separate the similar evolution patterns of chaotic systems under highly nonstationary conditions.

The following two scenarios are simulated towards evaluating the local recurrence modeling approach: (1) nonlinear and stationary signals generated by contaminating the first component of Lorenz attractor [9] with three different noise levels (signal noise ratios (SNR) between 7.37dB-21.35dB); (2) nonlinear and nonstationary signals obtained by dividing the contaminated Lorenz time series into several segments and randomly rearranging the sequence of these segments (SNR varied between 7.37dB-21.35dB).



(a)



(b)

Figure 9.5 (a) top - original Lorenz time series, middle – random Gaussian noise, bottom – random permuted Lorenz time series contaminated by noise; (b) reconstructed noise-free Lorenz attractor vs. random permuted Lorenz attractor contaminated by noise

Figure 9.5 (a) depicts the comparisons between original Lorenz time series and the randomly permuted noisy Lorenz time series. As illustrated in the Figure 9.5 (a) bottom plot, the structures of noise-free Lorenz time series are demolished by random noise and artificial generated nonstationarity. Figure 9.5 (b) evidently shows that it is difficult to

identify the clean patterns in the random permuted and noise contaminated Lorenz attractor. The nonstationarity and noise in the simulated data pose additional issues for the state space prediction. Local recurrence model delineates the near-stationary segments and suppresses noise components to track the relevant variations underlying the process and not the extraneous phenomena. The prediction results are compared at multiple locations to those from RBF and two classical time series models: ARMA(1,0) - a prediction model currently used in the practice, and ARMA(3,3) - the “optimal” model form emerged from a classical system identification standpoint.

Figure 9.6 shows the comparisons of prediction error statistics for noisy Lorenz time series (signal range: -25.25~27.25) in scenario (1). It may be noted that ARMA(1,0) step one prediction errors vary from 2.48~7.38 under three noise levels, ARMA(3,3) from 1.75~7.06, and local recurrence model from 1.93~6.25. Here, the aforementioned prediction error statistics are calculated in terms of root mean square errors between actual x_i and predicted value \tilde{x}_i at N prediction locations. In noise level 1, step one prediction errors are relevant low with reference to the signal range, and comparable for ARMA and local recurrence models. However, with the increase of noise levels, ARMA prediction models become inferior to the local recurrence model. For instance, the local recurrence model’s one step prediction RMS errors are lower by 12% (around 0.81~1.13) than both ARMA models in noise level 3 (see Figure 9.6). In addition, ARMA models become increasingly worse (around 0.75~5.06 higher RMS errors) than local recurrence model for multiple step-ahead (≥ 2) predictions under all three noise levels. This is because linear models cannot capture the chaotic dynamics underlying the Lorenz time series.

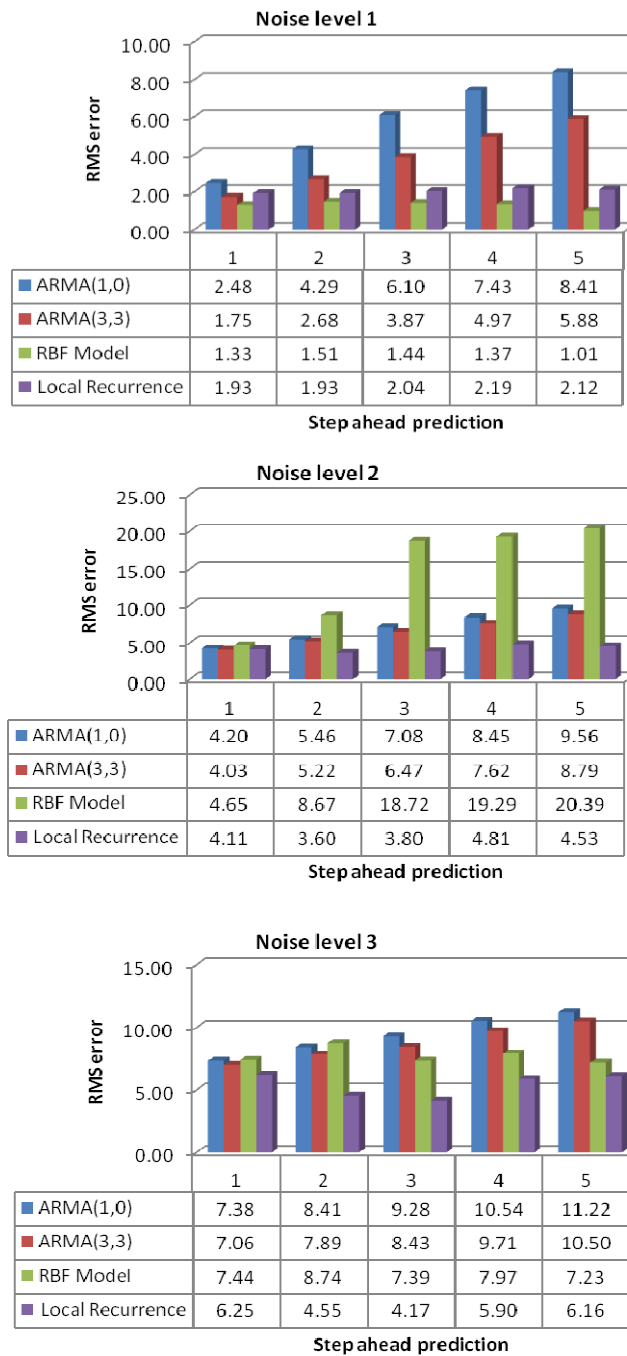


Figure 9.6 Five step prediction RMS error comparisons for Lorenz time series under different noise levels with various prediction models (ARMA(1,0), ARMA(3,3), RBF model and local recurrence model)

Both RBF and the local recurrence model can capture the system nonlinearity, but RBF model does not consider nonstationarity and is very sensitive to stochastic conditions. The prediction errors from the RBF models progressively deteriorate with an

increase of noise levels, for e.g., step one prediction errors are elevated from 1.33 (noise level 1) to 7.44 (noise level 3). The deterioration rate of RBF model is found to be higher than local recurrence model which is from 1.93 (noise level 1) to 6.25 (noise level 3). In noise level 3, local recurrence model five step prediction RMS errors vary from 4.17 to 6.25, on the other hand, RBF is from 7.23 to 8.74 (see Figure 9.6). The local recurrence model is shown to perform better under highly noisy conditions. It may also be noted that the prediction errors of the local recurrence model do not increase with prediction steps, for example, ARMA(1,0) prediction errors are increased from 4.20 to 8.45 with prediction steps in noise level 2, while variations of the local recurrence model (between 3.60 and 4.81) do not follow with prediction steps (see Figure 9.6). This is because eigen analysis of ensembles in a near-stationary segment guarantees that predictions always lie within the bounds of the reconstructed attractor. In contrast, RBF models depend on the size of training datasets. Multiple step-ahead predictions can sustain excessive divergence and instability because of the stochastic conditions and/or accumulated iterated prediction errors. As shown in noise level 2 in Figure 9.6, the RBF model is unstable and prediction results diverge with the steps. In a nutshell, Figure 9.6 shows that the local recurrence model can capture the nonlinearity as well as stochasticity in this case.

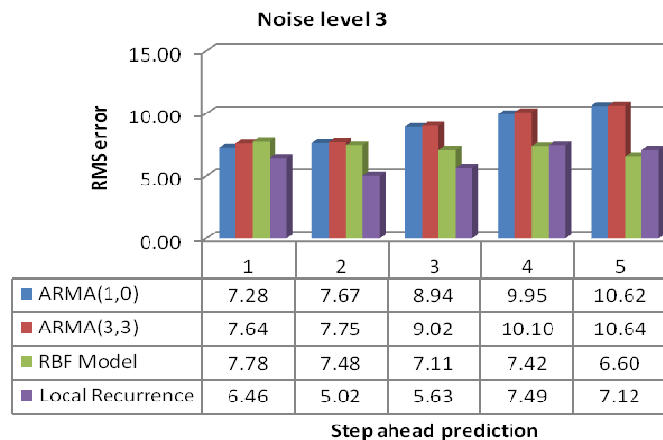
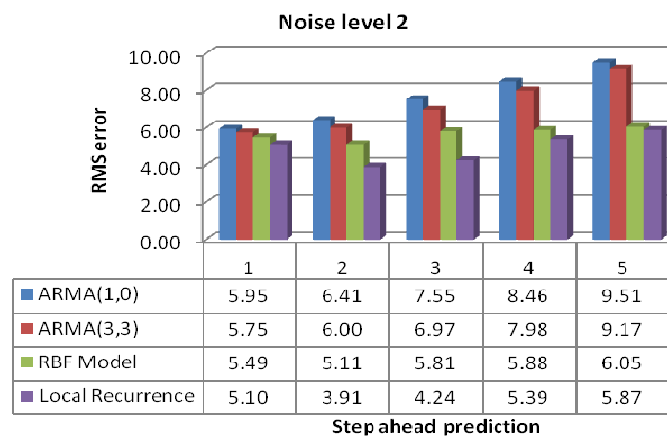
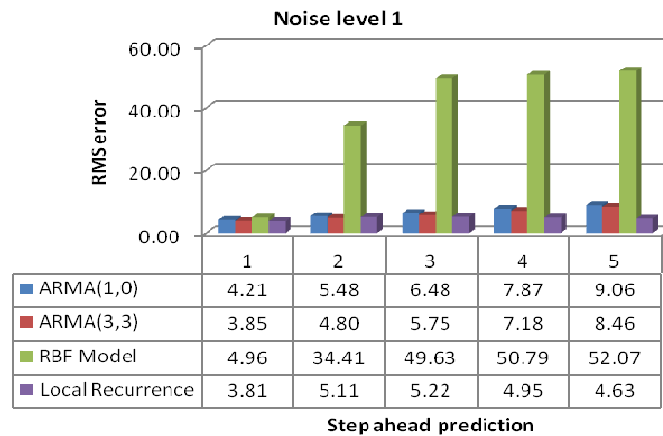


Figure 9.7 Five step prediction RMS error comparisons for randomly permuted Lorenz time series under different noise levels with various prediction models (ARMA(1,0), ARMA(3,3), RBF model and local recurrence model)

Figure 9.7 shows the prediction error statistics in scenario (2) – randomly permuted noisy Lorenz time series. The random permutation in arbitrarily lengths will

generate finite time detours from the vicinity of an attractor. This type of nonstationarity is quite different from the commonly considered seasonal trends. In this experiment, the local recurrence model is shown to significantly outperform all the other three models under all three noise levels. For five step prediction RMS errors under three noise levels, ARMA(1,0) ranges from 4.21 to 10.62, ARMA(3,3) from 3.85 to 10.64, RBF from 4.96 to 52.07, and the local recurrence model from 3.81 to 7.12. Moreover, noise level 1 plot (see Figure 9.7) reveals that nonstationarity increases the probability to drive RBF model unstable and divergent for more than one step predictions.

9.5 Summary

The present work is one of the first attempts to use recurrence analysis for prediction in the presence of generic forms of nonstationarities. It combines the principles of statistical estimation with dynamic systems theory. Most of current applications threshold recurrence plots for the exploration of nearest neighbors $\tilde{D}(t_i, t_j) := \Theta(\|\underline{x}(t_i) - \underline{x}(t_j)\| < r)$. In contrast, the proposed approach exploits the topological irregularity information contained in recurrence plots, and uses edge detection and pattern matching methods for stationary segmentation. The transition states that occur when the system behaviors are switched have found to be effectively captured. Experimentations using simulated datasets reveal the superiority of local recurrence model over other alternative models for nonlinear stochastic systems under transient conditions. It is conceivable that such a method can be applied to improve predictability of similar complex physical systems under nonstationary conditions.

9.6 References

- [1] R. H. Shumway and D. S. Stoffer, *Time Series Analysis and Its Applications: With R Examples*: Springer, 2006.
- [2] L. Ljung, *System Identification - Theory For the User*. N.J: PTR Prentice Hall, 1999.
- [3] M. Small, K. Judd, and A. Mees, "Modeling continuous processes from data," *Physical Review E*, vol. 65, p. 046704, 2002.
- [4] A. Freking, W. Kinzel, and I. Kanter, "Learning and predicting time series by neural networks," *Physical Review E*, vol. 65, p. 050903, 2002.
- [5] S. T. S. Bukkapatnam, S. R. Kumara, and A. Lakhtakia, "Local eigenfunctions-based suboptimal wavelet packet representation of contaminated chaotic signals," *IMA Journal of Applied Mathematics*, vol. 63, pp. 149-160, 1999.
- [6] F. Takens, *Detecting strange attractors in turbulence*, In *Lecture notes in mathematics* vol. 898: Springer, Berlin, 1981.
- [7] M. B. Kennel, R. Brown, and H. D. I. Abarbanel, "Determining embedding dimension for phase-space reconstruction using a geometrical construction," *Physical Review A*, vol. 45, p. 3403, 1992.
- [8] A. M. Fraser and H. L. Swinney, "Independent coordinates for strange attractors from mutual information," *Physical Review A*, vol. 33, p. 1134, 1986.
- [9] E. N. Lorenz, "Atmospheric predictability as revealed by naturally occurring analogues," *Journal of Atmosphere Sciences*, vol. 26, pp. 636-646, 1969.
- [10] F. V. A. Gleison, L. Christophe, and A. Luis Antonio, "Piecewise affine models of chaotic attractors: The Rossler and Lorenz systems," *Chaos: An Interdisciplinary Journal of Nonlinear Science*, vol. 16, p. 013115, 2006.

- [11] A. Katok and B. Hasselblatt, *Introduction to the Modern Theory of Dynamical Systems*, 1 ed.: Cambridge University Press, 1995.
- [12] J.-P. Eckmann, S. O. Kamphorst, and D. Ruelle, "Recurrence plots of dynamical systems," *Europhys Lett*, vol. 4, pp. 973-977, 1987.
- [13] N. Marwan, M. Carmen Romano, M. Thiel, and J. Kurths, "Recurrence plots for the analysis of complex systems," *Physics Reports*, vol. 438, pp. 237-329, 2007.
- [14] L. Matassini, H. Kantz, J. Holyst, and R. Hegger, "Optimizing of recurrence plots for noise reduction," *Physical Review E*, vol. 65, p. 021102, 2002.
- [15] R. Hegger, H. Kantz, and L. Matassini, "Denoising Human Speech Signals Using Chaoslike Features," *Physical Review Letters*, vol. 84, p. 3197, 2000.
- [16] H. Yang, S. T. Bukkapatnam, and R. Komanduri, "Nonlinear adaptive wavelet analysis of electrocardiogram signals," *Physical Review E (Statistical, Nonlinear, and Soft Matter Physics)*, vol. 76, p. 026214, 2007.

CHAPTER X

RADIAL BASIS FUNCTION SIMULATION MODELING OF VCG SIGNALS

This chapter will introduce an approach to construct a reasonable data-driven model for the analysis of heart system using heart monitoring signals (VCG and ECG). Such a heart model can help us gain a deeper understanding of underlying heart dynamics and explore the relationship among those signals. Moreover this data-driven model can be used to simulate the heart electric activities under a specific disease, and it will greatly facilitate the further research of cardiac diseases.

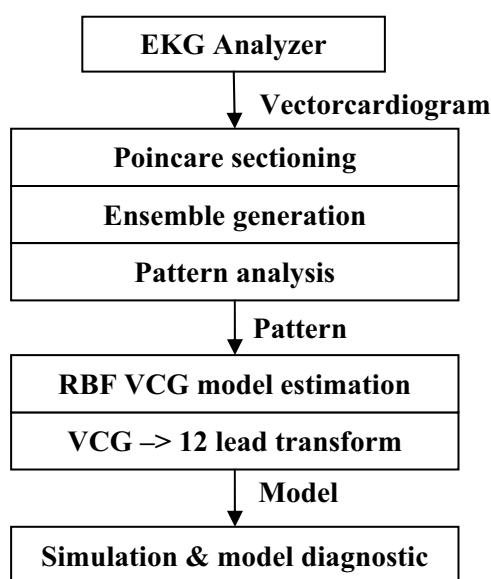


Figure 10.1 Overall framework of RBF simulation model of VCG signals

As shown in Figure 10.1, this chapter presents an approach to model and simulate the vectorcardiogram (VCG) and standard 12-lead electrocardiogram (ECG) using radial basis functions uniformly distributed along the VCG trajectory. In the first step, the

ensembles will be extracted by Poincare sectioning the VCG trajectory, and they will be aligned to the interval $[0, 2\pi]$ for the pattern analysis. Then we use the least square fit procedure to fit a Radial Basis Function (RBF) network structure to the extracted ensembles. The well trained RBF network model will provide the closely approximate of the real VCG data and share the similar 3D VCG trajectories. The standard 12 lead ECG signals are derived from VCG by transformation, and the transformation matrix can either use the famous Dower matrix [1] or be estimated from the experiment data [2-4]. Finally, the simulation model is evaluated and compared to the real experiment data in the time domain, frequency domain, and the recurrence quantification plots.

10.1 Poincare sectioning of vectorcardiogram

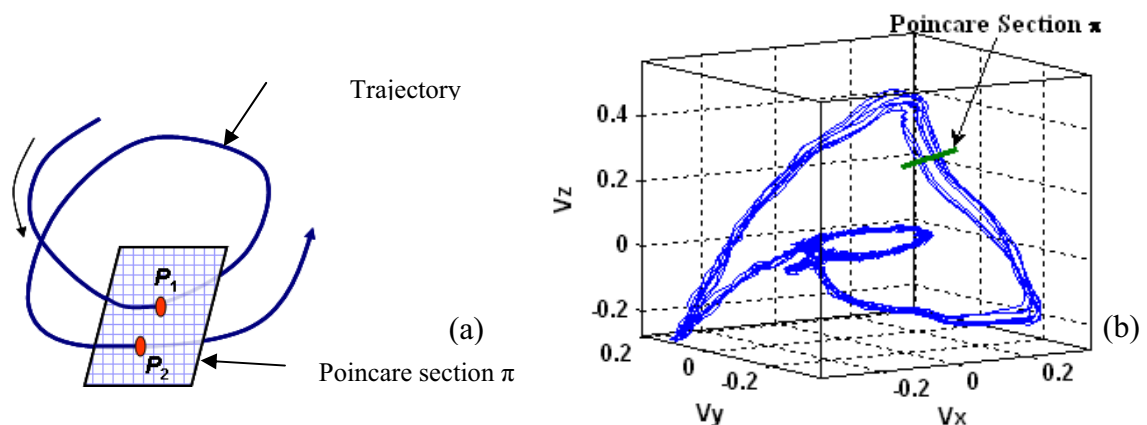


Figure 10.2 (a) An illustration of trajectories of an attractor intersecting a (planar) Poincare section; (b) Poincare sectioning of VCG trajectory

Poincare section is a d_E-1 dimensional hyperplane intersecting with the phase space trajectories (see Figure 10.2 (a)). The recurrence property of a chaotic attractor \mathbf{A} shows that for every $\varepsilon < 0$ and almost every $\underline{x}(0) \in \mathbf{A}$, $\exists t > 0$ such that $\|\underline{x}(0) - \underline{x}(t)\| < \varepsilon$, in effect, the trajectories with an attractor remain bounded. Those points P_i , $i = 1, 2, \dots$ at which the trajectory intersects the Poincare section follow a return map. For strictly

periodic trajectory, the points $P_i, i = 1, 2, \dots$ will overlap (i.e., $\varepsilon \equiv 0$) such that the duration between P_i to P_{i+1} along the trajectory constitutes the period.

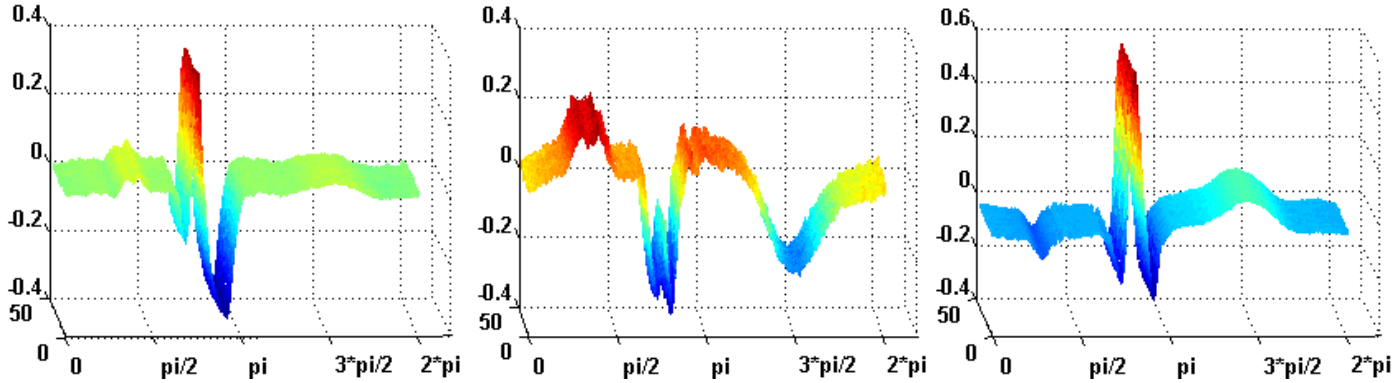


Figure 10.3 X, Y and Z ensemble components extracted from the Poincaré sectioning of VCG trajectory

For near-periodic signals, such as VCG, each strand emanating from a Poincaré section intersection point P_i and lasting approximately till the next intersection P_{i+1} along the trajectory may be treated as a realization of a stochastic process from an invariant probability space [5] (see Figure 10.2 (b)). Due to heart rate variability, some ensembles move faster, i.e., the two successive intersections occur over shorter intervals, compared to the others [6]. In this chapter, all the extracted ensembles will be aligned in the time interval $[0, 2\pi]$ (see

Figure 10.3), and the heartbeat variations will be simulated as a Weibull distribution as shown in the following section 10.2.

10.2 Heart rate variability

The variations of RR interval in the ECG/VCG time series produce the well-known heart rate variability. It has long been understood that a metronomic heart rate is

pathological, and that the healthy heart is influenced by multiple neural and hormonal inputs that result in variations in interbeat (RR) intervals, at time scales ranging from less than a second to 24 hours [7]. There is evidence that the underlying heart beat dynamics may have a multi-fractal temporal structure [8]. Heart rate variability analysis has been shown to provide an effective evaluation of cardiac disease such as different stages in the atrial fibrillation [9].

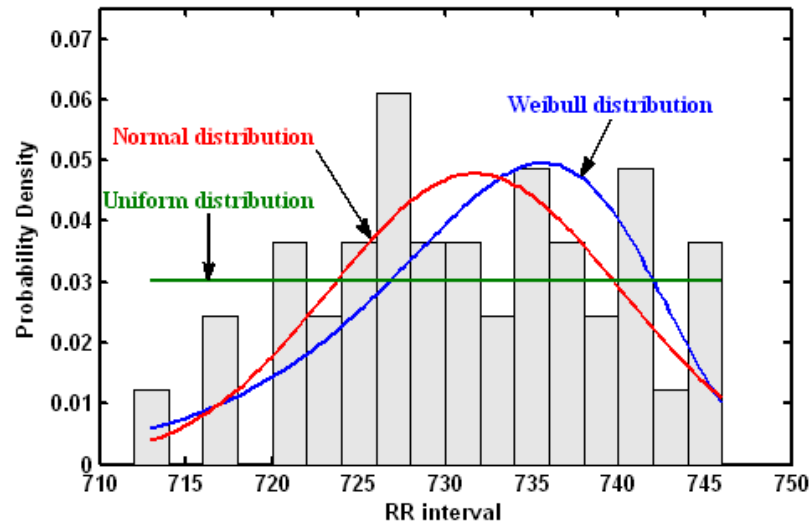


Figure 10.4 Weibull distribution fitting of RR interval time series

The complex interdependencies of heart beat variations at different scales make it difficult to model the RR interval time series, and each recording in the PTB database has less than 120 heart beats. Therefore, this chapter will only simulate the heartbeat variations as a Weibull distribution.

The Weibull distribution can mimic the behavior of other statistical distributions such as the normal and the exponential [10]. The Probability Density Function PDF associated with the Weibull distribution is:

$$f(x) = \left[\frac{b}{\theta} \left(\frac{x}{\theta} \right)^{b-1} \right] \exp \left\{ - \left(\frac{x}{\theta} \right)^b \right\} \quad (\text{Eq 10-1})$$

And the associated Cumulative Distribution Function (CDF) is a stretched exponential:

$$F(x) = 1 - \exp\left[-\left(\frac{x}{\theta}\right)^b\right] \quad (\text{Eq 10-2})$$

Where b is the Weibull slope, also referred to as the “shape parameter”, and θ is the characteristic value, also referred to as the “scale parameter”. The Weibull distribution is fitted into the heartbeat time series extracted from the Poincare sectioning of vectorcardiogram trajectories (see Figure 10.4), and it was found to yield better distribution evaluation than normal and uniform distribution. The estimated parameters b and θ will be used for the simulation of RR interval in the later section.

10.3 Research methodology

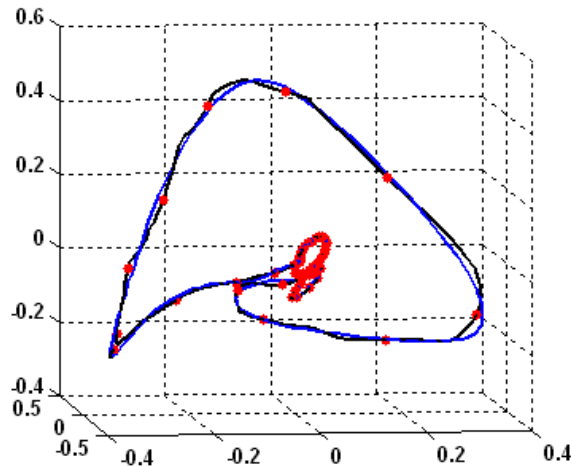


Figure 10.5 Uniform distributed radial basis function centers along VCG trajectory

The modeling of vectorcardiogram is that given N time vectors in $\mathfrak{R}^1: t^1, \dots, t^N$, and their corresponding target values in $\mathfrak{R}^3: y^1, \dots, y^N$, we are seeking a projection $h: \mathfrak{R}^1 \rightarrow \mathfrak{R}^3$, so that $\forall 1 \leq i \leq N, h(t^i) = y^i$ using the radial basis function network. The basis functions are using Gaussian functions, and the number of basis functions may be selected as N for the exact interpolation [11, 12]. However, this might lead to poor and complex results for new vectors by overfitting the data. For a compact solution with good generalization, the number of basis functions used in the VCG model is reduced from N to M ($M \ll N$) (see

Figure 10.5). The training vectorcardiogram (VCG) data is from the ensembles extracted from the Poincare sectioning.

The output of the VCG RBF network model is given by

$$y = \sum_j w_j \varphi_j(t) \quad (\text{Eq 10-3})$$

$$\varphi_j(t) = \exp(-\|t - c_j\| / \sqrt{2\sigma^2}) \quad (\text{Eq 10-4})$$

where c is the centre of the radial basis function j , t is the input data, and $\|t - c_j\|$ is the measure of the distance of the point from the radial centre, also called the *Euclidean* distance. From Eq 10-4, we can make the basis matrix G for all the centres ($j = 1, 2, \dots, M$), weight matrix W and target matrix V_N as following:

$$G = \begin{bmatrix} \varphi_1(t_1) & \varphi_1(t_2) & \cdots & \varphi_1(t_N) \\ \varphi_2(t_1) & \varphi_2(t_2) & \cdots & \varphi_2(t_N) \\ \vdots & \vdots & \vdots & \vdots \\ \varphi_M(t_1) & \varphi_M(t_2) & \cdots & \varphi_M(t_N) \end{bmatrix} \quad M \times N \quad t \in [0 \quad 2\pi] \quad (\text{Eq 10-5})$$

$$W = \begin{bmatrix} w_{11} & w_{12} & w_{1M} \\ w_{22} & w_{22} & w_{2M} \\ \vdots & \vdots & \vdots \\ w_{3M} & w_{3M} & w_{3M} \end{bmatrix} \quad 3 \times M \quad (\text{Eq 10-6})$$

$$V_N = \begin{bmatrix} v_{x1} & v_{x2} & \cdots & v_{xN} \\ v_{y1} & v_{y2} & \cdots & v_{yN} \\ v_{z1} & v_{z2} & \cdots & v_{zN} \end{bmatrix} \quad 3 \times N \quad (\text{Eq 10-7})$$

The N -sample estimate of the weight matrix \tilde{W}_N of the RBF network VCG model can be determined to minimize the objective function $F_N(W, V_N)$

$$F_N(W, V_N) = \frac{1}{N} \sum_{t=1}^N (V_N - WG) \quad (\text{Eq 10-8})$$

$$\tilde{W}_N = \arg \min_w \{F_N(W, V_N)\} \quad (\text{Eq 10-9})$$

and the estimate can be obtained using the pseudoinverse:

$$W = V_N (G^T G)^{-1} G^T \quad (\text{Eq 10-10})$$

10.4 Transformation from VCG to standard 12 lead ECG signals

Numerous attempts have been made previously to estimate the transformation matrix between 12-lead ECG and VCG signals [2, 13-17]. Dower matrix (see Eq 10-11) is the most famous and generalized one, and it can be used to derive the 12-lead ECG signals from the VCG. Therefore the whole measurements including 12-lead ECG and VCG can be simulated by this investigated RBF model.

$$\text{Dower transformation matrix } \mathbf{D} = \begin{bmatrix} -0.515 & 0.157 & -0.917 \\ 0.044 & 0.164 & -1.387 \\ 0.882 & 0.098 & -1.277 \\ 1.213 & 0.127 & -0.601 \\ 1.125 & 0.127 & -0.086 \\ 0.831 & 0.076 & 0.230 \\ 0.632 & -0.235 & 0.059 \\ 0.235 & 1.066 & -0.132 \end{bmatrix} \quad (\text{Eq 10-11})$$

If we have the VCG data in matrix $V (3 \times N)$, the eight leads (I, II, v1-v6) $S (8 \times N)$ can be derived by $S = DV$ except the mathematical calculated augment leads.

This generalized Dower matrix can be used to derive 12-lead ECGs when we only have VCG signals. If the 12-lead ECG signals are recorded simultaneously with VCG, the transformation matrix S can also be estimated for the specified person using either the linear or nonlinear regression (see Eq 10-12).

$$\tilde{D} = S (V^T V)^{-1} V^T \quad (\text{Eq 10-12})$$

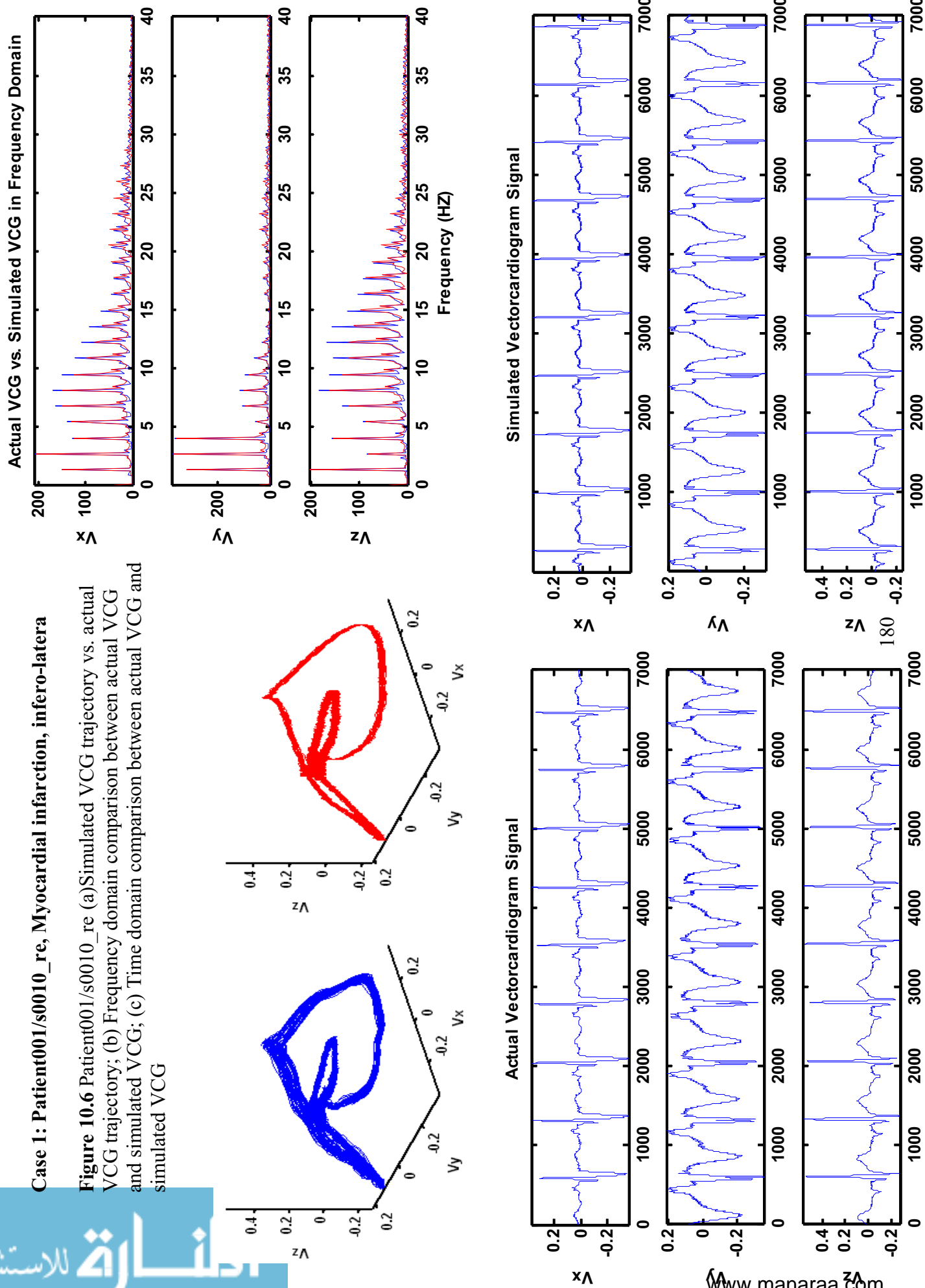
10.5 Implementation results

Figure 10.6, Figure 10.7, Figure 10.8, Figure 10.9, and Figure 10.10 show the implementations results of radial basis simulation models for healthy control subjects,

and patients with myocardial infarction, valvular heart disease, or bundle branch block. The simulated heart electrical activities in Frank XYZ orthogonal directions are compared in time domain, frequency domain, and state space domain. It is found that the investigated RBF simulation model can effectively track the pathological morphology patterns.

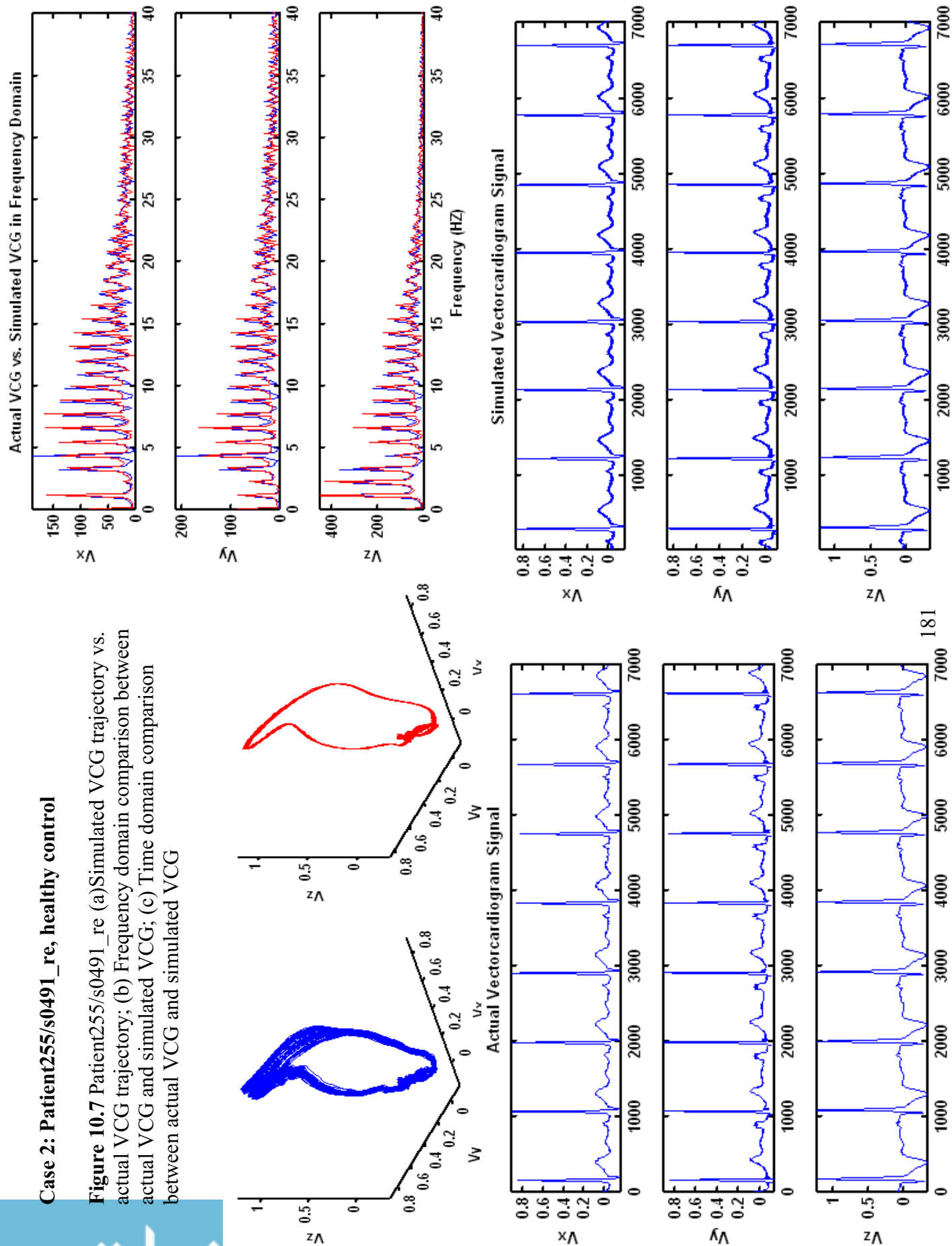
Case 1: Patient001/s0010_re, Myocardial infarction, infero-latera

Figure 10.6 Patient001/s0010_re (a) Simulated VCG trajectory vs. actual VCG trajectory; (b) Frequency domain comparison between actual VCG and simulated VCG; (c) Time domain comparison between actual VCG and simulated VCG



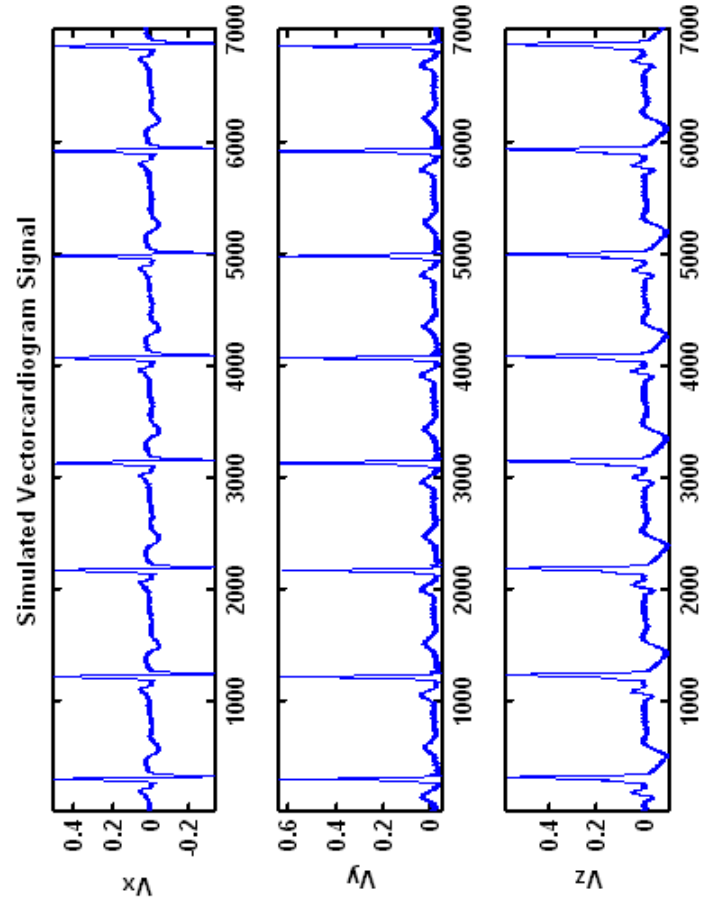
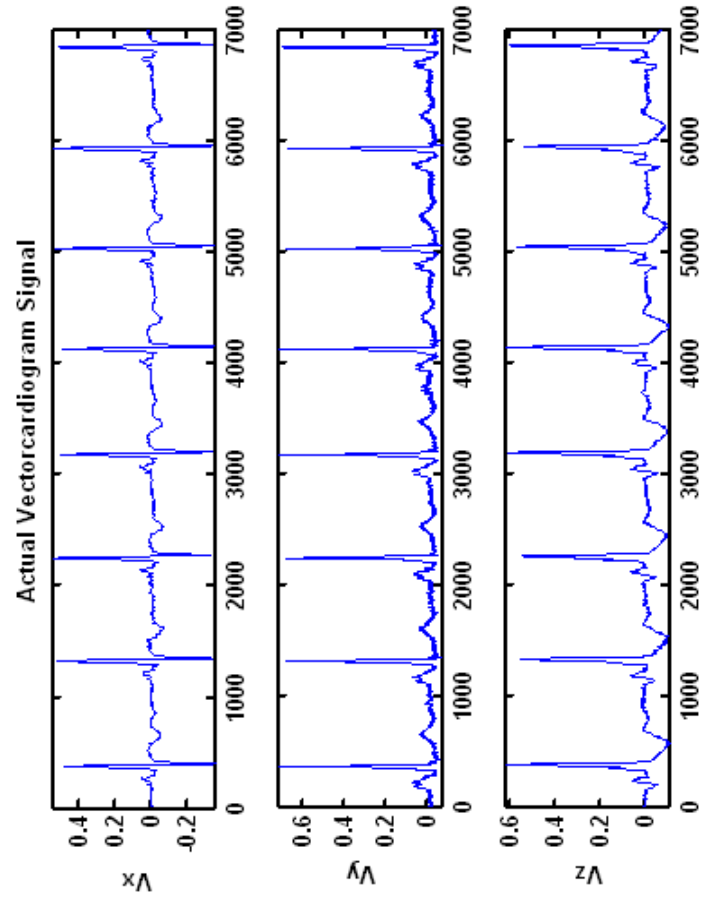
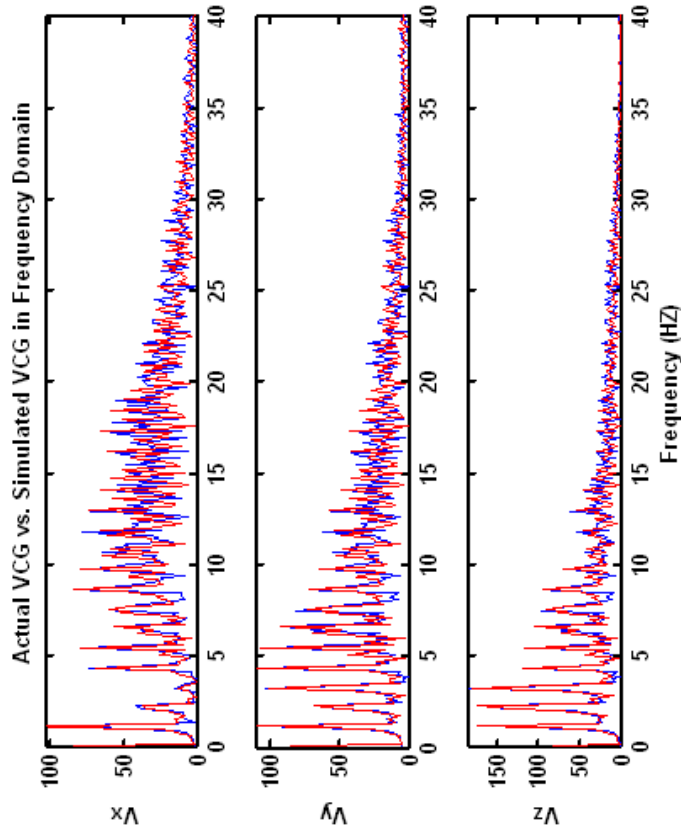
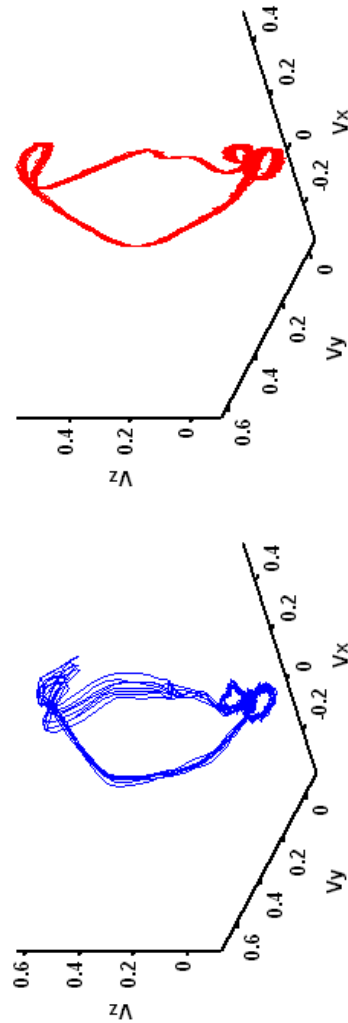
Case 2: Patient255/s0491_re, healthy control

Figure 10.7 Patient255/s0491_re (a) Simulated VCG trajectory vs. actual VCG trajectory; (b) Frequency domain comparison between actual VCG and simulated VCG; (c) Time domain comparison between actual VCG and simulated VCG



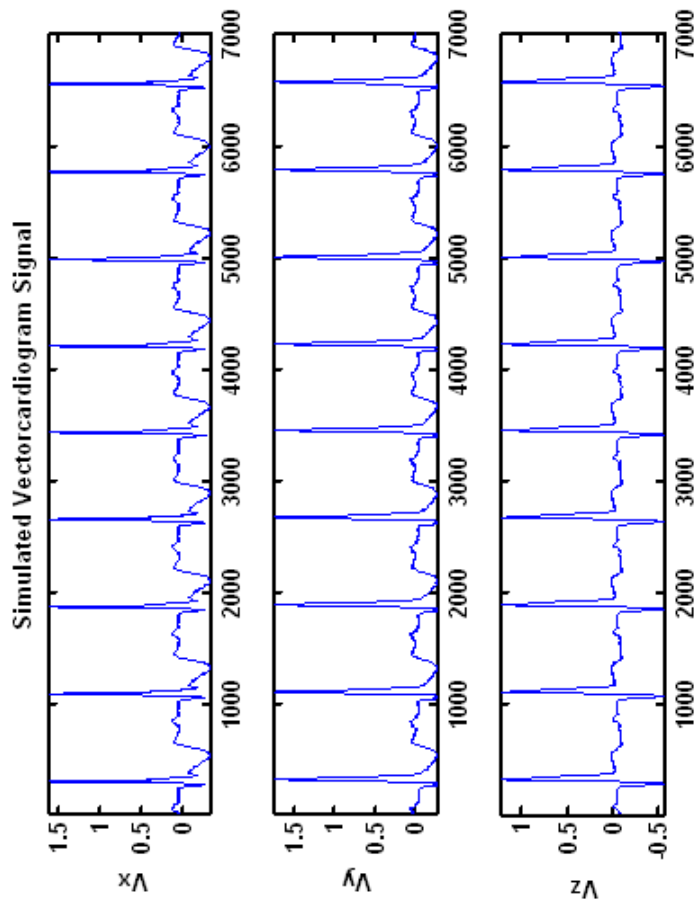
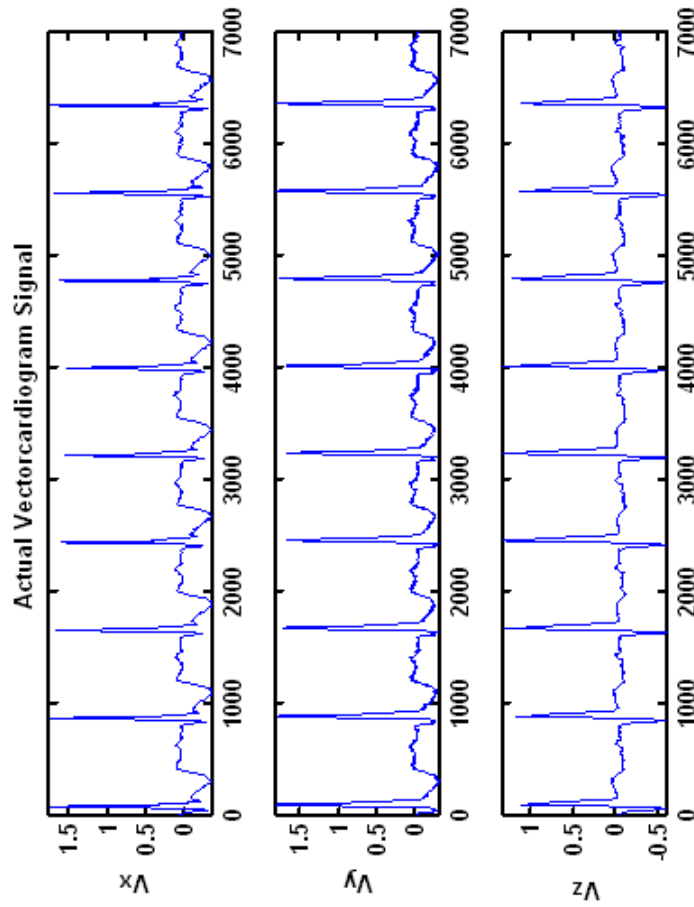
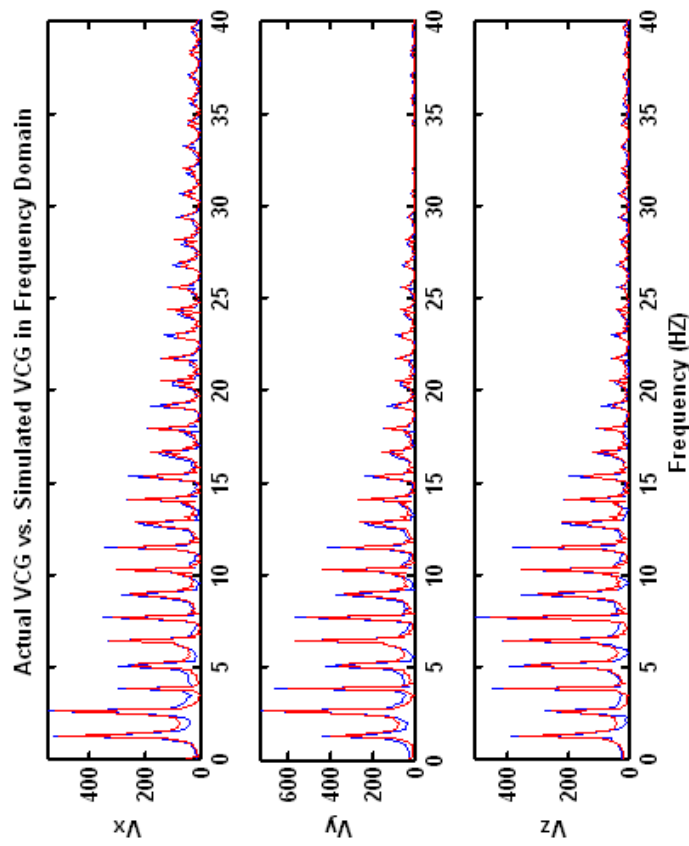
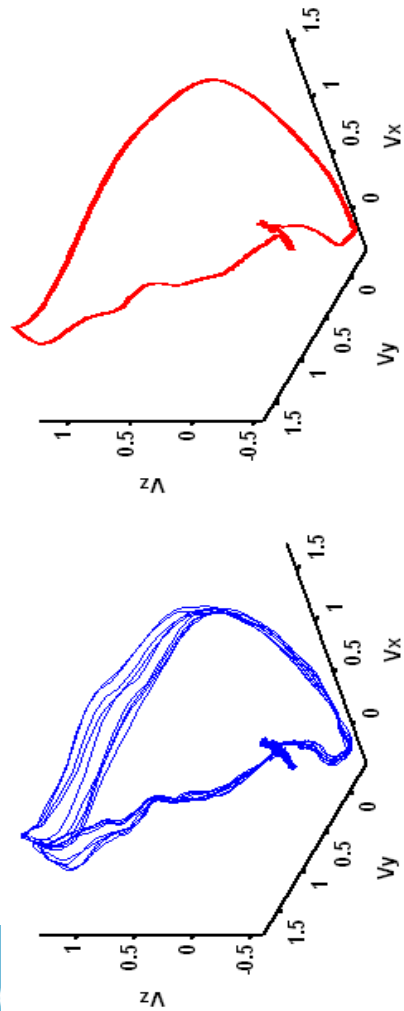
Case 3: Patient005/s0101Ire, Myocardial Infarction, Anterior

Figure 10.8 Patient005/s0101Ire (a) Simulated VCG trajectory vs. actual VCG trajectory; (b) Frequency domain comparison between actual VCG and simulated VCG; (c) Time domain comparison between actual VCG and simulated VCG



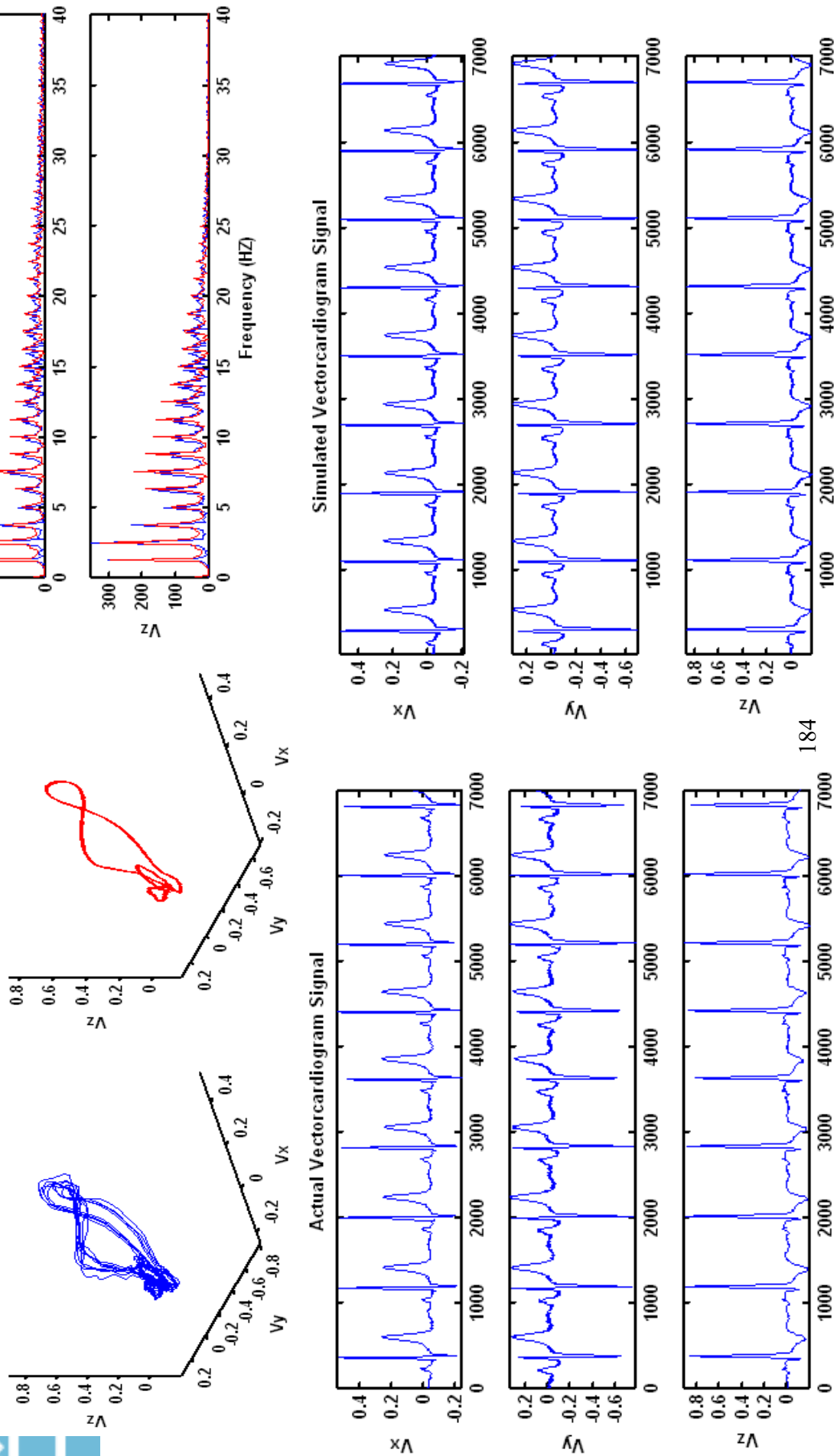
Case 4: Patient106/s0030_re, Valvular heart disease, prosthetic valve

Figure 10.9 Patient106/s0030_re (a) Simulated VCG trajectory vs. actual VCG trajectory; (b) Frequency domain comparison between actual VCG and simulated VCG; (c) Time domain comparison between actual VCG and simulated VCG



Case 5: Patient175/s0009_re, bundle branch block

Figure 10.10 Patient175/s0009_re (a) Simulated VCG trajectory vs. actual VCG trajectory; (b) Frequency domain comparison between actual VCG and simulated VCG; (c) Time domain comparison between actual VCG and simulated VCG



10.6 Summary

In this chapter, we have shown that the data-driven RBF network VCG model can effectively capture the topology of actual VCG trajectory, and yield similar spectrum in the frequency domain. The accurate modeling of VCG can facilitate the understanding of the heart dynamics. The possible applications of this data-driven model are listed as following:

(1) Feature extraction

The model parameters such as RBF weights, HRV distribution parameters can be used as features for the further diagnosis. Therefore, numerous VCG and ECG data is reduced to limited amount of features while preserve the same information.

(2) VCG and ECG data compression

We knew that hundreds of gigabytes VCG and ECG data will be stored for the real-time high sampling ECG recorder. Since the RBF model replicates the actual VCG topology, those parameters can be saved and used for simulating a long duration VCG data in the future. Therefore, the VCG and ECG data are compressed to save the disk storage space.

(3) Algorithm evaluation

This data-driven model can be fitted to different group of diseases and patients. The well trained model for different pathologies will be able to generate several various simulating VCG and ECG data which can be used to test the QRST characteristic point detection algorithms, QRST cancellation algorithms, adaptive filtering algorithms, and classification algorithms etc.

(4) Disease prognosis

The well trained model captures all the characteristics from the actual data, and the actual real-time heart monitoring signals can be compared the simulation model trained in the healthy conditions. The similarity differences can serve as the performance measure for the prognostic purpose.

The investigated RBF VCG model compressed information about the actual VCG trajectory dynamics, and the VCG signals can also be projected to standard 12-lead ECG signals with the transformation matrix. The future research will focus on exploring the above applications of the RBF network VCG model.

10.7 Reference

- [1] G. E. Dower and H. B. Machado, "XYZ data interpreted by a 12-lead computer program using the derived electrocardiogram," *Journal of electrocardiology*, vol. 12, pp. 249-261, 1979.
- [2] D. E. Gustafson, A. Akant, and T. L. Johnson, "Linear transformations relating the electrocardiogram and vectorcardiogram," *Computers and Biomedical Research*, vol. 9, pp. 337-348, 1976.
- [3] J. B. Kadtko and M. N. Kremlivsky, "Signal and pattern detection or classification by estimation of continuous dynamical models." vol. 20020133317 United States: Nonlinear Solutions, Inc., 2002.
- [4] D. M. Schreck, M. S. Viscito, and C. Brotea, "The derived N-Lead electrocardiogram," *Annals of Emergency Medicine*, vol. 44, pp. S73-S74, 2004.
- [5] H. Yang, S. T. Bukkapatnam, and R. Komanduri, "Nonlinear adaptive wavelet analysis of electrocardiogram signals," *Physical Review E (Statistical, Nonlinear, and Soft Matter Physics)*, vol. 76, p. 026214, 2007.

- [6] F. Marciano, M. L. Migaux, D. Acanfora, G. Furgi, and F. Rengo, "Quantification of Poincare maps for the evaluation of heart rate variability," 1994, pp. 577-580.
- [7] T. Kuusela, T. Shepherd, and J. Hietarinta, "Stochastic model for heart-rate fluctuations," *Physical Review E*, vol. 67, p. 061904, 2003.
- [8] P. C. Ivanov, L. A. N. Amaral, A. L. Goldberger, S. Havlin, M. G. Rosenblum, Z. R. Struzik, and H. E. Stanley, "Multifractality in human heartbeat dynamics," *Nature*, vol. 399, pp. 461-465, 1999.
- [9] S. T. S. Bukkapatnam, H. Yang, and R. Komanduri, "A comparative analysis of alternative approaches for the classification of atrial fibrillation (AF) episodes from EKG signals," *Journal of Electrocardiography (under review)*.
- [10] A. C. Cohen, "Maximum Likelihood Estimation in the Weibull Distribution Based on Complete and on Censored Samples," *Technometrics*, vol. 7, pp. 579-588, 1965.
- [11] M. T. Hagan, H. B. Demuth, and M. H. Beale, *Neural Network Design*: PWS Pub. Co., December 29, 1995.
- [12] P. E. McSharry, G. D. Clifford, L. Tarassenko, and L. A. Smith, "A dynamical model for generating synthetic electrocardiogram signals," *IEEE Transactions on Biomedical Engineering*, vol. 50, pp. 289-294, 2003.
- [13] S. P. Nelwan, J. A. Kors, S. H. Meij, J. H. van Bommel, and M. L. Simoons, "Reconstruction of the 12-lead electrocardiogram from reduced lead sets," *Journal of electrocardiology*, vol. 37, pp. 11-18, 2004.
- [14] G. E. Dower, H. B. Machado, and J. A. Osborne, "On deriving the electrocardiogram from vectorcardiographic leads," vol. 3, p. 87, 1980.
- [15] G. E. Dower, A. Yakush, S. B. Nazzal, R. V. Jutzy, and C. E. Ruiz, "Deriving the 12-lead electrocardiogram from four (EASI) electrodes," *Journal of electrocardiology*, vol. 21, pp. S182-S187, 1988.

- [16] L. Edenbrandt and O. Pahlm, "Vectorcardiogram synthesized from a 12-lead ECG: Superiority of the inverse Dower matrix," *Journal of electrocardiology*, vol. 21, pp. 361-367, 1988.
- [17] D. Wei, T. Kojima, T. Nakayama, and Y. Sakai, "Method for deriving standard 12-lead electrocardiogram, and monitoring apparatus using the same." vol. 20020045837: Kohden Corporation, 2002.

CHAPTER XI

CONCLUSIONS AND FUTURE WORK

One hundred years ago, researchers were striving on the design of meticulous cardiovascular sensor monitoring system. Nowadays, a variety of sensor networks and dedicated super computers are taken advantage to collect high precision heart monitoring signals in real time. The huge amount of observation data offers an unprecedented opportunity to understand the hidden heart nature buried in the sea of data. This dissertation focused on data driven nonlinear stochastic modeling and analysis of complex cardiovascular systems towards the diagnostic and prognostic applications. The major conclusions and future work recommendations are as follows:

11.1 Conclusions

A novel customized wavelet function approach is developed to resolve the big data issue in the cardiovascular monitoring field. This method uses near periodic patterns of electrocardiogram (ECG) signals to optimally design a wavelet for the specific cardiovascular applications. This customized wavelet successfully reduces the compactness of ECG signal representation by around two orders of magnitude, which directly increase data compression ratio and benefit the telemedicine.

Sophisticated visualization tools are also developed to explore unexpected patterns and interpret hidden evidences. Traditional representation habits, like time domain

representation, can prevent us from extracting new understandings. Frequency domain, time-frequency domain, animations, heart and torso finite element models, and state space domain will give new promising insights of system dynamics from different perspectives.

Advanced rigorous wavelet analysis and fractal dynamic study are also conducted to quantitatively extract more sensitive features to cardiovascular pathological variations instead of the extraneous noises. The medical diagnostic models are designed to mathematically associate the effective nonlinear features with two studied cardiovascular diseases - Myocardial Infarction (MI) and Atrial Fibrillation (AF). The classification accuracies are found to be as high as 96% in sensitivity for MI and >90% for different stages of AF.

In order to address the increasing complexity of datasets, a local recurrence model is developed to make effective forecasting in the nonstationary chaotic environments. This model investigates the system local recurrence behaviors by dividing the delay reconstructed system state space into multiple stationary segments. Simulation study shows significant prediction accuracy improvements over commonly used stationary methods. This model is also successfully implemented to predict shift-wise throughputs in multistage manufacturing assembly lines, and yields >74% accuracy improvement in the real world.

11.2 Future work

Aiming at healthcare excellence, future work will keep on sensor based modeling and analysis of complex heart system. The continued improvements and prospected studies will be as follows:

First, risk prognostic frameworks for the complex cardiovascular system will be further advanced and studied for the ischemia conditions and sleep apnea subjects. It is conceptually known that human heart is a complex organ system with a built-in capacity for self-regulation and adaptation. Myocardial infarction patients always have self-organizing transitions between ischemic and non-ischemic conditions, and sleep apnea patients have discontinuous pauses in respirations during sleep. There are high risks of sudden cardiac death from these cardiovascular transitions. The research objective is to on-line estimate the potential risk and real-time predict the future cardiovascular statuses. The accurate predictions will not only have great academic and economic impacts, but also give the cardiovascular patients a better chance for a healthy life.

In this dissertation, 12-lead ECG and 3-lead VCG signals are studied. The investigation can be extended to multi-sensor-fusion and monitoring schemes of cardiovascular systems. Monitoring sensor signals may include heart sound, respiration, blood pressure, electrooculogram (EOG), electromyography (EMG), electroencephalogram (EEG), magnetic resonance imaging (MRI), or nuclear magnetic resonance imaging (NMRI) etc. Multi-sensor-fusion may also be combined with nonlinear dynamics, fractal analysis, higher-order statistical processing and knowledge-based approaches towards effective interpretations of physiological activities. Given the

complexity of underlying process, this research direction has high potentials to give rise to the novel advanced signal processing approaches.

Thirdly, mathematical modeling of biomechanics in the physiological system will facilitate not only the understanding of exhibited physiological signals, but also autonomic organism functioning. The intriguing example is ancient Chinese medicine - acupuncture and moxibustion. The stimulation of certain spots in human body will help relieve pain and reach the body homeostasis. This acupuncture medicine is developed through practice for thousands of years and shows effective applications in various kinds of diseases like trigeminal neuralgia, palsy, tracheitis, arthritis and so on, but the underlying mechanics have not been fully understood yet. Sensor based modeling approach will assist the explanation of underlying biomechanics from a data-driven perspective of view. The effective mathematical biomechanical modeling will help further improve the current medicine treatments, and thus lead to the healthcare excellence.

VITA

Hui Yang

Candidate for the Degree of

Doctor of Philosophy

Dissertation: NONLINEAR STOCHASTIC MODELING AND ANALYSIS OF
CARDIOVASCULAR SYSTEM DYNAMICS – DIAGNOSTIC AND
PROGNOSTIC APPLICATIONS

Major Field: Industrial Engineering and Management

Biographical:

Personal Data: Born in Nanjing, Jiangsu province, People's Republic of China

Education:

Received Bachelor of Science degree in Electrical Engineering from China University of Mining and Technology in Beijing, P. R. China, in June 2002; received Master of Science degree with a major in Electrical Engineering at China University of Mining and Technology in Beijing, P. R. China, in June 2005; completed Doctor of Philosophy degree with a major in Industrial Engineering and Management at Oklahoma State University in May, 2009.

Experience:

Employed by Oklahoma State University, School of Industrial and Management as a graduate research assistant and teaching assistant, from August 2005 to December 2008.

Professional Memberships:

- Institute for Operations Research and the Management Sciences (INFORMS)
- The Industrial Engineering Honor Society (Alpha Pi Mu)
- Institute of Electrical and Electronics Engineers (IEEE)
- Institute for Industrial Engineers (IIE)
- American Society of Quality (ASQ)

Name: Hui Yang

Date of Degree: May, 2009

Institution: Oklahoma State University

Location: Stillwater, Oklahoma

Title of Study: NONLINEAR STOCHASTIC MODELING AND ANALYSIS OF
CARDIOVASCULAR SYSTEM DYNAMICS – DIAGNOSTIC AND
PROGNOSTIC APPLICATIONS

Pages in Study: 192

Candidate for the Degree of Doctor of Philosophy

Major Field: Industrial Engineering and Management

Scope and Method of Study:

The purpose of this investigation is to develop monitoring, diagnostic and prognostic schemes for cardiovascular diseases by studying the nonlinear stochastic dynamics underlying complex heart system. The employment of a nonlinear stochastic analysis combined with wavelet representations can extract effective cardiovascular features, which will be more sensitive to the pathological dynamics instead of the extraneous noises. While conventional statistical and linear systemic approaches have limitations for capturing signal variations resulting from changes in the cardiovascular system state. The research methodology includes signal representation using optimal wavelet function design, feature extraction using nonlinear recurrence analysis, and local recurrence modeling for state prediction.

Findings and Conclusions:

- New representation scheme for the ECG signals by an optimal wavelet function design which yields one order of magnitude compactness reduction compared to the conventional wavelets in terms of entropy.
- New spatiotemporal representation scheme for the VCG signals, which significantly assists the interpretation of vectorcardiogram and facilitates the exploration of related important spatiotemporal cardiovascular dynamics.
- Developed a classification and regression tree (CART) model to integrate the cardiologists' knowledge towards accurate classification of Atrial Fibrillation (AF) states from sparse datasets.
- Developed a Myocardial Infarction (MI) classification model using recurrence quantification analysis and spatial octant features of VCG attractor dynamics, which detects MI up to about 96% accuracy in both sensitivity and specificity.
- Designed a local recurrence prediction model for real time medical prognosis and risk assessment of cardiovascular problems, which is particularly suitable for the implementation in the nonlinear and nonstationary environment.

ADVISER'S APPROVAL: Dr. Satish T. S. Bukkapatnam Dr. Ranga Komanduri